

**Detailed Studies of neutrino oscillations with  
atmospheric neutrinos of wide energy range from 100  
MeV to 1000 GeV in Super-Kamiokande**

Jun Kameda

September 2002

Doctor Thesis, University of Tokyo



## Abstract

An experimental study on the neutrino oscillations with atmospheric neutrinos of wide energy range from 100 MeV to 1000 GeV was carried out with the data taken by the Super-Kamiokande detector. The data used in this thesis are 1144 days of fully-contained and partially-contained events, 1138 days of upward through-going muons, and 1117 days of upward-stopping muons. The data show a deficit of the upward-going  $\nu_\mu$ 's, and it implies neutrino oscillation.

Several theories predict neutrino oscillations which have  $L/E^n$  type energy dependence where  $E$  is the neutrino energy and  $L$  is the flight length of neutrino. We measured the energy dependence of the neutrino oscillation, and the result is  $n = 1.14 \pm 0.11$ . We found that the neutrino oscillation induced by the finite masses of neutrinos is the most favored theory. The allowed region of the oscillation parameters for the neutrino oscillation due to finite neutrino masses and mixing is obtained to be  $1.8 \times 10^{-3} \text{eV}^2 < \Delta m^2 < 4.5 \times 10^{-3} \text{eV}^2$  and  $0.89 < \sin^2 2\theta$  at 90% C.L..

Also we tested the neutrino oscillation induced by a flavour changing neutral current (FCNC) in matter in the Earth for massless neutrinos. We found that the hypothesis is excluded. The hypothesis of the neutrino decay to a sterile state  $\nu_3 \rightarrow X$  was also tested. We carried out analyses for two special cases:  $\Delta m^2 \rightarrow \infty$  and  $\Delta m^2 \rightarrow 0$ . We found the first case is quickly excluded, and the second case is also disfavoured at 90% C.L..

We conclude that the data observed in Super-Kamiokande show strong evidence for neutrino oscillation generated by neutrino masses and mixing.

## Acknowledgment

I would like to express my great appreciation to my advisor, Prof. Takaaki Kajita for introducing me to the Super-Kamiokande experiment. He has supported and encouraged me on many occasion during my graduate course. He also gave me a chance to study the atmospheric neutrino and I have learned many things under his excellent guidance. This thesis would never be completed without it.

I would like to express my gratitude to Prof. Y.Totsuka, the spokesperson of the Super-Kamiokande experiment, Prof. Y.Suzuki, Prof. M.Nakahata, and Prof. Y.Itow. They gave me advices and encouraged me in many cases.

I am grateful especially to the members of the atmospheric neutrino and proton decay analysis group. K.Kaneyuki, M.Miura, M.Shiozawa, S.Moriyama, T.Hayakawa, S.Kasuga, Y.Hayato, K.Ishihara, K.Okumura, Y.Obayashi, T.Toshito, M.Etoh, Y.Kanaya, K.Kobayshi, M.Ishitsuka, H.Sobel, E.Kerns, C.K.Jung, L.Wai, J.Gourge, C.McGrew, C.M.Mauger, M.Messier, K.Scholberg, C.W.Walter, A.Habig, G.Guillian and other U.S. colleagues gave me many support for my work on the atmospheric neutrino. This thesis is greatly indebted to them.

I also have to thank the other ICRR staff and graduate students, Y.Fukuda, Y.Takeuchi, Y.Koshio, N.Sakurai, S.Nakayama, and S.Yamada. They were willing to give me their useful knowledge which was necessary for my work and encourage me on many occasion. I am also thankful to all the Super-Kamiokande collaborators and the staff in the Kamioka Observatory for their continuous support and kind consideration. I gratefully acknowledge the cooperation of Kamioka Mining and Smelting Company.

Finally, I wish to express my deep gratitude to my family.

# Contents

<b>1</b>	<b>Introduction</b>	<b>1</b>
1.1	Neutrino . . . . .	1
1.2	Neutrino Oscillations . . . . .	3
1.2.1	Other Neutrino Oscillation Models . . . . .	4
1.2.2	Violation of Lorentz Invariance . . . . .	4
1.2.3	Violation of Equivalence Principle . . . . .	5
1.2.4	Flavour Changing Neutral Current(FCNC) . . . . .	6
1.3	Neutrino Decay . . . . .	6
1.4	Neutrino Oscillation Experiments . . . . .	7
1.4.1	Reactor Neutrino Experiments . . . . .	8
1.4.2	Accelerator Neutrino Experiments . . . . .	8
1.4.3	Meson Factory Experiments . . . . .	9
1.4.4	Solar Neutrino Experiments . . . . .	9
1.4.5	Atmospheric Neutrino Experiments . . . . .	10
1.5	Motivation of This Thesis . . . . .	13
<b>2</b>	<b>Atmospheric Neutrinos</b>	<b>15</b>
2.1	Overview . . . . .	15
2.2	Calculated Flux and the Systematic Uncertainties . . . . .	18
2.3	Observation of Atmospheric Neutrinos in Super-Kamiokande . . . . .	20
2.3.1	Fully Contained(FC) events . . . . .	22
2.3.2	Partially Contained(PC) events . . . . .	22
2.3.3	Upward-stopping muons and upward-through going muons . . . . .	22
<b>3</b>	<b>Super-Kamiokande Detector</b>	<b>25</b>
3.1	Overview . . . . .	25
3.2	Detection Principle . . . . .	29

3.3	Water Tank . . . . .	29
3.4	Photomultiplier Tubes . . . . .	31
3.4.1	PMT for Inner Detector . . . . .	31
3.4.2	PMT for Outer Detector . . . . .	32
3.4.3	Stability of the PMTs . . . . .	33
3.5	Veto Counters on Cable holes . . . . .	33
3.6	Ultra Pure Water and Purification System . . . . .	34
3.7	Rn-free Air System . . . . .	35
3.8	Data Acquisition System . . . . .	35
3.8.1	Inner Detector Data Acquisition System . . . . .	36
3.8.2	Outer Detector Data Acquisition System . . . . .	37
3.8.3	Trigger System . . . . .	37
3.8.4	Off-line System . . . . .	38
<b>4</b>	<b>Calibration</b> . . . . .	<b>49</b>
4.1	Overview . . . . .	49
4.2	Relative Gain Calibration . . . . .	49
4.3	Timing Calibration . . . . .	50
4.4	Water Attenuation Length Measurement I . . . . .	51
4.5	Water Attenuation Length Measurement II . . . . .	52
4.6	Absolute Energy Calibration . . . . .	55
4.6.1	Muon Decay Electrons . . . . .	55
4.6.2	Electrons from Linear accelerator (LINAC) . . . . .	57
4.6.3	Neutrino Induced $\pi^0$ . . . . .	59
4.6.4	Cosmic Ray Muons I . . . . .	59
4.6.5	Cosmic Ray Muons II . . . . .	60
4.6.6	Summary of the absolute energy calibration . . . . .	62
<b>5</b>	<b>Event Selection</b> . . . . .	<b>63</b>
5.1	Overview . . . . .	63
5.2	Event Selection for Fully Contained Events . . . . .	63
5.2.1	1st Reduction . . . . .	63
5.2.2	2nd Reduction . . . . .	65
5.2.3	3rd Reduction . . . . .	66
5.2.4	4th Reduction . . . . .	69
5.2.5	Eye Scanning . . . . .	70

5.3	Event Selection for Partially Contained Events . . . . .	71
5.3.1	1st Reduction . . . . .	71
5.3.2	2nd Reduction . . . . .	71
5.3.3	3rd Reduction . . . . .	75
5.3.4	4th Reduction . . . . .	77
5.3.5	5th Reduction . . . . .	78
5.3.6	Eye Scanning . . . . .	78
5.4	Event Selection for Upward-going Muons . . . . .	80
5.4.1	1st Reduction . . . . .	80
5.4.2	2nd Reduction . . . . .	80
5.4.3	3rd Reduction . . . . .	82
5.4.4	Eye Scanning and Manual Fitting . . . . .	82
5.5	Background Subtraction for Upward-going Muons . . . . .	83
<b>6</b>	<b>Event Reconstruction for FC and PC events</b>	<b>87</b>
6.1	Overview . . . . .	87
6.2	Vertex Fitter . . . . .	89
6.2.1	Pfit . . . . .	89
6.2.2	Ring Edge Finding . . . . .	89
6.2.3	TDC fit . . . . .	90
6.2.4	Performance of TDCfit . . . . .	92
6.3	Ring-Counting . . . . .	92
6.3.1	Ring Candidate Search . . . . .	92
6.3.2	Test of the Ring Candidate . . . . .	94
6.3.3	Performance of the Ring-Counting . . . . .	96
6.4	Particle-Identification . . . . .	96
6.4.1	Estimation of the Particle Type . . . . .	98
6.4.2	The Expected p.e. Distribution for Electrons . . . . .	99
6.4.3	The Expected p.e. Distribution for Muons . . . . .	99
6.4.4	The Expected p.e. Distribution for Scattered Light . . . . .	101
6.4.5	Performance of PID . . . . .	101
6.5	MS fit . . . . .	101
6.5.1	Performance of MS fit . . . . .	104
6.6	Momentum Estimation . . . . .	108

<b>7</b>	<b>Monte Carlo Simulation</b>	<b>111</b>
7.1	Overview	111
7.2	Neutrino interaction	111
7.2.1	Elastic scattering off electron ( $\nu + e^- \rightarrow \nu + e^-$ )	112
7.2.2	Quasi elastic scattering off nucleon ( $\nu + N \rightarrow l + N'$ )	112
7.2.3	Single meson productions via baryon resonances ( $\nu + N \rightarrow l(\nu) + N' + \text{meson}$ )	114
7.2.4	Coherent pion production off $^{16}\text{O}$ ( $\nu + ^{16}\text{O} \rightarrow l(\nu) + ^{16}\text{O} + \pi$ )	121
7.2.5	Deep inelastic scattering ( $\nu + N \rightarrow l(\nu) + N' + \text{hadrons}$ )	121
7.2.6	Fermi motion of a nucleon	123
7.2.7	Nuclear effects	124
7.3	Detector simulation	127
7.3.1	Propagation of Particles	127
7.3.2	Cherenkov photon propagation	128
7.3.3	Detection of Cherenkov photon	128
<b>8</b>	<b>Data Summary</b>	<b>131</b>
8.1	Fully Contained Events and Partially Contained Events	131
8.1.1	Vertex Distributions	133
8.1.2	Momentum Distributions	136
8.1.3	Number of Rings and PID distribution	136
8.1.4	Background Estimation	137
8.1.5	$\mu/e$ Double Ratio $R$	142
8.1.6	Zenith Angle Distributions	145
8.1.7	$Up/Down$ ratio	145
8.1.8	East-West Effect	148
8.2	Upward-going Muons	153
8.2.1	Zenith Angle Distribution for Upward-going Muons	155
8.3	Summary	156
<b>9</b>	<b>Analysis and Results</b>	<b>159</b>
9.1	Definition of $\chi^2$	159
9.2	Calculation Methods of Expected Event Rates	161
9.2.1	Expected Event Rate of FC and PC events	161
9.2.2	Systematic Uncertainties	162
9.2.3	Expected flux of Upward-going muons	166
9.2.4	Systematic Uncertainties	166

9.3	Correlations between the Systematic errors . . . . .	168
9.3.1	Correlations between $\beta_m$ , $\beta_s$ , $\rho$ , $\rho_s$ and $\rho_t$ . . . . .	169
9.3.2	Correlation between $\eta_s$ and $\eta_m$ . . . . .	171
9.4	$\nu_\mu \leftrightarrow \nu_\tau$ Oscillation . . . . .	171
9.5	Neutrino Oscillations with $L/E^n$ Dependence . . . . .	172
9.6	Flavour Changing Neutral Current . . . . .	179
9.7	Neutrino Decay . . . . .	181
9.7.1	Neutrino Decay Analysis using Neutral Current Events . . . . .	184
9.7.2	Systematic Uncertainty in the <i>Up/Down</i> Ratio of the NC Sample . . . . .	188
9.7.3	Definition of $\chi^2$ and Results . . . . .	191
<b>10</b>	<b>Conclusions</b>	<b>193</b>
<b>A</b>	<b>THRMU-fit</b>	<b>195</b>
<b>B</b>	<b>Calculation of Expected Flux of Upward-going Muons</b>	<b>197</b>
B.1	Calculation of Upward Going Muon Flux . . . . .	197



# Chapter 1

## Introduction

### 1.1 Neutrino

The first postulation of the neutrino was made by W.Pauli in 1930 as a massless and neutral particle with spin 1/2 to explain the missing momentum in  $\beta$  decay [1]. The existence of the neutrino was confirmed by F.Rines and C.Cowan in 1956 [2] by detecting anti-neutrinos from a nuclear reactor by the interaction:

$$\bar{\nu}_e + p \rightarrow e^+ + n \quad (1.1)$$

followed by the interaction  $e^+ + e^- \rightarrow 2\gamma$  and  $\gamma$  rays from neutron capture on the Cd nucleus. Another flavour of neutrino,  $\nu_\mu$ , was discovered by G.Danby *et al.* in 1962 by observing the interaction  $\nu_\mu + N \rightarrow \mu + X$  using a several GeV neutrino beam from the decay in flight of pions  $\pi \rightarrow \mu + \nu_\mu$  at Brookhaven [3].

The structure of the weak interaction (V-A type interaction) was settled by the postulation of parity violation by T.Lee and C.Yang [5], and afterwards by both the demonstration of parity violation by C.Wu *et al.* using  $^{60}\text{Co}$   $\beta$  decay in 1957 [6], and the measurement of the neutrino helicity by M.Goldhaber *et al.* in 1958 [4].

In the late 1960s, S.Glashow [7], S.Weinberg [8], and A.Salam *et al.* [9] proposed a  $SU(2) \times U(1)$  gauge theory which described the electromagnetic and the weak interactions in one framework (the electroweak theory). Over the last 30 years, this theory has been verified experimentally with high accuracy, and it constitutes a part of the theory of elementary particles at present. The first experimental support was given by the observation of the weak neutral current interaction by the interaction  $\bar{\nu}_\mu + e^- \rightarrow \bar{\nu}_\mu + e^-$  by F.Hasert *et al.* at CERN in 1973 [10]. The intermediate bosons,  $W^\pm$  and  $Z^0$ , were directly observed at the CERN  $p\bar{p}$  collider experiment in 1983 [11, 12]. The precise measurement of the decay width of  $Z^0$  boson in the high energy  $e^+e^-$  colliders, LEP at CERN and SLC at SLAC, gave another important discovery on neu-

Flavour	Mass limit(95% C.L.)
$\nu_e$	3 eV
$\nu_\mu$	0.17 MeV
$\nu_\tau$	18.2 MeV

Table 1.1: Experimental limits on neutrino masses.

trinos, namely that the number of active neutrinos with the mass  $m_\nu < M_{Z_0/2} \simeq 45$  GeV is 3 [13, 14, 15, 16, 17, 18].

Today, the elementary particles and their interactions are thought to be described by a  $SU(3) \times SU(2) \times U(1)$  gauge theory called the 'Standard Model'. In the Standard Model, neutrinos are described as exactly massless particles. But, there is no fundamental reason that forbids finite masses of neutrinos.

Experimentally, it is known that the neutrino masses are, if they exist, much smaller than those of other elementary particles. For example, the  $\nu_e$  is lighter than the electron by more than 5 orders of magnitude. Several experiments have been carried out to find finite neutrino masses by kinematical measurements in particle decays. Table 1.1 shows the recent experimental limits on neutrino masses. The upper limit on the  $\nu_e$  mass is obtained from the measurement of the  $\beta$  spectrum from  ${}^3\text{H}$  beta decay [19]. The upper limit on  $\nu_\mu$  mass is obtained from the muon spectrum measurement in the pion decay  $\pi \rightarrow \mu + \nu_\mu$  [20], and the limits on  $\nu_\tau$  mass is from the detailed analysis of  $\tau$  decay  $\tau \rightarrow \pi^- \pi^- \pi^+ \nu_\tau$  [21]. No evidence for finite neutrino masses is obtained from the direct measurement experiments. Another bound on neutrino masses comes from cosmology. The energy density of the background neutrinos which were produced in the early universe should be less than the critical density  $\rho_c$ . This condition requires  $\sum_i m_\nu^i < 100$  eV, where the suffix  $i$  runs over the three neutrino species.

The smallness of neutrino masses cannot be explained by the Standard Model in a natural way. The solution to the problem may be explained by a new physics beyond the Standard Model. For example, a theory known as the 'See-saw mechanism' [22] naturally explains the smallness of the neutrino mass, and also predicts that the smallness of neutrino mass has its origin in the new physics of a higher energy scale. Therefore, discovery of finite neutrino masses provides an important step toward a deeper understanding of elementary particle physics.

## 1.2 Neutrino Oscillations

A remarkable consequence of the finite masses of the neutrinos is neutrino oscillation. Flavour oscillations of neutrinos were first proposed by Maki, Nakagawa and Sakata in 1962 [28]. In general, flavour oscillation occurs under the following conditions:

1. Flavour eigenstates are superpositions of the Hamiltonian's eigenstates.
2. Hamiltonian eigenstates with the same momentum have different energies.

To simplify the situation, we concentrate on 2-flavour neutrino oscillation. First, let's assume that two eigenstates of Hamiltonian,  $|\nu_1\rangle$  and  $|\nu_2\rangle$ , exist:

$$H|\nu_1(p)\rangle = E_1|\nu_1(p)\rangle \quad , \quad H|\nu_2(p)\rangle = E_2|\nu_2(p)\rangle \quad (1.2)$$

$$E_1 \neq E_2 \quad (1.3)$$

where  $\nu_1$  and  $\nu_2$  represent the Hamiltonian's eigenstates with a momentum  $p$ , and  $E_1$  and  $E_2$  are their energies. The flavour eigenstates,  $|\nu_\alpha\rangle$  and  $|\nu_\beta\rangle$ , are the superpositions of the Hamiltonian's eigenstates:

$$\begin{pmatrix} |\nu_\alpha\rangle \\ |\nu_\beta\rangle \end{pmatrix} = \begin{pmatrix} \cos\theta & \sin\theta \\ -\sin\theta & \cos\theta \end{pmatrix} \begin{pmatrix} |\nu_1\rangle \\ |\nu_2\rangle \end{pmatrix} \equiv U \begin{pmatrix} |\nu_1\rangle \\ |\nu_2\rangle \end{pmatrix} \quad (1.4)$$

Let  $|\psi(t)\rangle$  represents the state at time  $t$ , and the time development of a state  $|\psi(t)\rangle$  be described by Shrödinger's equation:

$$i \frac{d}{dt} |\psi(t)\rangle = H |\psi(t)\rangle \quad (1.5)$$

In the case that Hamiltonian doesn't explicitly depend on time  $t$ , the solution of this equation can be written as:

$$|\psi(t)\rangle = \exp(-iHt) |\psi(0)\rangle \quad (1.6)$$

where  $|\psi(0)\rangle$  represents the state at  $t=0$ . If  $|\psi(0)\rangle$  is  $|\nu_\alpha\rangle$ ,  $|\psi(t)\rangle$  is written as:

$$|\psi(t)\rangle = \cos\theta \exp(-iE_1t) |\nu_1\rangle + \sin\theta \exp(-iE_2t) |\nu_2\rangle \quad (1.7)$$

Omitting a common phase, the amplitude that  $|\psi(t)\rangle$  is found in  $|\nu_\alpha\rangle$  is written as:

$$\langle \nu_\alpha | \psi(t) \rangle = \cos^2\theta \exp(-i\Delta Et) + \sin^2\theta \quad (1.8)$$

where  $\Delta E \equiv E_1 - E_2$ . Then, the survival probability of  $\nu_\alpha$  after time  $t$  is:

$$\begin{aligned} P(\nu_\alpha \rightarrow \nu_\alpha) &= |\langle \nu_\alpha | \psi(t) \rangle|^2 \\ &= 1 - \sin^2 2\theta \sin^2 \left( \frac{\Delta E}{2} \cdot L_\nu \right) \end{aligned} \quad (1.9)$$

where we have replaced  $t$  with neutrino flight length  $L_\nu \simeq c \cdot t$ . The survival probability of flavour eigenstates has an oscillating form. This is the reason for the name ‘neutrino oscillations’.

In the case that neutrinos have finite masses, the eigenvalues of each eigenstates become  $E_1 = \sqrt{m_1^2 + p^2}$  and  $E_2 = \sqrt{m_2^2 + p^2}$ , and  $\Delta E$  is:

$$\begin{aligned} \Delta E &= \sqrt{m_1^2 + p^2} - \sqrt{m_2^2 + p^2} \\ &\simeq (p + m_1^2/2p) - (p + m_2^2/2p) = \Delta m^2/2p \\ &\simeq \Delta m^2/2E_\nu \end{aligned} \tag{1.10}$$

where  $\Delta m^2 \equiv m_1^2 - m_2^2$ . Then, the survival probability of  $\nu_\alpha$  is written as:

$$P(\nu_\alpha \rightarrow \nu_\alpha) = 1 - \sin^2 2\theta \sin^2 \left( \frac{\Delta m^2}{4E_\nu} \cdot L_\nu \right) \tag{1.11}$$

The survival probability has a  $L_\nu/E_\nu$  dependence.

### 1.2.1 Other Neutrino Oscillation Models

The finite masses of neutrinos are not the only possible sources of neutrino oscillation. As described above, any differences between two eigenvalue of the Hamiltonian produces neutrino oscillations.

The neutrino oscillations induced by the finite masses of neutrinos predict the  $L/E$  dependence of the survival probability of neutrinos, but several other theories predict neutrino oscillations with the other types of  $E_\nu$  dependence. This can be written by the following formula:

$$P(\nu_\alpha \rightarrow \nu_\alpha) = 1 - \sin^2 2\theta \sin^2 \left( \beta \cdot \frac{L}{E^n} \right), \tag{1.12}$$

where  $\theta$  is a mixing angle of neutrinos,  $\beta$  is the frequency of the neutrino oscillation, and the power index  $n$  is a parameter which depends on each theory.

Examples of these theories are: violation of Lorentz invariance [29] ( $n = -1$ ), violation of the equivalence principle [30] ( $n = -1$ ), CPT violation [31] ( $n = 0$ ), and coupling to space-time torsion fields [32] ( $n = 0$ ). In the case of ‘standard oscillation’, the index  $n$  is 1. Some of these theories are described below.

### 1.2.2 Violation of Lorentz Invariance

If the Lorentz invariance is violated, one possible consequence is that the maximum attainable velocities of the particle depends on the particle identity [29]. Let’s assume the two neutrino states  $\nu_1$  and  $\nu_2$  have the maximum attainable velocity  $c_1$  and  $c_2$ , respectively. Flavour eigenstates of neutrinos should be superpositions of the  $\nu_1$  and  $\nu_2$  with the mixing angle  $\theta_\nu$ . The

energy of  $\nu_i$  of definite momentum  $p$  is written as:

$$E_i = c_i \sqrt{p^2 + m^2 c_i^2}, \quad (1.13)$$

Assuming that the difference of  $c_1$  and  $c_2$  is small and the neutrino mass is much smaller than the momentum, the difference between the energy of  $\nu_1$  and  $\nu_2$  is given by  $E_1 - E_2 \simeq \delta c E$  where  $\delta c \equiv (c_1 - c_2)$ . The survival probability of neutrinos can then be re-written as:

$$P(\nu_\alpha \rightarrow \nu_\alpha) = 1 - \sin^2 2\theta_v \sin^2 \left( \frac{\delta c E}{2} \cdot L_\nu \right). \quad (1.14)$$

The survival probability has the  $L_\nu \times E_\nu$  dependence in this case.

### 1.2.3 Violation of Equivalence Principle

If Einstein's equivalence principle is violated, there could be particle-identity-dependent gravitational couplings. If the coupling to the gravitational field has a dependence on neutrino identity, the difference of the gravitational potential between the two neutrinos generate neutrino oscillation even if neutrinos are massless [30].

Here we concentrate in the case of massless neutrinos. Let  $|\nu_{G1}\rangle$  and  $|\nu_{G2}\rangle$  denote the eigenstates of the gravitational couplings, then the flavour eigenstates are expressed in the superposition of  $|\nu_G\rangle$ :

$$\begin{pmatrix} |\nu_\alpha\rangle \\ |\nu_\beta\rangle \end{pmatrix} = \begin{pmatrix} \cos \theta_G & \sin \theta_G \\ -\sin \theta_G & \cos \theta_G \end{pmatrix} \begin{pmatrix} |\nu_{G1}\rangle \\ |\nu_{G2}\rangle \end{pmatrix} \quad (1.15)$$

where  $\theta_G$  represents the mixing angle of  $|\nu_G\rangle$ . The Hamiltonian can be written in the  $|\nu_G\rangle$  basis as:

$$H = p - g_i \phi p \quad (1.16)$$

where  $g_i$  is the particle-dependent couplings to the gravitational field, and  $\phi$  represents the effective gravitational potential. If the couplings to the gravitational field are not universal, the energy difference between the two eigenstates is:

$$\Delta E \equiv E_1 - E_2 = \delta g \phi p \simeq \delta g \phi E_\nu \quad (1.17)$$

where  $\delta g = g_1 - g_2$ . The survival probability of the flavour eigenstates is:

$$P(\nu_{w1} \rightarrow \nu_{w1}) = 1 - \sin^2 2\theta_G \sin^2 \left( \frac{\delta g E}{2} \cdot L_\nu \right) \quad (1.18)$$

The survival probability also has a  $L_\nu \times E_\nu$  dependence.

### 1.2.4 Flavour Changing Neutral Current(FCNC)

Flavour changing neutral currents (FCNC) are also a possible source of neutrino oscillations even if neutrinos are massless [24]. FCNC are forbidden in the Standard Model, but several Grand Unification Theories or the theories concerning about neutrino mass predict FCNC interactions at tree level [33, 34, 35, 36].

If a FCNC interaction with a fermion  $f$  in matter,  $\nu_\alpha + f \rightarrow \nu_\beta + f$  exists, the general form of the effective potential induced by FCNC forward scattering can be written as:

$$H = H_0 + V_{eff} \quad (1.19)$$

$$= \begin{pmatrix} p & 0 \\ 0 & p \end{pmatrix} + \sqrt{2}G_F\rho_f(l) \begin{pmatrix} 1 & \epsilon \\ \epsilon & 1 + \epsilon' \end{pmatrix} \quad (1.20)$$

where  $p$  is the neutrino momentum,  $G_F$  is the Fermi coupling constant,  $\epsilon$  represents the difference of the amplitude of NC interaction between  $\nu_\alpha$  and  $\nu_\beta$ , and  $\epsilon'$  represents the amplitude of FCNC, respectively.  $\rho_f(l)$  is the fermion density as a function of the position  $l$  along the neutrino path. In this case, the solution of the Shrödinger equation is written as:

$$|\psi(t)\rangle = \exp\left(-i \int_0^L H(l)dl\right) |\psi(0)\rangle \quad (1.21)$$

where  $L$  is the flight length of neutrino. The integration is carried out along the neutrino path. Then, the survival probability of  $\nu_\alpha$  is written as:

$$P(\nu_\alpha \rightarrow \nu_\alpha) = 1 - \frac{(\epsilon)^2}{\epsilon^2 + (\epsilon'/2)^2} \sin^2\left(\sqrt{2}G_F X_f \sqrt{\epsilon^2 + (\epsilon'/2)^2}\right) \quad (1.22)$$

where  $X_f$  is the column density of the fermion  $f$  along the neutrino path:

$$X_f = \int_0^L \rho_f(l)dl \quad (1.23)$$

We obtain oscillating form of neutrino survival probability, but the survival probability is a function of the column density of the fermion, and has no dependence on the neutrino energy.

## 1.3 Neutrino Decay

Neutrino decay predicts a similar survival probability of neutrinos as predicted by neutrino oscillations [37]. In the Standard Model, neutrinos cannot decay because they are massless. However, several models with neutrino masses predict the decay of neutrinos [38, 39]. The lower limits on the lifetime of neutrinos are obtained only for radiative decay channels. Non-radiative decay is not limited yet [19]. For example, the lower limit on the lifetime of  $\nu_\mu$  due to radiative

decay is  $\tau/m > 15.4 \text{ sec/eV}$  from an accelerator experiment [40], where  $\tau$  is the lifetime of neutrino in the neutrino rest frame, and  $m$  is the neutrino mass.

Phenomenologically, the effect of neutrino decay can be described by adding the term  $-i\frac{1}{2\tau_\nu}$  to the Hamiltonian, where  $\tau_\nu$  is a neutrino lifetime at neutrino rest frame. In general, neutrino decays and neutrino oscillation due to the mass difference of neutrinos can co-exist. Assuming that the neutrino  $\nu_\alpha$  is a mixing of  $\nu_1$  and  $\nu_2$  as described in Eq.(1.4), and  $\nu_2$  has a decay channel to a state  $X$ , then the survival probability is written as [37]:

$$P(\nu_\alpha \rightarrow \nu_\alpha) = \cos^4 \theta + \sin^4 \theta \exp\left(-\frac{m_2 L_\nu}{\tau_2 E_\nu}\right) + \frac{1}{2} \sin^2 2\theta \exp\left(-\frac{m_2 L_\nu}{2\tau_2 E_\nu}\right) \cos\left[\frac{\Delta m^2}{2E_\nu} L_\nu\right], \quad (1.24)$$

where  $m_2$  is a mass of  $\nu_2$ ,  $\tau_2$  is the mass and the lifetime of  $\nu_2$  at rest frame,  $\theta$  and  $\Delta m^2$  are the usual oscillation parameters, respectively. At  $\tau_\nu \rightarrow \infty$ , Eq.(1.24) becomes Eq.(1.11).

If  $\Delta m^2 \rightarrow 0$ , or the neutrino oscillation length ( $\lambda_{\text{osc}}$ ) becomes much longer than the neutrino decay length ( $\lambda_{\text{dec}}$ ) and the effect of neutrino oscillation is negligibly small, the survival probability is simply written as:

$$\begin{aligned} P(\nu_\alpha \rightarrow \nu_\alpha) &= \cos^4 \theta + \sin^4 \theta \exp\left(-\frac{m_2 L_\nu}{\tau_2 E_\nu}\right) + \frac{1}{2} \sin^2 2\theta \exp\left(-\frac{m_1 L_\nu}{2\tau_1 E_\nu}\right) \\ &= \left(\cos^2 \theta + \sin^2 \theta \exp\left(-\frac{m_2 L_\nu}{2\tau_2 E_\nu}\right)\right)^2 \end{aligned} \quad (1.25)$$

Fig. 1.1 shows the survival probability of neutrinos as a function of  $L_\nu/E_\nu$  which is predicted from Eq.(1.25) with typical parameters. Because we cannot observe the exact survival probability patterns because of the finite resolution of  $L_\nu/E_\nu$ , the neutrino oscillation and neutrino decay give similar experimental signatures.

## 1.4 Neutrino Oscillation Experiments

Neutrino oscillation has been experimentally studied by various experiments. Several neutrino sources (artificial or natural) have been used in these experiments. Neutrino sources and their neutrino flavours are as follows:

Artificial sources:

- Neutrinos from nuclear reactors ( $\bar{\nu}_e$ )
- High energy neutrinos produced by accelerators ( $\nu_\mu, \bar{\nu}_\mu$ )
- Low energy neutrinos produced by meson factories ( $\nu_e, \nu_\mu, \bar{\nu}_\mu$ )

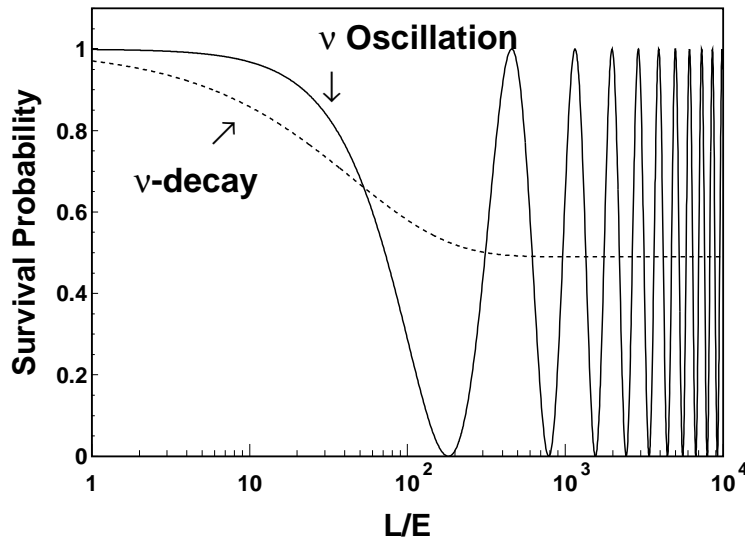


Figure 1.1: Predicted survival probabilities of neutrinos as a function of  $L/E$ . Solid line shows the prediction from neutrino oscillation, and dotted line shows the prediction from neutrino decay.

Natural sources:

- Neutrinos generated in the Sun (Solar neutrinos) ( $\nu_e$ )
- Neutrinos generated by the interaction of cosmic rays in the atmosphere (Atmospheric neutrinos) ( $\nu_e, \bar{\nu}_e, \nu_\mu, \bar{\nu}_\mu$ )

Each source is characterized by neutrino flavour, energy, and the flight length of neutrinos. The feature of each neutrino source and the experiments are described below.

#### 1.4.1 Reactor Neutrino Experiments

The  $\bar{\nu}_e$ 's from the core of a nuclear power reactor are used. The fission of  $^{235}\text{U}$ ,  $^{238}\text{U}$ ,  $^{239}\text{Pu}$ , and  $^{241}\text{Pu}$  produces neutron rich nuclei, and these nuclei get stabilized by  $\beta^-$  decay with  $\bar{\nu}_e$  emission. The mean energy of the neutrinos is a few MeV, and the spectrum of the neutrinos are well understood. The absolute flux of the neutrinos is also well understood with a few percent uncertainty, because the flux is proportional to the power of the reactor and the power is always controlled and monitored. The flight length of the neutrinos from the reactor core to the detector is accurately known and is 10's meters to 1 km. These experiments search for  $\bar{\nu}_e$  disappearance. From these experiments, no evidence for neutrino oscillation  $\bar{\nu}_e \rightarrow \bar{\nu}_X$  has been obtained. The excluded regions from Gösgen [57], Bugey [58], CHOOZ [59], and Palo Verde [60] are shown in Fig. 1.2.

#### 1.4.2 Accelerator Neutrino Experiments

High energy  $\nu_\mu$ 's or  $\bar{\nu}_\mu$ 's from decay in flight of the high energy mesons ( $\pi, K$ ) which are produced by a high energy proton beam focused on a target are used. The energy of the neutrinos ranges

from 1 GeV to over 100 GeV, and the flight length of the neutrinos varies from several 100's m to several 100's km. These experiments search for  $\nu_e$  appearance and  $\nu_\mu$  disappearance, and, if the neutrino energy is higher than the threshold for tau appearances ( $\simeq 3.6\text{GeV}$ ), then  $\nu_\tau$  appearances can be observed through the observation of  $\tau$  leptons produced by charged current (CC)  $\nu_\tau$  interactions.  $\nu_\tau$  appearance would be a direct confirmation of  $\nu_\mu \rightarrow \nu_\tau$  oscillation. FNAL E531 [70], CHORUS [67], NOMAD [68] were designed to search for  $\nu_\tau$  appearance by the CC  $\nu_\tau$  interactions followed by  $\tau$  lepton decay signals. CDHSW [71] searched for  $\nu_\mu$  disappearance. No evidence was observed from the experiments, and the excluded regions for neutrino oscillation parameters are shown in Fig. 1.3.

Recently, an accelerator experiment KEK-E362 (KEK to Kamioka long-baseline neutrino oscillation experiment) reported that the number of neutrino events observed in Super-Kamiokande after 250 km flight is smaller than expected by more than 2 standard deviations [69]. This result is consistent with the  $\nu_\mu$  deficit predicted by neutrino oscillations.

### 1.4.3 Meson Factory Experiments

Neutrinos from the decay chain of stopped pions (mostly  $\pi^+$ ),  $\pi^+ \rightarrow \mu^+ + \nu_\mu$  and  $\mu^+ \rightarrow e^+ + \nu_e + \bar{\nu}_\mu$ , are used. The  $\nu_\mu$ 's are monoenergetic with 29.8 MeV, and the  $\bar{\nu}_\mu$  and  $\nu_e$  have continuous energy distributions up to 52.8 MeV.  $\bar{\nu}_\mu \rightarrow \bar{\nu}_e$  oscillation was studied.

LSND (Liquid Scintillator Neutrino Detector) experiment at Los Alamos Meson Physics Facility reported in 1996 that they found the evidence for  $\bar{\nu}_e$  appearance from a pure  $\nu_\mu$ ,  $\nu_e$ , and  $\bar{\nu}_\mu$  beam by detecting the interaction  $\bar{\nu}_e + p \rightarrow e^+ + n$  followed by 2.2 MeV  $\gamma$  from neutron capture [74]. However, this result is controversial because an experiment with a similar beam, KARMEN [76] at Rutherford Appleton Laboratory, has not observed any positive effects. Fig. 1.2 shows the results from these experiments.

### 1.4.4 Solar Neutrino Experiments

Electron neutrinos are produced in the nuclear fusion reaction chains in the core of the Sun. The energy range of the solar neutrinos is up to about 15 MeV.

The solar neutrinos have been observed by several experiments. All of the experiments reported that the observed number of neutrinos are significantly smaller than expected. Thus deficit is often referred to as the 'solar neutrino problem'.

The Homestake experiment, which started in 1967 [61], was the first experiment which observed the solar neutrinos using the interaction  $\nu_e + {}^{37}\text{Cl} \rightarrow e^- + {}^{37}\text{Ar}$ . This reaction was observed by counting the number of the produced Ar atoms extracted by a chemical technique. The second experiment was Kamiokande [62] which was a water Cherenkov type experiment.

Solar neutrinos were observed by using the elastic scattering  $\nu_l + e^- \rightarrow \nu_l + e^-$  where  $l = e, \mu, \tau$ . The SAGE [63] and Gallex [64] experiments use  $\nu_e + {}^{71}\text{Ga} \rightarrow e^- + {}^{71}\text{Ge}$  interaction. This reaction was also observed by counting the number of Ge atoms extracted by a chemical technique. Super-Kamiokande which started in 1996 has observed the solar neutrinos by  $\nu_l + e^- \rightarrow \nu_l + e^-$  elastic scattering [65].

The SNO experiment which started observations in 1999, is also a Cherenkov detector that uses heavy water ( $\text{D}_2\text{O}$ ). The SNO experiment measures the pure CC interaction rate  $\nu_e^+ n \rightarrow e^- + p$ , while the elastic scattering  $\nu_l + e^- \rightarrow \nu_l + e^-$  includes both the  $\nu_e$  interactions and  $\nu_\mu$  and  $\nu_\tau$  interaction.

In June 2001, SNO experiment reported that the solar neutrino problem is explained by  $\nu_e \rightarrow \nu_{\mu/\tau}$  oscillation [66] by comparing their observation of  $\nu_e$  CC rate and the elastic scattering rate reported by Super-Kamiokande which has the sensitivity not only to  $\nu_e e^-$  interaction but also to  $\nu_\mu e^-$  or  $\nu_\tau e^-$  interactions. The scattering rate measured by SNO was smaller than the rate measured by Super-Kamiokande by 3.3 standard deviations.

#### 1.4.5 Atmospheric Neutrino Experiments

Atmospheric neutrinos are products of hadron showers in the atmosphere produced by primary cosmic rays. The first generation of the atmospheric neutrino experiments was designed to observe neutrino-induced upward-going muons. From the late 1970's, several large mass underground experiments started to search for nucleon decay, which is predicted by Grand Unified Theories (GUTs). These underground experiments also observed atmospheric neutrinos. Atmospheric neutrinos are the main source of background to nucleon decay searches, and the study of atmospheric neutrinos were started mainly as the study of these backgrounds.

These experiments were able to identify particles, and they could measure the number of  $\mu$  and  $e$  events, which were produced by  $\nu_\mu$  and  $\nu_e$  charged current interactions. Table 1.4.5 shows the reported results from these experiments.  $R$  represents the ratio of observed  $\mu/e$  ratio to the expected  $\mu/e$  ratio. Among these experiments, NUSEX [41], Fréjus [42] reported that observed  $\mu/e$  ratios were consistent with the expectation within the errors, but IMB [44], Kamiokande [43], Soudan-2 [46] reported that observed  $\mu/e$  ratio was significantly smaller than expected. Kamiokande also reported that the deficit of  $\mu$  events had zenith angle dependence, and the number of upward-going events were less than the number of downward-going events. These anomalies were known as the 'Atmospheric Neutrino Problem'.

Another type of atmospheric neutrino events, upward-going muons which are produced by the energetic  $\nu_\mu$  charged current interactions in the rock surrounding the detector, have been studied by Kamiokande [54], IMB [53], Baksan [55], MACRO [48], Results from Kamiokande,

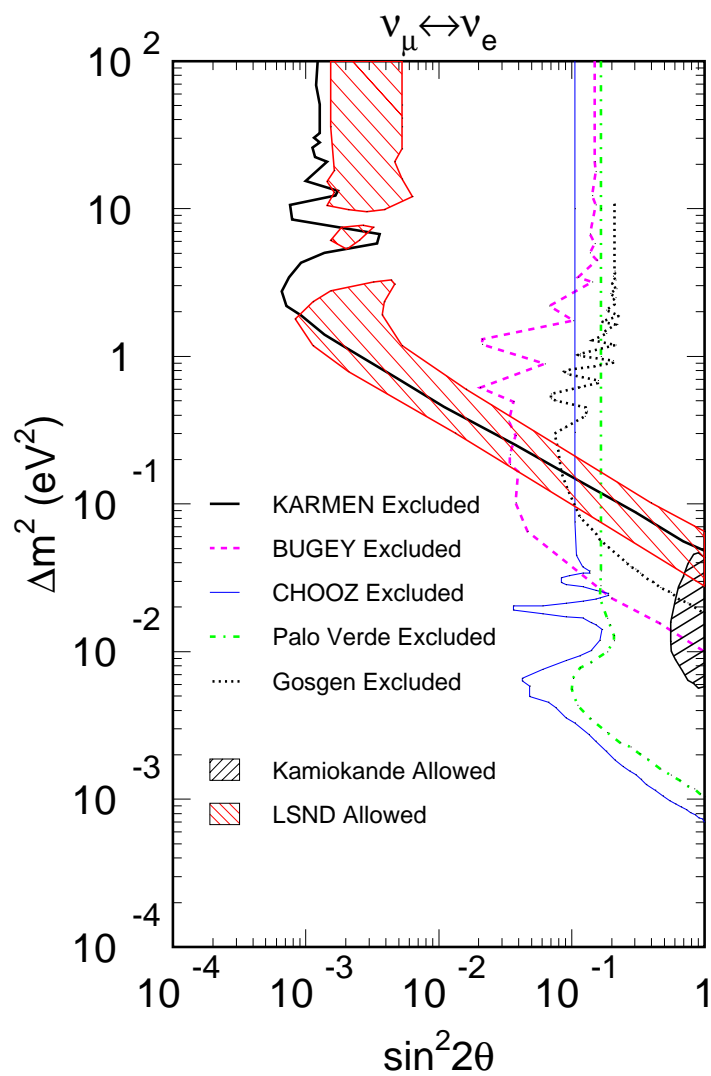


Figure 1.2: 90% C.L. allowed and excluded regions on the parameter space for  $\nu_{\mu} \leftrightarrow \nu_e$  2-flavour neutrino oscillations. Excluded regions lie to the right of the curves. These results are from the reactor neutrino experiments: Gösgen [57], BUGEY [58], Palo Verde [60], and CHOOZ [59], meson-factory type experiments: KARMEN [76] and LSND [75], atmospheric neutrino experiments: Kamiokande [47].

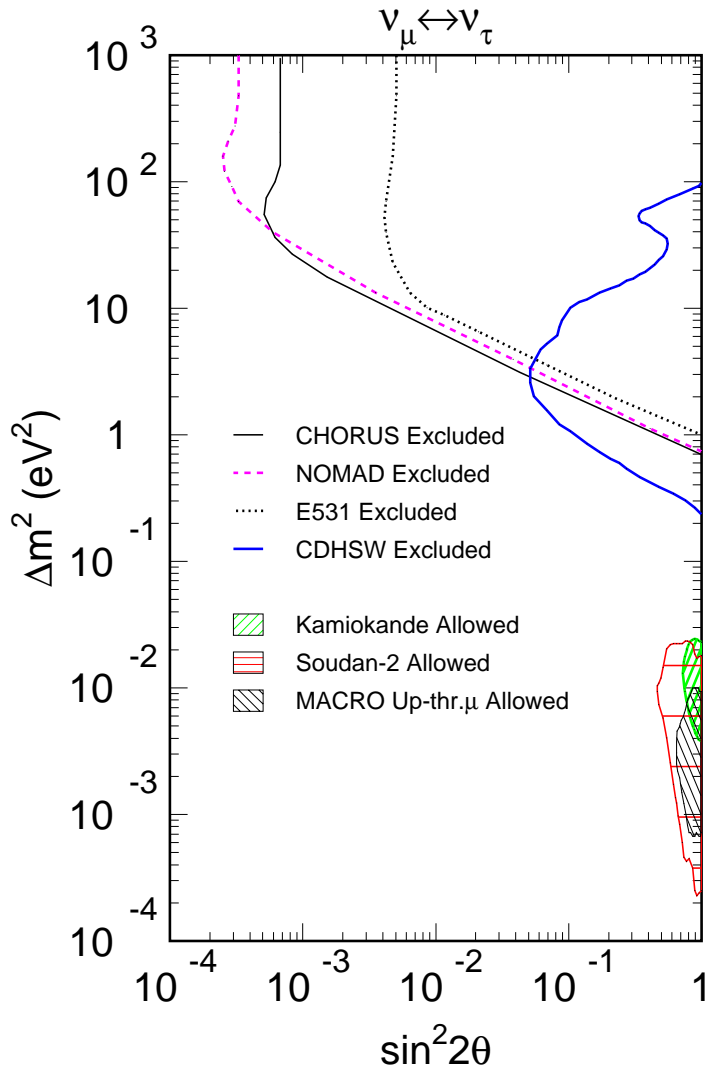


Figure 1.3: 90% C.L. allowed and excluded regions on parameter space for  $\nu_\mu \leftrightarrow \nu_\tau$  2-flavour neutrino oscillations. Excluded regions lie to the right of the curves. These are taken from the results from the accelerator experiments: CHORUS [67], NOMAD [68], FNAL E531 [70], and CDHSW [71]. Allowed regions are obtained from atmospheric neutrino experiments: Kamiokande [47], Soudan-2 [72], and MACRO [73].

Experiment name	Detector type	Exposure (kt·year)	Double ratio $R = (\mu/e)^{\text{obs}} / (\mu/e)^{\text{exp}}$
Kamiokande [43]	Water Cherenkov	7.7	$0.60_{-0.05}^{+0.06} \pm 0.05$ (Sub-GeV)
		8.2	$0.57_{-0.07}^{+0.08} \pm 0.07$ (Multi-GeV)
IMB-3 [44][45]	Water Cherenkov	7.7	$0.54 \pm 0.05 \pm 0.012$ (Sub-GeV)
		2.1	$1.4_{-0.3}^{+0.4} \pm 0.3$ (Multi-GeV)
Super-Kamiokande [49][50]	Water Cherenkov	70.4	$0.651_{-0.018}^{+0.019} \pm 0.05$ (Sub-GeV)
		70.4	$0.711_{-0.036}^{+0.036} \pm 0.085$ (Multi-GeV)
Soudan-2 [72]	Iron Calorimeter	5.1	$0.68 \pm 0.11 \pm 0.06$
Fréjus [42]	Iron Calorimeter	1.56	$1.00 \pm 0.15 \pm 0.08$
NUSEX [41]	Iron Calorimeter	0.74	$0.96_{-0.28}^{+0.32}$

Table 1.2: List of the atmospheric neutrino experiments. Definition of  $R$  is described in the text.

MACRO, and Super-Kamiokande are consistent with the neutrino oscillation  $\nu_\mu \leftrightarrow \nu_\tau$ . However, IMB reported that the observation was consistent with expectation without neutrino oscillations.

Super-Kamiokande, which started observation in 1996, reported the smallness of  $\mu/e$  ratio and zenith-angle-dependent deficit  $\mu$  events [49][50]. Super-Kamiokande also reported the observation of upward-going muons [56], and these results are consistent with the  $\nu_\mu \rightarrow \nu_\tau$  oscillation. In 1998, Super-Kamiokande concluded that the atmospheric neutrino data gave the evidence for neutrino oscillation [51].

The atmospheric neutrino data are consistent with two flavor  $\nu_\mu \rightarrow \nu_\tau$  oscillations. However, the periodicity of neutrino oscillation is not observed yet, and also,  $\nu_\tau$  appearance is not observed directly.

## 1.5 Motivation of This Thesis

The atmospheric neutrino problem is interpreted as the evidence for  $\nu_\mu \leftrightarrow \nu_\tau$  2-flavour neutrino oscillation. However, the observed anomaly is the deficit of the upward-going  $\mu$ -like events, and the periodicity of the neutrino oscillation and the appearance of  $\nu_\tau$  has not been observed yet. As described in Section 1.2.1, there are several theories which predict neutrino oscillations. In addition, neutrino decay predicts a similar deficit pattern of neutrinos. This could also be a possible solution to the atmospheric neutrino problem.

The motivation of this thesis is to identify the mechanism of the atmospheric neutrino

anomaly. The Super-Kamiokande experiment observes atmospheric neutrinos over a wide range of energies and flight lengths (from 100 MeV to 1000 GeV, and from 10 km to 13000 km). Detailed studies of the atmospheric neutrinos with these wide ranges make it possible to distinguish the hypotheses which predict different patterns of the neutrino disappearance.

## Chapter 2

# Atmospheric Neutrinos

### 2.1 Overview

Atmospheric neutrinos are decay products of secondary particles produced in the interactions of the primary cosmic rays on nuclei high in the atmosphere:

$$p(He) + A_{air} \rightarrow X + \pi, K, \text{ etc} \quad (2.1)$$

where  $A_{air}$  represents a nucleus in the air (N,O,C) and X represents some hadrons.

Then, the following decay chains of the mesons produce  $\nu_\mu(\bar{\nu}_\mu)$  and  $\nu_e(\bar{\nu}_e)$ :

$$\pi^\pm \rightarrow \mu^\pm \nu_\mu(\bar{\nu}_\mu) \quad (100\%) \quad (2.2)$$

$$K^\pm \rightarrow \mu^\pm \nu_\mu(\bar{\nu}_\mu) \quad (63.5\%) \quad (2.3)$$

$$K_L^0 \rightarrow \pi^\pm e^\mp \bar{\nu}_e(\nu_e) \quad (38.8\%)$$

$$\rightarrow \pi^\pm \mu^\mp \bar{\nu}_\mu(\nu_\mu) \quad (27.2\%) \quad (2.4)$$

$$\mu^\pm \rightarrow e^\pm \bar{\nu}_\mu \nu_e(\nu_\mu \bar{\nu}_e) \quad (100\%) \quad (2.5)$$

where the numbers represent the branching fractions for the modes.

Primary cosmic ray flux and its components were measured by several experiments. In the energy range below about 100 GeV, experiments with magnetic spectrometer borne by balloon or by Space Shuttle give several accurate results. Between 100 GeV and  $10^6$  GeV, calorimeters and emulsion chambers are used. Above  $10^6$  GeV, ground based experiments are used for the observation.

Fig. 2.1 shows the measured flux of the primary cosmic rays. The main component of the primary cosmic rays is proton. For kinetic energy above 2 GeV/nucleon, about 80% of nucleons

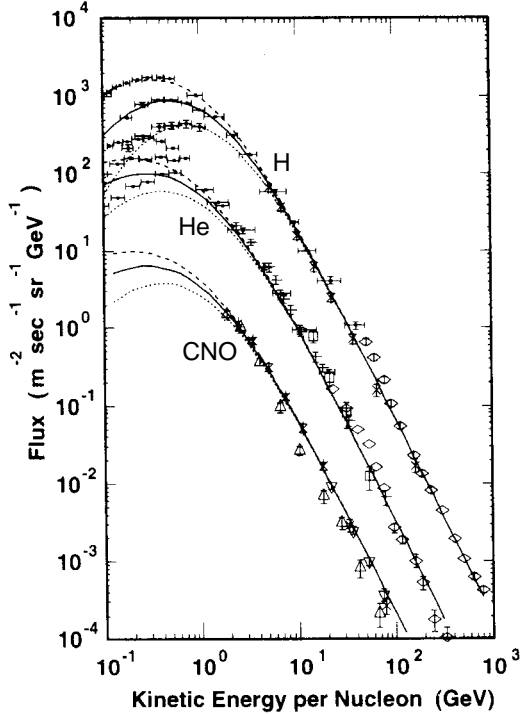


Figure 2.1: Measured flux of each chemical composition of the primary cosmic rays. Solid lines show the fitted results for middle solar activity, dashed lines for minimum solar activity, and dotted lines for maximum solar activity used in Ref. [78].

in primary cosmic rays are carried by proton, and 15% by He and 4% are carried by relatively heavy nucleus like C,N,O. Above  $\sim 10$  GeV/nucleon, primary cosmic ray flux approximately obeys a power function:

$$\text{Flux}(E) = A \times E^{-\gamma} \quad (2.6)$$

For protons,  $\gamma$  is estimated to be about 2.7.

Atmospheric neutrinos have two remarkable features.

1. Flux ratio  $(\nu_\mu + \bar{\nu}_\mu)/(\nu_e + \bar{\nu}_e)$  is 2 ( $>2$  for  $E_\nu \gtrsim 2$  GeV)
2. Zenith angle distribution has up/down symmetry

The first feature can be understood by the decay chains of mesons shown in Eq.s (2.2) and (2.5). Once  $\pi^+(\pi^-)$  is produced in the atmosphere, finally  $e^+, \nu_e, \nu_\mu, \bar{\nu}_\mu$  ( $e^-, \bar{\nu}_e, \bar{\nu}_\mu, \nu_\mu$ ) are produced. Then the flavour ratio is 2 irrespective to the absolute flux of the primary cosmic rays or the details of the  $\pi$  production. For higher energy neutrinos, the flavour ratio is larger than 2, because the probability of a  $\mu^\pm$  decay in flight before reaching at the ground (i.e., the  $\nu_e(\bar{\nu}_e)$  production probability) becomes smaller.

The second feature is due to a simple geometrical reason. Fig. 2.2 shows the schematic view of the atmospheric neutrino production. The point at zenith angle =  $\Theta$  and opposite point  $\Theta - \pi$  have same geometrical situation as far as the primary cosmic rays come isotropically. So,

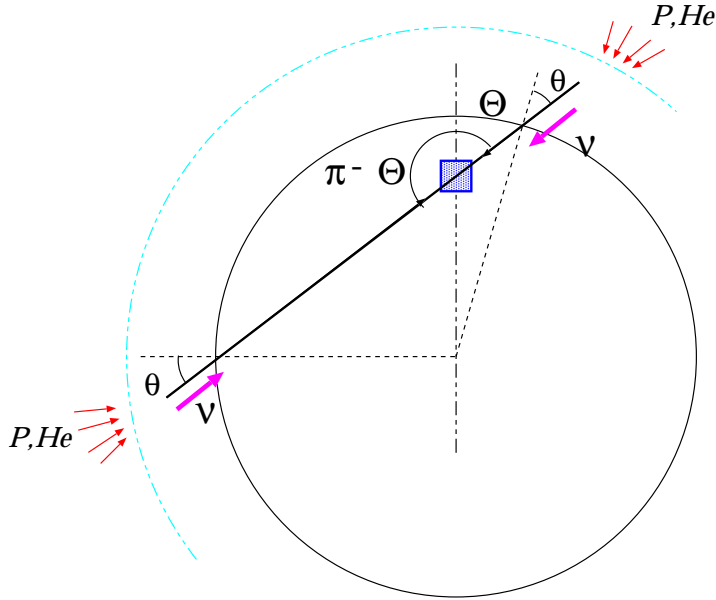


Figure 2.2: Schematic view of production of atmospheric neutrinos. The box represents the Super-Kamiokande detector.

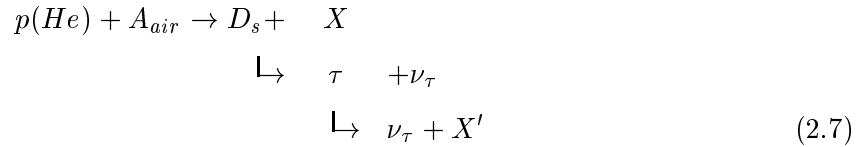
the neutrino flux from zenith angle  $= \Theta$  and  $\Theta - \pi$  are same. This feature is very robust and independent of the details of the primary cosmic ray or the hadronic interactions.

However, in fact, for low energy neutrinos ( $E_\nu \sim$  several GeV), up/down symmetry is affected by rigidity cutoff of the primary cosmic rays by geomagnetic field. The rigidity is defined to be the momentum divided by electric charge of the particle ( $\text{GeV}/c/eZ$ ). Low rigidity particles are reflected by the Lorentz force of the geomagnetic field and cannot arrive at the Earth. Then, the primary cosmic ray flux arriving at the Earth and therefore the neutrino flux have a directional dependence. For higher energy primary cosmic rays ( $E_{\text{primary}} \gg 10 \text{ GeV/nucleon}$ ) the effect of the geomagnetic field is negligibly small and up/down symmetry is realized.

The geomagnetic field also produces the 'East-West effect', which is the anisotropy of the cosmic ray flux from the easterly and the westerly direction. The azimuthal angle distribution of neutrino events will be described in Section 8.1.8.

Another source of the modulation of low energy neutrino flux is the solar activity. The magnetic field associated with the solar wind (an outflow of plasma from the Sun) drives back the low energy cosmic rays which are entering into the solar sphere. The solar activity varies with an 11 year cycle. Difference of the primary proton flux between minimum solar activity and maximum solar activity is estimated to be more than factor 2 for 1 GeV protons and about 10~20% for 10 GeV protons. Consequently, the modulation of the absolute neutrino flux is calculated to be  $\sim 8\%$  at 100 MeV and  $\sim 3\%$  at 1 GeV.

The existence of  $\nu_\tau$  in the atmospheric neutrinos can be a source of the systematic uncertainty of the neutrino flavour oscillation analyses. The main source of  $\nu_\tau$  is the leptonic decay of  $D_s$ :



where  $X$  and  $X'$  represent some hadrons. The branching fraction of  $D_s$  decay to this channel is about 4% [80]. The flux of atmospheric  $\nu_\tau$  is estimated to be about  $10^{-6}$  times lower than those of  $\nu_\mu$  or  $\nu_e$  [81], and the prompt  $\nu_\tau$  is completely negligible for the study of the neutrino flavour oscillations.

## 2.2 Calculated Flux and the Systematic Uncertainties

Atmospheric neutrino flux have been calculated by many authors. There are several detailed calculations, and we adopt Honda *et al.*, flux(Honda flux, hereafter) [78] for minimum solar activity in our study. The result of Agrawal *et al.*, flux (Bartol flux, hereafter) [79] calculation is also shown in comparison.

Fig. 2.3 shows the calculated flux of atmospheric neutrinos as a function of the neutrino energy. The systematic uncertainty of the absolute flux is estimated to be about 20% which is mainly due to the uncertainty of the absolute flux of the primary cosmic rays. Hadron interactions is also the main source of the systematic uncertainty.

The spectrum of the atmospheric neutrinos have an approximate form of a single power function,  $A \times E_\nu^{-\gamma}$ , for  $E_\nu$  larger than a few GeV. Spectrum index is estimated to be about 3.0 for  $\nu_\mu$  and 3.5 for  $\nu_e$  for neutrinos above a few GeV, and the systematic uncertainty is estimated to be  $\pm 0.05$ . This uncertainty is mainly due to the uncertainty of the spectrum index of the primary cosmic rays.

Fig. 2.4 (a) shows the  $(\nu_\mu + \bar{\nu}_\mu)/(\nu_e + \bar{\nu}_e)$  flux ratio as a function of the neutrino energy. The systematic uncertainty of the flux ratio is estimated to be about 5% below 10 GeV. In higher energy region ( $E_\nu > 30$  GeV), the production of  $K$  meson has an important contribution to the flux ratio.

Fig. 2.4 (b) shows the  $\nu/\bar{\nu}$  ratio. The systematic uncertainty of the ratio is estimated to be 5% for both  $\nu_\mu$  and  $\nu_e$ .

Fig. 2.5 shows the zenith angle distributions of  $\nu_\mu + \bar{\nu}_\mu$  and  $\nu_e + \bar{\nu}_e$  for several neutrino energies. The structures for low energy neutrinos are due to the geomagnetic field effects. The fluxes peaked at the horizontal direction ( $\cos \Theta = 0$ ) for higher energy neutrinos are due to the larger decay volume of muons in the horizontal direction.

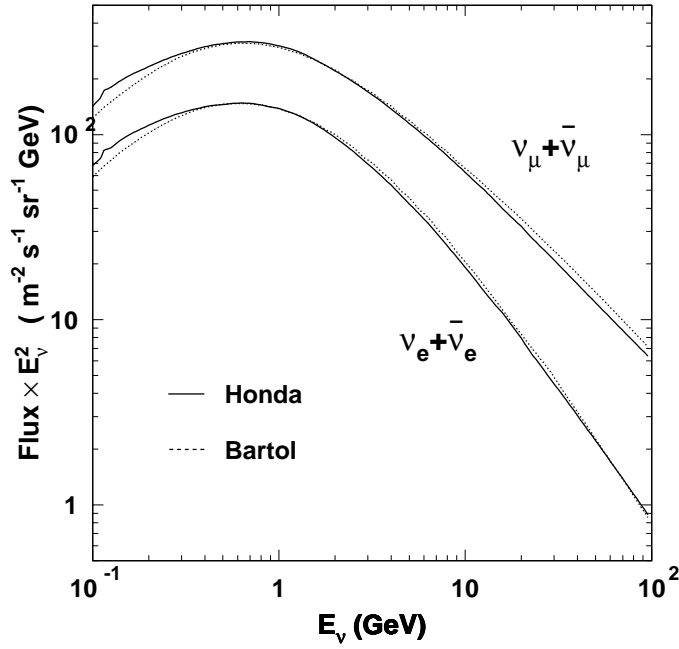


Figure 2.3: The calculated flux of the atmospheric neutrinos at the Kamioka site for middle solar activity. Solid lines show the Honda calculation [78], and dotted lines show the Bartol calculation [79]. These fluxes are averaged over the zenith and azimuthal angle.

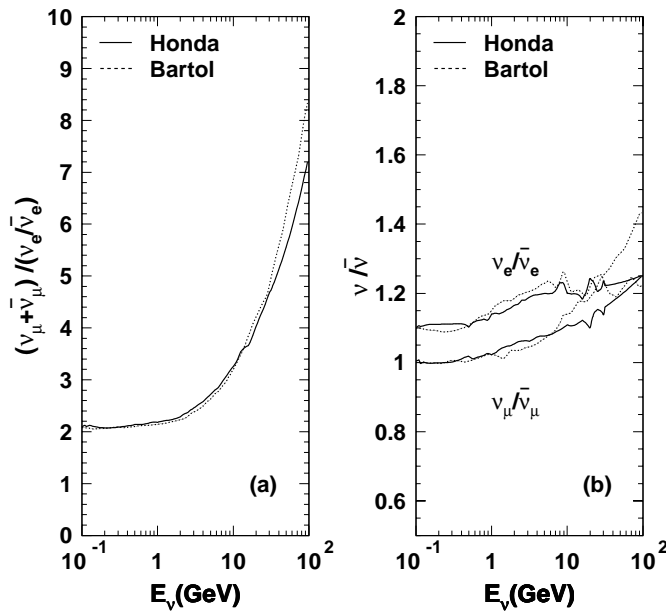


Figure 2.4: (a) The calculated flux ratio  $(\nu_\mu + \bar{\nu}_\mu)/(\nu_e + \bar{\nu}_e)$ . (b) The calculated  $\nu/\bar{\nu}$  ratio. Solid line shows the predictions by Honda calculation [78] and dashed line shows Bartol calculation [79].

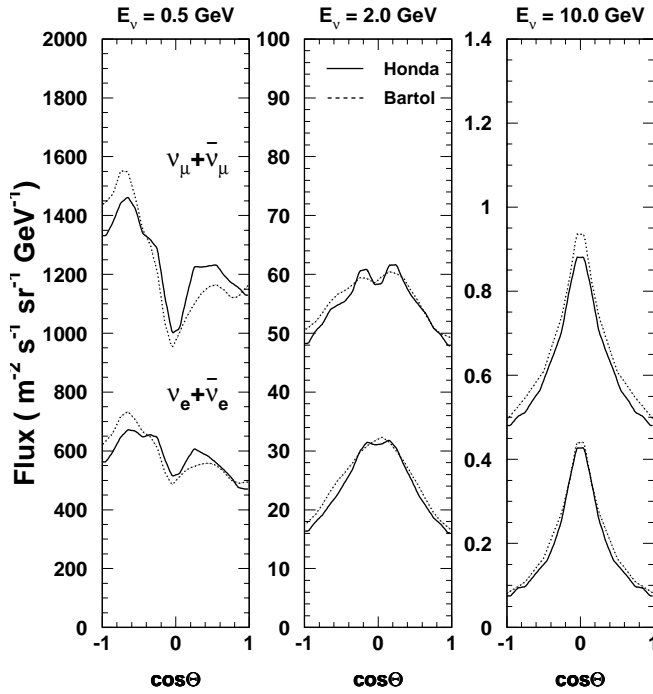


Figure 2.5: The zenith angle distributions for the calculated atmospheric neutrino fluxes for  $E_\nu = 0.5$  GeV (left), 2.0 GeV (center), and 10.0 GeV (right). The solid lines show the results from Honda calculation [78], and broken lines show the results from Bartol calculation [79].

The systematic uncertainty of the zenith angle distribution is an important source of the systematic errors in a neutrino oscillation analysis. The systematic uncertainty in up-down flux ratio for low energy neutrinos is estimated to be about 10% which is mainly due to the uncertainty of the geomagnetic field effect. Honda and Bartol calculations neglect the effect of the mountain above Super-Kamiokande which decreases the probability of the decay in flight of the vertically downward-going muons before reaching the ground. The effect is estimated to be about 1% uncertainty in the up-down ratio.

The cosmic ray muon flux is closely related to the neutrino flux, and a comparison between the calculated  $\mu^\pm$  flux and the measured flux gives an important check of the validity of the calculation. Fig. 2.6 shows the comparison between calculated  $\mu^\pm$  flux by Honda calculation and measured ones. The measured flux and calculated flux agree well.

## 2.3 Observation of Atmospheric Neutrinos in Super-Kamiokande

Atmospheric neutrino events observed in Super-Kamiokande are categorized into two types:

- (1) Neutrino interactions in the detector
- (2) Entering muons induced by neutrino interactions in the rock surrounding the detector.

Fig. 2.7 shows the schematic view of the observation of atmospheric neutrinos in Super-Kamiokande. Event type (1) is further categorized into two types: The events in which all visible particles

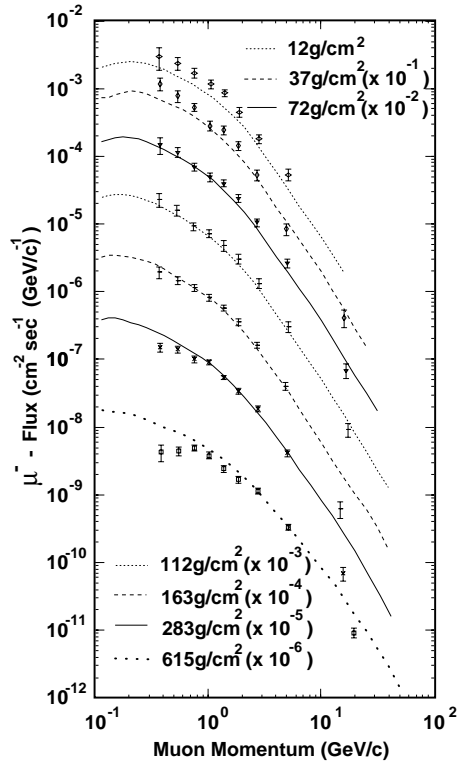


Figure 2.6: A comparison of the calculated  $\mu^-$  flux by Honda *et al.* [78] and the observed flux by the MASS experiment [82] for several depths of the atmosphere.

are contained in the detector are called 'Fully Contained (FC)' events. The events in which at least one visible particle escapes from the detector are called 'Partially Contained (PC)' events. Event type (2) is due to the energetic  $\nu_\mu(\bar{\nu}_\mu)$  neutrinos. To avoid a huge number of cosmic ray muons, we study only upward-going muons. The upward-going muons are categorized into two types: The muons stopping in the detector are called 'Upward-Stopping muons', and the muons passing through the detector are called 'Upward Through-going muons'.

Energy range of the parent neutrinos is different for each event category. Fig. 2.8 shows the energy distribution of parent neutrinos for each category. Our observation covers from 100 MeV to 1000 GeV neutrino energy.

The neutrinos are not directly observed, but we observe the produced charged particles by the neutrino interactions. Fig. 2.9 shows the angular correlation between parent neutrino and the produced charged lepton. The angular correlation is poor for low energy neutrinos, and becomes better as the neutrino energy increases. The typical angular correlation between neutrinos and charged lepton is about  $30^\circ$  for 1 GeV neutrinos in CC interactions.

The features of each category are described below.

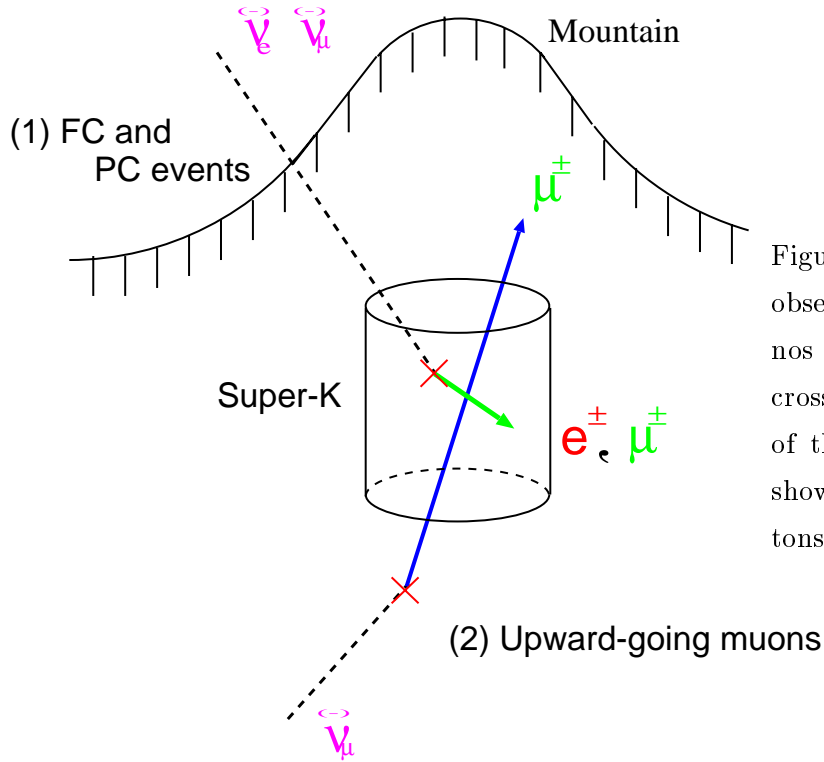


Figure 2.7: Schematic view of the observation of atmospheric neutrinos in Super-Kamiokande. The crosses show the interaction points of the neutrinos, and solid arrows show the direction of outgoing leptons.

### 2.3.1 Fully Contained(FC) events

Fully Contained (FC) event is defined by the condition that the interaction occurs in the detector and no visible particle escapes from the detector. We can estimate the momentum of the particles for FC events. The FC events are produced by  $\nu_e(\bar{\nu}_e)$  or  $\nu_\mu(\bar{\nu}_\mu)$  via either Charged Current(CC) or Neutral Current(NC) interactions. Typical energy of the parent neutrinos of the FC events is 1 GeV.

### 2.3.2 Partially Contained(PC) events

Partially Contained (PC) event is defined by the condition that the vertex is contained in the detector and a part of visible particles escape from the detector. About 97% of PC events are due to  $\nu_\mu$  and  $\bar{\nu}_\mu$  CC interactions. The energy of the parent neutrinos for PC events is typically 10 GeV.

### 2.3.3 Upward-stopping muons and upward-through going muons

Essentially, all of the upward-going muons are produced by  $\nu_\mu(\bar{\nu}_\mu)$  CC interactions, because muon is the only particle which can travel a long range in the rock. Other particles produced by neutrino interactions( $\gamma, e, \pi, \dots$ ) are quickly absorbed in the rock. The typical energy of the

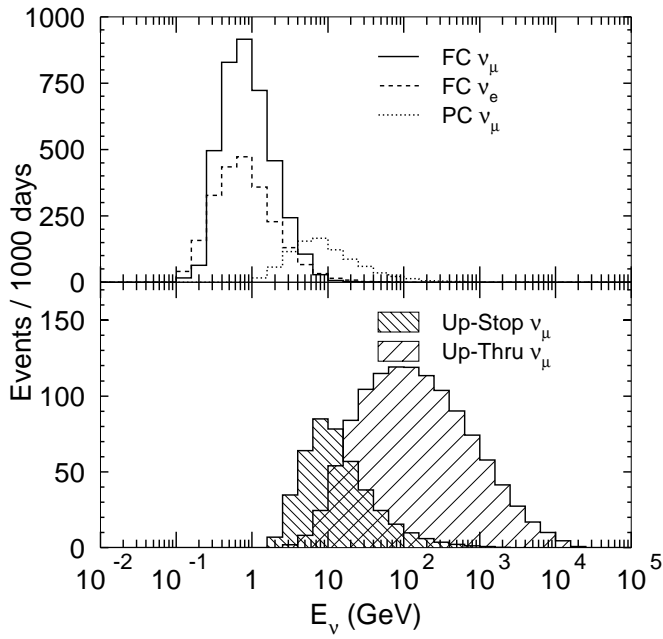


Figure 2.8: Energy distributions for the parent neutrinos for FC, PC, upward-stopping  $\mu$ , and upward-through  $\mu$ .

parent neutrinos is 10 GeV for upward stopping muons and 100 GeV for upward through-going muons. The observed muons well remember the parent neutrino directions.

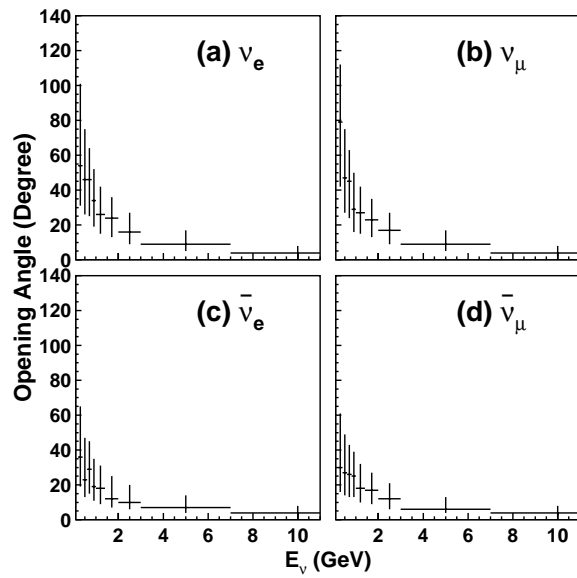


Figure 2.9: The estimated opening angle between incoming neutrinos and outgoing leptons for (a)  $\nu_e$  CC scattering (b)  $\nu_\mu$  CC scattering (c)  $\bar{\nu}_e$  CC scattering (d)  $\bar{\nu}_\mu$  CC scattering.

## Chapter 3

# Super-Kamiokande Detector

### 3.1 Overview

The Super-Kamiokande detector is a cylindrically-shaped water Cherenkov detector with 50 kiloton of ultra-pure water. It is located about 1000 m underground in the Kamioka Observatory in the Kamioka mine in Gifu Prefecture, Japan. The location is  $36.42^\circ\text{N}$  latitude and  $137.31^\circ\text{E}$  longitude, and the geomagnetic latitude is  $25.8^\circ\text{N}$ . The 1000 m thickness of rock is equivalent to 2700 m of water, thus the cosmic ray muon flux is reduced down to  $10^{-5}$  of that of the surface. The trigger rate due to cosmic ray muons is about 2 Hz.

The operation started in Apr 1996. The detector is operated 24 hours a day, and the status of the detector and environment is always monitored by physicists. Livetime of the detector is over 90%, and the about 10% dead time is mainly due to detector calibrations.

The physics topics studied in Super-Kamiokande experiment are solar neutrinos, super-novae neutrinos, nucleon decay, and atmospheric neutrinos. The relevant energy range of these topics spreads from a few MeV to over 1000 GeV.

Figs 3.1, 3.2, and 3.3 show the schematic views of the Super-Kamiokande detector. The Super-Kamiokande detector mainly consists of 4 parts.

- (1) Cylindrically-shaped water tank
- (2) Photomultiplier tubes
- (3) Ultra pure water and water purification system
- (4) Electronics and computers for data acquisition

Air-conditioner, networks for data transfer, radon-free air system, and status monitor systems are also used in the experiment.

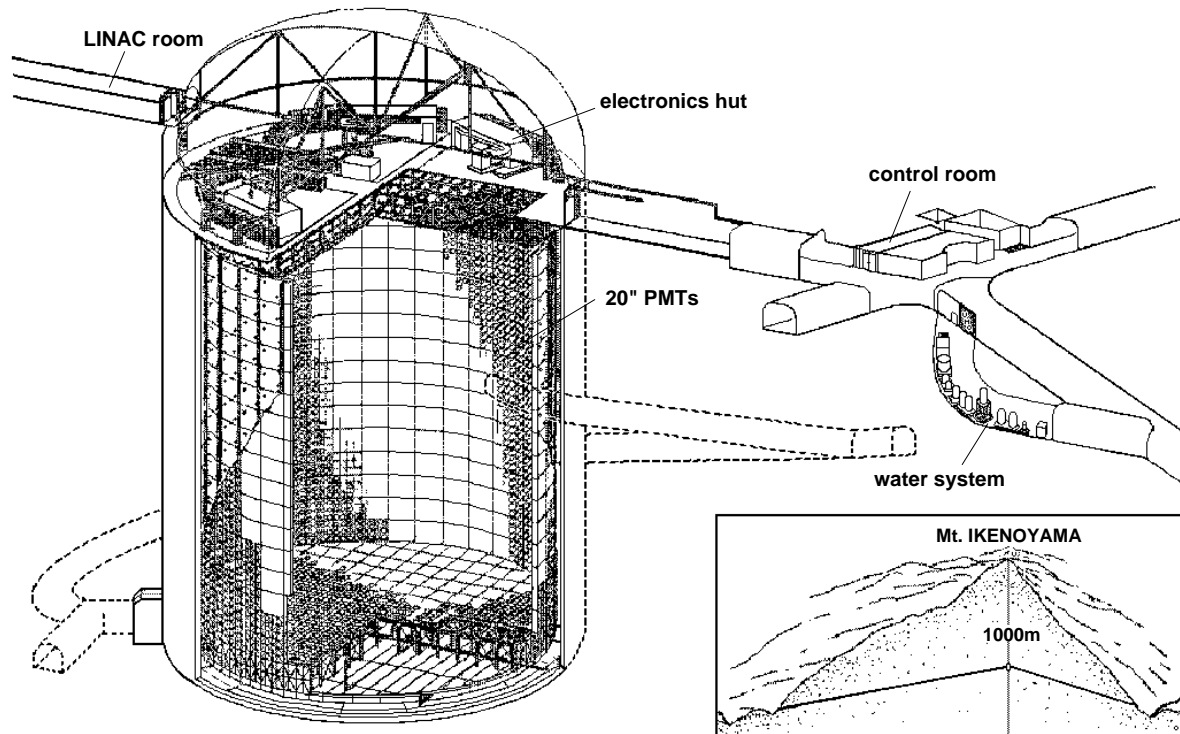


Figure 3.1: The Super-Kamiokande detector. Inset at bottom right shows the location within the mountain.

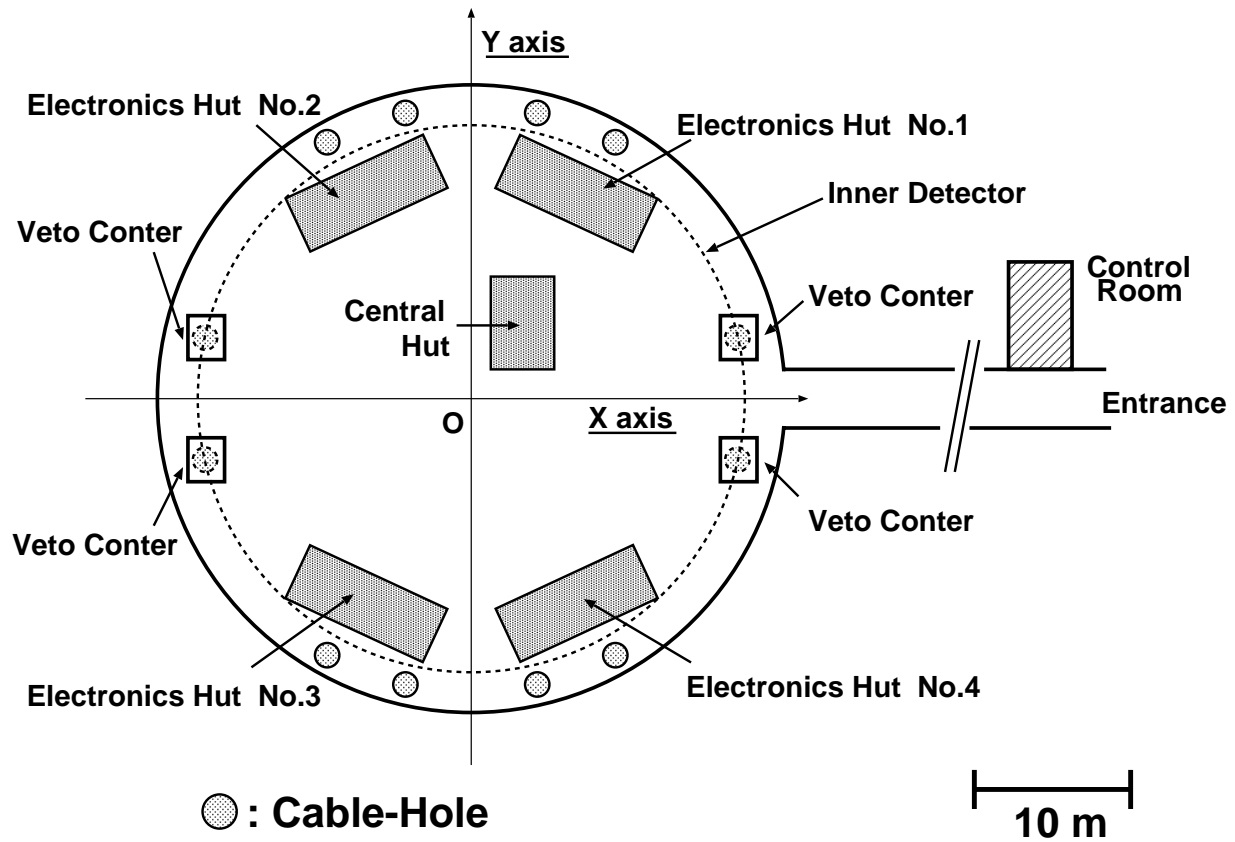


Figure 3.2: Schematic view of the top of the detector. The definition of the detector coordinate is also shown. Shaded circles represent cable extraction holes, and shaded boxes represent electronics huts.

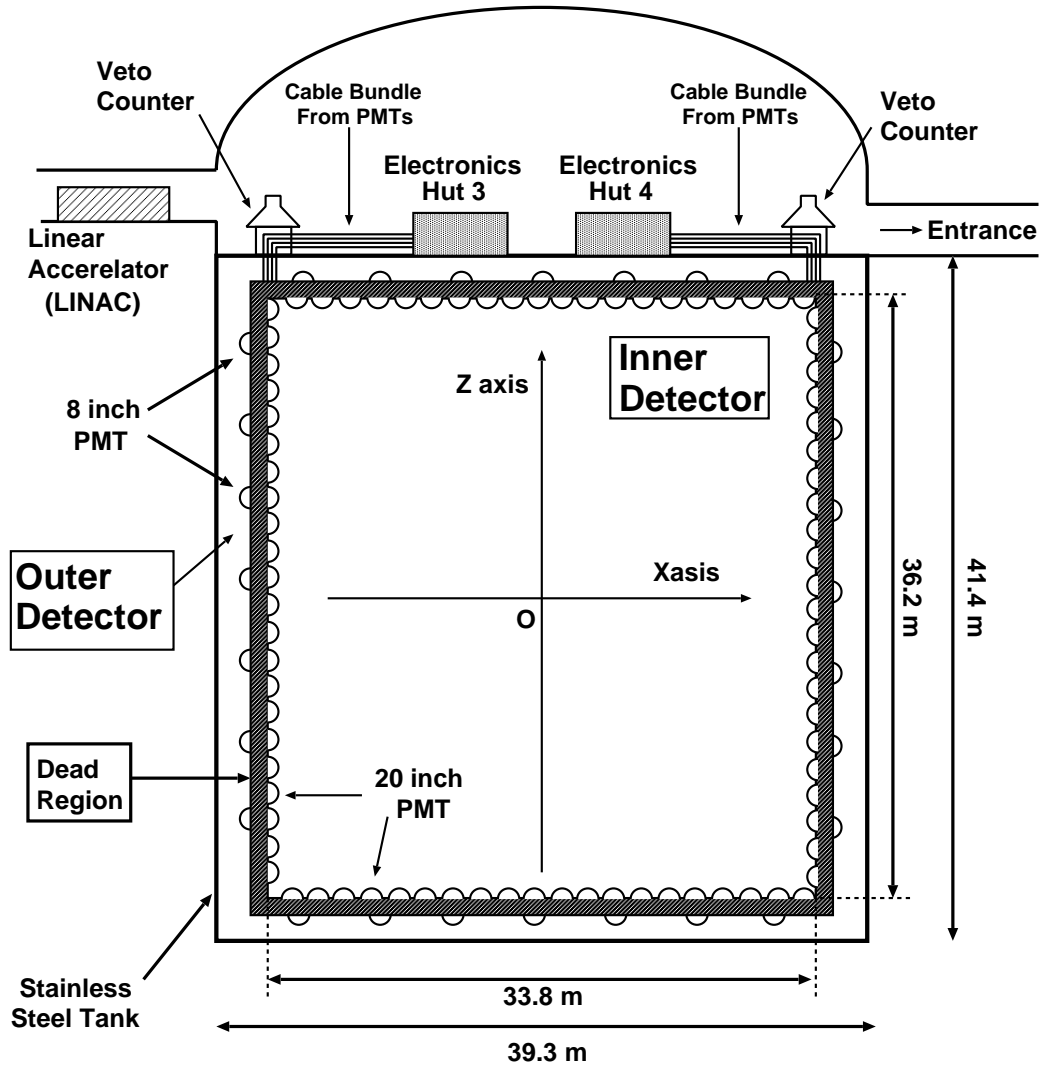


Figure 3.3: Schematic view of the cross section of the detector. The definition of the detector coordinate is also shown. A shaded region between the inner detector and the outer detector is a dead region of 55 cm thickness.

The principle of a water Cherenkov detector is described in Section 3.2 and details of the detector are presented in Sections 3.3 through 3.8.

## 3.2 Detection Principle

Super-Kamiokande detects relativistic charged particles through their emission of Cherenkov light in water. Cherenkov radiation was originally discovered by Cherenkov in 1934 and theoretically explained by Tamm and Frank [85]. Cherenkov radiation is a shock wave of the radiation created by a relativistic charged particle with the velocity greater than the light velocity in the medium:

$$v \geq \frac{c}{n} \quad (3.1)$$

where  $v$  is the particle velocity and  $n$  is the refractive index of the medium. The refractive index of water is about 1.34. Fig. 3.4 shows the schematic view of the Cherenkov radiation. Trajectories of Cherenkov photons form a cone along the particle track with a opening angle  $\theta_C$  as:

$$\cos \theta_C = \frac{1}{n\beta} \quad (3.2)$$

where  $\beta = v/c$ .

The number of Cherenkov photons  $N$  emitted in a unit wavelength  $d\lambda$  and a unit particle track  $dx$  is given by:

$$\frac{d^2 N}{dx d\lambda} = \frac{2\pi\alpha}{\lambda^2} \left( 1 - \frac{1}{(n\beta)^2} \right) \quad (3.3)$$

where  $\alpha$  is the fine structure constant.

In the case of a charged particle propagating in water with near light velocity ( $\beta \simeq 1$ ), opening angle  $\theta_C$  is about  $42^\circ$ , and about 340 photons/cm are emitted for the wavelength between 300 nm and 600 nm.

Cherenkov light makes a circular image projected on a surface plane of the detector. Super-Kamiokande can recognize the images of the Cherenkov rings by the photomultiplier tube array lied on the surface plane of the detector. Fig. 3.5 shows a view of a typical simulated event in Super-Kamiokande.

## 3.3 Water Tank

Figs 3.2 and 3.3 show the schematic view of the cross section of the detector. Water tank for Super-Kamiokande is a cylindrically-shaped stainless steel tank measuring 39.3 m in diameter and 41.4 m in height, and it holds 50 kiloton of water. The tank is tightly sealed to keep radon gas out. The tank is optically separated into three concentric cylindrical regions.

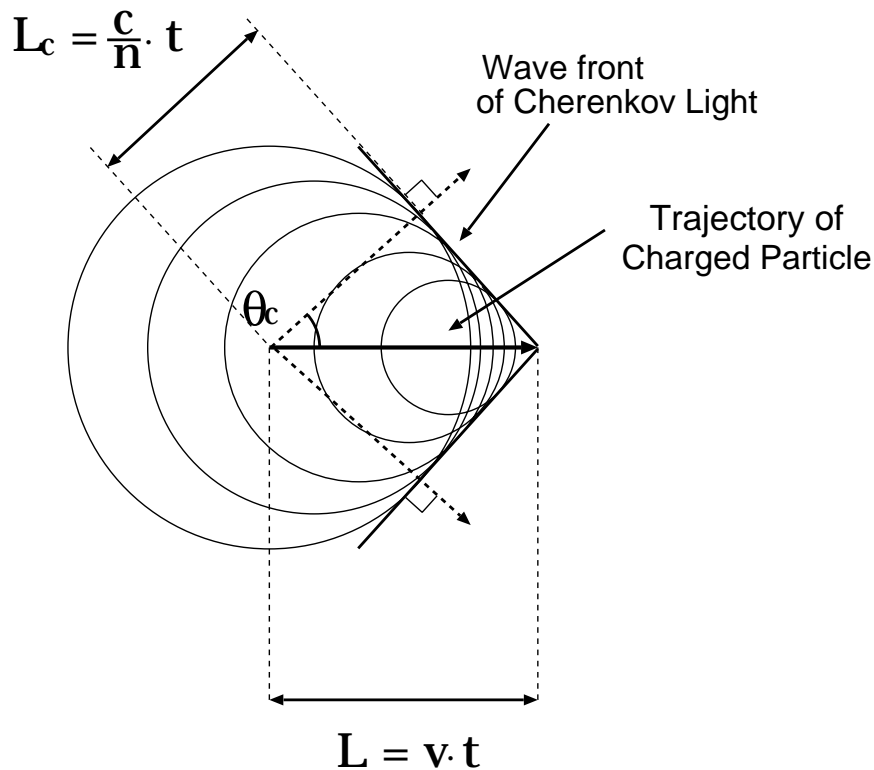


Figure 3.4: Schematic view of the Cherenkov radiation. A bold arrow shows the trajectory of a charged particle, dashed arrows show the direction of the Cherenkov light.  $t$  shows the time of flight of the charged particle, and  $v$  and  $c/n$  show the velocity of the charged particle and light velocity in the medium, respectively. Circles represent the radiation in the medium due to the charged particle, and bold lines touching to the circles show the wavefront of the Cherenkov light. Trajectories of the emitted Cherenkov photons form the cone with opening angle  $\theta_C$ .

The inner region is 36.2 m in height and 33.8 m in diameter (32 kiloton). This region is called 'Inner Detector (ID)'. ID is viewed by 11146 20-inch diameter custom made photomultiplier tubes (PMTs) facing inward. 7650 PMTs are mounted on the side surface, and 1748 PMTs are mounted on both of the top and bottom surfaces. These PMTs are uniformly arranged on a lattice with 70.7 cm interval, and are supported by the stainless steel structures shown in Fig. 3.6. The photocathode coverage is 40%. The border of the ID is lined with opaque black sheet made of polyethylene terephthalate. The Outer Detector (OD) completely surrounds the ID. OD is 2.0~2.2 m thick, and viewed by 1885 8-inch PMTs facing outward with 60 cm square wavelength shifter plates in order to enhance the Cherenkov light collection. 1279 PMTs are mounted on the side surface, and 302 (304) PMTs are mounted on the top (bottom) surface. The border of the OD is lined with a DuPont Tyvec, a white reflective material, to increase

the light collection. The purpose of the OD is to reject cosmic ray muons and to recognize the outgoing particles. 2.0 m thick of water in OD also functions as an absorber for the  $\gamma$ -rays and neutrons from the surrounding rock. The middle region between ID and OD is an about 0.55 m thick dead region which is not instrumented, and cables from 20-inch PMTs and 8-inch PMTs run through this region.

Geomagnetic field can affect the timing resolution of the PMTs. At the Kamioka site, the strength of the geomagnetic field is about 450 mG, and 26 sets of Helmholtz coil are located around the tank to compensate for the geomagnetic field. The magnetic field is reduced to 50 mG in every position of the detector.

The definition of the detector coordinate commonly used in this thesis is described in Fig.'s 3.2 Fig. 3.3.

## 3.4 Photomultiplier Tubes

### 3.4.1 PMT for Inner Detector

We use 20-inch diameter HAMAMATSU R3600-5 PMTs in ID, which was originally developed by HAMAMATSU Photonics Company and Kamiokande collaborators for the Kamiokande experiment [86] and were improved for use in Super-Kamiokande [87]. Fig. 3.7 shows the view of the 20-inch PMT, and the characteristics are summarized in Table 3.1.

The window of the PMT is made by 5 mm thick borosilicate glass because of its spectral transmittance and water durability. Photocathode material is chosen to be Bi-alkali because its quantum efficiency curve matches the spectrum of the Cherenkov light through pure water, as shown in Fig. 3.8. The dynode is chosen to be a Venetian blind configuration in order to cover the large area of the photocathode surface. The dynode structure was optimized for the Super-Kamiokande experiment to have a good timing response and single p.e. response [87]. Fig. 3.10 shows the relative transit time distribution. It shows that the timing resolution is about 2.2 nsec for single p.e. signals. Fig. 3.9 shows the pulse height distribution for single photoelectron signals by the PMT. A Clear peak of the single p.e. is seen. A signal from a PMT is read out through a  $\sim 70$  m co-axial cable connecting the PMT and electronics.

High voltage (HV) power supply system for ID PMTs consists of CAEN A933 AKP distributing power supply boards and CAEN SY527 multi-channel power supply systems. One high-voltage board can supply to 24 channels of PMTs, and one SY527 controls 10 boards. In total, 48 units are used in the Super-Kamiokande experiment. They are housed in the four quadrant huts on the top of the detector together with other electronics for data acquisition. The HV system can be remote-controlled via network. About 1500  $\sim$  2400 V is supplied for

Parameter	Description & values
Spectral Response	300 nm to 650 nm
Shape	Quasi-hemispherical
Window material	borosilicate glass
Photocathode material	Bialkali
Photocathode area	2400 cm <sup>2</sup>
Quantum efficiency	20% at $\lambda = 400$ nm
Dynode structure	Venetian blind
Number of stages of Dynode	11
Gain	$10^7$ at $\sim 2000$ V
Pressure tolerance	6 kg/cm <sup>2</sup> water proof
Cathode nonuniformity	< 10%
Anode nonuniformity	< 40%
Dark current	200nA at $10^7$ gain
Dark pulse rate	3 K Hz at $10^7$ gain
Transit time	90 nsec at $10^7$ gain
Transit time deviation	2.8 nsec RMS at 1 p.e. equivalent signal
Weight	13 kg

Table 3.1: Characteristics of HAMAMATSU R3600-5 20-inch PMT.

each PMT to obtain  $10^7$  gain. High voltage is very stable, and the measured stability of high voltage is typically within 3 mV [88]. The high voltage is supplied by a  $\sim 70$  m cable which runs along the signal cable.

### 3.4.2 PMT for Outer Detector

Outer detector uses 1885 8-inch HAMAMATSU R1408 PMTs. These PMTs were salvaged from the previous IMB experiment after operation of that experiment ended in 1991.

The PMTs are attached with 60 cm  $\times$  60 cm  $\times$  1.5 cm wavelength shifter plates to enhance the light collection [90]. The light collection is improved about 60% by the wavelength shifter plates. Timing resolution of the PMT is about 11 ns without wavelength shifter, and it is degraded to 15 ns with wavelength shifter.

High voltage supply system for OD PMT consists of LeCroy model 1415 mainframe unit and distributor boards specially developed by the Super-Kamiokande collaborator for this experiment. One distributor boards can supply HV up to 12 channels and one mainframe can control 40 individual boards. In total, 4 units are used in our experiment.

### 3.4.3 Stability of the PMTs

In the operation from April 1996, some PMTs died by water leak or some other reasons. Also, some PMTs become 'Flashing PMTs', which flash by the discharge between the dynodes and make a fake events. The activity of the PMTs is monitored by a realtime program. The flashing PMTs are turned off by physicists when they are found. These inactive PMTs are called 'bad-channels'.

Fig. 3.11 shows the number of bad-channels as a function of the elapsed days. About 1.5% (12%) of ID (OD) PMTs are bad-channels in March 2000. One of the reasons for the high dead rate of OD PMTs could be due to the difference in the water proof structures of the PMTs.

## 3.5 Veto Counters on Cable holes

After several months' data taking from May 1996, we found that there were insensitive regions in the outer detector under the cable extraction holes where the cables from PMTs are pulled out.

The reason for the insensitive OD regions under the cable holes is explained as follows. Beneath the cable extraction holes, there are large bundles of the cables from PMTs. The cosmic ray muons passing through the cable bundles are shaded and are not detected by the outer detector. We call these muon events as 'Cable-hole muon' events. Fig. 3.12 shows the schematic view of the cable-hole muons.

Super-Kamiokande has 12 cable holes on the top of it. Among them, only 4 cable holes have the insensitivity. It is because that these 4 cable holes locate about 2 m inner than the others as shown in Fig. 3.2, and the cable bundles are overlapping to the edge of the inner detector.

To compensate for the inefficiency of OD, we installed 4 veto counters above the inefficient cable hole regions in April 1997. The veto counter has a simple design. Fig. 3.13 shows the design of the veto counter. A veto counter uses 20 pieces of 50 cm  $\times$  50 cm  $\times$  25 mm plastic scintillators (2m  $\times$  2.5m area in total) and a 20-inch PMT. The plastic scintillators are placed about 10 cm above the cable bundles pulled out from the cable holes. The housing is made of aluminum and the inside is painted by a reflector paint to enhance the scintillation light collection. The bottom surface of the plastic scintillators are also painted with the reflector paint. The detection efficiency for cosmic ray muons was estimated to be almost 100% from a measurement using a  $^{60}\text{Co}$  gamma-ray source.

A signal from the veto counter is processed in the same way as the PMTs of the inner detector, but it does not participate in the event trigger described in Subsection 3.8.3. The informations of the veto counters are used only in the off-line data reduction as shown in Chapter 5.

Fig. 3.14 shows the reconstructed vertex distribution for Fully Contained  $\mu$ -like events for both before and after the installation of the veto counters. Only the events with  $Z \geq 0$  were plotted. The definition of Fully Contained  $\mu$ -like sample is described in Chapter 5 and Chapter 8. There were clear four clusters around cable holes before the veto counter installation. After the installation of the veto counters, no cluster are found in the vertex distributions. But from Apr. 1999 to Oct. 1999, two of the four veto counters were not operational because of a electronics trouble. Troubles were fixed and veto counters has been working normally since then.

A probability of accidental killing of an atmospheric neutrino event by an accidental hit of the veto counters is estimated to be of the order of  $10^{-5}$ .

### 3.6 Ultra Pure Water and Purification System

The source of the ultra-pure water filled in Super-Kamiokande is a plenty of clean natural spring water flowing in the mine. The water used in Super-Kamiokande experiment is required to have a good transparency and a very low radioactive contamination. As described in the beginning of this chapter, Super-Kamiokande also studies solar neutrino and supernova neutrinos whose energy region is from a few MeV to around 20 MeV, and the radioactivity such as  $^{222}\text{Rn}$  is a serious background for these studies.

Water purification systems is a product of ORGANO Company. The purification system consists of several components as shown in Fig. 3.15. Descriptions for each component are as follows:

- 1  $\mu\text{m}$  filter  
Remove small particles with  $1\mu\text{m}$  mesh filter.
- Heat exchanger  
Cool down the water which was heated by PMT and water pumps to around  $13^\circ\text{C}$ . Cooled water decreases PMT dark rate and suppresses the bacteria growth.
- Ion exchanger  
Remove heavy ions such as  $\text{Na}^+$ ,  $\text{Cl}^-$ ,  $\text{Ca}^{+2}$ .
- Ultra-Violet sterilizer  
Kill bacteria in water.
- Rn-free air dissolve tank  
Dissolve radon-free air in water in order to improve the efficiency of the following vacuum degasifier.

- Reverse osmosis

Water is fed to a reverse osmosis system to reject Radium and very small ( $\sim 1$  nm) particles. This system was installed in March 2000.

- Vacuum degasifier

Remove dissolving gases such as oxygen and radon.

- Cartridge polisher

Higher performance ion exchanger than used in Ion exchanger (see the 3rd item) Over 99% of ions are removed.

- Ultra filter

Ultra filter is consist of hollow fiber membrane filters. Remove the particles of the order of 10 nm.

- Reverse osmosis

The unfiltered water by the ultra filter and the reverse osmosis (6th item) is fed to the reverse osmosis with the buffer tank. The filtered water is fed into the main water flow line.

The water is circulated between Super-Kamiokande and the water purification system with about 30~50 ton/hour flow rate. After the water purification system, the typical number of particles larger than  $0.2 \mu\text{m}$  is about 6 prticles/cc, and the Rn concentration is measured to be about 10~20 mBq/m<sup>3</sup>. The attenuation length of light in the Super-Kamiokande detector is about 100 m at the wavelength of 400 nm (see Section 4.4).

### 3.7 Rn-free Air System

The air in Super-Kamiokande is purged by Rn-free air. Fig. 3.16 shows the Rn-free air system. The Rn-free air is made of the air in the mine. At first, the air is compressed to 7~8.5 atm. Then the air is sent through an air filter to remove dusts larger than  $0.3 \mu\text{m}$ , and stored in a buffer tank. An air drier removes CO<sub>2</sub> gas and moisture that affect the efficiency of the rejection of Rn gas in charcoal columns. Then four charcoal columns remove Rn gas and two air filters of  $0.1 \mu\text{m}$  and  $0.01 \mu\text{m}$  remove a remaining dust. Finally, a charcoal column cooled to  $-40^\circ\text{C}$  removes the remaining Rn gas. The concentration of Rn in the Rn-free air is about 3 mBq.

### 3.8 Data Acquisition System

Both ID and OD are separated into four quadrants. The signals from PMTs are sent to one of four huts in which electronics and HV system are housed. Another hut called 'central hut'

is located near the center of the top of the tank. The central hut generally controls the other four quadrant huts, and all data from four quadrant hut are collected and an event trigger is generated in this hut. Temperature of all huts are well controlled to about  $27^{\circ}\text{C}$  within  $\pm 0.5^{\circ}\text{C}$  in order to minimize the effects for electronics.

PMT signals are processed by different electronics for ID and OD. Each data acquisition(DAQ) system is described in the following sections.

### 3.8.1 Inner Detector Data Acquisition System

#### Front End Electronics

Fig. 3.17 shows the block diagram of the data taking system for ID. The PMT signals are processed by TKO(Tristan KEK On-Line) [91] ADC/TDC modules called ATM (Analog-Timing-Module) [92].

Fig. 3.18 shows the block diagram of an ATM channel. A PMT signal fed to an ATM module is split into four signals. One signal is fed to a discriminator after amplified by a factor of 100. The threshold of the discriminator is set to  $\sim 100$  mV which corresponds to about 0.3 p.e.. If the signal is over the threshold level, HITSUM signal with 200 nsec width and 15 mV height is generated and sent to a TRG(TRiGger) module in order to generate a global trigger. And also, a gate signal with 900 nsec width is sent to TAC (Timing to Analog Converter) circuit to start the timing measurement, and QAC (Charge to Analog Converter) circuit to start the charge integration. One of the other signals fed to QAC circuit are integrated with a 400 nsec time window. TAC (Timing to Analog Converter) circuit integrates a charge with a constant current until the global trigger signal arrives within  $1.3 \mu\text{sec}$ .

Each channel has two sets of TAC and QAC circuits as shown in Fig. 3.18 in order to process two successive events, (muon decay, high rate event such as supernova neutrinos, etc.) without any serious dead time.

If a global trigger is sent to ATM, charge informations of TAC and QAC are digitized by ADC (Analog-Digital-Converter) and stored in an internal memory of ATM called FIFO (FastIn FastOut). If the global trigger is not issued, the informations in TAC and QAC within  $1.3 \mu\text{sec}$  are discarded. TRG modules also send the event number to ATM through a master module of ATM modules called GONG (GO-NoGo) via the bus-interface module between TKO modules and VME modules called SCH (Super-Controller-Header). The event number is stamped to the digitized T and Q data of all channels. Charge and timing data are digitized into 12 bit digital data. ATM provides a  $1.3 \mu\text{sec}$  dynamic range with 0.3 nsec resolution and 600pC dynamic range with 0.2 p.e. resolution.

One ATM board handles 12 PMTs, hence 946 ATM boards are used in Super-Kamiokande.

### **On-Line System**

Digitized data stored in FIFO are read out by on-line computers through a memory modules called SMP (Super-Memory-Partner) via SCH. These data-handling on-line computers are called 'slave' computers. Super-Kamiokande uses 8 slave computers and 48 SMPs, and one SMP handles 20 ATMs through a set of GONG and SCH (see Fig. 3.17). These data collected by the slave computers are transferred to the 'host' computer via the FDDI network. The host computer build a complete date of an event by merging ID and OD PMTs informations, and trigger informations.

### **3.8.2 Outer Detector Data Acquisition System**

#### **Front End Electronics**

Both signals and HV of OD PMTs are carried through the same co-axial cables. The signals separated from the HV by custom made electronics are fed to a module called QTC (Charge-to-Time-Converter). A QTC module encodes the PMT signal into a rectangle pulse with the leading edge holding the PMT hit timing and the width containing the observed charge. QTC module also makes a HITSUM pulse when the PMT signal goes over a threshold. The threshold is set to 0.25 p.e.. These HITSUM signals are summed and fed to TRG module.

If a global trigger is issued, leading and trailing edge of the signals are digitized and stored in memory by LeCroy 1877 multi-hit TDC modules. The dynamic range of the TDC is set to 16  $\mu$ sec with the 0.5 nsec timing resolution. Event number is stamped to the digitized data.

### **On-Line System**

TDC data from the quadrant huts are read by a slave computer, which resides in the central hut, through a FASTBUS module called FSCC (Smart-Crate-Control module) via Ethernet. These collected data are transferred to the host computer and merged with the data from ID.

### **3.8.3 Trigger System**

All HITSUM signals from ATMs are summed and fed to the TRG module to generate a grand HITSUM signal. The HITSUM signals from the QTC modules are also summed separately to generate a grand HITSUM of the outer detector. If the grand HITSUM signal goes over a threshold, a global trigger signal is issued to all electronics. There are several kinds of trigger types: Low Energy (LE) trigger, High Energy (HE) trigger, OD trigger, and Super-Low-Energy (SLE) trigger.

LE trigger requires the grand HITSUM of ID goes over -320mV which corresponds to 29 hits within 200 nsec timing window. LE trigger threshold corresponds to the signals of about 5.7 MeV electron. HE trigger requires the grand HITSUM of ID goes over -340mV which corresponds to 31 hits within 200 nsec timing window. OD trigger requires 19 hits of OD PMTs within 200 nsec timing window. These trigger types can co-exist, and whenever a HE trigger is issued, a LE trigger is also issued. SLE trigger is installed in May 1997. The SLE trigger aims about 4.5 MeV electrons. The SLE trigger is irrelevant to this thesis and we don't describe the details of it.

When the global trigger is issued, the TRG module also generates the 16 bits event number and distribute it to the quadrant huts. The trigger informations such as event number, trigger timing and trigger type are recorded in TRG module, are read by a separate slave computer and transferred to the host computer.

#### 3.8.4 Off-line System

The event data assembled by the on-line host computer are transferred to an off-line computer system after converted to ZBS format [93] which is suitable for data analyses. The off-line system resides in the laboratory out of the mine and connected to Super-Kamiokande by FDDI network.

The off-line system consists of the data storage system and computers for various analyses. All of the data taken in Super-Kamiokande are recorded in the data storage system, and the size of the data is about 27Gbyte/day. Until Jan. 1998, the data storage system was Magnetic-Tape-Library(MTL) which had 12 Tbyte capacity with 10.8 MByte/sec data flow rate. It has been upgraded to SONY PetaSite which has 100 Tbyte capacity with 144 Mbyte/sec data flow rate from Feb. 1998.

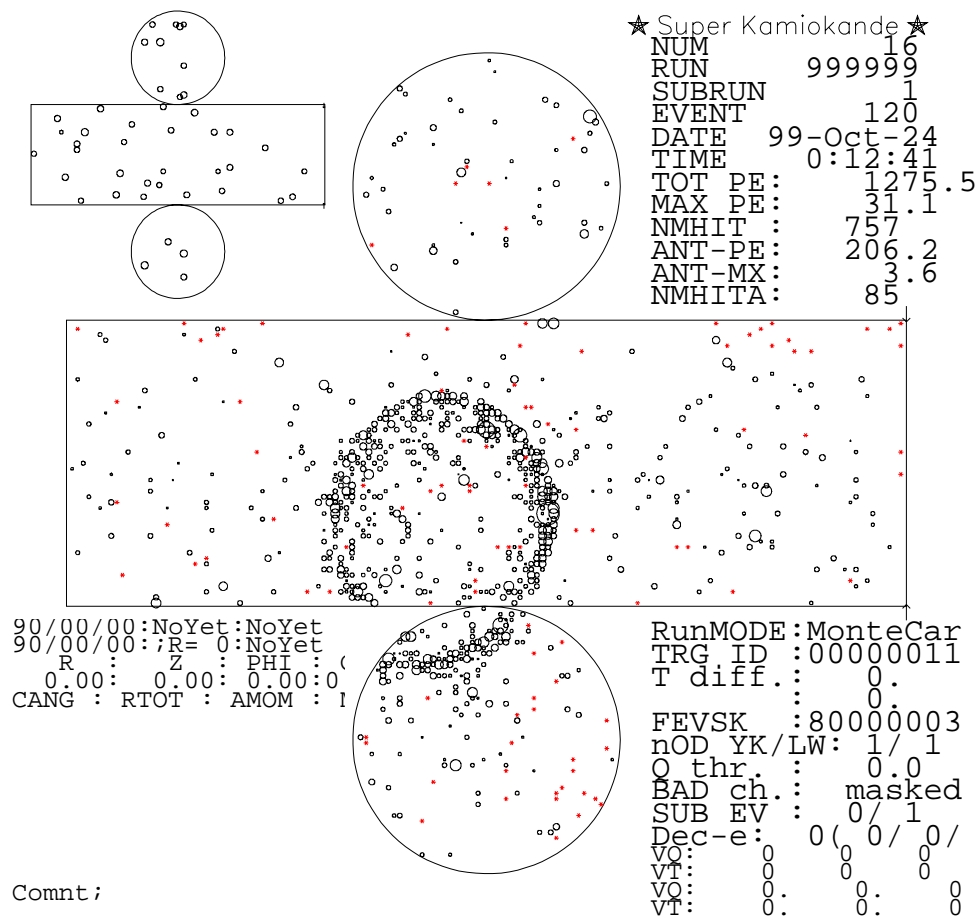


Figure 3.5: The unrolled view of the Super-Kamiokande detector for a typical simulated event of a muon with  $350 \text{ MeV}/c$ . The unrolled figure of the large cylinder shows the inner detector, and the small cylinder at the left top shows the outer detector. Small circles on the unrolled cylinder represents PMTs, and the surface area of the circle represents the detected photoelectrons in each PMT.

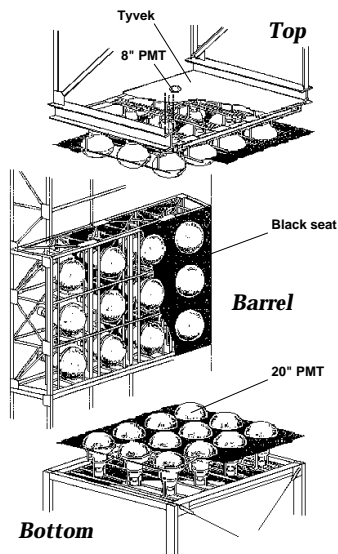


Figure 3.6: Support structure of PMTs. 12 PMTs are mounted in one supporting structure.

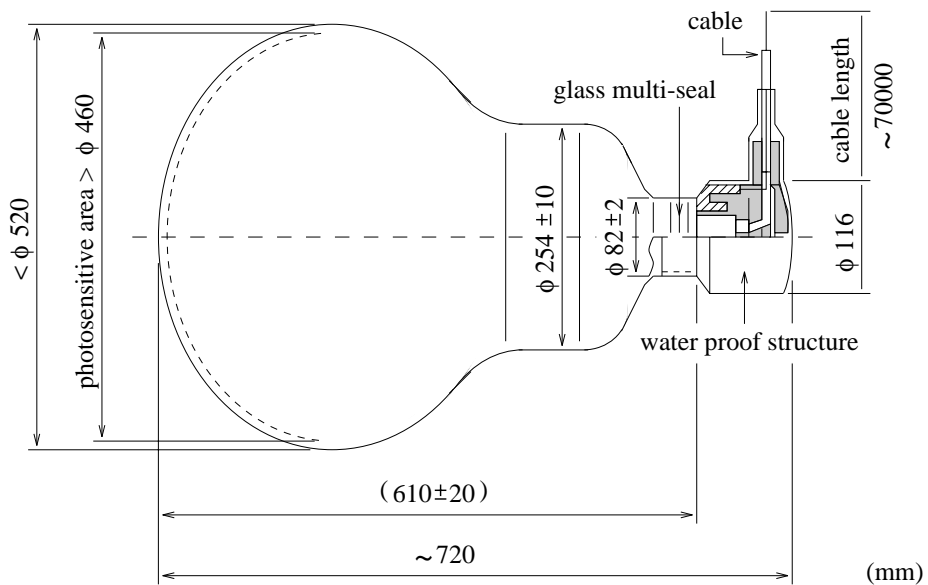


Figure 3.7: Schematic view of the HAMAMATSU R3600-5 20-inch PMT.

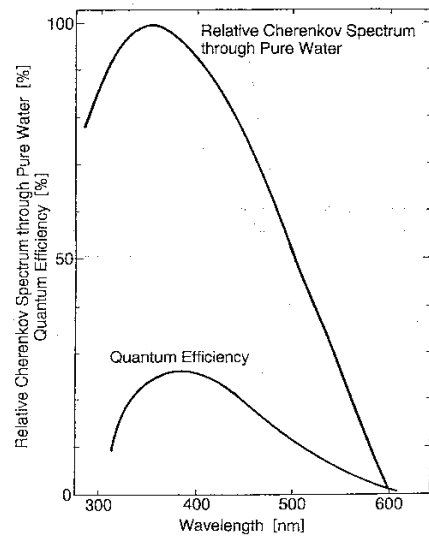


Figure 3.8: Quantum efficiency of 20-inch PMT and relative spectrum of Cherenkov light through pure water.

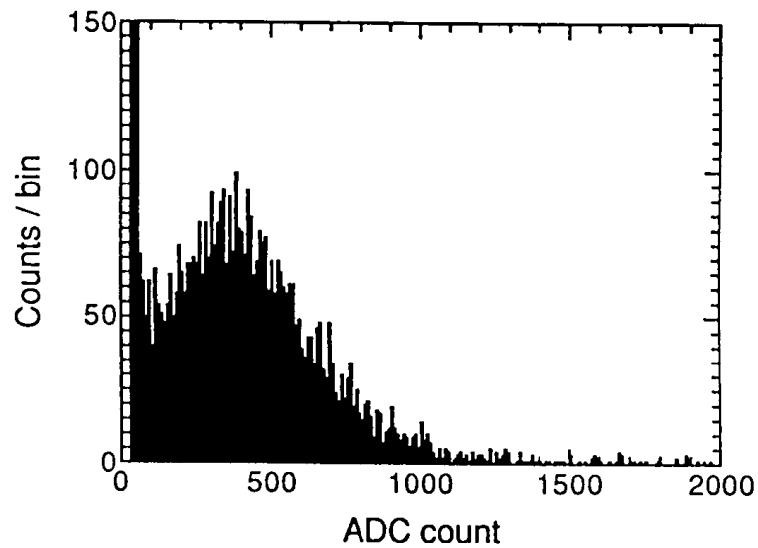


Figure 3.9: Pulse height distribution for single-photoelectron signals.

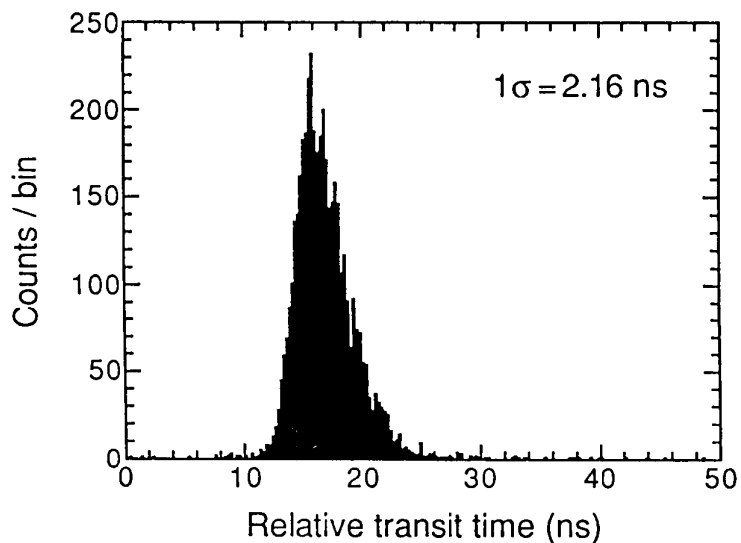


Figure 3.10: Relative transit timing distribution of the 20-inch PMT [87].

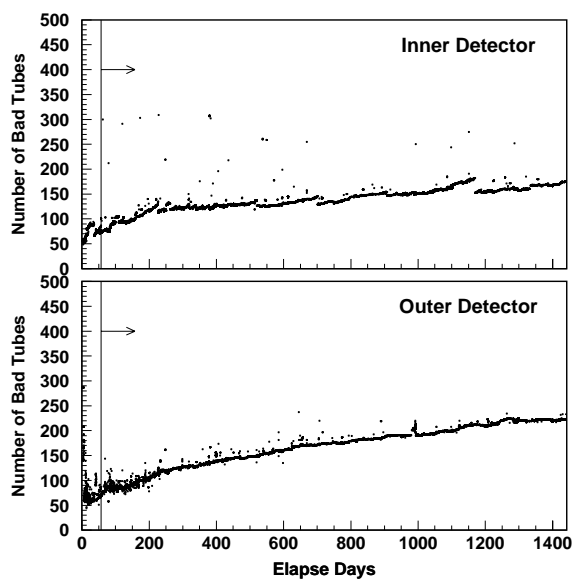


Figure 3.11: Number of bad-channels as a function of elapse days from the start of the experiment. Upper figure shows the number of bad-channels in ID, and lower figure shows the number of bad-channels in OD. Several jump-ups are caused by the disorders of high voltage power supply or data acquisition electronics.

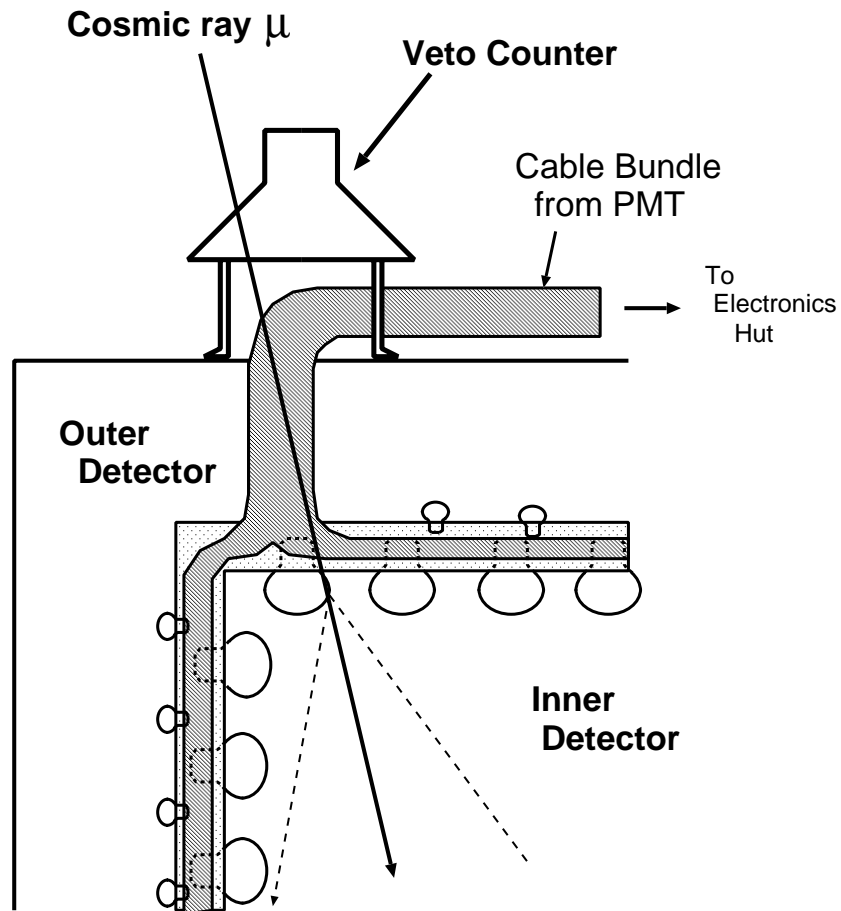


Figure 3.12: Schematic view of a 'Cable-hole' muon. The cosmic ray muon passing through the cable bundle is shaded and not detected by the outer detector.

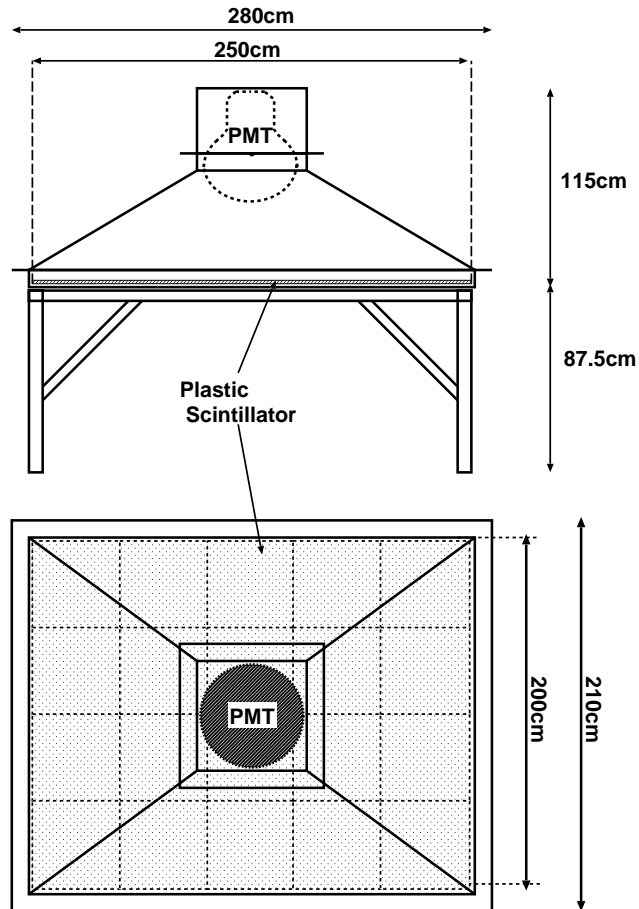


Figure 3.13: Design of the veto counter. Shaded squares represent plastic scintillators.

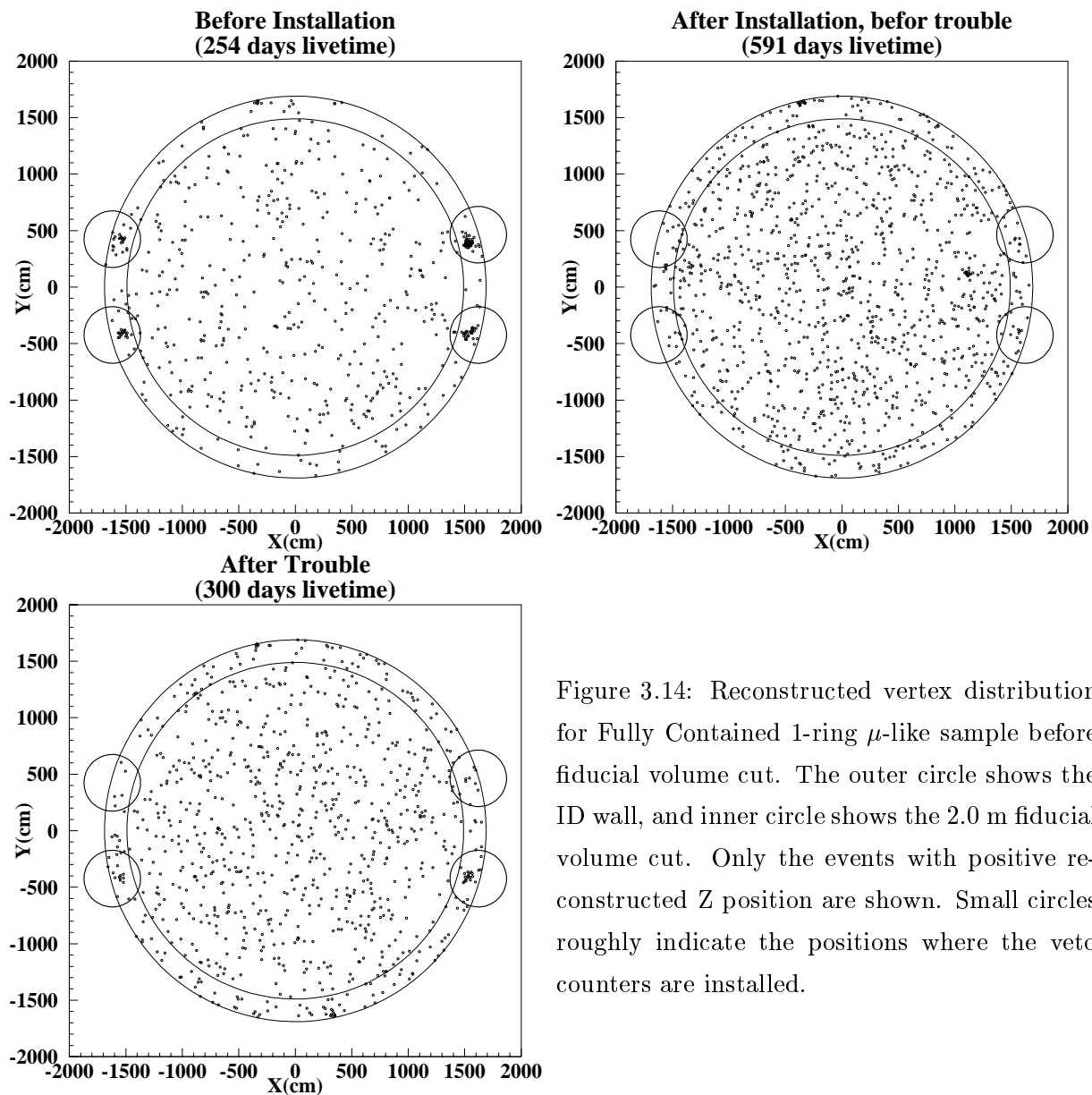


Figure 3.14: Reconstructed vertex distribution for Fully Contained 1-ring  $\mu$ -like sample before fiducial volume cut. The outer circle shows the ID wall, and inner circle shows the 2.0 m fiducial volume cut. Only the events with positive reconstructed Z position are shown. Small circles roughly indicate the positions where the veto counters are installed.

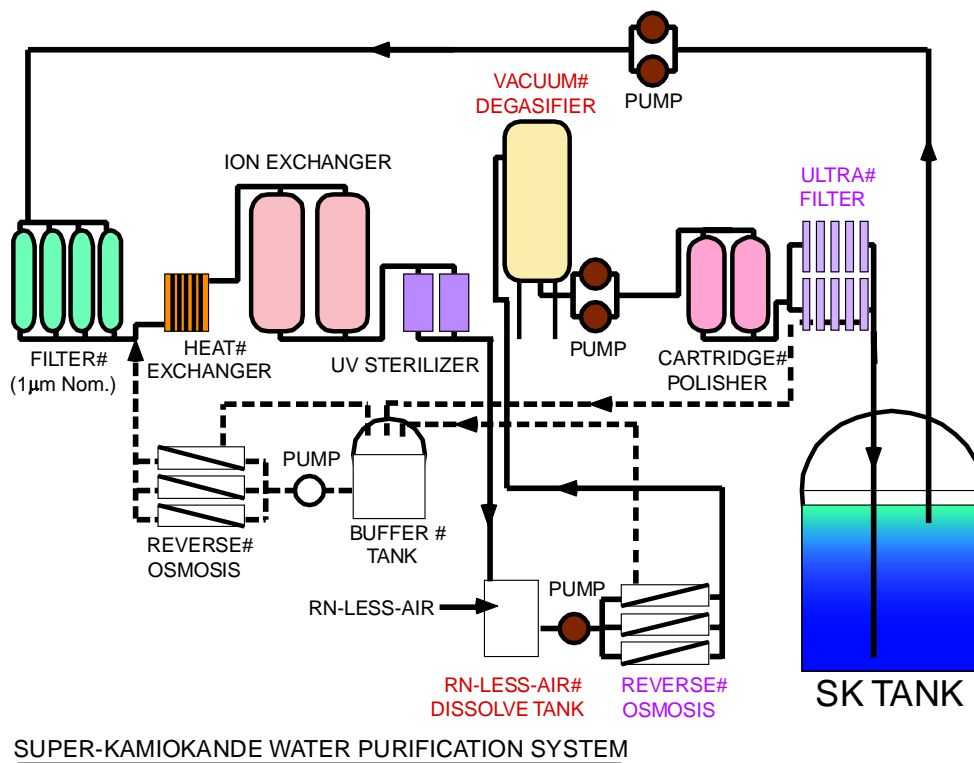


Figure 3.15: The water purification system for Super-Kamiokande.

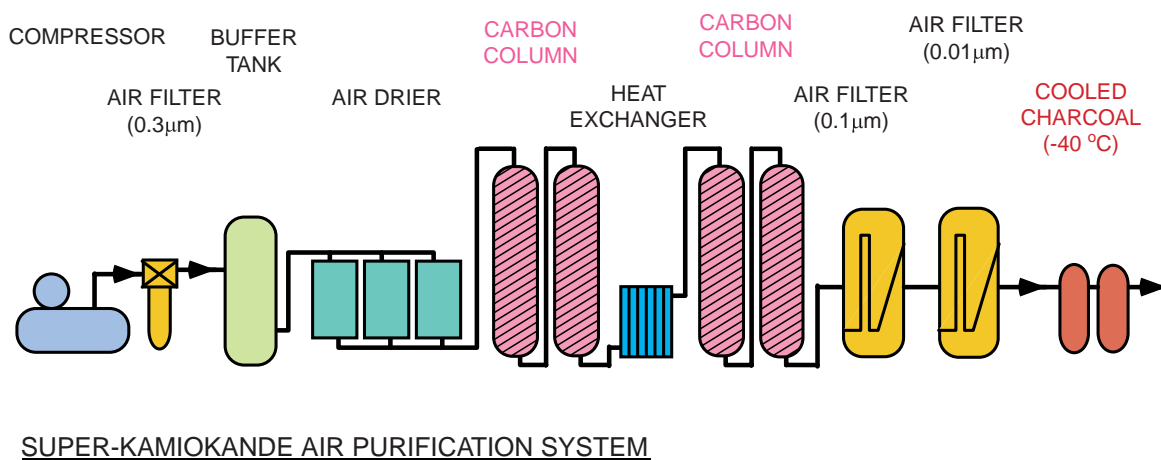


Figure 3.16: The Rn-free air system for Super-Kamiokande.

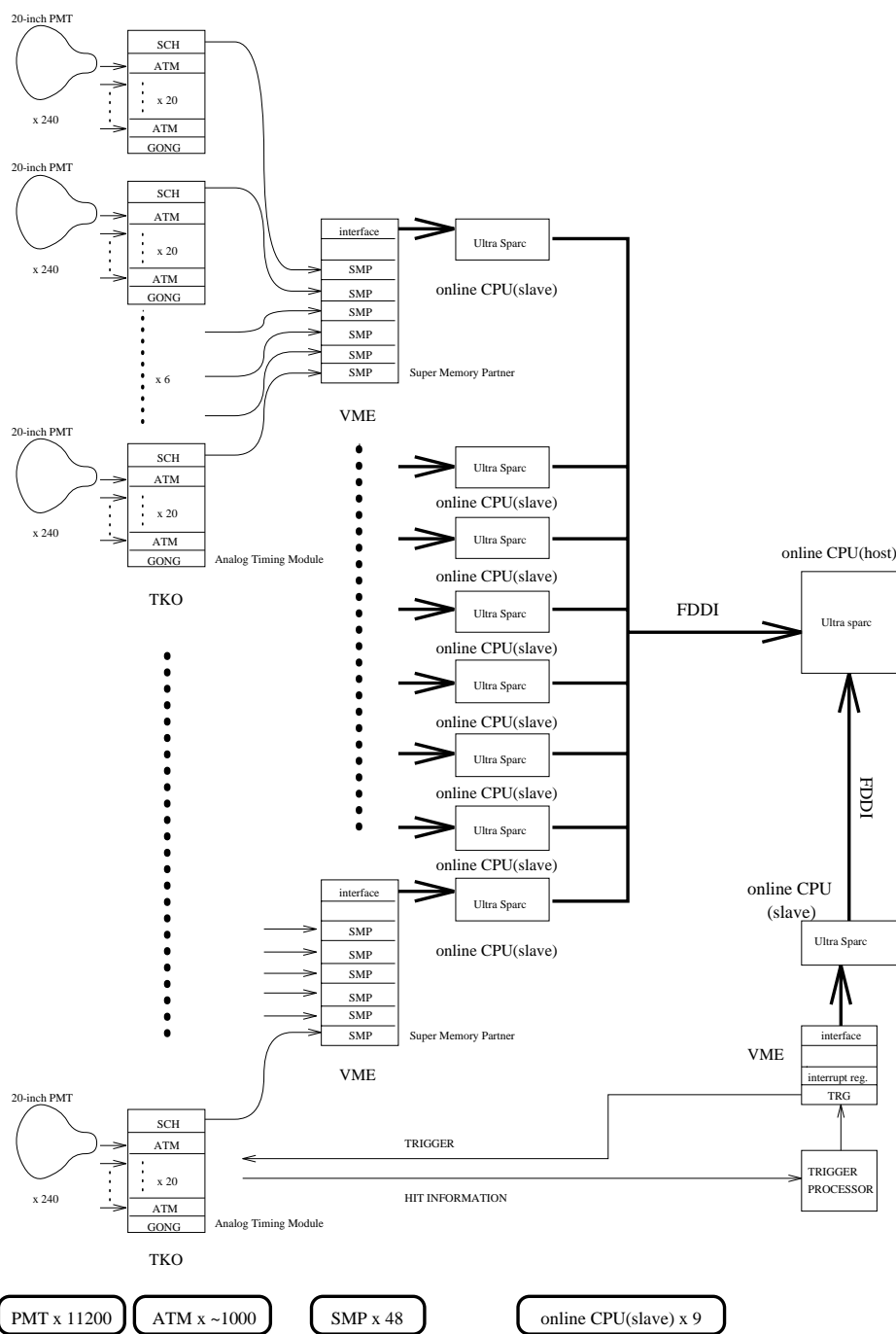


Figure 3.17: Overview of data acquisition system for ID. This figure shows the system at the beginning of the experiment.

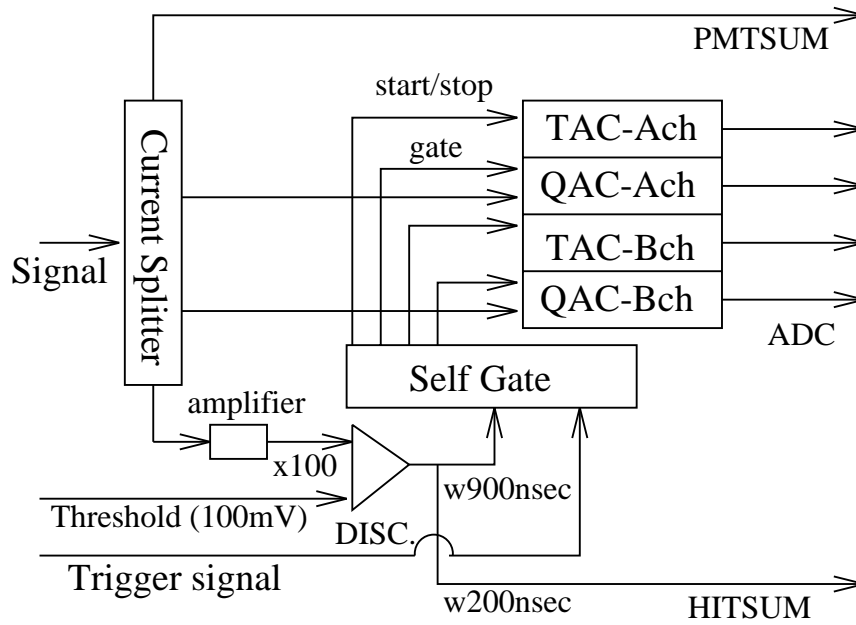


Figure 3.18: Block diagram of an ATM module.

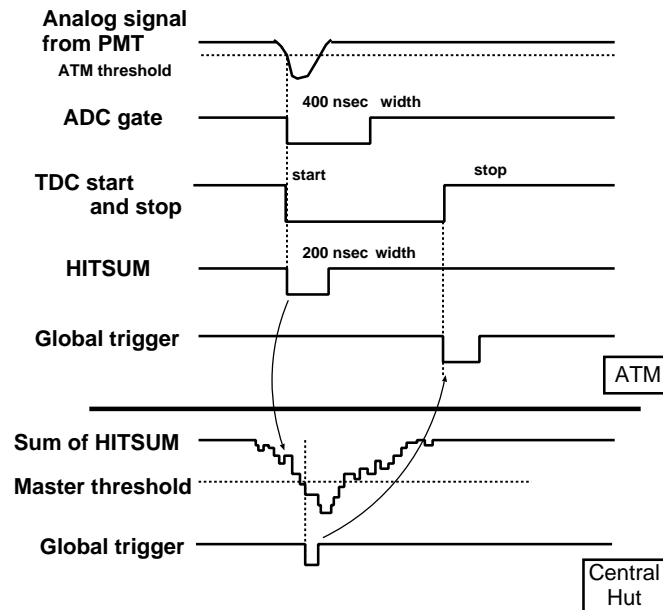


Figure 3.19: Timing chart of DAQ processes in an ATM.

# Chapter 4

## Calibration

### 4.1 Overview

In this chapter, we describe the calibration methods used in the Super-Kamiokande experiment. The gain of the PMTs, the timing response of the channels, and the attenuation length of the water in the tank are the most fundamental characteristics of the detector. The uniformity for both timing and gain is a crucial condition for an unbiased observation. We calibrate these characteristics by several methods described in the following sections. The absolute energy scale is calibrated based on several sources such as cosmic ray muons, neutrino-induced  $\pi^0$ , decay electrons from cosmic ray muons, electrons from a linear accelerator (LINAC).

### 4.2 Relative Gain Calibration

At the beginning of the experiment, the relative gain of the PMTs were measured and the high voltage was set so that all the PMTs have a common gain. After starting the operation, we have regularly measured the relative gain to keep the uniformity.

The schematic view of the relative gain calibration is shown in Fig. 4.1. The light generated by a Xe-lamp filtered by an ultra-violet (UV) filter and ND filter is injected into a scintillator ball located in the inner tank through an optical fiber. The light intensity is monitored by a PMT and photodiodes, and the signals are used for generating an event trigger.

The scintillator ball is made of acrylic resin mixed with BBOT scintillator and MgO powder. The BBOT scintillator has a role of wavelength shifter, which absorbs UV light and re-emits light whose wavelength is peaked at 440 nm. The MgO powder is used as a light diffuser.

The relative gain of the  $i$ th PMT,  $G_i$ , is expressed as:

$$G_i = \alpha \cdot \frac{Q_i}{f(\Theta_i)} \cdot r_i^2 \cdot \exp\left(\frac{r_i}{L}\right) \quad (4.1)$$

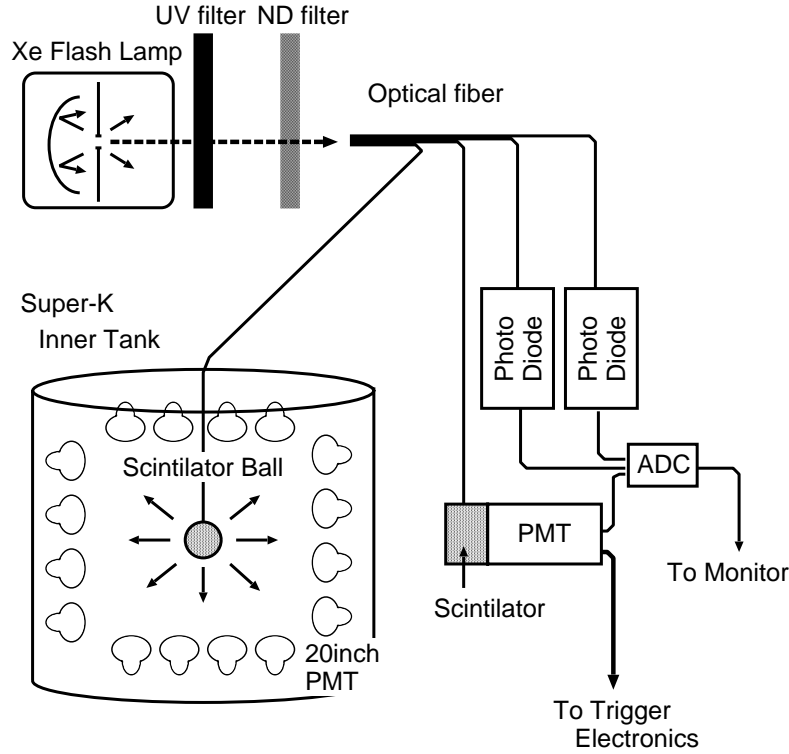


Figure 4.1: Schematic view of the gain calibration system.

where  $\alpha$  is a normalization factor,  $Q_i$  is an observed charge by the  $i$ th PMT,  $\Theta_i$  is the angle between the photon arrival direction and the PMT facing direction,  $f(\Theta_i)$  is the correction function of the acceptance of the  $i$ th PMT,  $L$  is the light attenuation length, and  $r_i$  is the distance of the  $i$ th PMT from the scintillator ball.

The gain of the PMTs are measured by varying the height of the scintillator ball to minimize the position dependence of the measurement. The relative gain spread after adjusting HV is about 7%, and the differences of the gain are corrected in software.

### 4.3 Timing Calibration

Measured hit timing of the PMTs have offsets depending on the cable length (about 70 m) and characteristics of the PMTs. Also, the measured timing has a dependence on the observed photoelectrons caused by the slewing effect of the ATM discriminator.

To understand the timing response of each channel precisely, we carry out a timing calibration using a laser. Fig. 4.2 shows the experimental setup of the timing calibration. We use a  $N_2$  pulse laser which emits 337 nm wavelength, short width pulse ( $\sim 3$  nsec) and has a small jitter

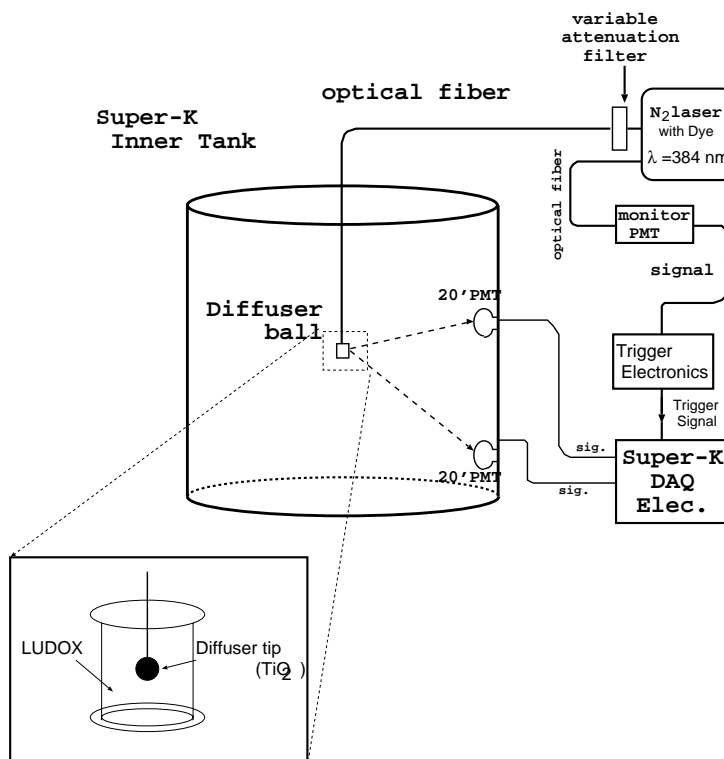


Figure 4.2: Experimental setup of the timing calibration.

time ( $\sim \pm 0.5$  nsec). The light is converted to 384 nm wavelength by a dye module and guided by an optical fiber to a diffuser ball located at the center of the inner detector. The diffuser ball contains  $\text{TiO}_2$  reflector tip at the center of the ball, and filled with a diffuser LUDOX which is a silica-gel which is 20 nm glass fragments. We take the data with various light intensities using a variable attenuation filter.

Fig. 4.3 shows a measured timing-charge correlation map (we call 'TQ-map') for a typical 20-inch PMT. Dots show the data, and circles and error bars show the averaged hit timing for each bin and its resolutions, respectively. A higher charge hit has a earlier hit timing and better timing resolution. Fig. 4.4 shows the measured timing resolution for a typical 20-inch PMT. Measured timing information for each PMT is corrected by its TQ-map in software.

## 4.4 Water Attenuation Length Measurement I

A direct measurement of the attenuation length of the water in the Super-Kamiokande detector is carried out using a dye laser and CCD camera system. Fig. 4.5 shows the experimental setup of the measurement [94]. We use a  $\text{N}_2$  pulse laser (337 nm wavelength) and dye modules which

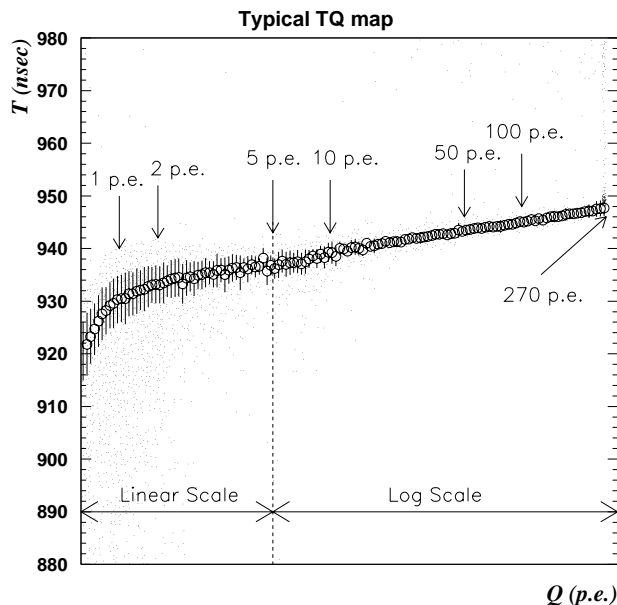


Figure 4.3: Measured TQ-Map distribution for a typical 20-inch PMT.

produce monochromatic 337, 365, 400, 420, 460, 500 and 580 nm wavelength laser lights. The laser is guided to the diffuser ball located in the inner tank through an optical fiber. The light intensity is monitored by a reference 2-inch PMT.

The image of the diffuser ball is taken by a CCD camera which is located on the top of the tank. From the image, we calculate the light intensity after passing through the water by subtracting laser-off images and making a correction of the acceptance of the scintillator ball and the refraction on the surface of the water. We measure the light intensity varying the depth of the diffuser ball.

Fig. 4.6 shows the light intensity divided by the reference PMT signal as a function of the distance of the diffuser ball from the CCD camera. It shows that the light intensity is well reproduced by an exponential curve. Fig. 4.7 shows the wavelength dependence of the measured attenuation length. The maximum attenuation length is about 100 m at 400 nm. For both the shorter and longer wavelength the attenuation length is shorter.

## 4.5 Water Attenuation Length Measurement II

Another water transparency measurement is carried out using Cherenkov light from cosmic ray muons passing through the detector vertically downward. This measurement gives a continuous monitoring of the attenuation length of the water, but the wavelength dependence of the

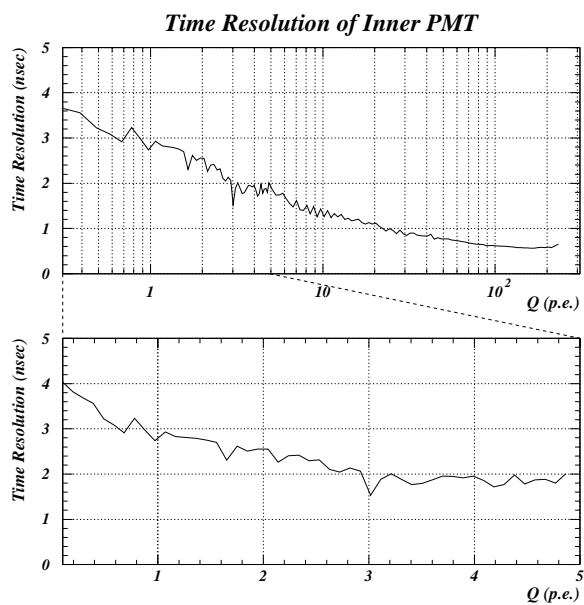


Figure 4.4: Measured timing resolution of a typical 20-inch PMT as a function of the detected photoelectrons.

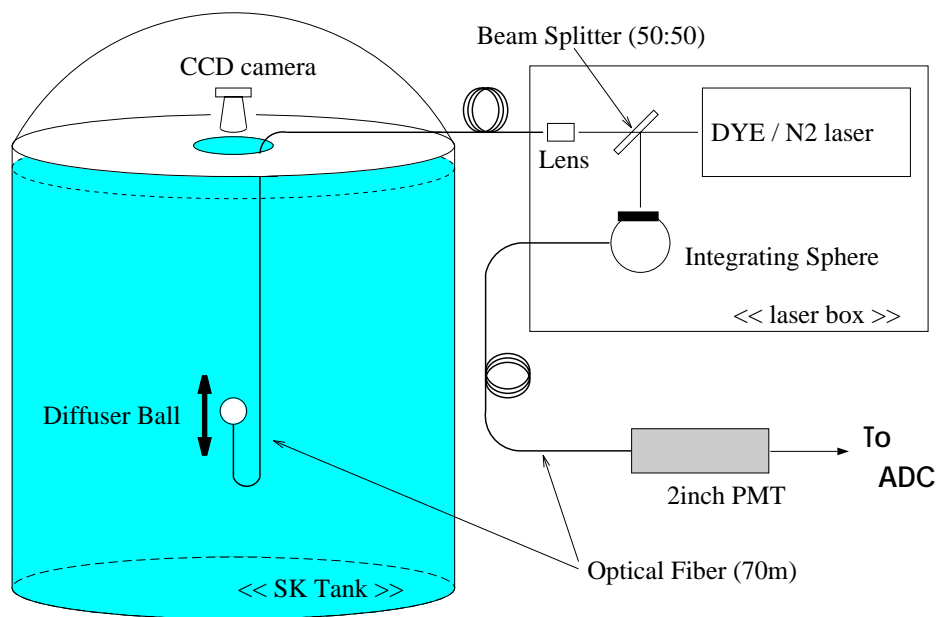


Figure 4.5: Schematic view of the water transparency measurement.

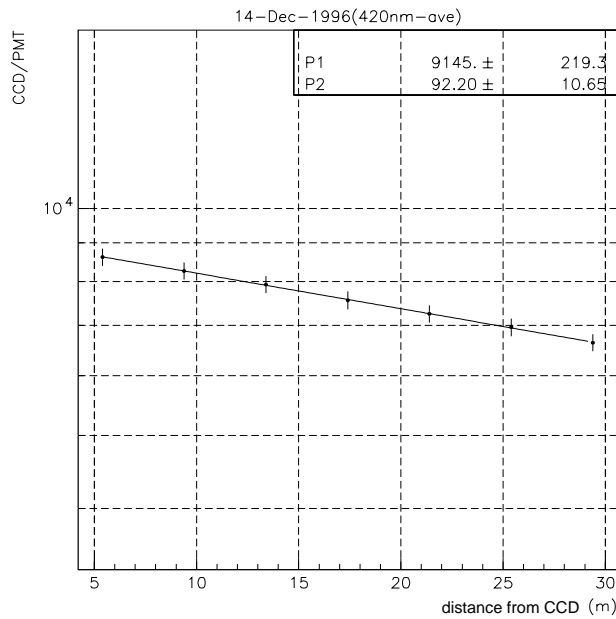


Figure 4.6: The ratio of corrected CCD signal to the reference PMT signal as a function of the distance between the CCD camera and the diffuser ball for 420 nm wavelength. From this measurement the attenuation length is estimated to be 92.2 m.

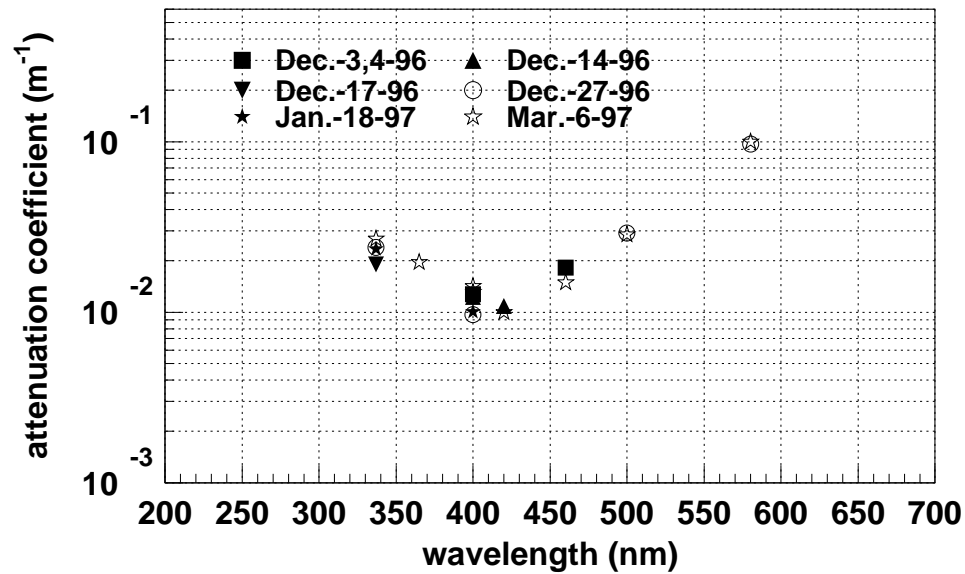


Figure 4.7: The wavelength dependence of the attenuation length directly measured by the laser and a CCD system.

attenuation length is not obtained from this measurement.

The selection criteria for the muons are:

- 50000 p.e. < total p.e. < 125000 p.e.
- Reconstructed entrance point is on the top wall and  $\sqrt{x_{in}^2 + y_{in}^2} < 15.9$  m
- Reconstructed exiting point is on the bottom wall and  $\sqrt{x_{out}^2 + y_{out}^2} < 15.9$  m
- $\sqrt{(x_{in} - x_{out})^2 + (y_{in} - y_{out})^2} < 5$  m

where  $(x_{in}, y_{in})$  and  $(x_{out}, y_{out})$  represent the entrance and exiting points of the muon, respectively. The first criterion is required to reject short track muons and hard-interacting muons.

Fig. 4.8 shows the schematic view of the measurement. We calculate the corrected p.e.s,  $Q_i^{corr}$ , from the measured p.e.s:

$$Q_i^{corr} \equiv \frac{Q_i \cdot l_i}{f(\Theta_i)} \quad (4.2)$$

where  $Q_i$  is the measured p.e.s,  $l_i$  is the travel length of the Cherenkov photons to the  $i$ th PMT, and  $f(\Theta_i)$  is correction function of the PMT acceptance.  $l_i$  is estimated assuming that the emitting angle of Cherenkov photons is  $42^\circ$  to the muon track.  $Q_i^{corr}$  is proportional to the number of photons surviving after traveling  $l_i$  through the water.

Fig. 4.9 shows  $Q^{corr}$  as a function of  $l_i$  for a typical measurement.  $Q^{corr}$  is well reproduced by an exponential curve, and the attenuation length is estimated to be about 95 m. Fig. 4.10 shows the light attenuation length obtained from the cosmic ray muon analysis as a function of the elapse days. The attenuation length varies around 100 m.

## 4.6 Absolute Energy Calibration

### 4.6.1 Muon Decay Electrons

Electrons from the decay of cosmic ray muons stopped in the inner detector are used for checking the absolute energy scale. The selection criteria are:

- Electrons triggered within  $1.5 \mu\text{sec}$  and  $8.0 \mu\text{sec}$  after the trigger of a parent muon
- The number of hit ID PMTs within 50 nsec time window is greater than 40.
- Vertex should be reconstructed within the fiducial volumes (2 m inside from the PMT array).

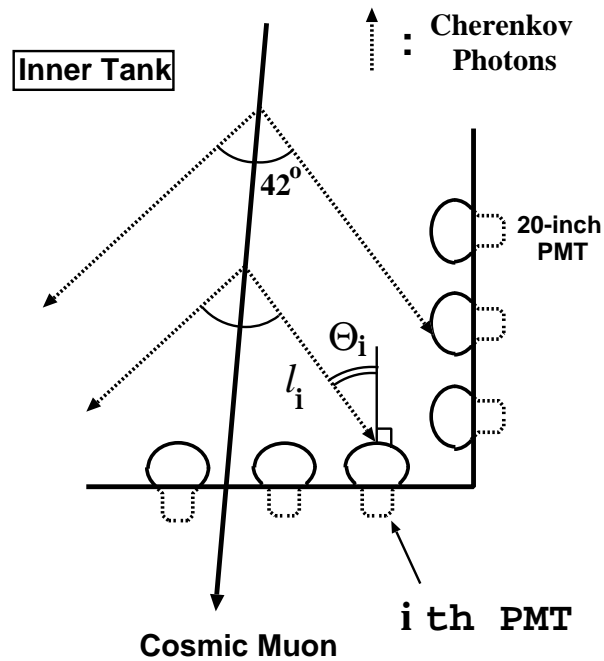


Figure 4.8: Schematic view of the attenuation length measurement using vertically penetrating cosmic ray muons. Dotted arrows show the trajectories of Cherenkov photons and  $l_i$  shows the flight length of the Cherenkov photons detected by the  $i$ th PMT.

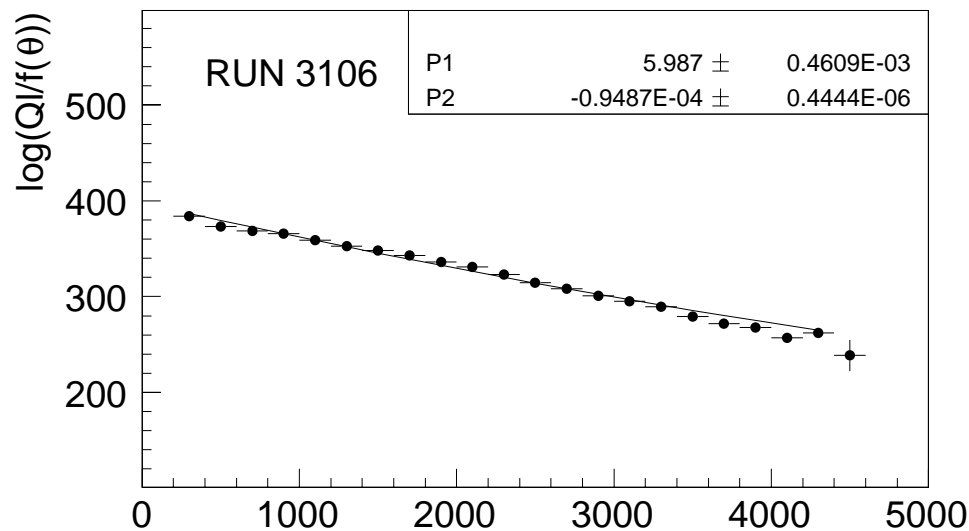


Figure 4.9: Corrected photoelectrons as a function of flight length of Cherenkov photons. The line shows the fitted result by a exponential function. The measured attenuation length  $L$  is about 95 m.

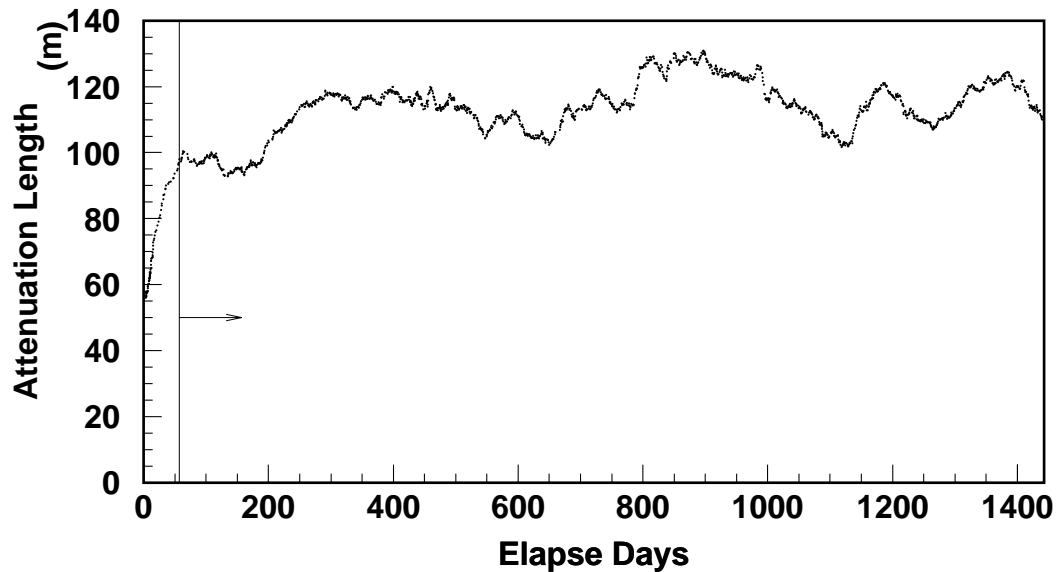


Figure 4.10: The time variation of the light attenuation length as a function of elapse days obtained from the cosmic ray muons analysis. The line and arrow indicate the period where the data are used in the physics analyses.

The electron and positron spectrum precisely calculated from  $V - A$  theory as:

$$\frac{d\Gamma}{dE_e} = \frac{G_F^2}{12\pi^2} m_\mu^2 E_e^2 \left( 3 - \frac{4E_e}{m_\mu} \right), \quad E_e \leq \frac{m_\mu}{2} \quad (4.3)$$

where  $E_e$  is the electron energy,  $m_\mu$  is muon mass,  $G_F$  is Fermi coupling constant. However, the trap of  $\mu^-$  in a  $^{16}\text{O}$  orbit distorts the energy spectrum of electron [96], and this effect is taken into account for our calculation. The  $\mu^+/\mu^-$  ratio of the cosmic ray muons are taken from an experimental data [97]. Fig. 4.11 shows the comparison of the reconstructed energy spectrum between the real data and Monte Carlo simulation. The difference between the data and Monte Carlo is within 2.0%.

#### 4.6.2 Electrons from Linear accelerator (LINAC)

An electron linear accelerator (LINAC) is instrumented at the Super-Kamiokande site for the study of the performance of the detector to low energy electrons [98]. The LINAC can produce electrons with a monochromatic energy from 5 MeV to 16 MeV. The electrons are injected downward into the tank at various points through a beam pipe which is inserted into the inner tank. For the study of atmospheric neutrinos, 16 MeV monochromatic electrons are used at  $(x, y, z) = (1237\text{cm}, -70.7\text{cm}, 1206\text{ cm})$ . Fig. 4.12 shows the reconstructed momentum distribution for both data and Monte Carlo simulation. The difference between data and Monte Carlo is about 2.4%.

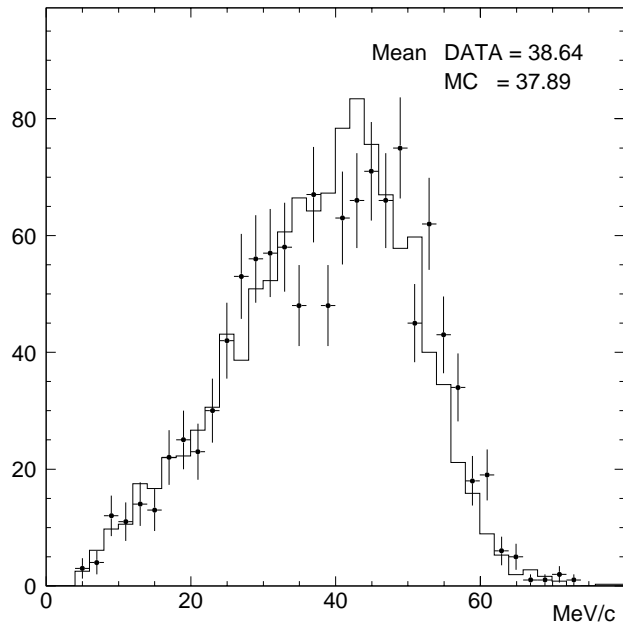


Figure 4.11: The reconstructed momentum distributions for muon-decay electrons. Points show the data and histogram shows Monte Carlo simulation.

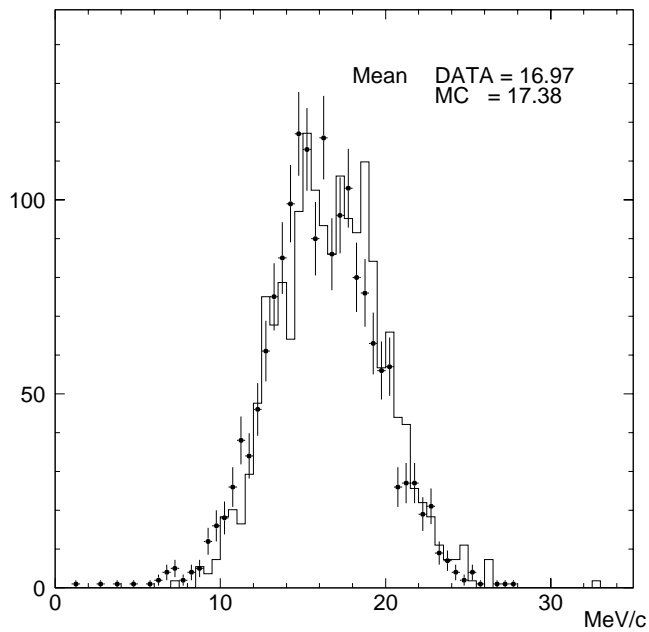


Figure 4.12: Reconstructed momentum distribution for LINAC electrons. Points shows the data and histogram shows the MC simulation.

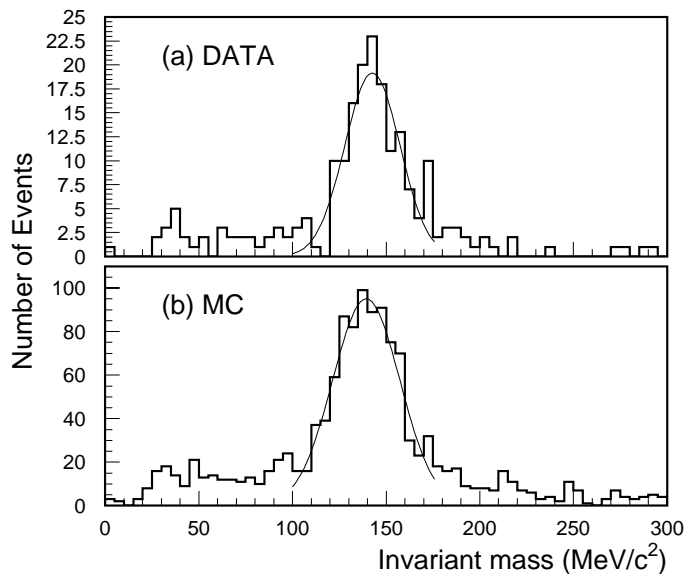


Figure 4.13: The reconstructed  $\pi^0$  mass distributions for (a) data and (b) Monte Carlo simulation. The peaks are fitted by Gaussian distributions.

### 4.6.3 Neutrino Induced $\pi^0$

The invariant mass of  $\pi^0$ 's produced by the atmospheric neutrinos are used for the energy calibration. Atmospheric neutrinos produce  $\pi^0$  by the neutral current interactions, and the produced  $\pi^0$  immediately decay to  $2\gamma$ 's.

The selection criteria for  $\pi^0$  events are as follows:

- Number of observed Cherenkov rings is 2.
- Reconstructed  $\pi^0$  momentum is smaller than  $400 \text{ MeV}/c$ .
- Reconstructed vertex position is in the fiducial volume.

Fig. 4.13 show the reconstructed invariant mass distributions for data and Monte Carlo simulation. The two distributions agree well, and the difference of the peak between data and Monte Carlo is about 2.2%.

### 4.6.4 Cosmic Ray Muons I

The track length of the energetic muons stopping in the detector is approximately proportional to their momentum. We can estimate the track length of the cosmic ray muon from the reconstructed entrance point and the vertex of its decay electron, and it gives a momentum measurement independent of the estimation based on the observed photoelectrons which is used in the atmospheric neutrino analyses.

We select the muons by the following criteria:

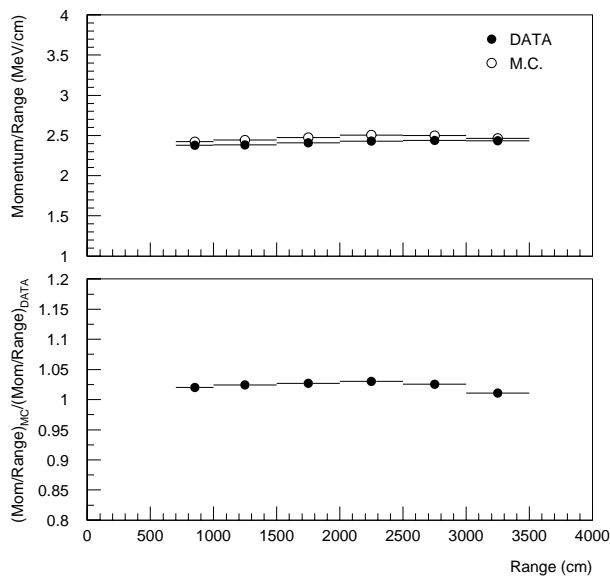


Figure 4.14: The momentum/range ratio as a function of reconstructed momentum for data and MC (upper figure). The ratio for the (momentum/range) ratio for MC to that of the data. The difference is within 2.5%.

- The muons entering from the top wall, vertically downward ( $\cos \Theta > 0.94$ )
- Reconstructed track is longer than 7 m.
- One cluster of hit PMTs exists in OD.
- One decay electron with a time difference of  $>0.8 \mu\text{sec}$

Fig. 4.14 shows the (momentum)/(range) ratio for data and Monte Carlo, and their ratio between the data and MC. The difference of the momentum/range ratio is within 2.5% between the data and MC.

#### 4.6.5 Cosmic Ray Muons II

Another calibration method utilizes the opening angle of the Cherenkov cone of the low energy cosmic ray muons. The opening angle of the Cherenkov cone,  $\theta_c$ , is a function of the muon momentum  $p$ :

$$\cos \theta_c = \frac{1}{n\beta} = \frac{1}{n} \sqrt{1 + \frac{m_\mu^2}{p^2}} \quad (4.4)$$

and the opening angle gives an estimation of the muon momentum.

Fig. 4.15 shows the reconstructed opening angle as a function of the reconstructed momentum based on the observed photoelectrons. We calculate the ratio  $R$  which is defined to be the ratio of the reconstructed momentum to the momentum estimated from the opening angle by Eq.(4.4). Fig. 4.16 shows the ratio of  $R_{\text{data}}$  to  $R_{\text{MC}}$ . The difference between data and MC is estimated to be within 2.5%.

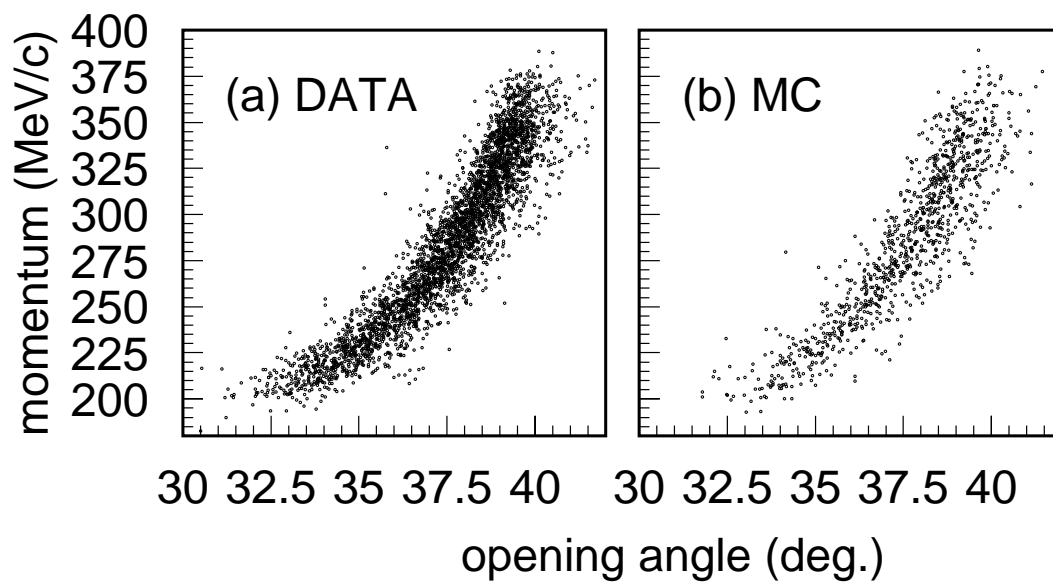


Figure 4.15: The reconstructed Cherenkov opening angle versus reconstructed momentum distributions for stopping cosmic ray muons for (a) data and (b) Monte Carlo.

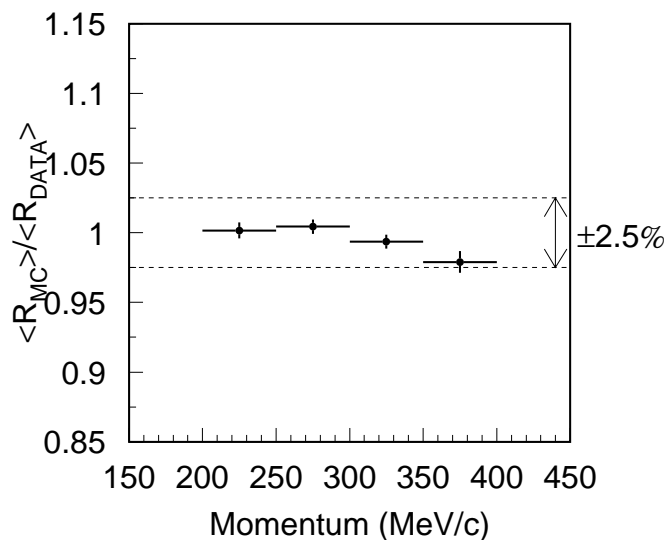


Figure 4.16: The  $R_{\text{data}}/R_{\text{MC}}$  ratio as a function of the reconstructed momentum. The difference is within 2.5%.

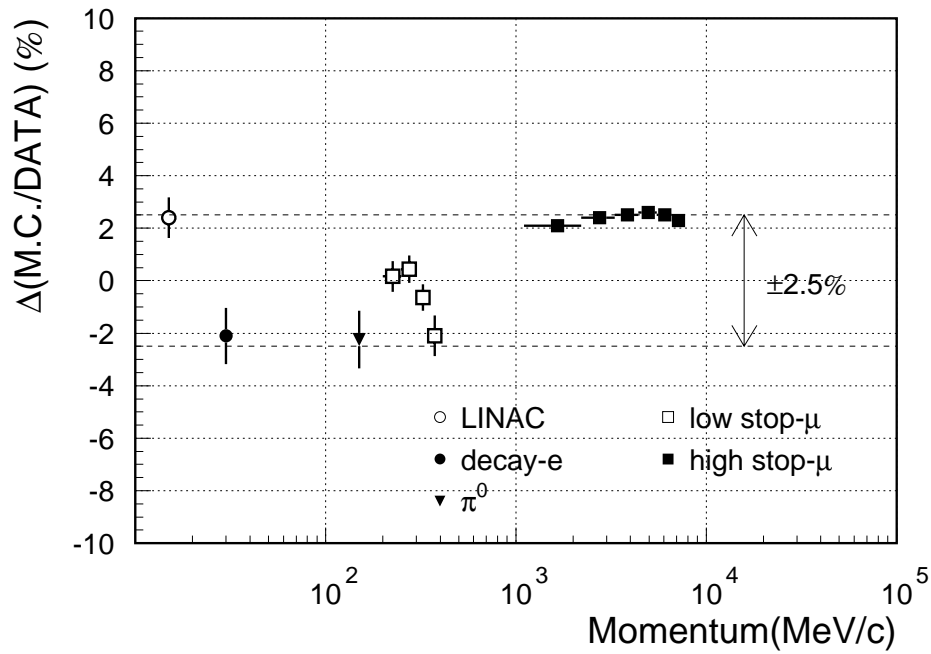


Figure 4.17: The summary of the absolute energy scale calibration. The uncertainty of the energy scale is estimated to be within  $\pm 2.5\%$

#### 4.6.6 Summary of the absolute energy calibration

Fig. 4.17 shows the summary of the absolute energy calibration. Events with the momentum from 16  $\text{MeV}/c$  to about 10  $\text{GeV}/c$  are examined and the uncertainty of the energy scale is estimated to be within  $\pm 2.5\%$ .

# Chapter 5

## Event Selection

### 5.1 Overview

Super-Kamiokande triggers about  $10^6$  events/day (excluding SLE-triggered events). Most of these events are due to cosmic ray muons and low energy signals induced by the radioactivity. We select the atmospheric neutrino events using the information of the timing and photoelectrons of PMTs' of both ID and OD. The event selection methods are specified for FC, PC, upward through-going muons, and upward-stopping muons because of their different event topologies (see Section 2.3). The methods are described in the following sections.

### 5.2 Event Selection for Fully Contained Events

Fig. 5.1 shows the reduction steps for FC events. A FC event is defined by the condition that the interaction occurs in the detector and no visible particle escapes from the detector. Each reduction step is described in the following sections.

#### 5.2.1 1st Reduction

The first step of the event selection for FC events is aimed to reject cosmic ray muon events and low energy events due to the radioactivities. The following criteria are required for FC events.

1. The number of hit OD PMTs within fixed 800 nsec width time window ( $N_{OD}(800\text{ns})$ ) is less than 50.
2. Total photoelectrons of ID within a sliding 300 nsec width time window ( $PE_{300}$ ) is greater than 200 p.e. which corresponds to visible energy greater than 23 MeV.

## Reduction Steps for FC sample

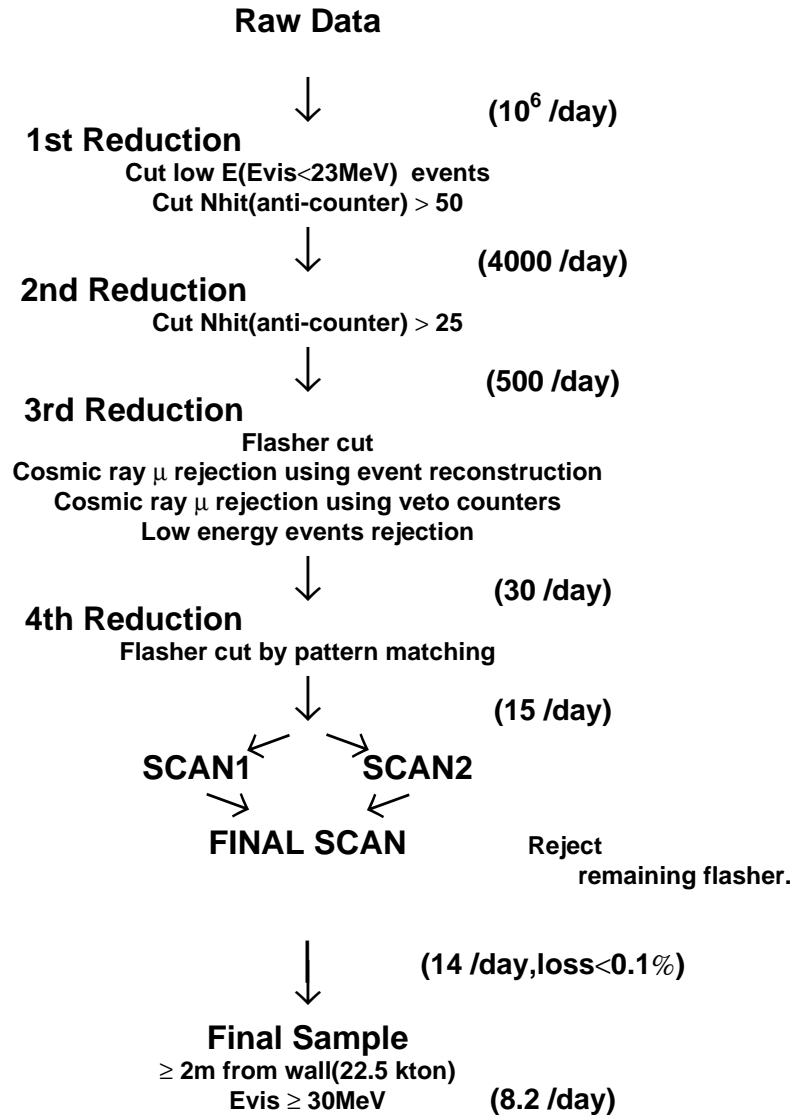


Figure 5.1: Reduction steps for FC sample.

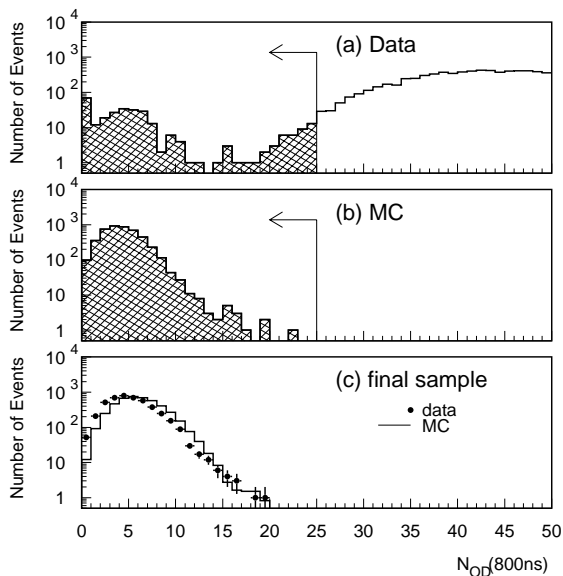


Figure 5.2: The  $N_{OD}(800ns)$  distribution for (a) data (b) atmospheric neutrino MC events in which no charged particle escapes from the detector (c) final sample data (circle) and MC events normalized by the number of events (solid line). The allows show the cut criterion in the 2nd reduction.

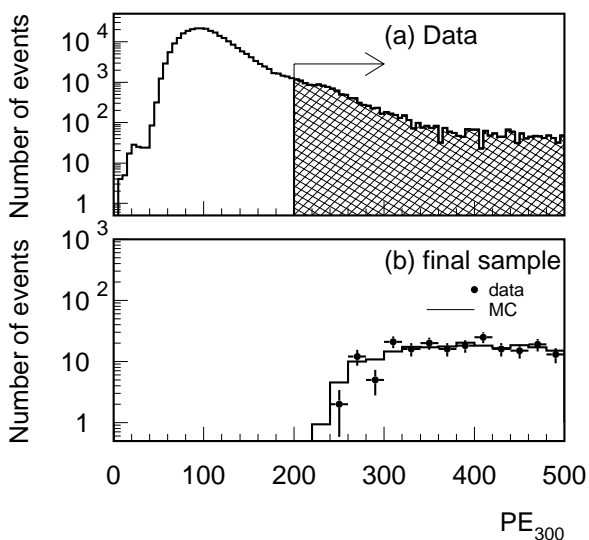


Figure 5.3: The  $PE_{300}$  distribution for (a) data (b) final sample data (circle) and MC events normalized by the number of events (solid line).

Fig. 5.2 and Fig. 5.3 show the  $N_{OD}(800ns)$  and  $PE_{300}$  distributions for data and atmospheric neutrino Monte Carlo events, respectively.

### 5.2.2 2nd Reduction

In this step, cosmic ray muons and flashing PMT events are rejected. The following criteria are required for FC events:

1.  $N_{OD}(800ns) < 25$
2. The ratio of  $PE_{max}$  to  $PE_{300}$  is less than 0.5, where  $PE_{max}$  is the maximum p.e. of a PMT.

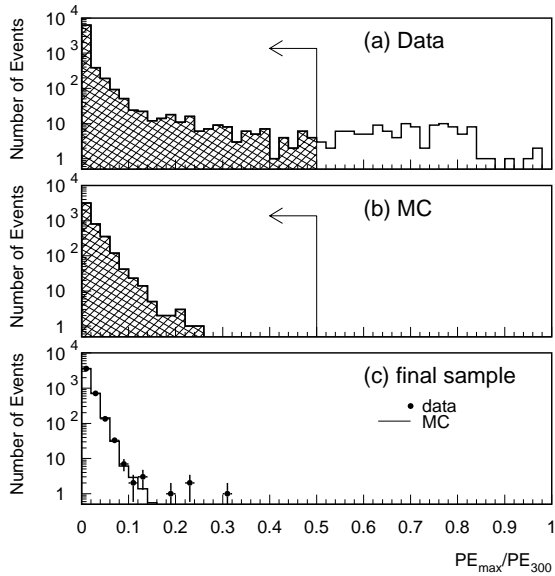


Figure 5.4: The ratio of  $PE_{\max}$  to  $PE_{300}$  distribution for (a) data (b) atmospheric neutrino MC events whose vertices are within 1m from the PMT wall (c) final sample data (circle) and MC events normalized by the number of events (solid line).

The first criterion is essentially same but tighter than that in the 1st reduction. The second criterion is to reject flashing PMT events. Flashing PMT events have a tendency to have a large charge at the flashing PMT only, so the ratio is expected to be large. Fig. 5.4 shows the  $PE_{\max} / PE_{300}$  ratio distributions.

### 5.2.3 3rd Reduction

In this step, more intelligent algorithms are employed to reject the remaining cosmic ray muons, low energy events, and flashing PMT events.

#### Through-going Muon Cut

Cosmic ray muons passing through the Super-Kamiokande detector make ideally two hit clusters in the OD around the entrance and exit points. Also, they emit a large number of Cherenkov photons in ID.

We employ a muon track fitter, '*THRMU-fit*', which is specified to the through-going muons (see Appendix A).

The rejection criteria for the through-going muons are as follows:

1.  $PE_{\max} > 230$  p.e.
2. The total number of hit PMTs in ID ( $N_{\text{TOTID}}$ ) is greater than 1000
3. The goodness of THRMU-fit ( $G_{\text{through}}$ ) is greater than 0.75, and the number of hit PMTs of OD within 500 cm sphere centered on the estimated entrance or exit points ( $N_{\text{OD}}(\text{In})$  or  $N_{\text{OD}}(\text{Out})$ ) is greater than 10.

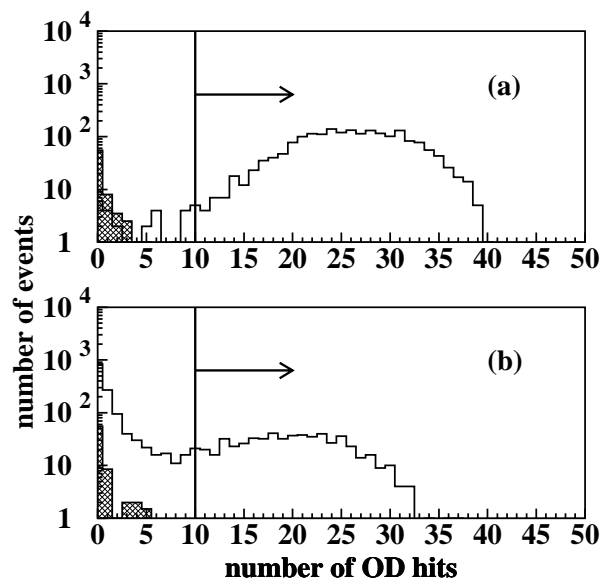


Figure 5.5: The number of hit PMTs in OD (a) within 500 cm of the estimated entrance point (b) within 500 cm of the estimated exit point. Solid histograms show the cosmic ray through-going muons and hatched ones show the atmospheric neutrino MC, respectively. The allows show the rejected events as cosmic ray muons.

The criterion 1 requires the exit point of a muon. The ID PMTs near the exit point of the muon observed a large number of Cherenkov photons, and ADC counts of them are often overflowed. The criterion 3 rejects the event which has a clear entrance and/or exiting signal in OD.

Fig. 5.5 shows  $N_{\text{OD}}(\text{In})$  and  $N_{\text{OD}}(\text{Out})$  distributions for cosmic ray through-going muons and atmospheric neutrino MC events.

### Stopping Muon Cut

A vertex and direction fitter, '*STOPMU-fit*', which is specified to stopping muons is used to reconstruct the vertex and direction of stopping muons. The vertex is estimated at the position of the clustered earliest hit PMTs, and the direction is estimated by maximizing the p.e.s within the cone of  $42^\circ$  opening angle.

The selection criteria for stopping muons are as follows:

1.  $N_{\text{OD}}(\text{In}) > 10$ , or goodness of the *STOPMU-fit* is greater than 0.5 and  $N_{\text{OD}}(\text{In}) > 5$

The definition of  $N_{\text{OD}}(\text{In})$  is same as above. Fig. 5.6 shows the number of OD hits within 500 cm of the estimated entrance point for cosmic ray stopping muons and atmospheric MC FC events, respectively.

### Low Energy Events Cut

There are still remaining low energy events which are caused by radioactivity or flashing PMTs. To reject these events, the following criteria are requested for FC sample.

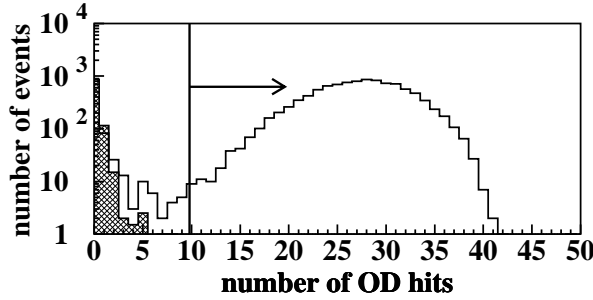


Figure 5.6: The number of OD hits within 500 cm of the estimated entrance point for data (solid histograms) and MC events (hatched histograms). The arrow shows the rejected events as stopping muons.

1. The maximum number of hit ID PMTs within sliding 50 nsec time window after subtraction of the time of flight of the Cherenkov photons (  $NMAX(50 \text{ nsec})$  ) is greater than 50.

We use a simple vertex fitter using the timing information of ID PMTs to calculate  $NMAX(50 \text{ nsec})$ .  $NMAX(50 \text{ nsec}) = 50$  roughly corresponds to 10 MeV.

### Flashing PMT Cut

A flashing PMT makes a broader timing distribution than that of neutrino events due to the duration time of the discharge. Fig. 5.7 shows timing distributions for a typical flashing PMT event and a typical FC neutrino event. To reject the flashing PMT events, the following criterion is required:

1. The minimum number of hit PMTs within sliding 100 nsec width timing window between 1200 and 1700 (  $NMIN(100 \text{ nsec})$  ) is greater than 14 (or greater than 9 in the case that the total p.e.s of ID is less than 800 p.e.)

### Cable-hole Muon Cut

The cosmic ray muons which passed through the insensitive region of OD near cable holes are rejected using the veto counters on the cable holes (see Subsection 3.5). The criteria for the cosmic ray muons are as follows:

1. Veto counter has a on-timing muon signal
2. The estimated entrance point by *STOPMU-fit* is within 4 m from the cable hole where the veto counter hit is observed.

The second criterion is to avoid killing neutrino events by chance. The results of this cut are shown in Subsection 3.5.

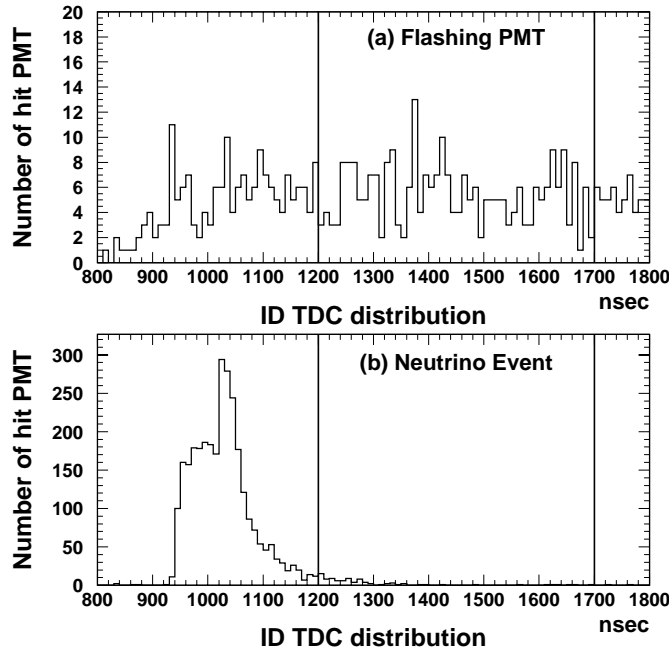


Figure 5.7: The timing distribution of (a) a typical long-tail flashing PMTs, (b) a typical FC neutrino event.  $N_{MIN}(100 \text{ nsec})$  is calculated to be 40 for (a) and 1 for (b), respectively.

### Accidental Coincidence Event Cut

There are some events that have a low energy signal followed by a cosmic ray muon within the timing window of the events. These events have a number of off-timing hits after the trigger timing. The criteria for these accidental events are:

1. The number of hit OD PMTs with in a off-timing time window fixed between 1300 nsec and 1800 nsec is greater than 19
2. The total number of p.e.s of ID during a off-timing time window fixed between 1300 nsec and 1800 nsec is greater than 5000 p.e.

### 5.2.4 4th Reduction

In this step, an intelligent pattern matching algorithm is used for eliminating the remaining flashing PMT events. A flashing PMT makes events with a similar hit PMT pattern due to the flashing.

The algorithm of the pattern matching is as follows:

- divide the ID wall into 1350 regions of roughly  $2 \text{ m} \times 2 \text{ m}$  patches.
- compute the sum of charge in the  $i$ -th patch ( $Q_i$ ).

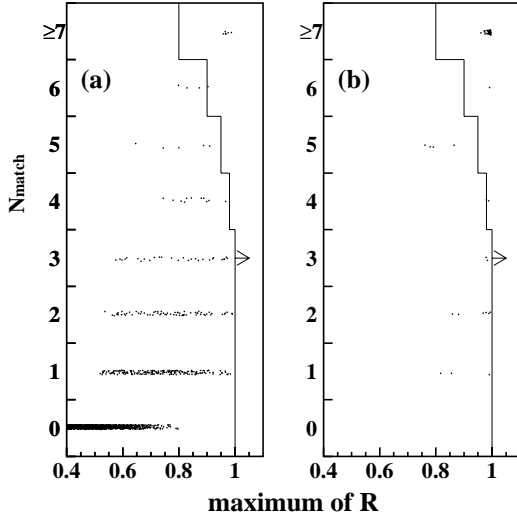


Figure 5.8: The (maximum of  $R$ ,  $N_{\text{match}}$ ) plot for (a) FC events selected by eye scan (b) flashing PMT events selected by eye scan. Solid lines show the cut criteria for the 4th reduction. The events at the right side of the cut lines are rejected as flashing PMT events.

- for two independent events A and B, compute a linear correlation:

$$R = \frac{1}{N} \sum_i \frac{(Q_i^A - \langle Q^A \rangle) \times (Q_i^B - \langle Q^B \rangle)}{\sigma_A \times \sigma_B} \quad (5.1)$$

where  $\langle Q^{A(B)} \rangle$  and  $\sigma_{A(B)}$  is the average and the standard deviation of  $Q_i^{A(B)}$ , respectively. If  $R$  exceeds the threshold  $R_{\text{th}}$ , event A and event B are recognized as 'matching' events.

- calculate  $R$  against to all other events, and count the number of matching events ( $N_{\text{match}}$ ).
- reject the events which have a large  $R$  or large  $N_{\text{match}}$ .

Fig 5.8 shows the exclusion region on (maximum of  $R$  -  $N_{\text{match}}$ ) plane.

### 5.2.5 Eye Scanning

The events after the 4th reduction is doubly checked by physicists to check the quality of the data and to rejects the remaining background events. The double-scannings are independently carried out, and another physicist check the consistency after the double-scanning.

The reduction inefficiency for atmospheric neutrino FC final sample is estimated to be less than 0.1 percent from a Monte Carlo study. The contamination of the background in the FC final sample is estimated to be very small (see Section 8.1.4).

## 5.3 Event Selection for Partially Contained Events

Fig. 5.9 shows the reduction steps for PC events. PC event is defined by the condition that the interaction occurs in ID and a part of visible particles escape from ID. Each reduction step is described in the following sections.

### 5.3.1 1st Reduction

The first reduction for the PC sample is aimed to reject low energy events and through-going cosmic ray muons. The following criteria are required for PC events.

1. Total p.e. of ID ( $PE_{\text{tot}}$ ) is greater than 1000 p.e.
2. The width of the OD timing distribution ( $T_{\text{ODwidth}}$ ) is less than 240 nsec
3. The number of clusters in OD ( $N_{\text{clust}}$ ) is less than or equal to 1

The criterion 1 rejects low energy events. The total p.e.s of 1000 p.e. roughly corresponds to 310 MeV/ $c$  muon momentum. For final sample of PC, we require that the vertex is within 2.0 m inside from the PMT walls which corresponds to the muon momentum greater than 700 MeV/ $c$ . Therefore the efficiency of the criterion 1 is essentially 100% for the PC events in the fiducial volume.

The criterion 2 rejects through-going muons. Fig. 5.10 shows a event display and the OD timing distribution for a typical through-going muon event. The OD timing distributions of through-going muons are broader than that of the PC events because of the two separate hit clusters around the entrance and exit points of the muon. Fig. 5.11 shows the  $T_{\text{ODwidth}}$  distributions for the data and atmospheric neutrino MC.

The criterion 3 rejects through-going muon and multi-muon events. A cluster is formed around a PMT that observed more than 8 p.e., and the clusters which lie within 8 m are merged. Fig. 5.12 shows the  $N_{\text{clust}}$  distributions.

### 5.3.2 2nd Reduction

In this step, another clustering algorithm of OD hit is employed. The schematic view of the clustering algorithm is shown in Fig. 5.13. The OD PMTs are separated into the grids of about 10 m  $\times$  10 m size. The OD hits are clustered according to the charge gradient of each grid.

The criteria for PC sample are as follows:

1. The number of hit clusters in OD which have more than 7 hit PMT ( $N_{\text{clust}}$ ) is less than or equal to 1

## Reduction Steps for PC sample

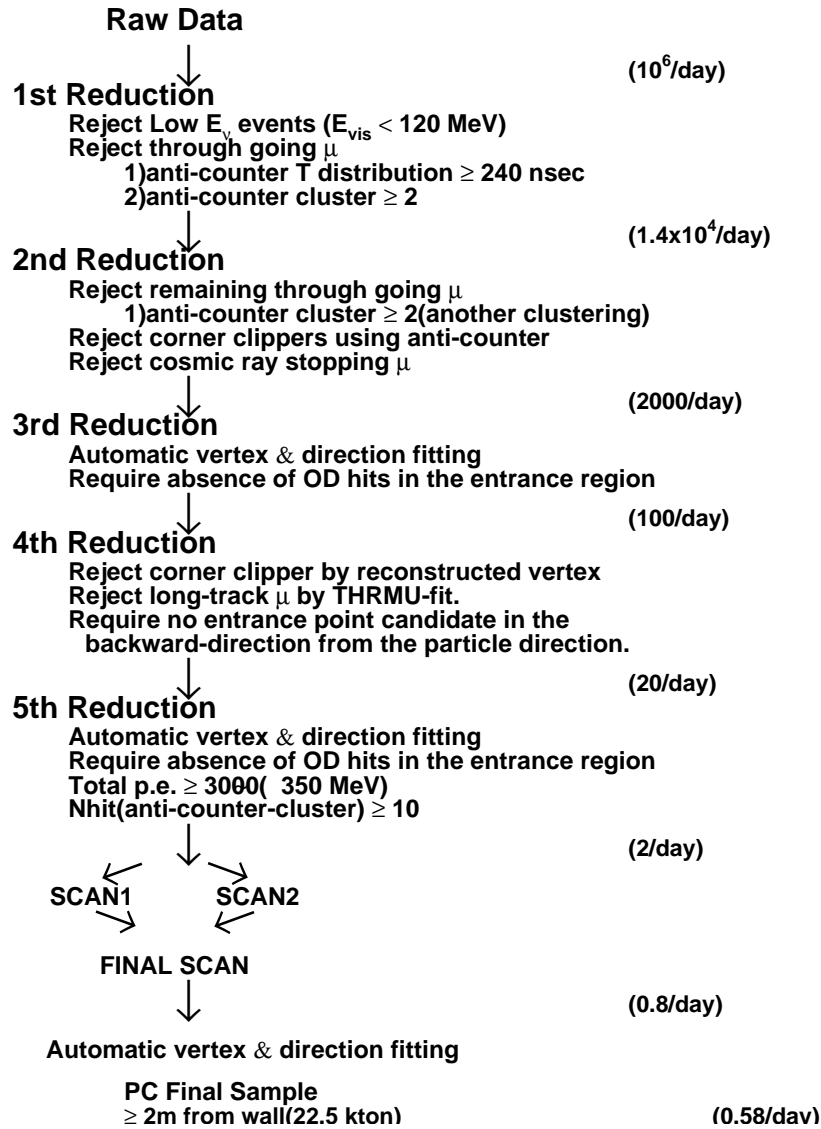
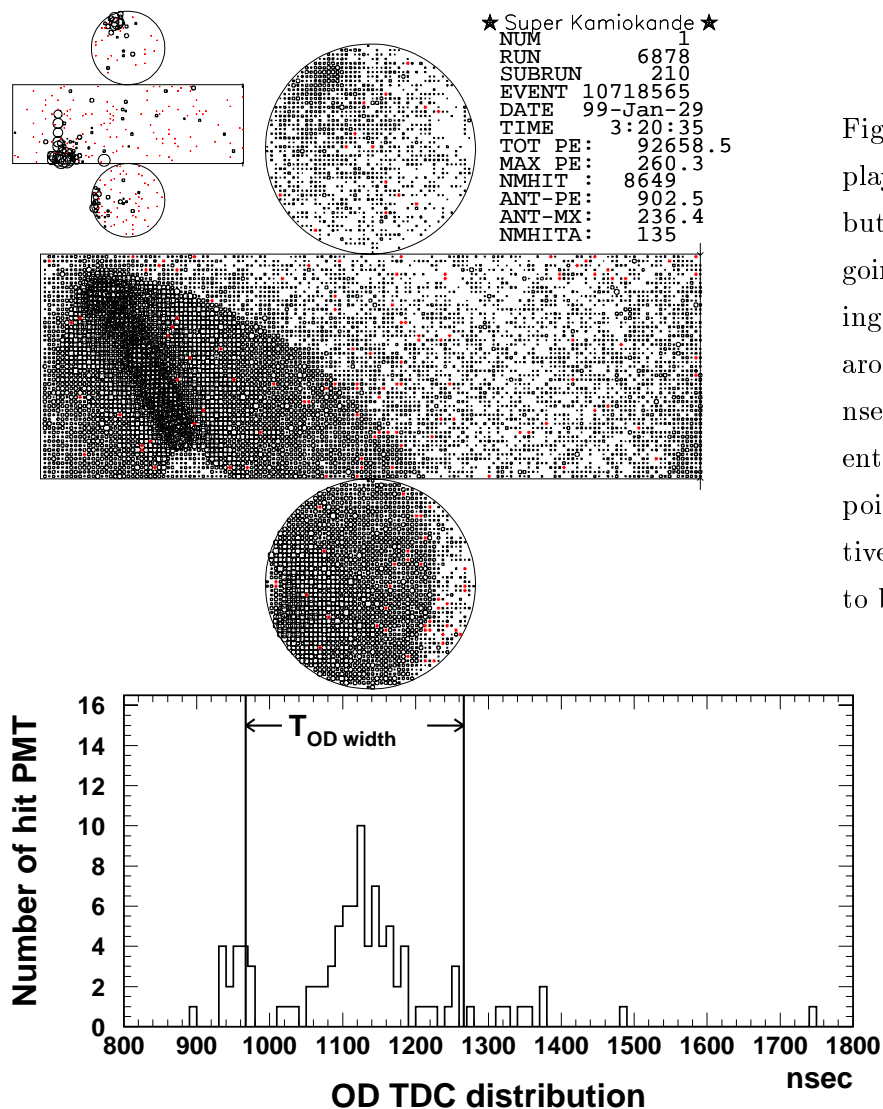


Figure 5.9: Reduction steps for PC events.



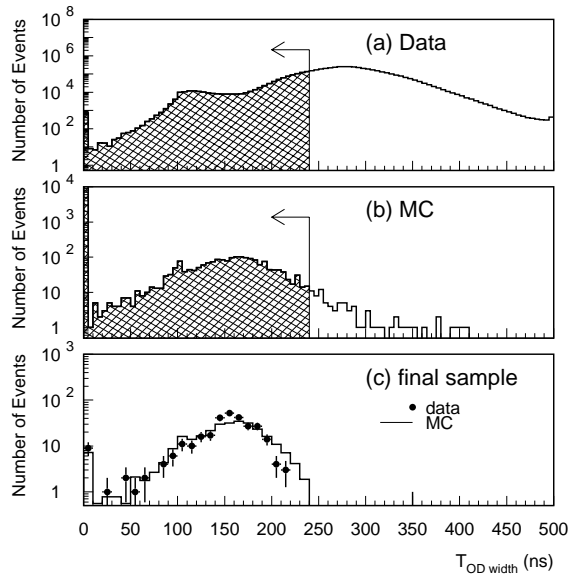


Figure 5.11:  $T_{ODwidth}$  distributions for (a) data (b) atmospheric neutrino MC events whose vertices are within 1m from the PMT wall (c) final sample data (circle) and MC events normalized by the number of events (solid line).

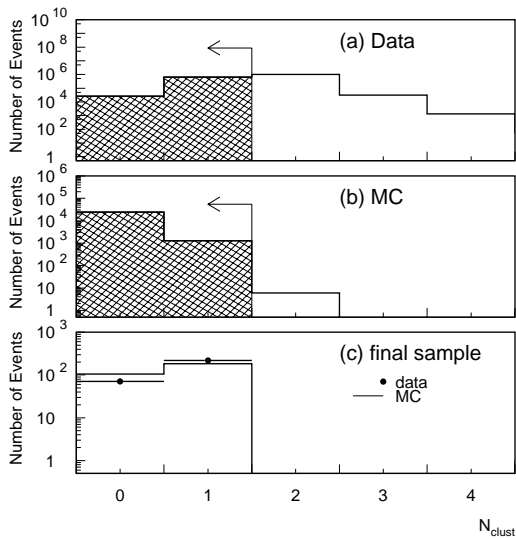


Figure 5.12:  $N_{clust}$  distribution for (a) data (b) atmospheric neutrino MC events whose vertices are within 1m from the PMT wall (c) final sample data (circle) and MC events normalized by the number of events (solid line).

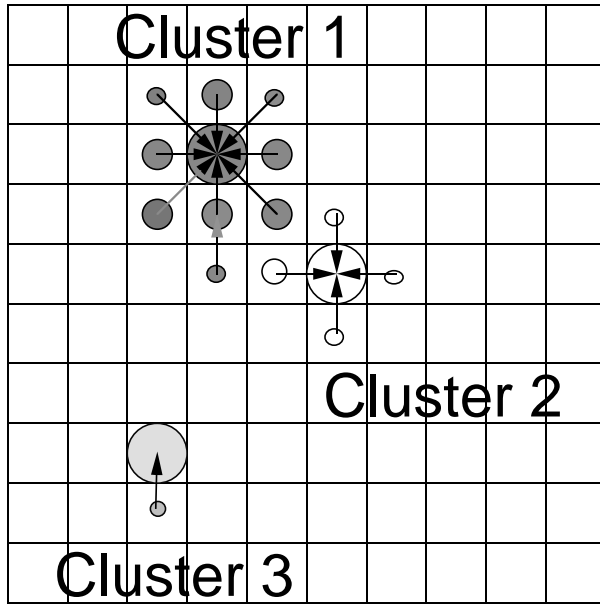


Figure 5.13: The schematic view of the search for OD hit clusters. The circles represent the observed charge in each bin. The hit PMTs are merged according to the gradient of the charge of each grid.

2. The second minimum number of hits in the side, top, or bottom wall for the highest p.e. OD cluster ( $N_{\text{clustmin}}$ ) should be less than 7
3. The sum of the p.e. within 200 cm of the highest p.e. ID PMT in the ID cluster ( $PE_{200}$ ) nearest to the OD cluster is greater than 1000 p.e.

The criterion 1 rejects through-going muons which make the entrance and exit hit clusters in OD. The criterion 2 rejects cosmic ray muons which clip the corner of the detector. This criterion requires that the OD hit cluster should locate in the single face (top, bottom, or barrel) of OD. Fig. 5.14 show the  $N_{\text{clustmin}}$  distributions. The criterion 3 rejects the stopping muons. PC event makes a bright hit cluster in ID in the upper stream of OD hit cluster. On the other hand, an ID cluster for a stopping muon event is not correlated to the OD cluster position. Fig. 5.15 shows the effect of the 2nd reduction on a 2-dimensional plot of  $PE_{200}$  and the number of the clusters.

### 5.3.3 3rd Reduction

The 3rd reduction rejects the remaining cosmic ray muons using reconstructed vertices and directions of the events. Also, the flashing PMT events are rejected in this step. The following criteria are required for PC events:

1. The same criterion as FC 3rd reduction for flashing PMT cut are required (see Section 5.2.3)

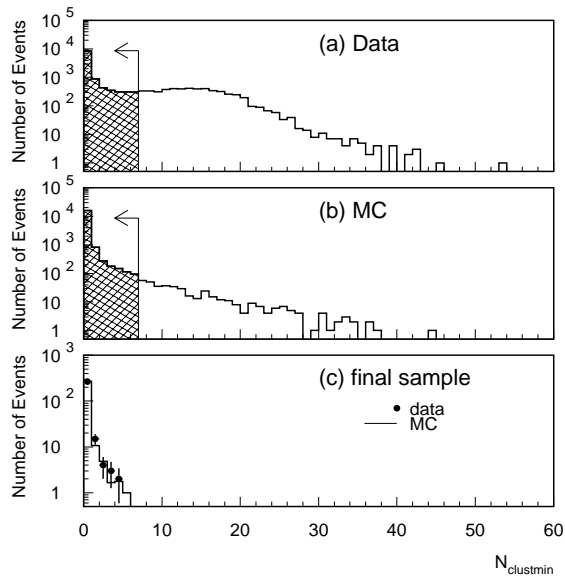


Figure 5.14:  $N_{\text{clustmin}}$  distribution for (a) data (b) atmospheric neutrino MC events whose vertices are within 1m from the PMT wall (c) PC final sample (circle) and MC events normalized by the number of events (solid line).

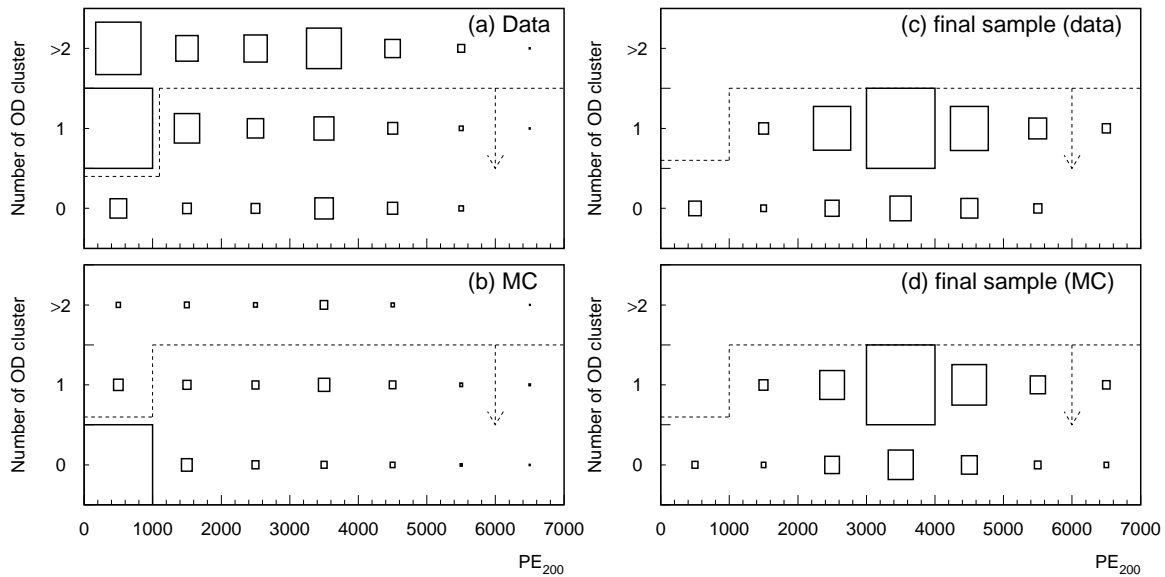


Figure 5.15: 2-dimensional plot of the number of OD cluster and  $PE_{200}$  for (a) data (b) atmospheric neutrino MC (c) final sample data (d) MC PC final sample. The size of the boxes show the number of events. The lines and arrows show the selected region in the second reduction.

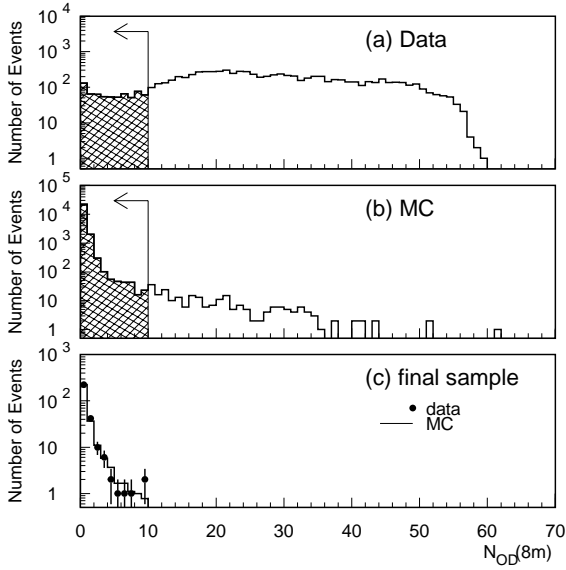


Figure 5.16:  $N_{\text{OD}}(8m)$  distributions for (a) data (b) atmospheric neutrino MC (c) final sample of PC events.

2. The number of OD hit PMTs within 8 m of the estimated entrance point ( $N_{\text{OD}}(8m)$ ) is less than 10.

The criterion 2 rejects cosmic ray muons. The estimation of the entrance point is carried out by back-extrapolation of the reconstructed vertex along the reconstructed direction which are obtained by 'Pfit' described in Section 6.2.1. Fig. 5.16 shows  $N_{\text{OD}}(8m)$  distributions.

### 5.3.4 4th Reduction

The remaining background after the 3rd reduction is through-going cosmic ray muons with no clear entrance OD hit cluster due to inefficiency of OD, or the muons clipped the corner of the detector. To reject the through-going muons events, we use THRMU-fit which is used in the 3rd reduction step of FC sample(see Section 5.2.3). If one of the following criteria is satisfied, an event is rejected:

1. The reconstructed direction of Pfit,  $\vec{d}_{\text{pfit}}$ , and the direction from the vertex to the clustered earliest hit PMT,  $\vec{d}_{\text{pmt}}$ , is opposite ( $\vec{d}_{\text{pfit}} \cdot \vec{d}_{\text{pmt}} < -0.8$ ).
2. The goodness of the THRMU-fit is larger than 0.85 and the estimated track length of the muon is longer than 30 m
3. The distance of the estimated vertex by Pfit from the detector fringe ( $D_{\text{fringe}}$ ) is less than 150 cm.

The criterion 1 rejects events which have the candidate of the entrance point in the back-extrapolated direction along the reconstructed direction of Pfit. The earliest hit cluster in ID

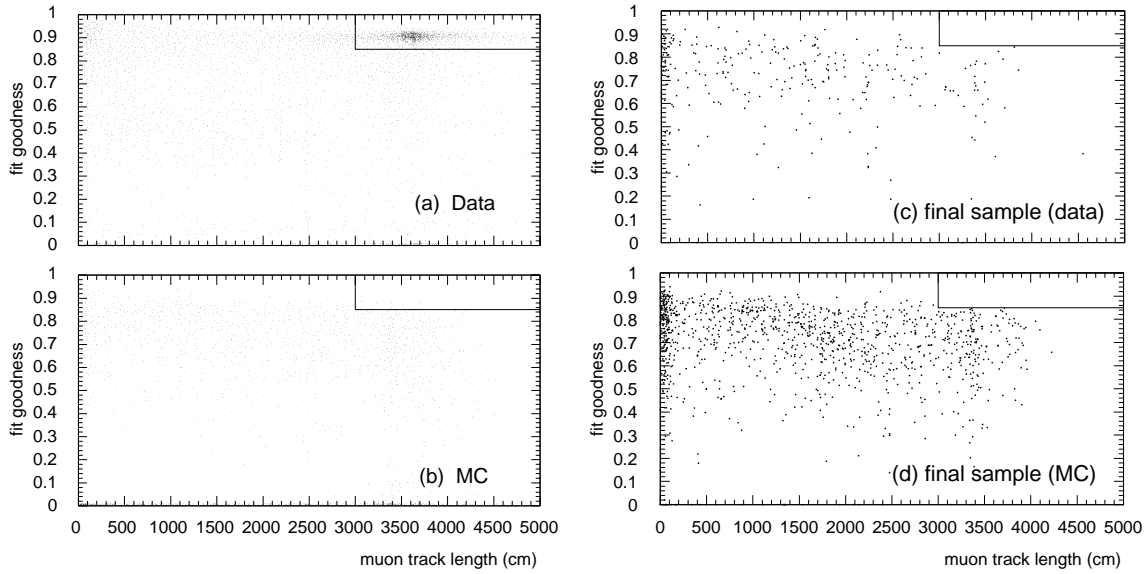


Figure 5.17: 2-dimensional distribution of muon track length and muon fitter goodness for (a) Data (b) atmospheric neutrino MC (c) data final sample (d) MC PC final sample. The events in the upper-right region are rejected by the cut.

is a candidate of the entrance point of muons. The criterion 2 rejects long track through-going muons. Fig. 5.17 shows the effect of this cut. The criterion 3 rejects the candidate of the corner clipping muons. Fig. 5.18 show the  $D_{\text{fringe}}$  distributions.

### 5.3.5 5th Reduction

In this step, TDCfit is used (see Section 6.2). The rejection criterion is:

1. The number of the OD hits within 8 m of the estimated entrance point is greater than 9

This criterion is same as the one in the 3rd reduction except for the vertex reconstruction program. TDCfit has a better vertex resolution than Pfit.

### 5.3.6 Eye Scanning

The events after 5th reduction are doubly checked by physicists. Remaining cosmic ray muons and the flashing PMT events are rejected by eye scanning. Finally, another physicist checks the consistency of the double-scanning. The scanning efficiency is estimated  $\geq 99\%$  for the events in the fiducial volume.

The reduction efficiency after the whole reduction steps is estimated to be 88%. And the background level is estimated to be about 0.2%. The details of the background estimation for

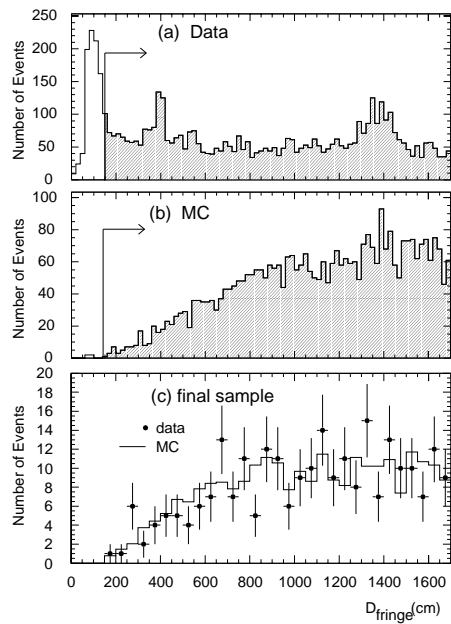


Figure 5.18: Distribution of the distance of the vertex from the detector fringe ( $D_{\text{fringe}}$ ) for (a) data (b) atmospheric neutrino MC (c) final sample of PC events.

PC are described in Section 8.1.4.

## 5.4 Event Selection for Upward-going Muons

The upward-going muons are characterized by the following conditions:

- An entrance point exists in OD.
- An exit point exists in OD for through-going muons.
- The reconstructed direction of muon is upward.

Fig. 5.19 shows the event selection steps for upward-going muons. The steps are described below. After all reduction steps they are eye-scanned by physicists and reconstructed by manual fittings.

### 5.4.1 1st Reduction

The first step rejects short track events:

1. An event must have  $PE_{\text{tot}} > 8000$  p.e.s which corresponds to about 350 cm track length

where  $PE_{\text{tot}}$  is the total photoelectrons of ID. We require for final sample that the muon track should be longer than 7m, and the criterion is safe.

### 5.4.2 2nd Reduction

The events are classified into three types by the number of OD hit cluster ( $N_{\text{clust}}$ ) and the width of the OD timing OD distribution ( $T_{\text{ODwidth}}$ ) which are same quantities used in PC 1st reduction(see Section 5.3.1):

- multiple-muon event :  $N_{\text{clust}} > 2$
- through-going muon :  $N_{\text{clust}} = 2$  and  $T_{\text{ODwidth}} > 240$  nsec.
- stopping muon : the others

Next, we apply a muon track fitter to reject the downward-going cosmic ray muons. The events are processed as follows:

1. If the event is reconstructed as downward ( $\cos \Theta > 0.12$ ), the events is rejected.
2. If the event is reconstructed as upward ( $\cos \Theta < 0.0$ ) and classified as through-going or stopping muon, the event is saved for eye-scanning as the candidates of upward-going muons.

## Reduction Steps for Upward-going muons

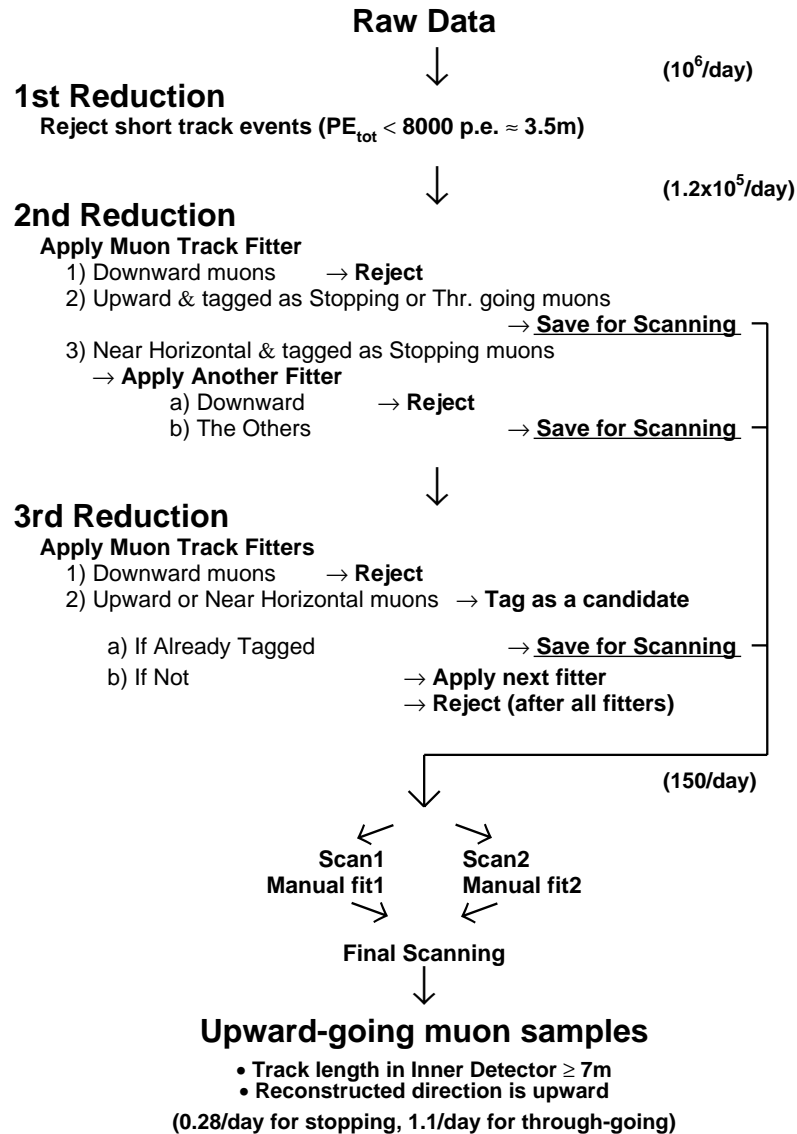


Figure 5.19: Reduction steps for Upward-going muons.

3. If the event is reconstructed as nearly horizontal ( $0.0 < \cos \Theta < 0.12$ ) and classified as stopping muon, we apply another muon track fitter which is specified to the stopping muons. If the newly estimated direction is downward ( $\cos \Theta > 0.12$ ), the event is rejected, and if not, the event is saved for eye-scannings.

We keep the nearly horizontal events ( $0.0 < \cos \Theta < 0.12$ ) in order not to kill the upward-going neutrino events due to the finite fitter resolution. Also, the nearly horizontal events are used for background estimation described in Section 5.5.

The events which were not reconstructed well by the first muon track fitter, or reconstructed as upward or near horizontal but not classified as stopping nor through-going muons are sent to the next reduction steps.

### 5.4.3 3rd Reduction

The third step rejects the downward-going muons using four independent muon track fitters. The procedure is as follows:

1. Apply a muon fitter.
2. If the reconstructed direction is downward, the event is rejected.
3. If the reconstructed direction is upward or nearly horizontal, the event is tagged as a candidate for the upward-going muons. If the event was already tagged by a previous fitter, or reconstructed as upward or nearly horizontal in 2nd reduction, the event is saved for the eye-scanning.
4. Go to the next fitter.

This procedure is repeated four times using the four independent fitters. If the event is not tagged twice, it is rejected.

The reduction efficiency for the upward-going muons with the reconstructed track longer than 7 m is estimated to be better than 99% by a Monte Carlo study.

### 5.4.4 Eye Scanning and Manual Fitting

The candidates for the upward-going muons are doubly eye-scanned and manually fitted by physicists using an interactive graphic event display. The manual event reconstruction is carried out using the informations of PMT hit timing, Cherenkov ring edge, and OD hit clusters. If an OD hit cluster exists at the estimated muon exit points, the event is categorized as through-going muon, and if not, the event is categorized as stopping muon.

The final samples of the upward-going muons are required the following conditions:

1. reconstructed direction is upward ( $\cos \Theta \leq 0.0$ )
2. reconstructed track length in ID is greater than 7.0 m

The second criterion is for keeping the quality of the event reconstruction. For the through-going muons, the track length is calculated by connecting the entrance and exit point, and for the upward stopping muons, the track length is estimated from the observed p.e.s corrected by PMT acceptance and water transparency. The systematic uncertainty of the reconstructed track length for the upward stopping muons is estimated to be 5% by Monte Carlo study.

## 5.5 Background Subtraction for Upward-going Muons

The cosmic ray muons passing through the mountain from the nearly horizontal direction can be a source of the background due to the fitting resolution and the multiple scatterings of muons in the rock. The cosmic ray muons are stopped by the mountains surrounding the Super-Kamiokande. However, in the data taking from May 1996, we found several 'thinner-mountain spots' where relatively low energy ( $< 1$  TeV) cosmic ray muons can pass through.

Fig. 5.20 shows the reconstructed direction distributions of the upward-going muons including nearly horizontal direction. There are several clusters in  $\cos \Theta > 0.0$  which are due to the thinner-mountain spots.

To estimate the background contamination from the thinner mountain spots, we divided the azimuthal region into two parts, 'thicker-mountain' region and 'thinner-mountain' region, as shown in Figs. 5.20 (c) and (d). The 'thinner-mountain' region is defined to  $60^\circ < \Theta < 240^\circ$  for upward through-going muons and  $60^\circ < \Theta < 310^\circ$  for upward stopping muons. As shown in Figs. 5.20 (c) and (d), the azimuthal angle distributions for the upward-going events ( $\cos \Theta < 0.0$ ) are flat, suggesting that the contamination of the cosmic ray muons is small.

Fig. 5.21 shows the zenith angle distributions for both thinner-mountain regions and thicker mountain regions. We fitted the exponential + constant function to the zenith angle distribution of thinner-mountain region at  $\cos \Theta > 0.0$  to estimate the background contamination. The background contamination is significant only for the most horizontal bin, and the estimated background is  $9.1 \pm 0.8$  events for the  $-0.1 < \cos \Theta < 0.0$  zenith angle bin of the upward through-going muons and  $21.4 \pm 8.8$  events for the  $-0.2 < \cos \Theta < 0.0$  zenith angle bin of the upward stopping muons for the 1138 days and 1117 days livetime, respectively. The errors represent the statistical uncertainty of the fitting, and this uncertainty causes about 0.3% systematic uncertainty for the most horizontal bin of the upward through-going muons and 8.3% for the most horizontal bin of the upward stopping muons, respectively.

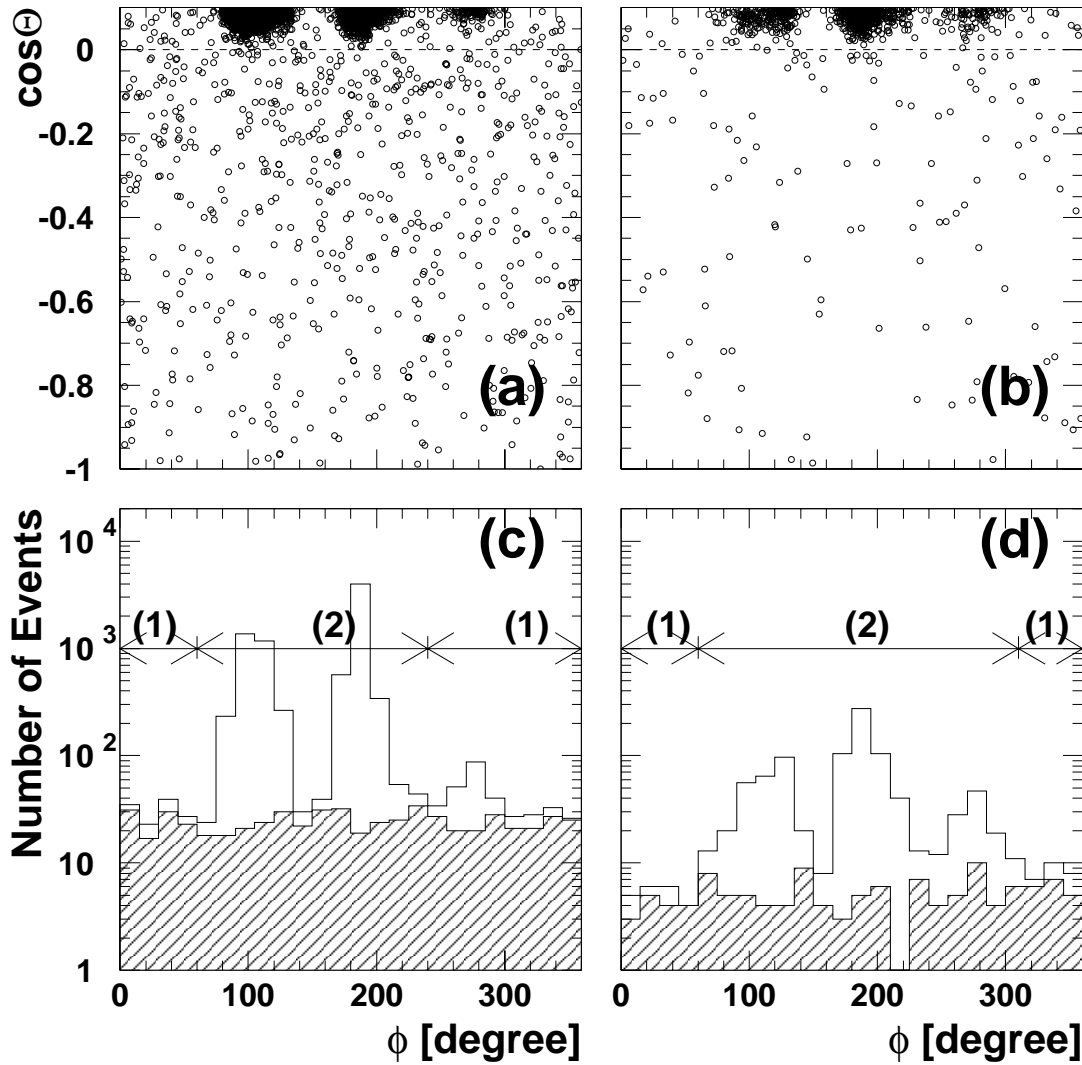


Figure 5.20: (Upper figures) Zenith angle vs azimuthal distributions for final samples of (a) upward through-going muons and (b) upward stopping muons. The clusters in  $0.0 < \cos \Theta$  region is due to the cosmic ray muons passing through the 'thinner-mountain' regions. (Lower figures) Azimuthal distribution for (c) upward through-going muons and (d) upward stopping muons. Blank histograms show the  $-1.0 < \cos \Theta < 0.1$  events. The shaded histograms show the  $-1.0 \cos \Theta < 0.0$  events. The regions denoted (2) show the thinner-mountain regions which are defined to  $60^\circ < \Theta < 240^\circ$  for through-going muons and  $60^\circ < \Theta < 310^\circ$  for stopping muons, respectively.

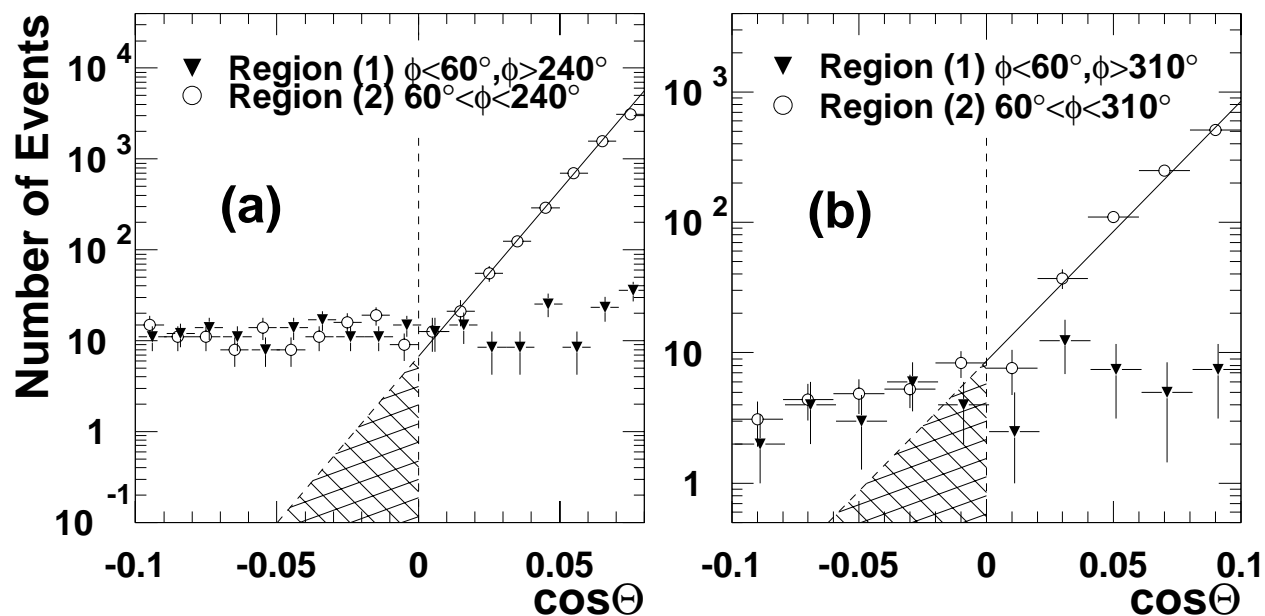


Figure 5.21: Zenith angle distributions for (a) upward through-going muons and (b) upward stopping muons near horizontal direction. Open circles show the zenith angle distributions for 'thinner-mountain' regions, and reverse triangles show the distributions for 'thicker-mountain' regions. The distributions for the thinner-mountain regions are normalized by the area of the azimuthal angles. Solid lines shows the fitted curves to the thinner-mountain regions. The hatched areas show the estimated background contaminations.



## Chapter 6

# Event Reconstruction for FC and PC events

### 6.1 Overview

We describe the details of the event reconstruction for FC and PC events. After the event selection processes, we reconstruct the event kinematics from the observed timing and photoelectron information of the ID PMTs.

For FC and PC events, the following information is reconstructed:

- Vertex
- Number of Cherenkov rings
- Particle types
- 3-momentum of each ring

The outline of the event reconstruction is shown in Fig. 6.1. First, the vertex of the event is reconstructed. The second step is to find the Cherenkov rings. The third step is particle identification. After the particle identification, we carry out further fitting for the events with a single Cherenkov ring assuming a particle type. The fifth step is the momentum estimation using the photoelectron information of the rings.

The reconstruction procedures for FC and PC are fully automatic, and there is no human biases. Both real data and MC are handled by the same programs.

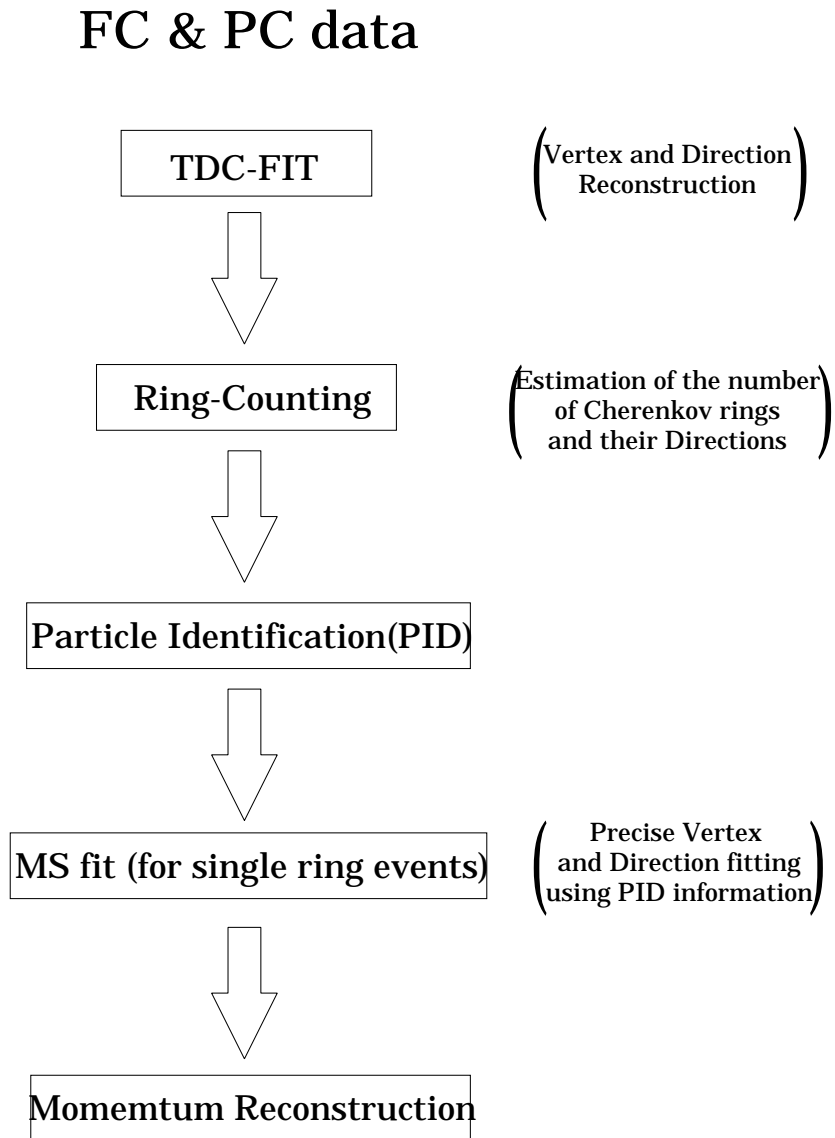


Figure 6.1: The flow chart of reconstruction procedure for FC and PC. The results of Ring-Counting and Particle Identification for PC are not used in physics analyses.

## 6.2 Vertex Fitter

First, the vertex is estimated using timing information of the PMTs. The procedure has three steps.

- (1) Pfit : roughly find the vertex using the timing information
- (2) Ring edge search : find Cherenkov ring edge
- (3) TDCfit : fit precisely using (1) and (2) results

These steps are described below.

### 6.2.1 Pfit

The vertex fitter searches for the position at which the timing residuals of the entire hit PMTs are approximately equal. The time residual of the  $i$ th PMT,  $t_i$ , is calculated by subtracting the time of flight of the photons from the hit timing of the  $i$ th PMT,  $t_i^0$ :

$$t_i = t_i^0 - \frac{n}{c} \times |\vec{P}_i - \vec{O}| \quad (6.1)$$

where  $n$  is the refractive index in water,  $O$  is the assumed vertex position, and  $P_i$  is the position of the  $i$ th PMT. To estimate the vertex, we use the estimator  $G_p$  for the goodness of the fitting:

$$G_p = \frac{1}{N} \sum_i \exp \left( -\frac{1}{2} \left( \frac{t_i - t_0}{1.5 \times \sigma} \right)^2 \right) \quad (6.2)$$

where  $N$  is the number of hit PMTs,  $\sigma$  is the typical timing resolution of a PMT (2.5 nsec), and  $t_0$  is the offset value of the time residual which is properly set in the fitting. The factor 1.5 in the denominator is chosen to optimize the fitter performance.  $G_p$  takes a value between 0 and 1. The fitter searches for the vertex position with which  $G_p$  takes the maximum value.

### 6.2.2 Ring Edge Finding

In this step, the edge of a Cherenkov ring is estimated. The information of the Cherenkov ring is used in the precise vertex fitter in the next step. The procedures of this step are as follows:

1. Make the angular distribution of the p.e.s,  $PE(\theta)$ , as a function of the opening angle  $\theta$  between the assumed ring direction and the Cherenkov photon direction. The PMT acceptance and the transparency of water are taken into account in this calculation.
2. Obtain the Cherenkov opening angle  $\theta_{\text{edge}}$  which satisfies the following criteria:

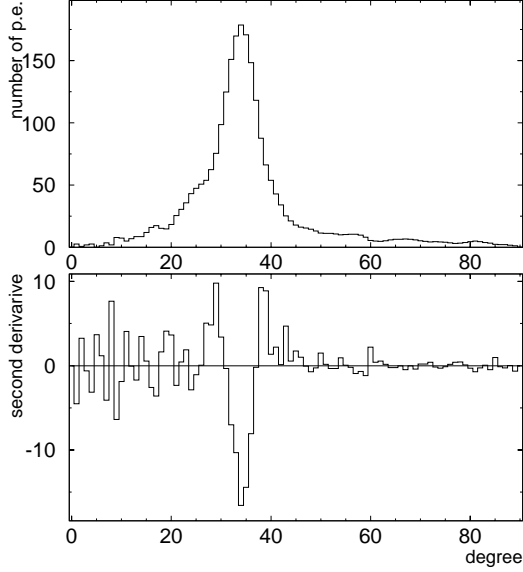


Figure 6.2: Upper figure shows the typical  $PE(\theta)$  distribution and lower figure shows the second derivative of  $PE(\theta)$ .

- $\left. \frac{d^2 PE(\theta)}{d^2 \theta} \right|_{\theta_{\text{edge}}} = 0$
- $\theta_{\text{edge}} > \theta_{\text{peak}}$  where  $\theta_{\text{peak}}$  is the angle at which  $PE(\theta)$  has a peak

If there are several  $\theta_{\text{edge}}$  candidates, the  $\theta_{\text{edge}}$  nearest to  $\theta_{\text{peak}}$  is selected.

3. Calculate the estimator,  $Q$ , which is defined as:

$$Q = \frac{\int_0^{\theta_{\text{edge}}} d\theta PE(\theta)}{\sin \theta_{\text{edge}}} \times \left( \left. \frac{dPE(\theta)}{d\theta} \right|_{\theta_{\text{edge}}} \right)^2 \times \exp \left( -\frac{(\theta_{\text{edge}} - \theta_{\text{exp}})^2}{2\sigma_\theta^2} \right) \quad (6.3)$$

where  $\theta_{\text{exp}}$  and  $\sigma_\theta$  are the opening angle and its resolution of the Cherenkov cone expected from the p.e.s in the assumed Cherenkov ring, respectively.

Fig. 6.2 shows the typical  $PE(\theta)$  distribution and its second derivative.  $Q$  is maximized by changing the direction of the ring. These three steps are iterated until the maximum  $Q$  is found.

### 6.2.3 TDC fit

The final step is a precise vertex fitting using the results of the previous steps. In this procedure, the track length of the charged particle and the scattered Cherenkov photons are considered.

The time residual is calculated as:

$$t_i = \begin{cases} t_i^0 - \frac{1}{c} \times |\vec{X}_i - \vec{O}| - \frac{n}{c} \times |\vec{P}_i - \vec{X}_i| & \text{Inside the Cherenkov ring} \\ t_i^0 - \frac{n}{c} \times |\vec{P}_i - \vec{O}| & \text{Outside the Cherenkov ring} \end{cases} \quad (6.4)$$

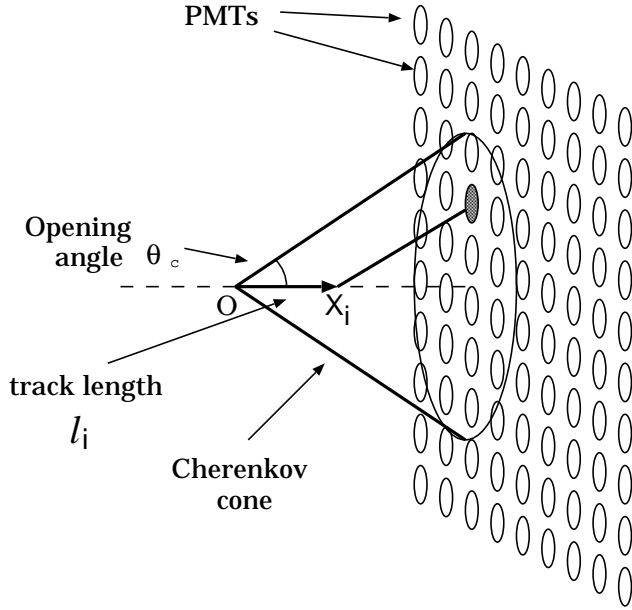


Figure 6.3: Schematic view of Cherenkov radiation. The Cherenkov photons to the  $i$ th PMT were emitted at  $X_i$ .  $l_i$  is the track length of the charged particle from the vertex.

where  $\vec{P}_i$  is the position of the  $i$ th PMT,  $X_i$  is the estimated point at which the photons were emitted to the  $i$ th PMT, and  $n$  is the refractive index of water. Fig. 6.3 shows the schematic view of the Cherenkov radiation.

We define the estimators,  $G_I$  and  $G_O$ , for the inside and outside of the Cherenkov ring, respectively.  $G_I$  is defined as follows:

$$G_I = \sum_i \frac{1}{\sigma_i^2} \exp \left( -\frac{1}{2} \cdot \left( \frac{t_i - t_0}{1.5 \cdot \sigma} \right)^2 \right) \quad (6.5)$$

where  $\sigma_i$  is the timing resolution of the  $i$ th PMT as a function of  $q_i$  (see Fig. 4.4),  $\sigma$  is the timing resolution averaged over all hit PMTs, and  $t_i$  and  $t_0$  are the time residual of the  $i$ th PMTs and its offset, respectively.

For the PMTs outside the Cherenkov ring, the effect of the scattered light is considered. We define the estimators,  $G_{O_1}$  and  $G_{O_2}$  according to the time residual of the PMTs:

$$G_{O_1} = \sum_i \frac{1}{\sigma_i^2} \left( \max \left[ \exp \left( -\frac{1}{2} \cdot \left( \frac{t_i - t_0}{1.5 \cdot \sigma} \right)^2 \right), G_{\text{scatt}}(t_i, t_0) \right] \times 2 - 1 \right) \quad (\text{for } t_i > t_0 \text{ PMTs}) \quad (6.6)$$

$$G_{O_2} = \sum_i \frac{1}{\sigma_i^2} \left( \exp \left( -\frac{1}{2} \cdot \left( \frac{t_i - t_0}{1.5 \cdot \sigma} \right)^2 \right) \times 2 - 1 \right) \quad (\text{for } t_i \leq t_0 \text{ PMTs}) \quad (6.7)$$

where

$$G_{\text{scatt}}(t_i, t_0) = \frac{R_q}{1.5^2} \times \exp\left(-\frac{1}{2} \cdot \left(\frac{t_i - t_0}{1.5 \cdot \sigma}\right)^2\right) + \left(1 - \frac{R_q}{1.5^2}\right) \exp\left(-\frac{t_i - t_0}{60 \text{ nsec}}\right) \quad (6.8)$$

$$R_q = \frac{\sum_{\theta < \theta_c + 3.0} q_i}{\sum_{\theta < 70^\circ} q_i} \quad : \text{ Fractional p.e.s detected within Cherenkov ring} \quad (6.9)$$

The numerical factors in Eqs.(6.5-6.9) are optimized by a Monte Carlo simulation study.

Finally, the estimator of the fitting,  $G_T$ , is defined as:

$$G_T = \frac{G_I + G_{O_1} + G_{O_2}}{\sum_i \frac{1}{\sigma_i^2}} \quad (6.10)$$

The vertex position which maximizes  $G_T$  is defined to be the best fit vertex position by TDCfit.

#### 6.2.4 Performance of TDCfit

Fig. 6.4 shows the resolution of TDCfit estimated by atmospheric neutrino Monte Carlo events. The resolution is defined as the distance where 68% of the total events are covered. The resolutions are estimated to be 61 cm, 51 cm, 114 cm for FC 1 ring, FC multi-ring, and PC events, respectively.

### 6.3 Ring-Counting

The Ring-Counting procedure finds and reconstructs the other Cherenkov rings which are not found in the vertex fitting.

The Ring-Counting process has two steps:

- (1) Find Cherenkov ring candidates
- (2) Test whether the candidate is true Cherenkov ring or not

We iterate the two steps until no more rings are found. Each step is described below.

#### 6.3.1 Ring Candidate Search

Fig 6.5 shows the basic concept of the search for the ring candidates. Let's assume that Cherenkov photons are detected on a flat plane perpendicular to the particle direction. If we draw circles centered at the hit PMTs with the same radius as the Cherenkov ring, the maximum overlapping point is the center of the Cherenkov ring.

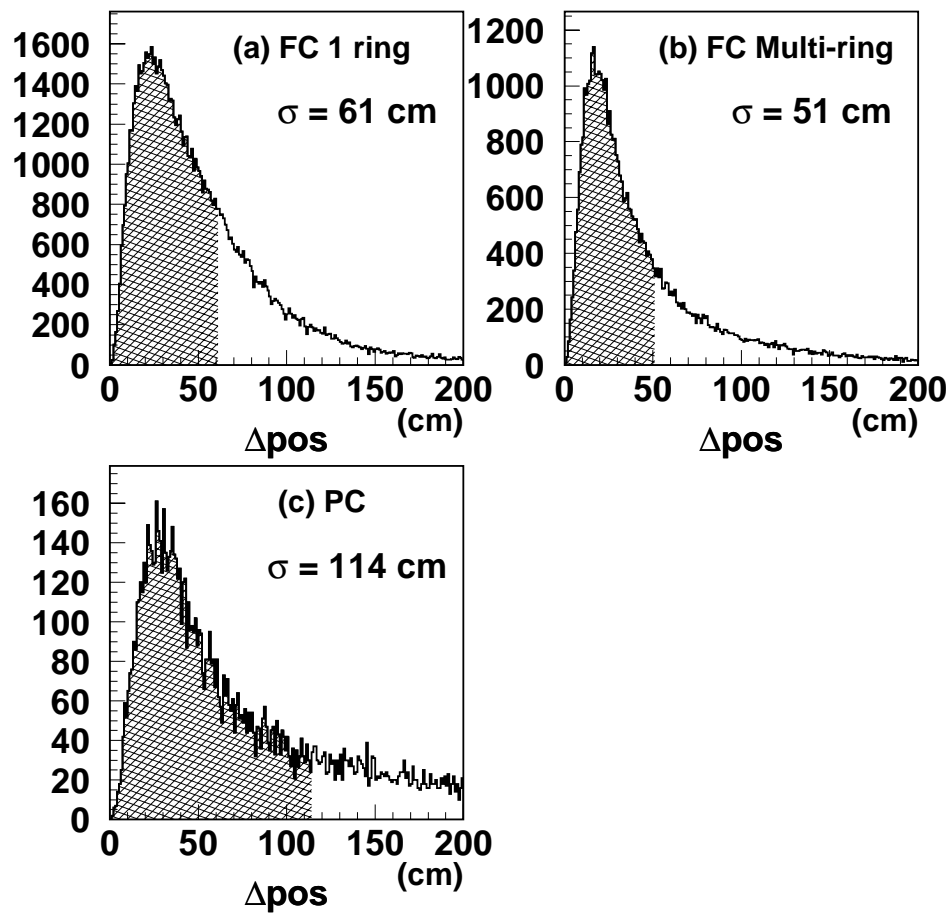


Figure 6.4: The vertex resolution of TDCfit for (a) FC single-ring, (b) FC multi-ring (c) PC samples estimated from atmospheric neutrino Monte Carlo events. Hatched regions show the 68% of total events. The vertex resolution is estimated to be 61cm for FC single-ring sample, 51cm for FC multi-ring sample, and 114cm for PC sample, respectively.

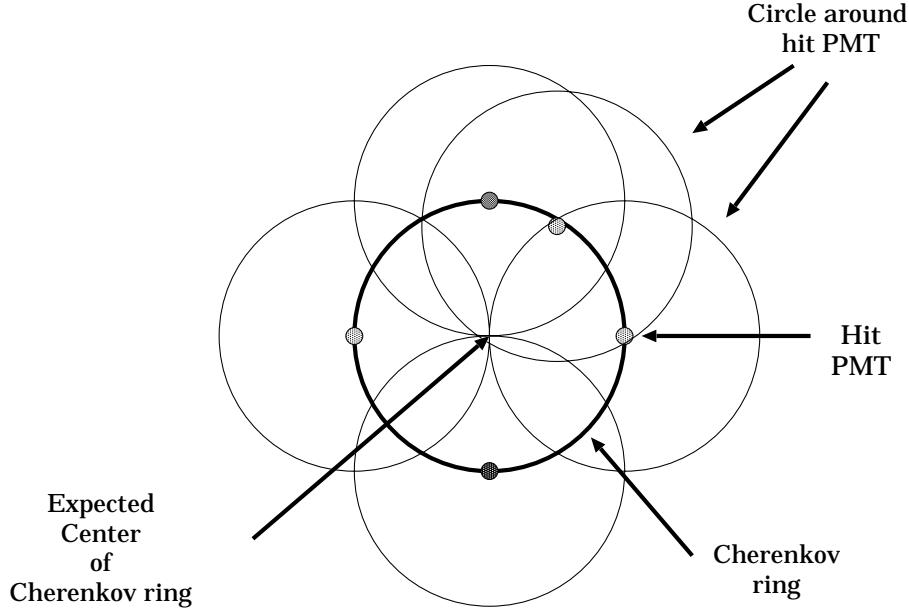


Figure 6.5: Schematic view of the search for the center of the Cherenkov ring. The most overlapping point is the candidate of the center of the Cherenkov ring.

In the real data analysis, we make a 2-dimensional photoelectron map of polar angle  $\Theta$  and azimuthal angle  $\Phi$  measured from the vertex ( $36 \times 72$  bins). Before making the p.e. map, we subtract the p.e.s of the Cherenkov rings which were already found. Instead of drawing the circle, we map the observed p.e.s of the hit PMT onto the  $(\Theta, \Phi)$  map according to the weight function,  $f_e(\theta)$ , which is the expected p.e.s distribution for the Cherenkov ring of a 500 MeV/c electron event. Here,  $\theta$  means the opening angle between the direction to the hit PMT and the bins. Fig. 6.6 shows the p.e.s map of a typical event. Two clear peaks can be seen.

### 6.3.2 Test of the Ring Candidate

The ring candidate found in the p.e.s map is tested by a likelihood method. The test of the  $(N + 1)$ -th ring is carried out by comparing the likelihood for a  $(N + 1)$  rings assumption and the likelihood for a  $N$  ring assumption.

The likelihood function for the  $(N + 1)$  ring assumption is:

$$L^{N+1} = - \sum_i \log \left( \text{prob} \left( q_i^{\text{obs}}, \sum_{n=1}^{N+1} \alpha_n \cdot q_{i,n}^{\text{exp}} \right) \right) \quad (6.11)$$

where  $q_i^{\text{obs}}$  is the observed p.e.s, and  $q_{i,n}^{\text{exp}}$  is the expected p.e.s of the  $i$ th PMT from the  $n$ th ring, and  $\alpha_n$  is a normalization factor. Summation is made over the PMTs which satisfy the

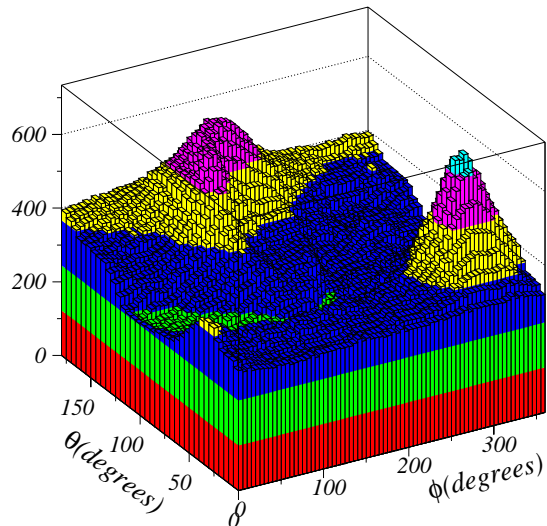


Figure 6.6: The p.e.s map for a typical two ring event. Clear two peak can be seen.

condition that at least one of the opening angles towards  $(N+1)$  rings is smaller than 1.2 times of the estimated opening angle of the Cherenkov ring. The probability function,  $prob(q_i^{\text{obs}}, q_i^{\text{exp}})$ , is defined as:

$$prob(q_i^{\text{obs}}, q_i^{\text{exp}}) = \begin{cases} \frac{1}{\sqrt{2\pi}\sigma_i} \exp\left(-\frac{(q_i^{\text{obs}} - q_i^{\text{exp}})^2}{2\sigma_i^2}\right) & (\text{for } q_i^{\text{exp}} > 20 \text{ p.e.}) \\ \text{Corrected poisson distribution for} \\ \text{single p.e. pulse height distribution} & (\text{for } q_i^{\text{exp}} \leq 20 \text{ p.e.}) \end{cases} \quad (6.12)$$

where  $\sigma_i^2$  is the expected resolution for  $q_i^{\text{exp}}$ .

$L^{N+1}$  is maximized by changing  $\alpha_n$  ( $n = 1, \dots, N+1$ ) while  $q_{i,n}^{\text{exp}}$  ( $n = 1, \dots, N+1$ ) are fixed. The expected p.e. distribution for the  $(N+1)$ -th ring is calculated using that for an electron described in Section 6.3.1.

In addition to the likelihood  $L^{N+1}$ , we use the following quantities in order to get a high performance of the Ring-Counting process:

- The averaged p.e.s around the edge of the  $(N+1)$ -th ring,  $Q_{\text{edge}}$ , is used. The averaged is made over non-overlapping region of the rings.
- The difference between  $Q_{\text{edge}}$  and the averaged p.e.s for outside the Cherenkov rings,  $Q_{\text{out}}$ , is used.
- The residual p.e.s distribution after subtraction the expected p.e.'s of  $N$  rings is used. We calculate the weighted vector sum  $\vec{V} = \sum_i q_i^{\text{res}} \cdot \vec{e}_i$  where  $q_i^{\text{res}}$  is the residual p.e.s for

the  $i$ th PMT and  $\vec{e}_i$  is a unit vector from the reconstructed vertex to the  $i$ th PMT. If  $(N + 1)$ -th ring is a true one,  $|\vec{V}|$  should have a larger value.

We calculate the evaluation functions,  $F_1(L^{N+1} - L^N)$ ,  $F_2(Q_{\text{edge}})$ ,  $F_3(Q_{\text{edge}} - Q_{\text{out}})$  and  $F_4(|\vec{V}|)$ . The weighted sum of these four functions is used for the  $(N + 1)$ -th ring test. If the  $(N + 1)$ -ring is determined as a true one, the number of the rings is changed to  $N + 1$ , and the procedure goes back to the ring candidate search.

Before going to the next ring, the observed p.e.s of the  $i$ th PMT is separated into the fractional p.e.s from the  $n$ th ring,  $q_{i,n}^{\text{obs}}$ :

$$q_{i,n}^{\text{obs}} = q_i^{\text{obs}} \times \frac{\alpha_n \cdot q_{i,n}^{\text{exp}}}{\sum_{n=1}^N \alpha_n \cdot q_{i,n}^{\text{exp}}} \quad (6.13)$$

and we replace the  $q_{i,n}^{\text{exp}}$  ( $n = 1, \dots, N + 1$ ) by  $q_{i,n}^{\text{obs}}$ 's.

The Ring-Counting process continues until no new Cherenkov ring is found. In the current analysis of the atmospheric neutrinos, the maximum number of the rings is set to be 5.

### 6.3.3 Performance of the Ring-Counting

The performance of the Ring-Counting procedure was tested by atmospheric neutrino Monte Carlo events. Fig. 6.7 shows the efficiency that CC quasi-elastic event  $\nu_l + N \rightarrow l + N'$  is identified as single ring. The efficiency is about 96% for 1.0 GeV/ $c$  electrons and muons. The decreasing efficiency for the high energy electrons is due to their diffused Cherenkov images. Fig. 6.8 shows the efficiency that the a NC  $\pi^0$  production event  $\nu + N \rightarrow \nu + N + \pi^0$  is identified as a two-ring event.  $\pi^0$  decays into two  $\gamma$ 's, the  $\gamma$  rays produce two electromagnetic showers and consequently two Cherenkov rings. The decreasing efficiency for the energetic  $\pi^0$  is due to the smaller angle between the two  $\gamma$ 's by the Lorentz boost effect.

## 6.4 Particle-Identification

Particle-Identification(PID) procedure estimates the particle types of the reconstructed Cherenkov rings using their patterns and the opening angles. The Cherenkov rings are categorized into 2 types: shower type which we call 'e-like', and non-shower type which we call ' $\mu$ -like'.

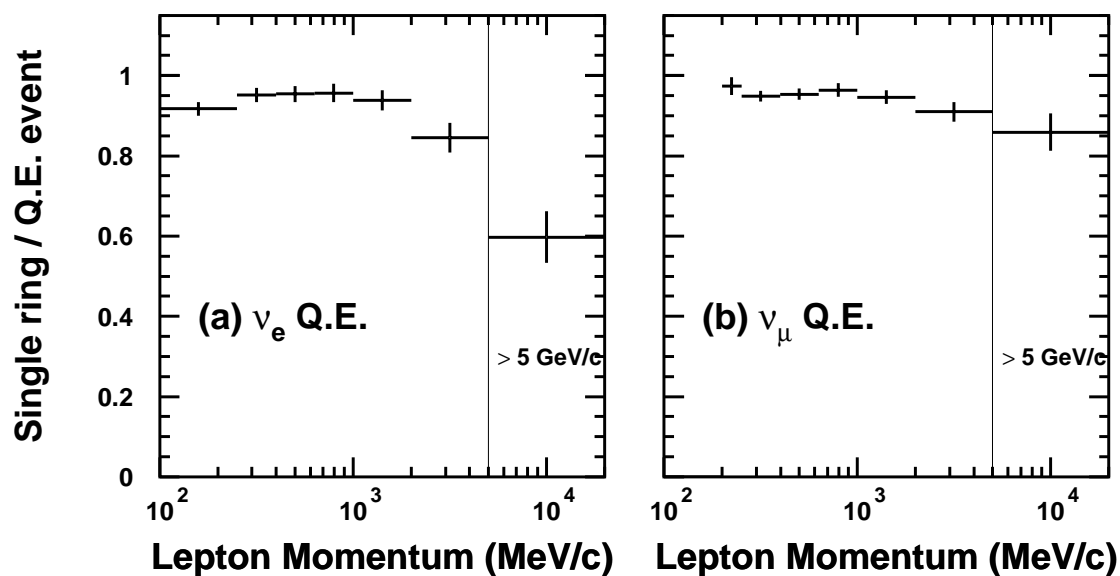


Figure 6.7: The efficiency that a CC quasi-elastic event  $\nu + N \rightarrow l + N'$  is identified as a single-ring event, as a function of a charged lepton momentum for (a)  $\nu_e$  and (b)  $\nu_\mu$ .

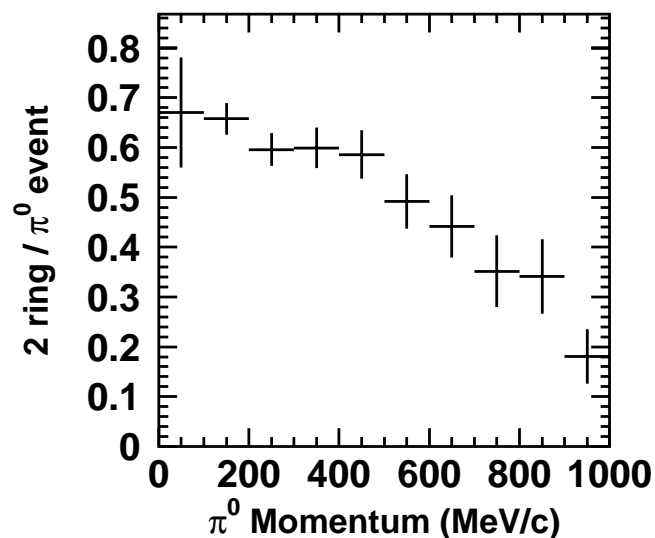


Figure 6.8: The efficiency that a NC  $\pi^0$  production event is identified as a 2-ring event, as a function of the  $\pi^0$  momentum.

### 6.4.1 Estimation of the Particle Type

We define a likelihood function  $L_l$  for the electron assumption ( $l = e$ ) and the muon assumption ( $l = \mu$ ). The definition of  $L_l$  for the  $n$ th ring is:

$$L_l(n) = \prod_{\substack{i \\ \theta_{i,n} < 1.5\theta_{c,n}}} prob \left( q_i^{\text{obs}}, q_{i,n}^{\text{exp},l} + \sum_{n' \neq n} q_{i,n'}^{\text{exp},l} \right) \quad (6.14)$$

where  $q_i^{\text{obs}}$  is the observed p.e.s for the  $i$ th PMT and  $q_{i,n}^{\text{exp},l}$  is the expected p.e.s from the  $n$ th ring assuming the particle type is  $l$  ( $l = e$  or  $\mu$ ). The function  $prob(q_i^{\text{obs}}, q_i^{\text{exp},l})$  is the same function as used in the Ring-Counting procedure (defined by Eq.(6.12)). The product in Eq.(6.14) is made for the PMTs whose opening angle from the  $n$ th ring direction is within 1.5 times the estimated Cherenkov opening angle of the  $n$ th ring. The calculation of the expected p.e.s are described in the following subsections.  $L_l$  is maximized by changing the direction and the opening angle of the  $n$ th ring while  $q_{i,n'}^{\text{exp},l}$  ( $n' \neq n$ ) are fixed.

In order to combine the information of Cherenkov ring pattern and Cherenkov opening angle, the likelihood  $L_l$  is transformed into the  $\chi^2$  function:

$$\chi_l^2(n) = -2 \ln L_l(n) - \text{const.} \quad (6.15)$$

The probability from the Cherenkov pattern is written as:

$$P_l^{\text{pattern}}(n) = \exp \left( -\frac{1}{2} \frac{(\chi_l^2(n) - \chi_{\text{min}}^2)^2}{\sigma_{\chi^2}^2} \right) \quad (6.16)$$

where  $\chi_{\text{min}}^2 = \min[\chi_e^2, \chi_\mu^2]$ ,  $\sigma_{\chi^2}$  is  $\sqrt{2N_D}$ , and  $N_D$  is the number of PMTs which were used in the calculation of  $L_l$ .

The probability from the Cherenkov opening angle is written as:

$$P_l^{\text{angle}}(n) = \exp \left( -\frac{1}{2} \frac{(\theta_{c,n} - \theta_n^{\text{exp},l})^2}{\sigma_\theta^2} \right) \quad (6.17)$$

where  $\theta_{c,n}$  is the reconstructed Cherenkov opening angle of the  $n$ th ring,  $\theta_n^{\text{exp},l}$  is the expected opening angle for particle type  $l$  (electron or muon),  $\sigma_\theta$  is the resolution of the estimated Cherenkov angle.

The total probability is defined as the product of  $P_{\text{pattern}}(n)$  and  $P_{\text{angle}}(n)$ :

$$P_l^{\text{total}}(n) = P_l^{\text{pattern}}(n) \times P_l^{\text{angle}}(n) \quad (6.18)$$

where suffix  $l$  is  $e$  or  $\mu$ .

If  $P_e^{\text{total}}(n) > P_\mu^{\text{total}}(n)$ , the  $n$ th ring is determined as  $e$ -like and vice versa. For multi-ring events, we adopt the ring pattern probability  $P^{\text{pattern}}$  only, because the performance of the reconstruction of Cherenkov angle is relatively poor than in the case of single ring events.

### 6.4.2 The Expected p.e. Distribution for Electrons

The expected p.e. distributions for electrons are made using a Monte Carlo simulation. In advance, we calculate the expected p.e. distribution,  $Q_e^{\text{exp}}(p_e, \theta)$ , which will be detected by a circular area of 50 cm diameter (same size as the 20 inch diameter PMTs) on a hypothetical spherical surface with the radius  $R^{\text{sph}}=16.9\text{m}$  (radius of the inner tank).  $Q_e^{\text{exp}}(p_e, \theta)$  is given as a function of electron momentum  $p_e$  (MeV/c) and the opening angle  $\theta$  from the electron direction.

The expected p.e. for the  $i$ th PMT due to the  $n$ th ring is calculated as:

$$q_{i,n}^e = \alpha_{n,e} \times Q_e(p_e, \theta_{i,n}) \times \left( \frac{R^{\text{sph}}}{r_i} \right)^{1.5} \times \exp\left(-\frac{r_i}{\lambda}\right) \times f(\Theta_i) \quad (6.19)$$

where

- $q_{i,n}^e$  : expected p.e.s for the  $i$ th PMT due to the  $n$ th ring
- $\alpha_{n,e}$  : normalization factor
- $\theta_{i,n}$  : opening angle between the  $n$ th ring direction and the direction from the vertex to the  $i$ th PMT
- $r_i$  : distance from the vertex to the  $i$ th PMT
- $\Theta_i$  : angle of photon arriving direction relative to the  $i$ th PMT's facing direction
- $f(\Theta_i)$  : correction function of the PMT acceptance
- $\lambda$  : attenuation length of light in water (see Section 4.5)

The factor  $(R^{\text{sph}}/r_i)^{1.5}$  takes into account the  $r_i$  dependence of the intensity of the Cherenkov light. The index 1.5 was determined by a Monte Carlo study.

### 6.4.3 The Expected p.e. Distribution for Muons

The expected p.e. distribution for a muon is analytically calculated by the following equation:

$$q_{i,n}^\mu = \left( \alpha_{n,\mu} \times \frac{\sin^2 \theta_{i,n}}{r_i \left( \sin \theta_{i,n} + r_i \frac{d\theta}{dx} \Big|_{x=x_i} \right)} + q_i^{\text{knock}} \right) \times \exp\left(-\frac{r_i}{\lambda}\right) \times f(\Theta_i) \quad (6.20)$$

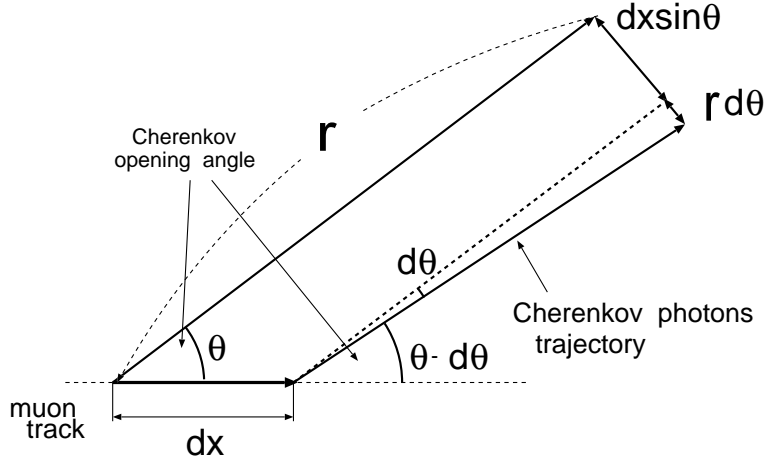


Figure 6.9: Schematic view of Cherenkov radiation from a muon. Cherenkov opening angle  $\theta$  changes as the muon momentum changes due to the energy loss in water. The Cherenkov photons are emitted into the region  $dx \cdot \sin \theta + r \cdot d\theta$  during the muon propagation  $dx$ .

where

$q_{i,n}^{\mu}$  : expected p.e.s for the  $i$ th PMT due to the  $n$ th ring

$\alpha_{n,\mu}$  : normalization factor

$q_i^{\text{knock}}$  : observed p.e.s for the  $i$ th PMT due to the knock-on electrons

$x$  : distance from the vertex along the muon trajectory

$x_i$  : distance from the vertex to the Cherenkov emission point  
for the  $i$  th PMT

$r_i, \theta_{i,n}, \lambda, \Theta_i, f(\Theta)$  : same quantities as in Eq.(6.19)

The numerator  $\sin^2 \theta$  in Eq.(6.20) comes from the number of emitted Cherenkov photons to the direction  $\theta_{i,n}$  (see Eq.(3.2)). The denominator  $r_i(\sin \theta + r_i \frac{d\theta}{dx})$  comes from the area where Cherenkov photons are emitted to. Fig. 6.9 shows the schematic view of the Cherenkov photon emission. The area changes due to the decreasing of the Cherenkov opening angle caused by the energy loss of the muon.

$q_i^{\text{knock}}$  is the contribution from the knock on electrons which is estimated by a Monte Carlo simulation.

#### 6.4.4 The Expected p.e. Distribution for Scattered Light

A PMT hit by the scattered light can be distinguished from a PMT hit by direct photons using the timing information. The 'Off timing' hit PMTs are chosen by the criteria:

$$t_{peak} - 30\text{nsec} < t'_i < t_{peak} + 2\sigma_i + 5\text{nsec} \quad : \text{ direct photons} \quad (6.21)$$

$$t_{peak} + 2\sigma_i + 5\text{nsec} < t'_i \quad : \text{ scattering photons} \quad (6.22)$$

where  $t'_i$  is the time residual for the  $i$ th PMT defined in Eq.(6.4),  $t_{peak}$  is the time at peak position of the time residual distribution, and  $\sigma_i$  is the measured timing resolution as a function of observed p.e.s as shown in Fig. 4.4.

The number of p.e.s due to the scattered photons,  $q_i^{\text{scatt}}$ , is estimated from the 'Off timing' PMTs and added to the expected p.e.s for the  $i$ th PMT:

$$q_i^{\text{exp},l} = q_i^l(\text{direct}) + q_i^{\text{scatt}} \quad (6.23)$$

where the suffix  $l$  represents  $e$  or  $\mu$ .

#### 6.4.5 Performance of PID

The performance of PID is estimated by a Monte Carlo study. Figs. 6.10 and 6.11 show the PID parameter  $\sqrt{-\log P_e} - \sqrt{-\log P_\mu}$  distributions for the final sample. 'Sub-GeV' sample is defined as the events with visible energy below 1.33 GeV, and 'Multi-GeV' sample is defined as the events with visible energy over 1.33 GeV. The MC events are shown separately for CC  $\nu_e$ , CC  $\nu_\mu$  and NC events. The peaks in  $e$ -like and  $\mu$ -like events are clearly separated. Fig. 6.12 shows the PID efficiency for CC Q.E. events which are identified as single ring, and a function of the charged lepton momentum. The efficiency is very high for all energy region, and the misidentification probabilities are estimated to be 0.5% for CC Q.E.  $\nu_e$  events and 1.2% for CC Q.E.  $\nu_\mu$  events.

### 6.5 MS fit

The vertex fitter described in Section 6.2 uses the timing information, and it consequently has a relatively poor vertex resolution along the direction, especially for the single ring events. It is because a vertex shift along the direction almost equally changes the time residuals of the PMTs, and it doesn't change the goodness of the fitting substantially.

To improve the resolution of the vertex, we employ another fitter called 'MS fit'. MS fit find the vertex by a pattern matching between the observed Cherenkov pattern and the expected pattern assuming the estimated particle type. The vertex search parallel to the ring direction is

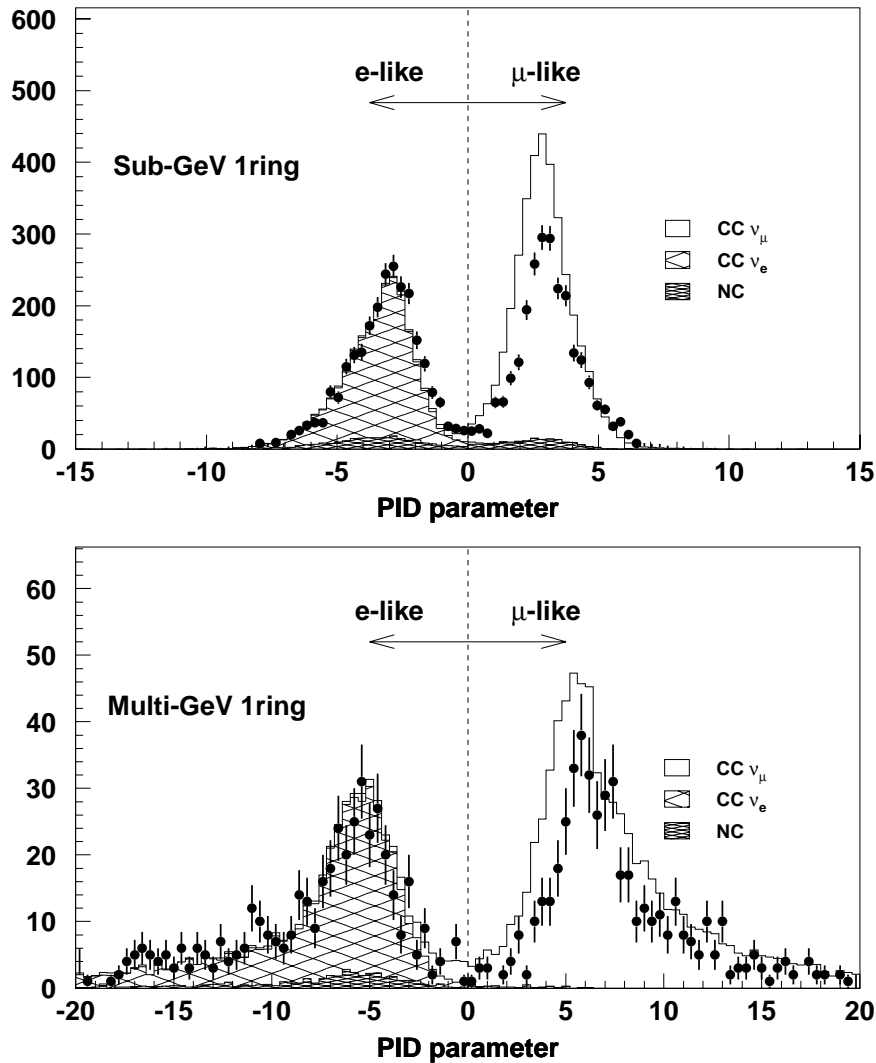


Figure 6.10: PID parameter  $\sqrt{-\log P_e} - \sqrt{-\log P_\mu}$  distributions for the final sample 1-ring Sub-GeV (visible energy is below 1.33 GeV) and Multi-GeV (visible energy is over 1.33 GeV) events. Points show the data and histograms show the MC prediction. MC predictions are normalized by the livetime. Events with a negative (positive) value of PID parameter are defined to be *e*-like (*μ*-like). Monte Carlo predictions are separately shown for CC  $\nu_e$ , CC  $\nu_\mu$ , and NC events.

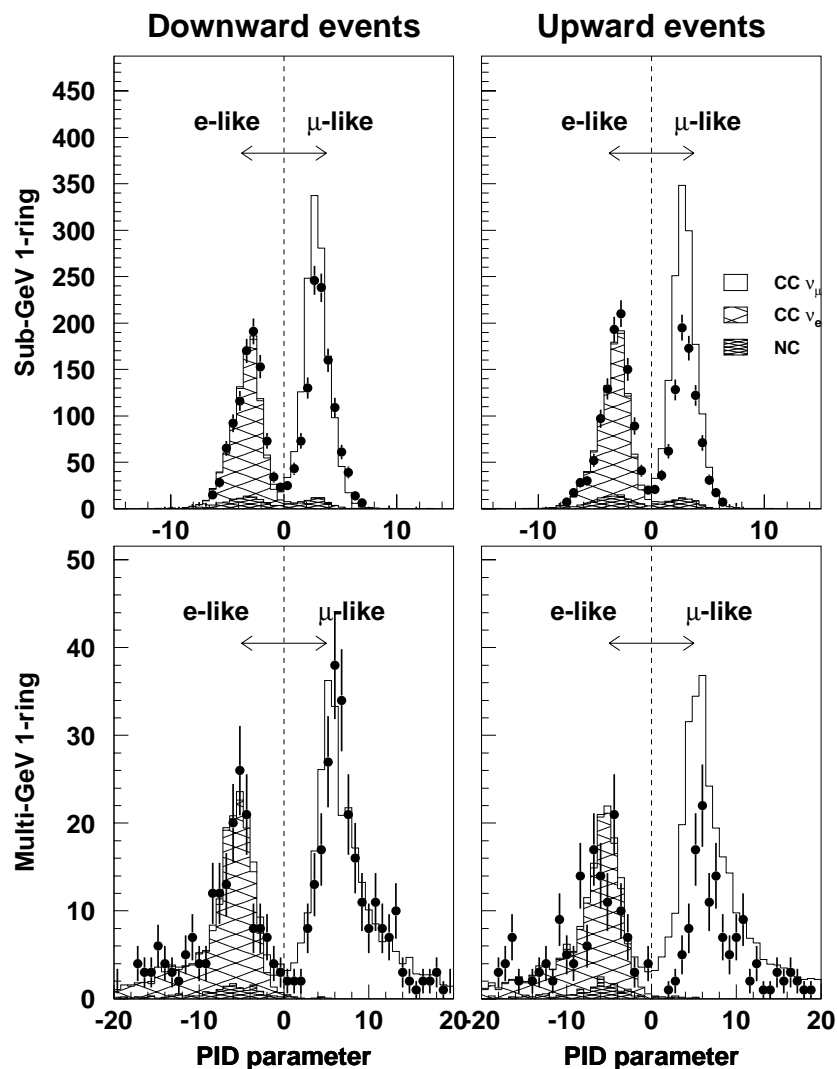


Figure 6.11: PID parameter distributions for the final sample Sub-GeV 1-ring and Multi-GeV 1-ring events. Upward-going events (reconstructed cosine zenith angle  $< -0.2$ ) and downward-going events (reconstructed cosine zenith angle  $> 0.2$ ) are separately shown. Points show the data and histograms show the MC prediction. MC predictions are normalized by the livetime.

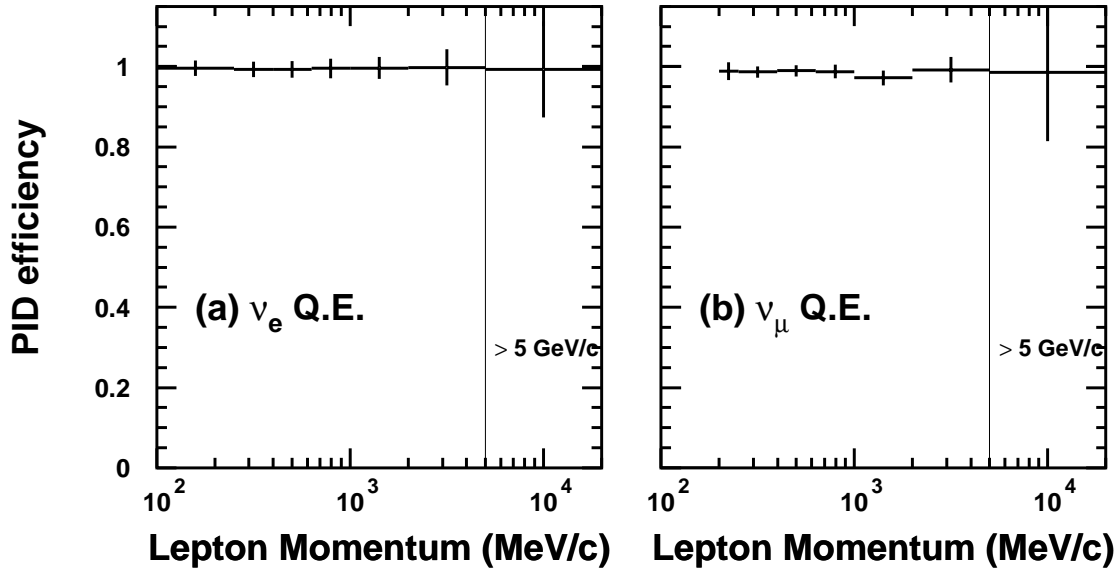


Figure 6.12: The PID efficiency for CC quasi-elastic single-ring event as a function of charged lepton momentum for (a)  $\nu_e$  and (b)  $\nu_\mu$ .

carried out by the pattern matching using the same likelihood methods as used in PID procedure (see Section 6.4). The vertex search perpendicular to the ring direction is carried out using the estimator  $G_T$  which is used in TDCfit (see Section 6.2).

This procedure is applied only for the single ring events. For PC 1 ring events, the MS fit is carried out assuming  $\mu$ -like PID.

### 6.5.1 Performance of MS fit

Fig. 6.13 shows the vertex resolution of MS fit estimated by an atmospheric neutrino Monte Carlo simulation. The vertex resolutions for single ring events are estimated to be 28 cm, 24 cm, 47 cm, 23 cm, and 29 cm for Sub-GeV  $e$ -like, Sub-GeV  $\mu$ -like, Multi-GeV  $e$ -like, Multi-GeV  $\mu$ -like, and PC events, respectively. Fig. 6.14 shows the vertex resolution along the particle direction. Upper figures show the vertex resolution for TDCfit, and lower figures show the vertex resolution for MS fit. TDCfit have a tendency to reconstruct the vertex forwards along the particle direction, especially for  $e$ -like and PC events. MS fit improves the tendency and gives a good vertex resolution.

Fig. 6.15 shows the estimated angular resolutions. The angular resolution is estimated to be  $3.2^\circ$ ,  $1.9^\circ$ ,  $1.6^\circ$ ,  $0.8^\circ$ ,  $1.1^\circ$  for Sub-GeV  $e$ -like, Sub-GeV  $\mu$ -like, Multi-GeV  $e$ -like, Multi-GeV  $\mu$ -like, and PC single-ring events, respectively.

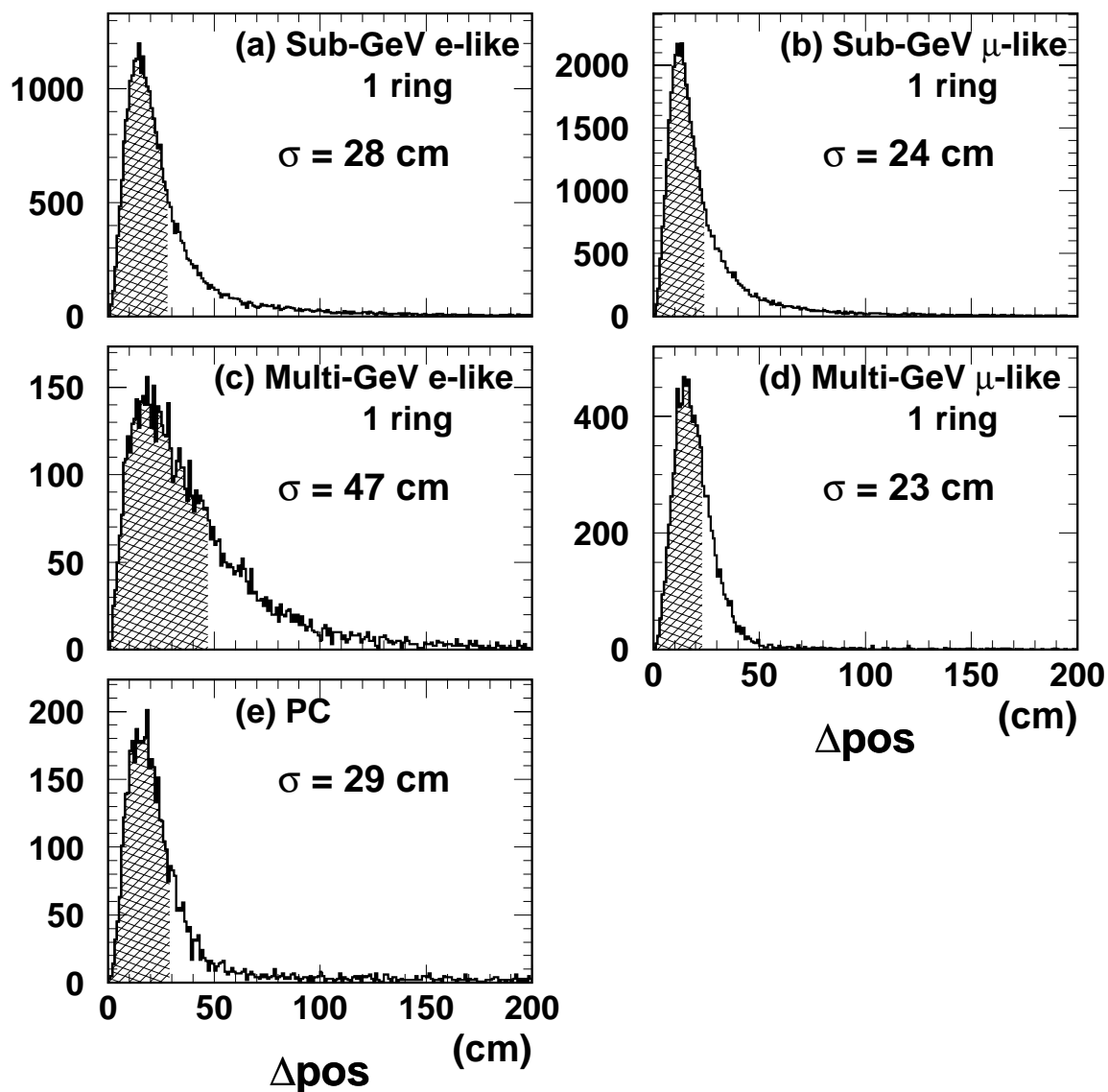


Figure 6.13: The vertex resolution of MS fit for (a) Sub-GeV  $e$ -like single-ring events (b) Sub-GeV  $\mu$ -like single-ring events (c) Multi-GeV  $e$ -like single-ring events (d) Multi-GeV  $\mu$ -like single-ring events (e) PC single-ring events estimated from atmospheric neutrino Monte Carlo simulation. Hatched regions show the 68% of the total events.

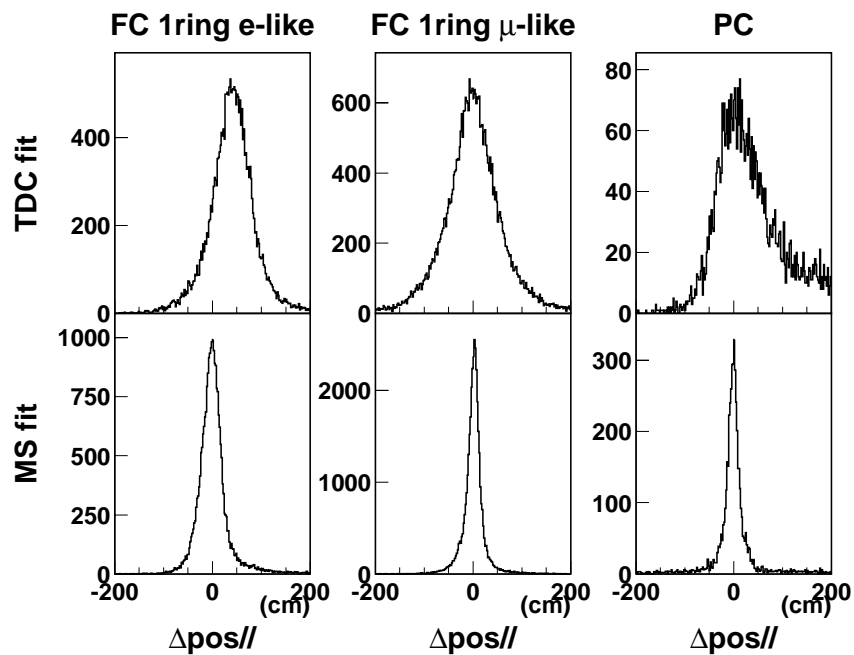


Figure 6.14: The vertex resolution along the particle direction. Upper figures show the result of TDCfit, and lower figures show the result of MS fit. TDCfit has a tendency to reconstructs the vertex fowards to the particle direction ( $\Delta pos_{\parallel} > 0$ ), but MS fit improves the vertex resolution significantly.

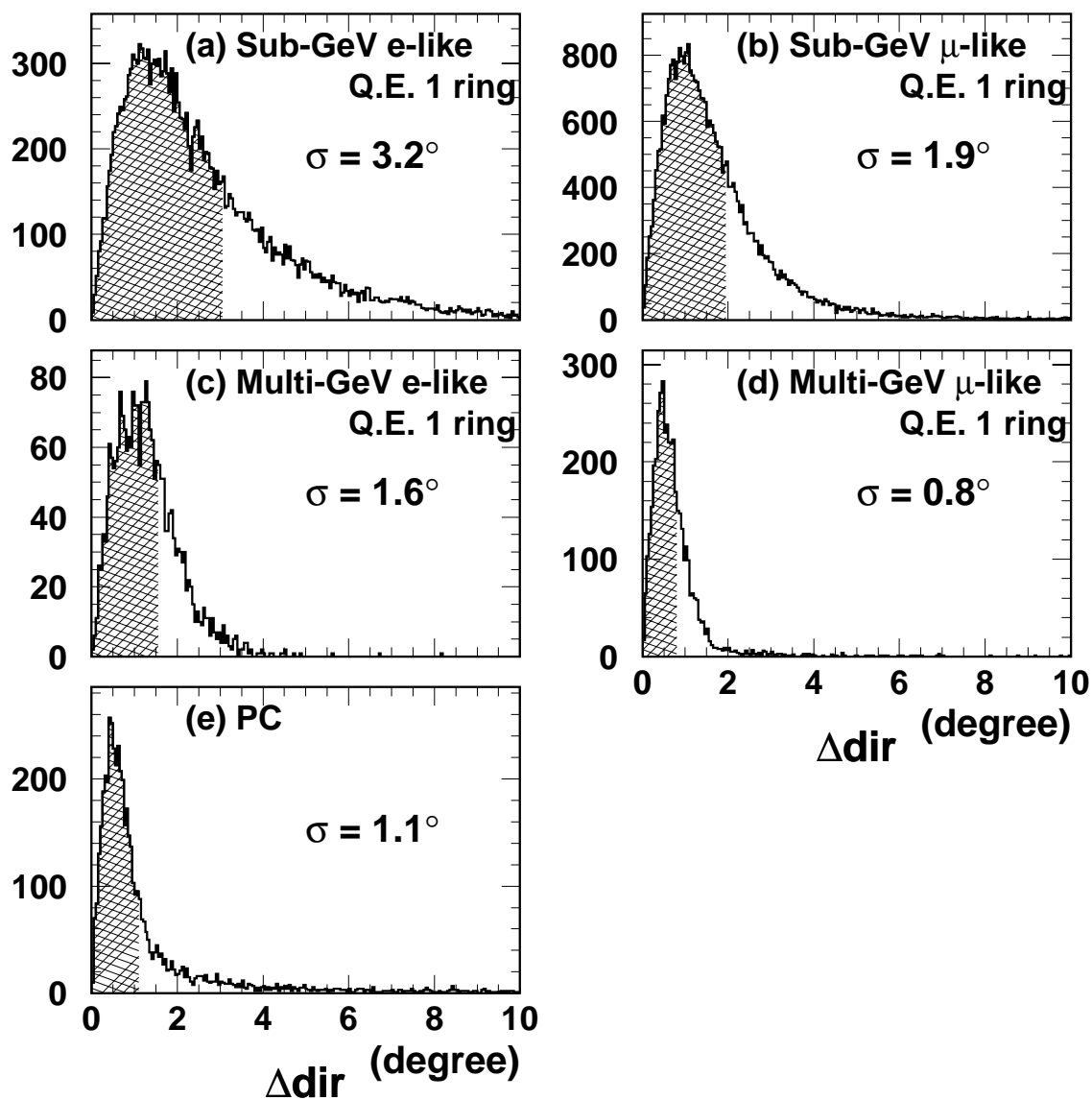


Figure 6.15: The angular resolution of MS fit for single-ring events. Hatched regions show the 68% of the total events. The angular resolution is  $3.2^\circ$ ,  $1.9^\circ$ ,  $1.6^\circ$ ,  $0.8^\circ$ , and  $1.1^\circ$  for Sub-GeV  $e$ -like  $\nu_e$  Q.E. events, Sub-GeV  $\mu$ -like  $\nu_\mu$  Q.E. events, Multi-GeV  $e$ -like  $\nu_e$  Q.E. events, Multi-GeV  $\mu$ -like  $\nu_\mu$  Q.E. events, and PC single-ring events, respectively.

## 6.6 Momentum Estimation

The momentum estimation is based on the relation between the number of emitted Cherenkov photons and the momentum of the particles.

To estimate the momentum of the particles, we calculate the corrected total photoelectrons,  $R_{tot}(n)$ , which is defined as:

$$R_{tot}(n) = \frac{G_{MC}}{G_{data}} \left[ \alpha \times \sum_{\substack{\theta_{i,n} < 70^\circ \\ -50\text{nsec} < t_i^{res} < 250\text{nsec}}} q_{i,n}^{obs} \times \exp\left(-\frac{r_i}{\lambda}\right) \times \frac{\cos \Theta}{f(\Theta_i)} - \sum_{\theta_{i,n} < 70^\circ} S_i \right] \quad (6.24)$$

where

- $\alpha$  : normalization factor
- $G_{data}, G_{MC}$  : relative PMT gain for the data and MC
- $q_{i,n}^{obs}$  : observed p.e.s for the  $i$ th PMT due to the  $n$ th ring
- $\Theta_{i,n}$  : angle of photon arriving direction relative to the  $i$ th PMT facing direction
- $f(\Theta)$  : correction function of PMT acceptance
- $r_i$  : distance from vertex to the  $i$ th PMT
- $\lambda$  : attenuation length of light in the water (see Section 4.5)
- $S_i$  : expected scattered light for the  $i$ th PMT
- $t_i^{res}$  : time from the peak of time residuals
- $\theta_{i,n}$  : opening angle of the  $i$ th PMT towards the direction of the  $n$ th ring

In the calculation of  $R_{tot}$ , we use the PMTs whose timing is within -50 to +250 nsec timing window from the peak of the timing residual to avoid the effect of the decay electrons. Also we choose the PMTs which is within a cone with  $70^\circ$  opening angle toward the  $n$ th ring direction.

Fig. 6.16 shows the estimated momentum resolution for electrons and muons. The momentum resolution is approximately described as:

$$\sigma_p = \begin{cases} 0.6 + \frac{2.6}{\sqrt{p(\text{GeV}/c)}} \% & \text{for electron} \\ 1.7 + \frac{0.7}{\sqrt{p(\text{GeV}/c)}} \% & \text{for muon} \end{cases} \quad (6.25)$$

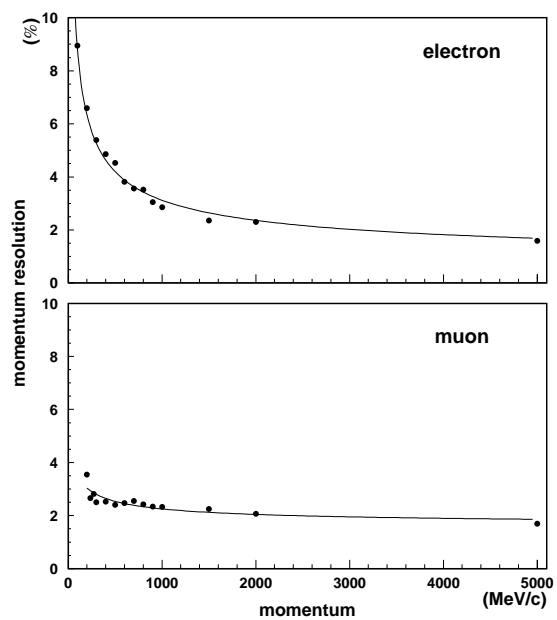


Figure 6.16: Momentum resolution for (a)electron and (b)muon. solid lines show the fitted result, estimated from the MC events in the fiducial volume.



# Chapter 7

## Monte Carlo Simulation

### 7.1 Overview

In this chapter, the details of a Monte Carlo simulation used in the Super-Kamiokande experiment are described. The Monte Carlo simulation is used to understand the details of the neutrino interactions and the behaviour of the Super-Kamiokande detector.

Monte Carlo simulation consists of 4 parts.

1. Atmospheric neutrino fluxes
2. Neutrino interactions
3. Propagation of particles and Cherenkov photons in the detector
4. Detection of Cherenkov light

The details of the atmospheric neutrino fluxes are already described in Chapter 2. Detailed descriptions for the other parts are described below.

### 7.2 Neutrino interaction

Neutrino interactions in the energy region concerning to the Super-Kamiokande experiment ( $\sim 0.1$  GeV to 1000 GeV) are categorized into the following types:

1. CC and NC elastic scattering off electron ( $\nu + e^- \rightarrow \nu + e^-$ )
2. CC quasi elastic scattering off nucleon ( $\nu + N \rightarrow l + N'$ )
3. NC elastic scattering off nucleon ( $\nu + N \rightarrow \nu + N$ )
4. CC single meson production ( $\nu + N \rightarrow l + N' + \text{meson}$ )
5. NC single meson production ( $\nu + N \rightarrow \nu + N' + \text{meson}$ )

6. CC deep inelastic scattering ( $\nu + N \rightarrow l + N' + \text{hadrons}$ )
7. NC deep inelastic scattering ( $\nu + N \rightarrow \nu + N' + \text{hadrons}$ )
8. CC coherent pion production ( $\nu + {}^{16}\text{O} \rightarrow l + {}^{16}\text{O} + \pi$ )
9. NC coherent pion production ( $\nu + {}^{16}\text{O} \rightarrow \nu + {}^{16}\text{O} + \pi$ )

where  $l$  represents a charged lepton, and  $N$  and  $N'$  represents nucleons, respectively.

### 7.2.1 Elastic scattering off electron ( $\nu + e^- \rightarrow \nu + e^-$ )

CC and NC elastic scatterings off electron are well described by the Weinberg-Salamn model (Standard Model). The cross section of this interaction is order of  $10^{-41}\text{cm}^2$  at  $E_\nu = 1.0\text{ GeV}$ , and it is about  $10^3$  order of magnitude smaller than the other interactions. Thus, we neglect this scattering in our simulation.

### 7.2.2 Quasi elastic scattering off nucleon ( $\nu + N \rightarrow l + N'$ )

Our simulation for this interaction is based on Llewellyn Smith's theory [99]. The amplitude of this process is described by the product of the hadron and lepton weak currents:

$$T = \frac{G_F}{\sqrt{2}} \bar{u}_l(k_2) \gamma^\mu (1 - \gamma_5) u_\nu(k_1) \langle N'(p_2) | J_\mu^{\text{hadron}} | N(p_1) \rangle \quad (7.1)$$

where  $G_F$  is the Fermi coupling constant,  $p_1(p_2)$  is a initial(final) nucleon 4-momentum, and  $k_1(k_2)$  is a initial(final) lepton 4-momentum, respectively. The hadronic weak current,  $J^{\text{hadron}}$ , is expressed as:

$$\langle N' | J_\mu^{\text{hadron}} | N \rangle = \cos \theta_c \bar{u}_{N'}(p_2) \left[ \gamma_\mu F_V^1(q^2) + \frac{i\sigma_{\mu\nu} q^\nu \xi F_V^2(q^2)}{M} + \gamma_\mu \gamma_5 F_A(q^2) \right] u_N(p_1) \quad (7.2)$$

where  $F_V^1(q^2)$  and  $F_V^2(q^2)$  are the vector form factor,  $F_A(q^2)$  is the axial vector form factors,  $q \equiv k_1 - k_2$  is a 4-momentum transfer,  $M$  is the target nucleon mass,  $\theta_c$  is the Cabibbo angle, respectively. If we assume the conserved vector current (CVC) hypothesis [100],  $F_V^1(q^2)$  and  $F_V^2(q^2)$  are written in terms of the electric and magnetic form factors,  $G_E$  and  $G_M$ :

$$\begin{aligned} F_V^1(q^2) &= \left(1 - \frac{q^2}{4M^2}\right)^{-1} \left[ G_E(q^2) - \frac{q^2}{4M^2} G_M(q^2) \right] \\ \xi F_V^2(q^2) &= \left(1 - \frac{q^2}{4M^2}\right)^{-1} [G_E(q^2) - G_M(q^2)] \\ \xi &\equiv \mu_p - \mu_n = 3.71 \quad \mu: \text{anomalous magnetic dipole moment} \end{aligned}$$

The electric and magnetic form factor have dipole forms which are experimentally determined by electron scattering experiments:

$$G_E(q^2) = (1 + \xi)^{-1} G_M(q^2) = \frac{1}{\left(1 - \frac{q^2}{M_V^2}\right)^2} \quad (7.3)$$

where  $M_V$  is vector mass which is set to be  $0.84 \text{ GeV}/c^2$  in our MC simulation.

By analogy with the vector form factor, we assume the axial vector form factor  $F_A$  has a dipole form:

$$F_A(q^2) = -\frac{1.23}{\left(1 - \frac{q^2}{M_A^2}\right)^2} \quad (7.4)$$

where  $M_A$  is the axial vector mass. Several experiments suggested that  $0.9 \text{ GeV}/c^2 < M_A < 1.1 \text{ GeV}/c^2$  [122]. We adopt  $1.01 \text{ GeV}/c^2$  in our MC simulation.  $F_A(0) = -1.23$  is obtained from neutron  $\beta$  decay experiments [101].

The differential cross sections  $d\sigma/dq^2$  are written as:

$$\frac{d\sigma^{\nu(\bar{\nu})}}{dq^2} = \frac{M^2 G_F^2 \cos^2 \theta_c}{8\pi E_\nu^2} \left[ A(q^2) \mp B(q^2) \frac{s-u}{M^2} + C(q^2) \frac{(s-u)^2}{M^4} \right] \quad (7.5)$$

where  $s$  and  $u$  are Mandelsam variables which are defined to be  $s \equiv (k_1 + p_1)^2$  and  $u \equiv (k_1 - p_1)^2$ ,  $E_\nu$  is a neutrino energy,  $m$  is an outgoing lepton mass, respectively.  $A(q^2)$ ,  $B(q^2)$ , and  $C(q^2)$  are written as follows:

$$\begin{aligned} A(q^2) &= \frac{m^2 - q^2}{4M^2} \left[ \left(4 - \frac{q^2}{M^2}\right) |F_A|^2 - \left(4 + \frac{q^2}{M^2}\right) |F_V^1|^2 \right. \\ &\quad \left. - \frac{q^2}{M^2} |\xi F_V^2|^2 \left(1 + \frac{q^2}{4M^2}\right) - \frac{4q^2 F_V^1 \xi F_V^2}{M^2} - \frac{m^2}{M^2} \left( (F_V^1 + \xi F_V^2)^2 + |F_A|^2 \right) \right] \\ B(q^2) &= \frac{q^2}{M^2} (F_A(F_V^1 + \xi F_V^2)) \\ C(q^2) &= \frac{1}{4} \left( |F_A|^2 + |F_V^1|^2 - \frac{q^2}{4M^2} |\xi F_V^2|^2 \right) \end{aligned} \quad (7.6)$$

Fig. 7.1 shows the calculated  $d\sigma/dq^2$  distribution for  $\nu_\mu + n \rightarrow \mu^- + p$  interaction as a function of  $q^2$  with experimental data from BNL experiment [102]. Our calculation well reproduces the observed shape of the  $d\sigma/dq^2$  distribution. Fig. 7.2 shows the integrated cross section for  $\nu_\mu$  and  $\bar{\nu}_\mu$  quasi elastic scatterings as a function of neutrino energy. The data are taken from several experiments [103, 104, 105, 106, 107]. Again, our calculations well reproduce the data.

In the case that the target nucleon is bound in an oxygen nucleus, we consider the Fermi motion of the target nucleon and the Pauli blocking effect. The Fermi motion will be is described in Subsection 7.2.6. The Pauli blocking effect is considered as follows: if outgoing nucleon's momentum  $p_{nuc}$  is larger than the Fermi surface momentum  $P_f$ , quasi elastic scattering is allowed, but if not, the scattering is forbidden. We adopt  $P_f = 217 \text{ MeV}/c$  from Ref. [144].

NC elastic cross sections are calculated by multiplying factors to CC quasi elastic scattering

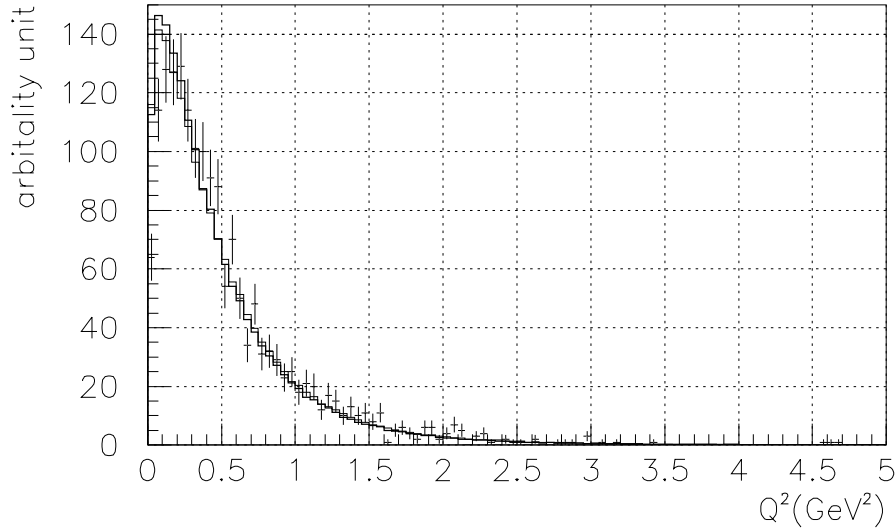


Figure 7.1: Differential cross section  $d\sigma/dq^2$  for  $\nu_\mu + n \rightarrow \mu^- + p$  interaction. Solid line is our calculation and points show experimental data from BNL bubble chamber experiment [102].

cross sections:

$$\sigma(\nu p \rightarrow \nu p) = 0.153 \times \sigma(\nu n \rightarrow e^- p) \quad (7.7)$$

$$\sigma(\bar{\nu} p \rightarrow \bar{\nu} p) = 0.218 \times \sigma(\bar{\nu} p \rightarrow e^+ n) \quad (7.8)$$

$$\sigma(\nu n \rightarrow \nu n) = 1.5 \times \sigma(\nu p \rightarrow \nu p) \quad (7.9)$$

$$\sigma(\bar{\nu} n \rightarrow \bar{\nu} n) = 1.0 \times \sigma(\bar{\nu} p \rightarrow \bar{\nu} p) \quad (7.10)$$

These numerical factors are taken from Ref. [108, 109].

### 7.2.3 Single meson productions via baryon resonances ( $\nu + N \rightarrow l(\nu) + N' + \text{meson}$ )

The single-meson productions via resonances are the dominant hadron production processes in the region where the invariant mass of the hadron system ( $W$ ) is less than about  $2.0 \text{ GeV}/c^2$ .

We simulate the single-meson productions via resonances based on Rein and Sehgal's theory [110]. The Rein & Sehgal's theory was originally developed for single-pion productions, but we extended their methods in order to include  $\eta$  and  $K$  meson productions.

In this theory, single-meson production is considered in 2 steps:

$$\text{Resonance production} \quad \nu + N \rightarrow l(\nu) + N^*$$

$$\text{Resonance decay} \quad N^* \rightarrow N' + \pi(\eta, K)$$

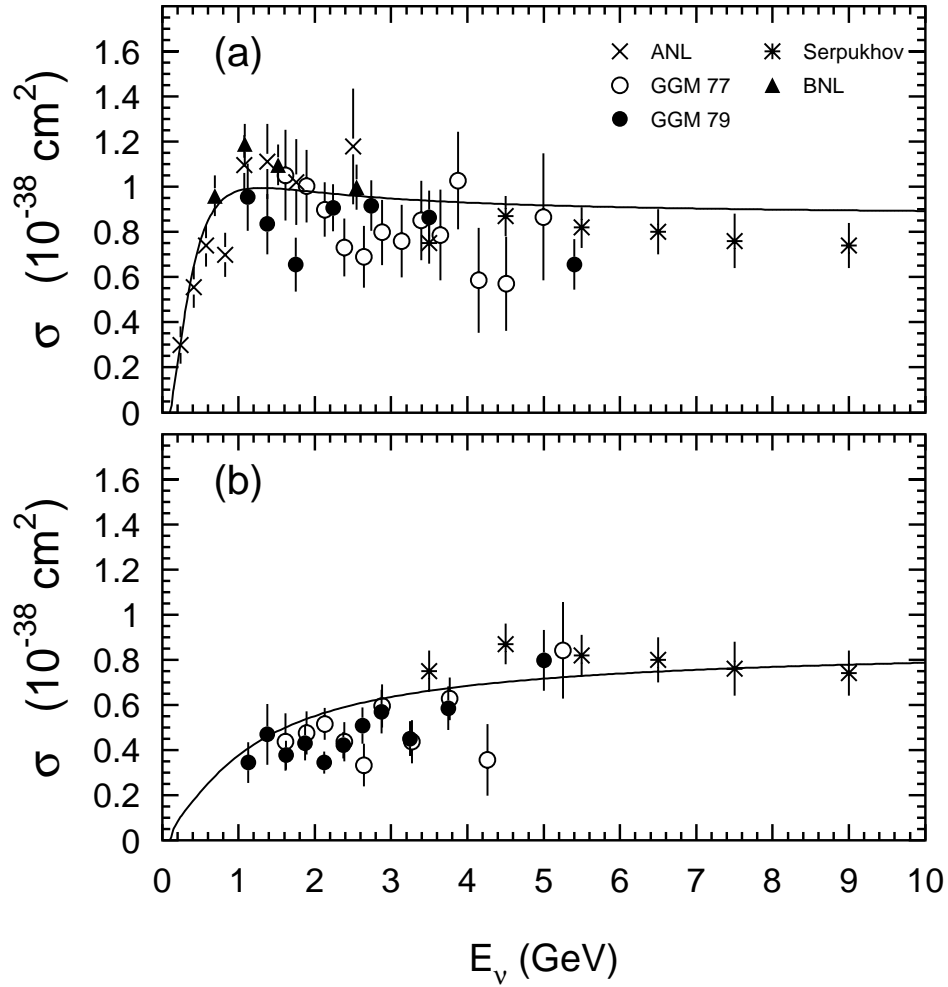


Figure 7.2: Cross section for (a)  $\nu_\mu + n \rightarrow \mu^- + p$  interaction and (b)  $\bar{\nu}_\mu + p \rightarrow \mu^+ + n$  interaction. Solid lines show our calculation and points show experimental data from ANL 12' [103], Gargamelle [104, 105], BNL 7' [106] bubble chambers and a spark chamber experiment at Serpukhov [107].

where  $N^*$  is a baryon resonance,  $N$  and  $N'$  are nucleons, and  $l$  is a outgoing lepton. The amplitude of a baryon excitation is described as:

$$T(\nu N \rightarrow l N^*) = \frac{G_F}{\sqrt{2}} \bar{u}_l \gamma^\mu (1 - \gamma_5) u_\nu \langle N^* | J_\mu^h | N \rangle \quad (7.11)$$

where  $\langle N^* | J_\mu^h | N \rangle$  is the weak hadron current for this process. The matrix element of the hadron current is calculated by the FKR(Feynman,Kislinger,Ravndal) baryon model [111], which describes the baryon as a relativistic 3-body system. The amplitude of the resonance decay,  $\langle N \pi | N^* \rangle$ , is expressed by Breit-Wigner formula with experimentally measured decay width and branching ratio of each resonance [19]. These interactions are characterized by  $q^2$  and  $W$ , and the differential cross section is written as:

$$\frac{d^2\sigma}{dq^2 dW} = \frac{1}{32\pi M E_\nu^2} \cdot \frac{1}{2} \left| \sum_{j,spin} T(\nu N \rightarrow l N_j^*) \cdot \sqrt{\chi_E} \cdot \left( sign(N_j) \sqrt{\frac{\Gamma_j}{2\pi}} \cdot \frac{1}{W - M_j + i\frac{\Gamma_j}{2}} \right) \right|^2 \quad (7.12)$$

where

- $N_j^*$  : j's baryon resonance
- $E_\nu$  : Neutrino energy
- $\chi_E$  : Branching ratio of  $N_j^*$  to  $N' + \text{meson}$
- $M_j$  :  $N_j^*$ 's mass
- $\Gamma_j$  : the total decay width of  $N_j^*$
- $sign(N_j)$  : sign of the decay amplitude of  $N_j^*$

The  $sign(N_j)^*$  is a sign of the decay amplitude of  $N_j^*$  which is lost in the experimentally measured decay width. This factor is calculated by the FKR model, and added to the decay amplitude in order to consider the interference effects of the neighboring resonances correctly. Summation in Eq.(7.12) is over all relevant resonances and their spin. In our simulation, a region where  $W < 2.0 \text{ GeV}/c^2$  is covered and 18 resonances ( $\Delta(1232)$ ,  $N^*(1440)$ , etc.) are taken into account. The interferences of the resonances are correctly considered in Eq.(7.12).

Figs. 7.3, 7.4, and 7.5 show the calculated cross sections for single pion productions compared with the experimental data. Our calculations well reproduce the data. Figs. 7.3 (a') is the integrated cross section for  $\nu_\mu + p \rightarrow \mu^- + \Delta^{++}(1232)$  interaction ( $\nu_\mu + p \rightarrow \mu^- + p + \pi^+$  with  $W < 1.4 \text{ GeV}/c^2$  cut). This process is a dominant channel for  $\nu_\mu + p \rightarrow \mu^- + p + \pi^+$  interaction, and our calculation well reproduces the data. Fig. 7.6 shows the differential cross section for  $\nu_\mu + p \rightarrow \mu^- + \Delta^{++}(1232)$  interaction. Again our calculation well reproduces the  $q^2$  dependence of the cross section of the data.

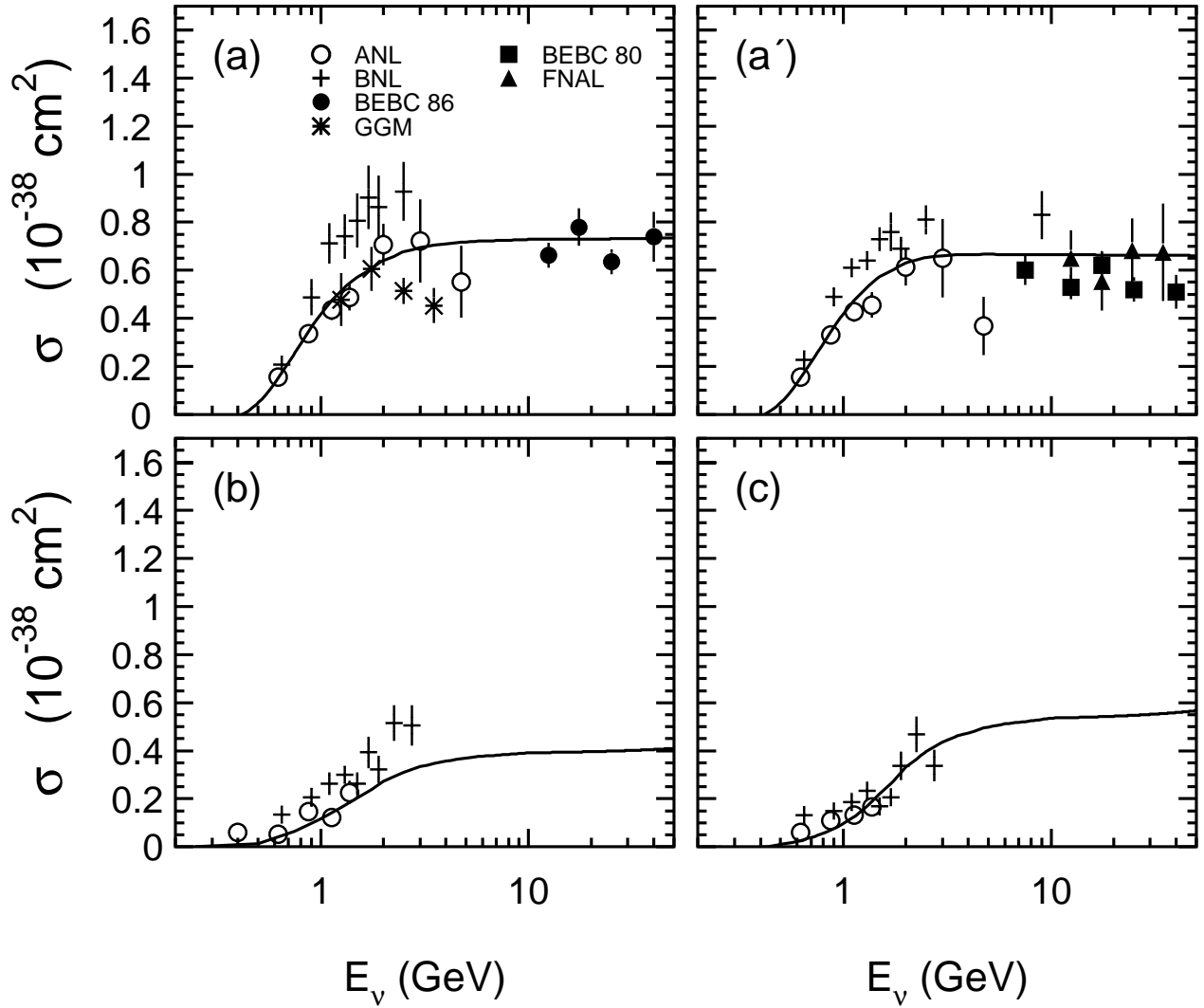


Figure 7.3: Total cross sections for CC  $\nu_\mu$  single pion productions. (a)  $\nu_\mu + p \rightarrow \mu^- + p + \pi^+$  (a')  $\nu_\mu + p \rightarrow \mu^- + \Delta^{++}$  ( $\nu_\mu + p \rightarrow \mu^- + p + \pi^+$  with  $W < 1.4 \text{ GeV}/c^2$  cut) (b)  $\nu_\mu + n \rightarrow \mu^- + p + \pi^0$  (c)  $\nu_\mu + n \rightarrow \mu^- + n + \pi^+$ . Solid lines show the calculations used in our MC simulation, and points show the experimental data taken from bubble chamber experiments: ANL [113], BNL [114], BEBC [115, 116], Gargamelle [117], FNAL [118].

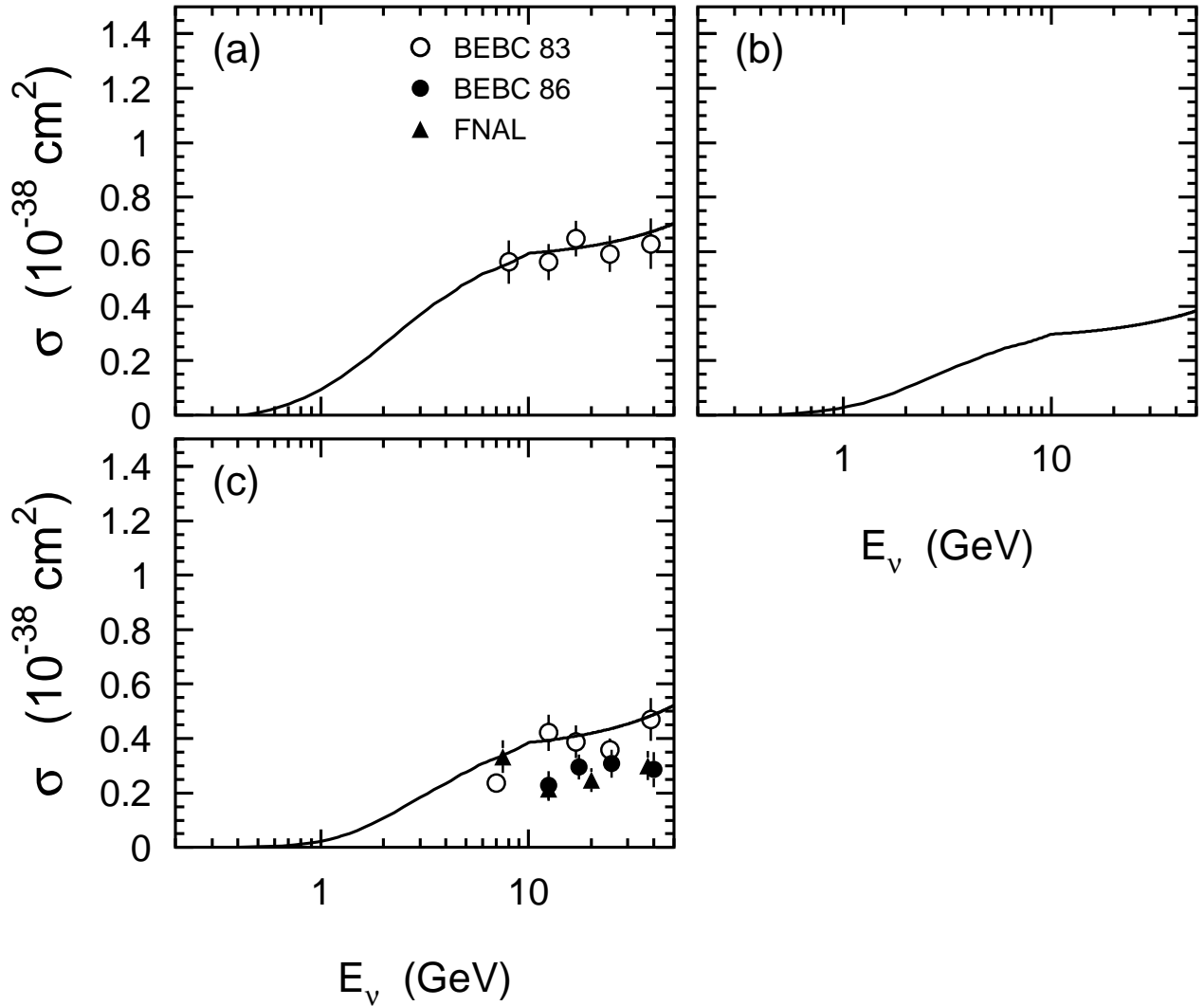


Figure 7.4: Cross sections for CC  $\bar{\nu}_\mu$  single pion productions. (a)  $\bar{\nu}_\mu + n \rightarrow \mu^+ + n + \pi^-$  (b)  $\bar{\nu}_\mu + p \rightarrow \mu^+ + n + \pi^0$  (c)  $\bar{\nu}_\mu + p \rightarrow \mu^+ + p + \pi^-$ . Solid lines show the calculations used in our MC simulation, and points show the experimental data taken from bubble chamber experiments: BEBC [119, 115], FNAL [120].

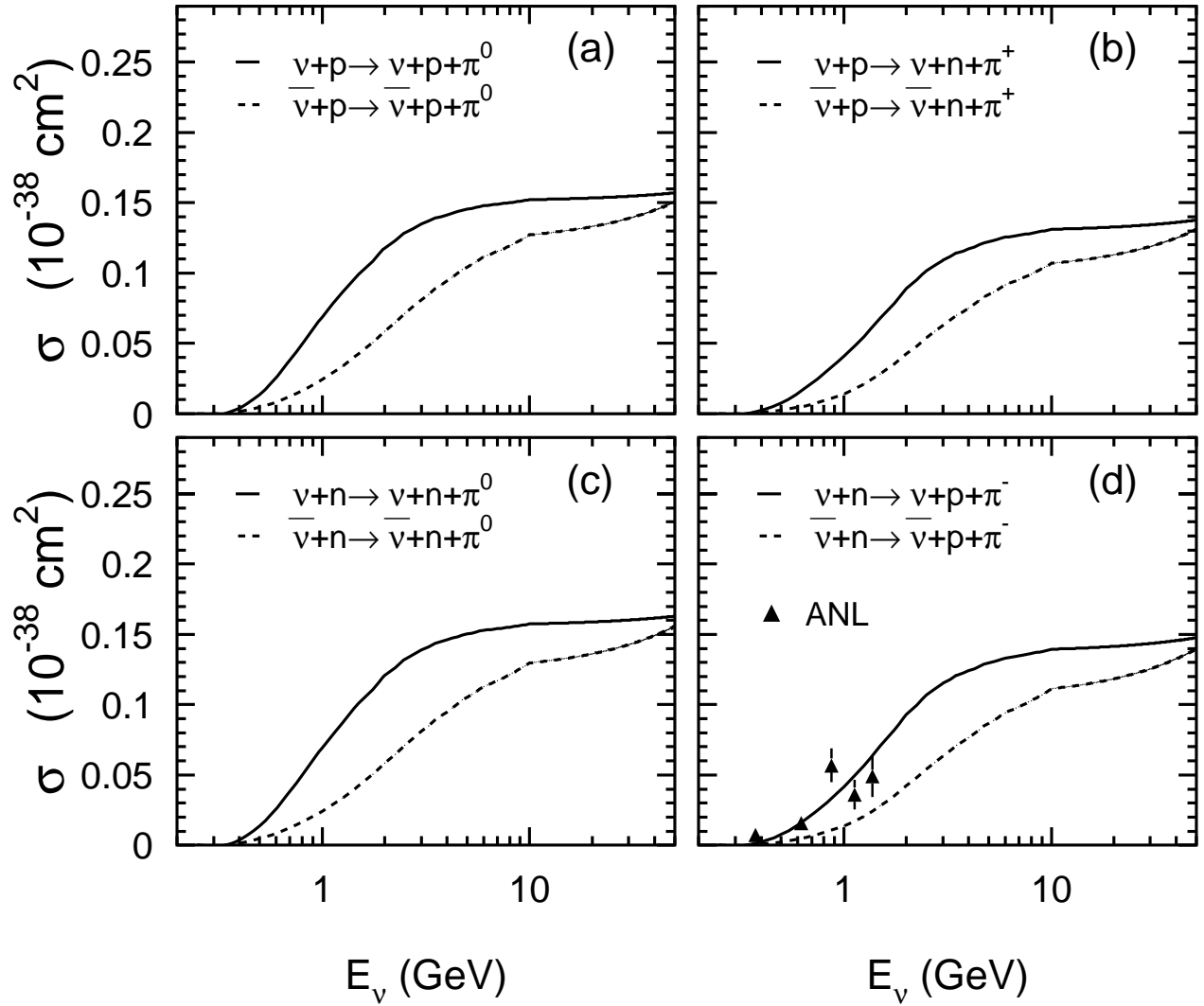


Figure 7.5: Cross sections for NC  $\nu_\mu$  and  $\bar{\nu}_\mu$  single pion productions. Solid(Broken) lines show the calculated cross sections for  $\nu_\mu(\bar{\nu}_\mu)$  interactions, and points show the experimental data taken from ANL [121].

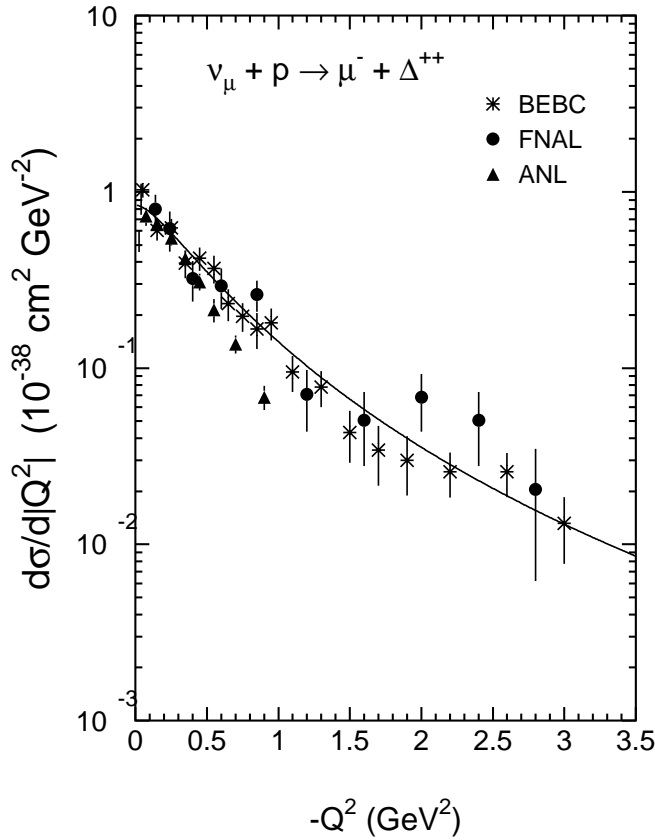


Figure 7.6:  $d\sigma/dq^2$  distribution for  $\nu_\mu + p \rightarrow \mu^- + \Delta^{++}$  interaction ( $\nu_\mu + p \rightarrow \mu^- + p + \pi^+$  interaction with  $W < 1.4$   $\text{GeV}/c^2$  cut). Solid line shows our calculation with  $E_\nu = 20$   $\text{GeV}$ , and points show the data taken from ANL [113], BEBC [116], FNAL [118].

In the Rein and Sehgal's methods, the final kinematics of the hadron system is determined so that the effects of the polarization of the produced resonances and the interference are properly considered. In our simulation, we employ their detailed methods only for  $\Delta(1232)$ , and we simply assume that the mesons are emitted isotropically in resonance rest frame for other resonances.

It is known that a baryon resonance in a nucleus can disappear without meson emissions via the following interaction:

$$N^* + N \rightarrow N' + N'' \quad (7.13)$$

where  $N^*$  is a baryon resonance, and  $N, N', N''$  are nucleons. The rate of the interactions are estimated from theoretical calculation [112]. We assume that 20% of resonances in  $^{16}\text{O}$  disappear without meson emissions.

Fermi momentum of nucleons are considered as in the quasi elastic interaction case. The Pauli blocking effect on the nucleon from the baryon resonances decay is also taken into account.

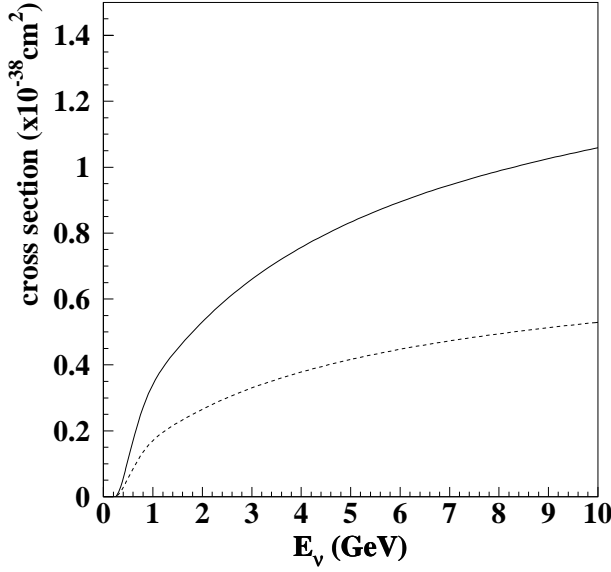


Figure 7.7: Cross section of coherent pion production. Solid(Broken) line is for CC(NC) interaction.

#### 7.2.4 Coherent pion production off $^{16}\text{O}$ ( $\nu + ^{16}\text{O} \rightarrow l(\nu) + ^{16}\text{O} + \pi$ )

Coherent pion production is a neutrino interaction with a nucleus as a whole. Differential cross section of coherent pion production is calculated by Rein & Sehgal [123]:

$$\begin{aligned} \frac{d^3\sigma}{dx dy d|t|} &= \frac{G_F^2 M}{2\pi^2} f_\pi^2 A^2 E_\nu (1-y) \frac{1}{16\pi} \left[ \sigma_{tot}^{\pi^0 N}(E_\nu y) \right]^2 \left( 1 + \left( \frac{\text{Re}(f_{\pi N}(0))}{\text{Im}(f_{\pi N}(0))} \right)^2 \right) \\ &\times \left( \frac{M_A^2}{M_A^2 + Q^2} \right)^2 \exp\left(-\frac{1}{3} R^{2/3} |t|\right) F_{abs} \end{aligned} \quad (7.14)$$

where  $x$  and  $y$  are the Bjorken parameters,  $t$  is a square of 3-momentum transfer,  $f_\pi$  is pion decay constant ( $=0.93m_\pi$ ),  $f_{\pi N}$  is the pion-nucleon scattering amplitude,  $A$  is the atomic number of oxygen ( $=16$ ),  $M_A$  is axial vector mass,  $M$  is the nucleon mass,  $R$  is the radius of oxygen nucleus,  $\sigma_{tot}^{\pi^0 N}$  is the averaged cross section of pion-nucleon scattering,  $F_{abs}$  is a  $t$ -independent factor representing the effect of pion absorption in the nucleus, respectively.

Fig. 7.7 shows the calculated cross section for coherent pion production.

#### 7.2.5 Deep inelastic scattering ( $\nu + N \rightarrow l(\nu) + N' + \text{hadrons}$ )

The differential cross section for the deep inelastic scattering is described as follows [124]:

$$\begin{aligned} \frac{d^2\sigma^{\nu(\bar{\nu})}}{dx dy} &= \frac{G_F^2 M E_\nu}{\pi} \left( \left( 1 - y + \frac{y^2}{2} + C_1 \right) F_2(x, q^2) \pm y \left( 1 - \frac{y}{2} + C_2 \right) (x F_3(x, q^2)) \right), \\ C_1 &= \frac{ym^2}{4ME_\nu x} - \frac{xyM}{2E_\nu} - \frac{m^2}{4E_\nu^2} - \frac{m^2}{2ME_\nu x}, \\ C_2 &= -\frac{m^2}{4ME_\nu x} \end{aligned} \quad (7.15)$$

where  $x, y$  are Bjorken parameters,  $F_2(q^2, x)$  and  $xF_3(q^2, x)$  are the nucleon structure functions,  $M$  and  $m$  are the target nucleon mass and the outgoing lepton mass, respectively. We adopt GRV94 parton distribution function [125, 126] for the calculation of  $F_2$  and  $xF_3$ .

In order to keep the consistency with the other interaction modes, we consider this interaction in the region where  $W > 1.3 \text{ GeV}/c^2$ , and we require that the number of produced pions via the deep inelastic scattering should be greater than 1 for a region  $1.3 \text{ GeV}/c^2 < W < 2.0 \text{ GeV}/c^2$ .

The final kinematics of the hadron system is obtained in 2 different ways. For a region where  $1.3 \text{ GeV}/c^2 < W < 2.0 \text{ GeV}/c^2$ , the produced mesons are assumed to be pions. We determine the pion multiplicity from the measured charged pion multiplicity by FNL 7-foot hydrogen bubble chamber experiment [131]:

$$\langle n_{\pi^\pm} \rangle = (0.06 \pm 0.06) + (1.22 \pm 0.03) \ln(W^2) \quad (7.16)$$

where  $\langle n_{\pi^\pm} \rangle$  is the mean multiplicity of charged pions. Assuming  $\langle n_{\pi^+} \rangle = \langle n_{\pi^-} \rangle = \langle n_{\pi^0} \rangle$ , the mean multiplicity of pion  $\langle n_\pi \rangle$  is described as:

$$\langle n_\pi \rangle = 0.09 + 1.83 \ln(W^2) \quad (7.17)$$

For individual Monte Carlo events, the pion multiplicity are determined using KNO(Koba-Nielsen-Olesen) scaling which describes the pion multiplicity distribution with the mean multiplicity  $\langle n_\pi \rangle$ . We also consider the forward-backward asymmetry of pion multiplicity ( $n_\pi^F/n_\pi^B$ ) in the hadronic center of the mass system [127]:

$$\frac{n_\pi^F}{n_\pi^B} = \frac{0.35 + 0.41 \ln(W^2)}{0.5 + 0.09 \ln(W^2)} \quad (7.18)$$

where forward means the direction of the hadronic system in the laboratory frame.

For a region where  $W > 2.0 \text{ GeV}/c^2$ , final kinematics of hadrons is determined by JETSET 7.4 package [130] which is commonly used in high energy physics. The package considers other particles productions than pions ( $K, \eta, \rho$ , etc.).

For NC deep inelastic scattering, differential cross sections are calculated by multiplying the factors to CC cross sections estimated from experimental results shown in Ref. [128, 129]:

$$\frac{\sigma(\nu N \rightarrow \nu X)}{\sigma(\nu N \rightarrow \mu^- X)} = \begin{cases} 0.26 & (E_\nu \leq 3\text{GeV}) \\ 0.26 + 0.04 \times \frac{E_\nu - 3}{3} & (3 < E_\nu < 6\text{GeV}) \\ 0.30 & (E_\nu \geq 6\text{GeV}) \end{cases} \quad (7.19)$$

$$\frac{\sigma(\bar{\nu} N \rightarrow \bar{\nu} X)}{\sigma(\bar{\nu} N \rightarrow \mu^+ X)} = \begin{cases} 0.39 & (E_\nu \leq 3\text{GeV}) \\ 0.39 - 0.02 \times \frac{E_\nu - 3}{3} & (3 < E_\nu < 6\text{GeV}) \\ 0.37 & (E_\nu \geq 6\text{GeV}) \end{cases} \quad (7.20)$$

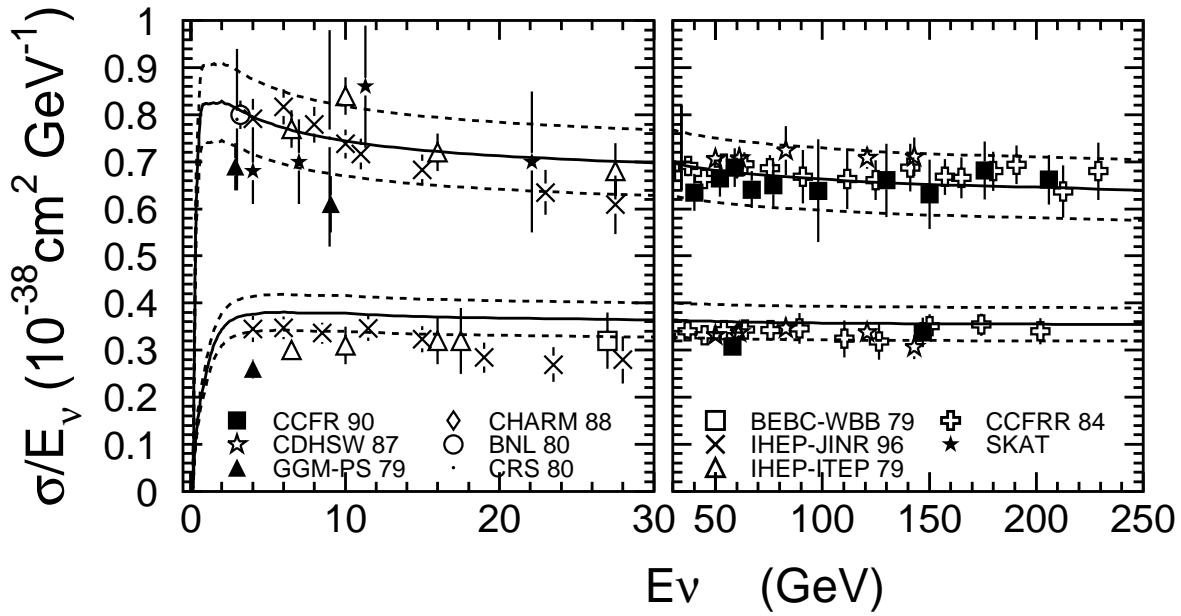


Figure 7.8: Cross sections for CC inclusive interactions on iso-scalar target for (a)  $\nu_\mu + N \rightarrow \mu^- + X$ , and (b)  $\bar{\nu}_\mu + N \rightarrow \mu^+ + X$ . Solid lines are the sum of the cross sections of all interaction modes described in the text, and dashed lines show  $\pm 10\%$  scaled lines. Points show experimental data from CCFR [132], CDHSW [133], Gargamelle [134, 135], CHARM [136], BNL [137], CRS [138], BEBC-WWB [139], IHEP-JINR [140], IHEP-ITEP [141], CCFRR [142], SKAT [143].

Fig. 7.8 shows the total cross section as a function of neutrino energy compared with experimental data. The total cross section is calculated as  $\sigma(\text{Q.E.}) + \sigma(\text{Single meson}) + \sigma(\text{coherent } \pi) + \sigma(\text{DIS})$ . The experimental data are the cross sections of the inclusive neutrino and antineutrino interactions  $\nu_\mu(\bar{\nu}_\mu) + N \rightarrow \mu^\pm + X$  taken from Ref. [132, 133, 134, 135, 136, 137, 138, 139, 140, 141, 142, 143].

### 7.2.6 Fermi motion of a nucleon

A nucleon bound in a nucleus has a non-zero momentum (Fermi momentum). We use the Fermi momentum distribution in  $^{16}\text{O}$  which was estimated from electron scattering experiment on  $^{12}\text{C}$  target [144], taking into account that 4 nucleons (2 protons and 2 neutrons) are in the 1S state and the other 12 nucleons are in the 1P state. The distributions of the Fermi momentum are shown in Figure 7.9.

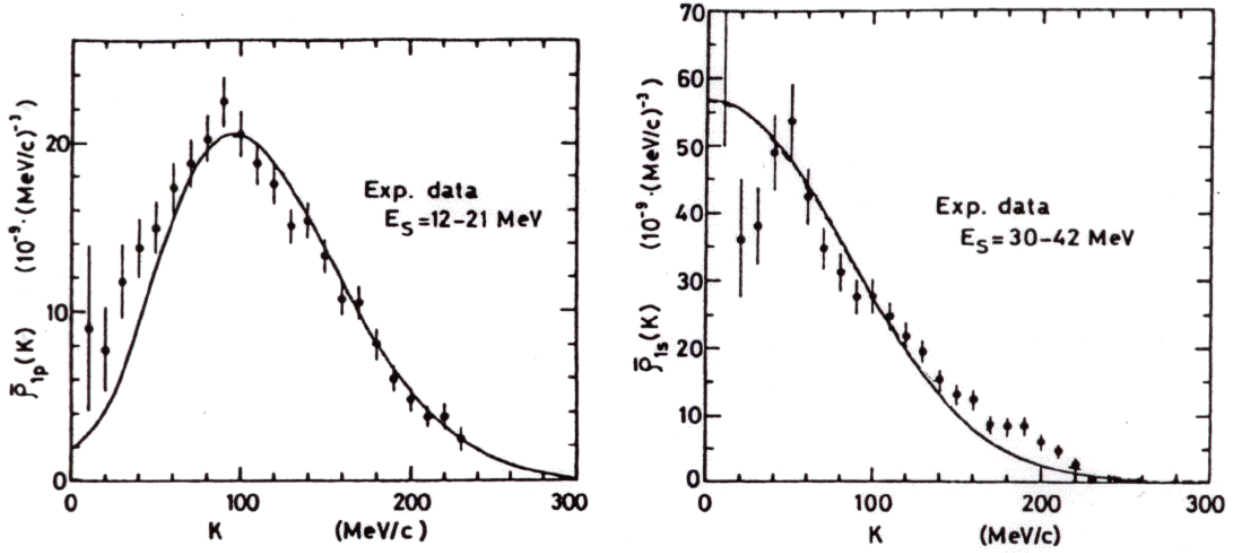


Figure 7.9: Fermi momentum distributions for P-state(left figure) and S-state(right figure). The points show experimental data measured by  $^{12}\text{C}(e^-, e^-)$  experiment [144] and the lines show the theoretical calculation [144]. We use the calculated distributions in the simulation.

### 7.2.7 Nuclear effects

Particles produced in  $^{16}\text{O}$  undergo secondary interactions before leaving the nucleus. We consider the interactions of mesons ( $\pi$ ,  $K$ ,  $\eta$ ) in a  $^{16}\text{O}$  nucleus in our simulation. The interactions of leptons and nucleons are not considered in our simulation. Nuclear effects for each meson are as follows.

#### 1. $\pi^\pm, \pi^0$

Inelastic scattering, charge exchange, and absorption are considered. The cross section of each interaction is calculated by the model of L.Salcedo *et al.*[145]. The momentum and angular distribution of the scattered pions are determined from the results of the phase shift analysis using the experimental results on  $\pi$ - $N$  scattering [146]. The nucleon density in  $^{16}\text{O}$  is taken to be the Wood-Saxon form:

$$\rho(r) = \frac{Z}{A} \rho_0 \frac{1}{1 + \exp(\frac{r-c}{a})} \quad (7.21)$$

where  $r$  is the distance from the center of  $^{16}\text{O}$ . We choose  $\rho_0 = 0.48 m_\pi^3$ ,  $a = 0.41$  fm,  $c = 2.69$  fm,  $Z = 8$ , and  $A = 16$  for  $^{16}\text{O}$ .

We consider the Pauli blocking effects in  $\pi - N$  scattering in  $^{16}\text{O}$ . The Fermi surface momentum of nucleons  $P_f(r)$  is calculated assuming a Fermi gas model using the nucleon density

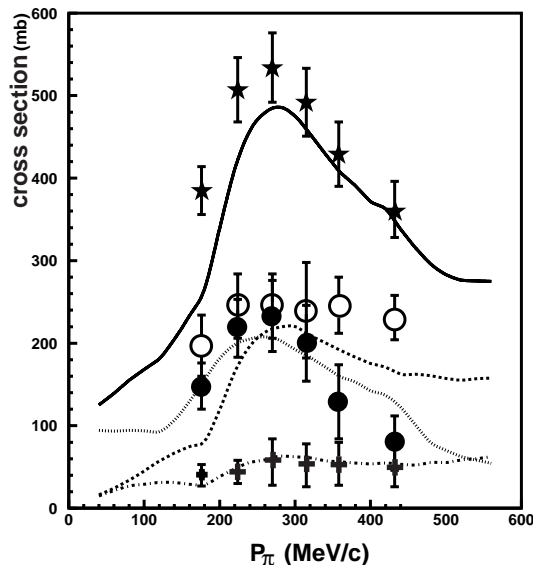


Figure 7.10: The calculated cross sections of  $\pi-^{16}\text{O}$  interaction compared with the experimental data [149]. The lines show the calculated cross sections. The stars (solid line) shows the total cross section, the white circles (broken line) show the inelastic scattering cross section the black circles (dashed line) show the absorption cross section, and the crosses (dashed dotted line) show the charge exchanges cross section, respectively.

function:

$$P_f(r) = \left( \frac{3}{2} \pi^2 \rho(r) \right)^{\frac{1}{3}} \quad (7.22)$$

To check the validity of our calculation, several simulation results are compared with experimental data. Figs. 7.10 and 7.11 show the calculated  $\pi-^{16}\text{O}$  scattering cross section compared with the experimental results [149, 150]. Fig 7.12 shows the photo-production cross section for calculation and experimental results [151, 152]. Our calculation well reproduces the data.

## 2. $K^\pm, K^0, \overline{K}^0$

Elastic scattering and charge exchange are considered. The cross sections of the interactions are based on the measured  $K^\pm N$  scattering data from Ref. [19]. The cross sections for  $K^0$  and  $\overline{K}^0$  are obtained from  $K^\pm N$  results assuming the isospin symmetry.

## 3. $\eta$

Interactions via baryon resonances  $\eta + N \rightarrow N^* \rightarrow N + X$  are considered, where  $X$  is either  $\eta$ ,  $\pi$ , or  $\pi\pi$ .  $N(1535)$  and  $N(1650)$  are the relevant resonances concerning about  $\eta$  interactions [19]. Cross section is given by Breit Wigner formula:

$$\sigma(k) = \frac{\pi}{k^2} \frac{\Gamma_{\eta N} \Gamma_X}{(W - M_{N^*})^2 + \Gamma_{tot}^2/4} \quad (7.23)$$

where  $W$  and  $M_{N^*}$  are the invariant mass of the hadron system and the mass of the resonance,  $k$  is the momentum of  $\eta$  in  $N\eta$  CMS,  $\Gamma_{\eta N}$  is the partial decay width of  $N^* \rightarrow \eta + N$ ,  $\Gamma_{tot}$  is the total width of  $N^*$ ,  $\Gamma_X$  is the partial width to the final state  $X$  described above, respectively. The direction of the scattered  $\eta$  meson is assumed to be isotropic in the resonance rest frame.

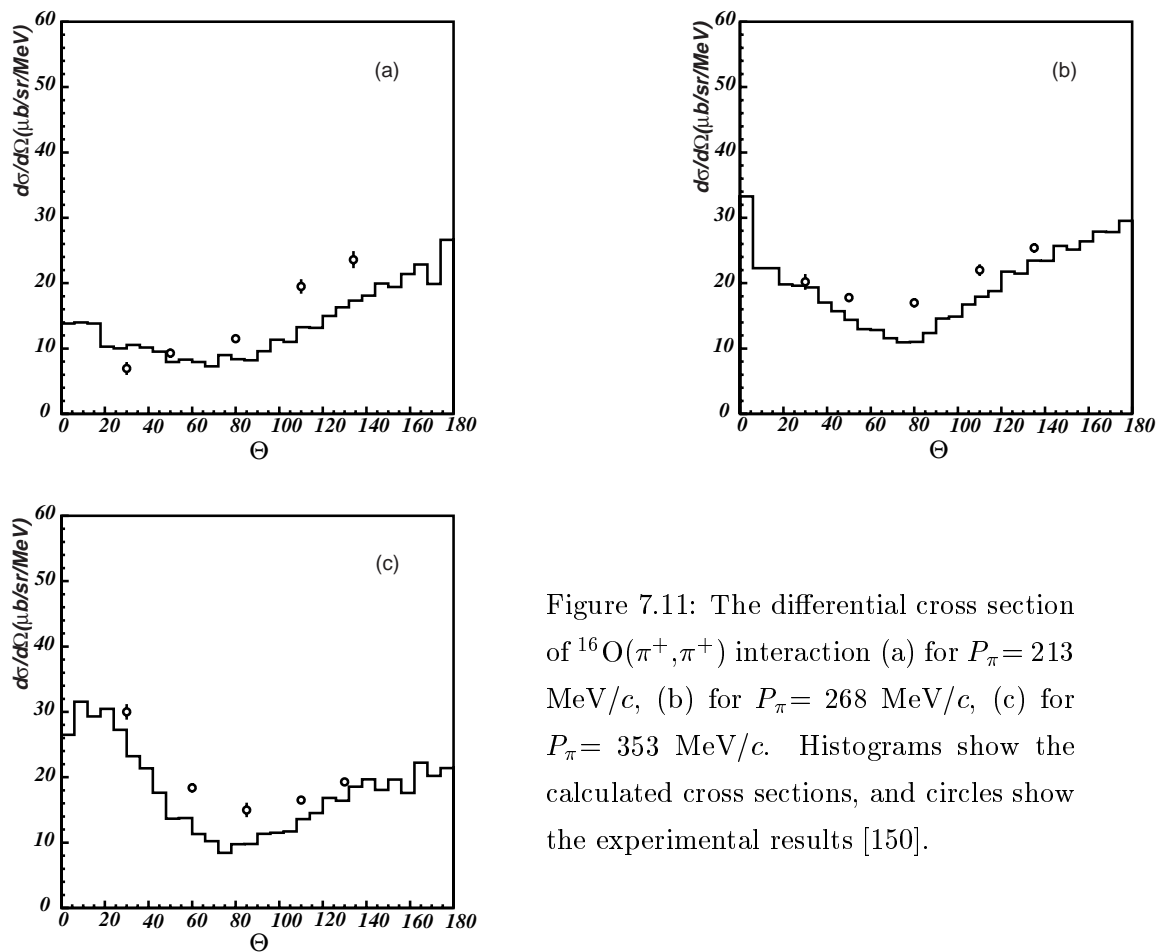


Figure 7.11: The differential cross section of  $^{16}\text{O}(\pi^+, \pi^+)$  interaction (a) for  $P_\pi = 213$  MeV/c, (b) for  $P_\pi = 268$  MeV/c, (c) for  $P_\pi = 353$  MeV/c. Histograms show the calculated cross sections, and circles show the experimental results [150].

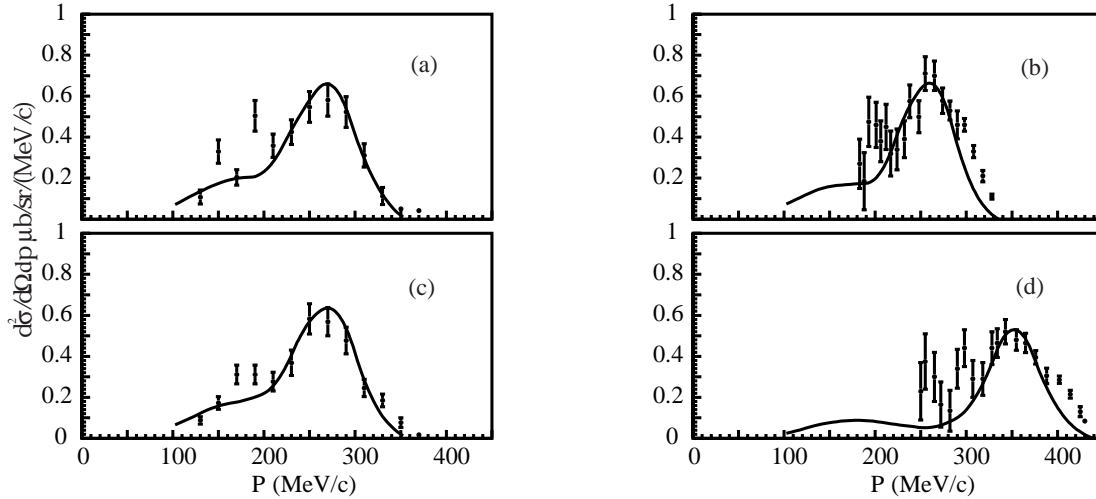


Figure 7.12: The differential cross section for pion photo-productions as a function of the produced pion momentum. Solid lines show the calculated cross sections, and dots show the experimental results for  $\gamma + {}^{12}\text{C} \rightarrow \pi^- + X$  (a) with  $E_\gamma = 391\text{MeV}$  ( $\theta_{\gamma\pi} = 52^\circ$ ), (b) with  $E_\gamma = 368\text{MeV}$  ( $\theta_{\gamma\pi} = 44.2^\circ$  [151]), and for  $\gamma + {}^{12}\text{C} \rightarrow \pi^+ + X'$  (c) with  $E_\gamma = 391\text{MeV}$  ( $\theta_{\gamma\pi} = 52^\circ$ ), (d) with  $E_\gamma = 468\text{MeV}$  ( $\theta_{\gamma\pi} = 44.2^\circ$ ) [152].

## 7.3 Detector simulation

We simulate the propagation of the particles produced by a neutrino interaction in the detector. This simulation program can be divided into 3 parts.

- Propagation of the particles in water and Cherenkov radiations
- Propagation of the Cherenkov photons
- Detection of Cherenkov photons (including the response of ADC and TDC)

### 7.3.1 Propagation of Particles

Propagations and interactions of charged leptons ( $e^\pm, \mu^\pm$ ), hadrons ( $p, n, \pi^\pm, K$ , etc), and  $\gamma$  are considered in the simulation. The simulation program is developed based on GEANT package [154]. Interactions of the particles considered in the detector simulation are listed in Table 7.1

For the hadronic interactions, we adopt CALOR package [155] which well simulates the hadronic interactions. For low energy pions ( $p_\pi < 500\text{ MeV}/c$ ), we adopt custom made simulation programs [156] which use the measured pion cross sections from a  $\pi$ - ${}^{16}\text{O}$  scattering

Particle	Simulated processes
$e^\pm$	Multiple scattering, Ionization, $\delta$ -ray production, Bremsstrahlung, $e^+$ annihilation, Cherenkov radiation
$\mu^\pm$	Multiple scattering, Ionization, $\delta$ -rays production, Bremsstrahlung, Nuclear interaction, Decay, Cherenkov radiation, $\mu^-$ capture in $^{16}\text{O}$
$\gamma$	$(e^+, e^-)$ pair conversion, Compton scattering, Photoelectron effect
Hadrons	Multiple scattering, Nuclear interaction, Ionization, $\delta$ ray production, Decay, Cherenkov radiation

Table 7.1: List of the interactions considered in our detector simulation

experiment [147] and a  $\pi$ - $p$  scattering experiment [148]. In these custom made programs, we consider elastic scattering, inelastic scattering, absorption, and charge exchange of pions.

### 7.3.2 Cherenkov photon propagation

Cherenkov photons are generated according to Eq.(3.2) and Eq.(3.3). Generated photons propagate in water with a group velocity  $c/n'$ . We consider Rayleigh scattering, Mie scattering and the absorption of the photons in water. Rayleigh scattering is the dominant interaction which is caused by the  $\text{H}_2\text{O}$  molecule. Differential cross section of Rayleigh scattering has a wavelength dependence ( $\sigma \sim \lambda^{-4}$ ), and is larger for shorter wave length photons. Mie scattering is caused by relatively larger particles, and it makes a sharp forward peak and has a complicated wavelength dependence.

We adjust attenuation coefficients of Rayleigh scattering and Mie scattering so that the simulation results reproduce several measurements such as cosmic ray muons data which are described in Section 4.5.

Light reflections on the materials in the detector (PMTs' surface, black sheets, tyvec) is simulated according to the measured reflective coefficient and the angular distribution of the scattered photons.

### 7.3.3 Detection of Cherenkov photon

According to the quantum efficiency shown in Fig. 3.8, we convert the number of photons arrived at the PMT's surface to the number of photoelectrons. The ADC signal for each PMT

is calculated according to the 1 photoelectron distribution shown in Fig. 3.9. Photon arrival timing is simulated by smearing the timing according to the measured timing resolutions shown in Fig. 4.3.



# Chapter 8

## Data Summary

We summarize the atmospheric neutrino events observed in Super-Kamiokande. We have accumulated 1144.4 days of FC and PC data, 1138 days of upward through-going muons, and 1117 days of upward stopping muons. We also generated Monte Carlo simulated events equivalent to 40 live-years. They are processed by the same event-selection and event reconstruction steps as the real events.

### 8.1 Fully Contained Events and Partially Contained Events

Final samples of FC events and PC events are obtained by requiring the following criteria after all reduction steps and reconstruction steps:

- FC sample
  - (1) Visible energy ( $E_{vis}$ ) is greater than 30 MeV
  - (2) Distance of the reconstructed vertex from the nearest PMT wall ( $D_{wall}$ )  $>$  200 cm
  - (3) Number of hit PMTs in the largest OD hit cluster  $<$ 10
  - (4)  $p_{\mu} >$  200 MeV/ $c$  for 1-ring  $\mu$ -like events, and  $p_e >$  100 MeV/ $c$  for 1-ring  $e$ -like events
  - (5)  $E_{vis} \leq$  1.33 GeV for Sub-GeV sample and  $E_{vis} >$  1.33 GeV for Multi-GeV sample
- PC sample
  - (1)  $D_{wall} >$  200 cm
  - (2) Number of hit PMTs in the largest OD cluster  $\geq$  10

The first criterion for the FC sample eliminates the remaining low energy background events. The second criterion is required in order to keep the qualities of the event reconstruction, and

	Data	Monte Carlo
Sub-GeV		
Single-ring	5037	6023.5
<i>e</i> -like	2542	2402.6
<i>μ</i> -like	2495	3620.9
Multi-ring	1916	2321.5
Multi-GeV		
Single-ring	1036	1294.1
<i>e</i> -like	539	555.4
<i>μ</i> -like	497	738.7
Multi-ring	1162	1470.1
FC Total	9151	11109.2
PC	665	945.1

Table 8.1: Summary of FC and PC data. MC is normalized by the livetime.

to reject the remaining background due to cosmic ray muons, flashing PMTs, neutrons and  $\gamma$ -rays from the rock surrounding the detector. The third criterion requires that there is no clear entrance or exiting point in OD. The fifth criterion divides the FC sample into two energy regions according to the reconstructed visible energy. We call the samples below 1.33 GeV as *Sub-GeV* sample, and above 1.33 GeV as *Multi-GeV* sample. This criterion is mainly required by the historical reasons. Kamiokande used this division in their analysis, and we retain for comparison of the results. The first criterion for PC events is required for the same reason as for FC events, and the second criterion for PC sample requires a clear exiting point in OD. The numbers of events for each sample are summarized in Table 8.1. The numbers of Sub-GeV and Multi-GeV 1-ring *e*-like events agree with the MC prediction, but the numbers of 1-ring *μ*-like and PC events are significantly smaller than the predictions. Table 8.2 shows the fraction of each neutrino interaction channel for FC 1-ring and PC events estimated by the Monte Carlo events. FC 1-ring sample has a high fraction of CC  $\nu_\mu$  and  $\nu_e$  interactions. The fraction of CC  $\nu_\mu(\nu_e)$  interactions in 1-ring *μ*-like(*e*-like) events is estimated to be 95.4%(87.3%) for Sub-GeV and 99.5%(83.5%) for Multi-GeV sample. The lower purity of  $\nu_e$  in the *e*-like events is caused mainly by the backgrounds of NC  $\pi^0$  productions which produces an electromagnetic shower.

		Sub-GeV 1-ring $e$ -like	Sub-GeV 1-ring $\mu$ -like	Multi-GeV 1-ring $e$ -like	Multi-GeV 1-ring $\mu$ -like	PC
CC $\nu_e\bar{\nu}_e$	Q.E.	20147 (65.9%)	115 (0.3%)	2424 (34.2%)	4 (0.04%)	40(0.3%)
	1-meson	5601 (18.3%)	47 (0.1%)	1974 (27.8%)	4 (0.04%)	38(0.3%)
	multi $\pi$	960 (3.1%)	10 (0.02%)	1530 (21.5%)	11 (0.12%)	156(1.29%)
CC $\nu_\mu\bar{\nu}_\mu$	Q.E.	387 (1.3%)	33236 (71.9%)	71 (1.0%)	4318 (45.8%)	1995(16.54%)
	1-meson	385 (1.3%)	9303 (20.1%)	97 (1.4%)	3208 (34.0%)	2739(22.70%)
	multi $\pi$	195 (0.6%)	1566 (3.4%)	347 (4.9%)	1859 (19.7%)	6984(57.89%)
NC	elastic	38 (0.12%)	230 (0.5%)	0 (0.0%)	0 (0.0%)	0(0.0%)
	1-meson	2147 (7.0%)	1079 (2.3%)	119 (1.68%)	1 (0.01%)	5(0.04%)
	multi $\pi$	709 (2.3%)	640 (1.4%)	529 (7.46%)	25 (0.3%)	108(0.9%)
Total		30673	46226	7091	9430	12065

Table 8.2: Summary of the 40-year Monte Carlo events.

### 8.1.1 Vertex Distributions

Figs. 8.1 and 8.2 show the reconstructed vertex distributions for FC 1-ring and PC samples projected to  $Z$  and  $R^2 \equiv (X^2 + Y^2)$  axes. Points show the real data, and histograms show the MC predictions normalized by the livetime. Lines and arrows in these figures show the fiducial volume cut. The vertex distributions of the data and MC agrees well except for the small number of events for FC  $\mu$ -like events and PC events.

Near the PMT wall, the event rate for FC Multi-GeV  $\mu$ -like events decreases, and the event rate for PC events increases. It is because energetic muons produced by neutrino interactions near the wall escape from ID and are identified as PC events.

Peaks near the edge of ID for both the MC and the data in  $R^2$  distributions are caused by the design of the vertex reconstruction programs: the reconstructed vertex positions are restricted within ID, and the events which had the best fit vertex outside the ID were forcedly reconstructed near the wall of ID.

In  $Z$  distribution for FC Multi-GeV  $\mu$ -like data, there is a peak at  $Z = 1810.0$  cm where the upper edge of ID exists. The peak is due to the cosmic ray muons passing through OD inefficient regions. These muons are safely rejected by the fiducial volume cut, and the shape of the vertex distributions of the data and MC agree well in the fiducial volume. The possible sources of the background and their contaminations are described in Section 8.1.4.

### Z Distribution

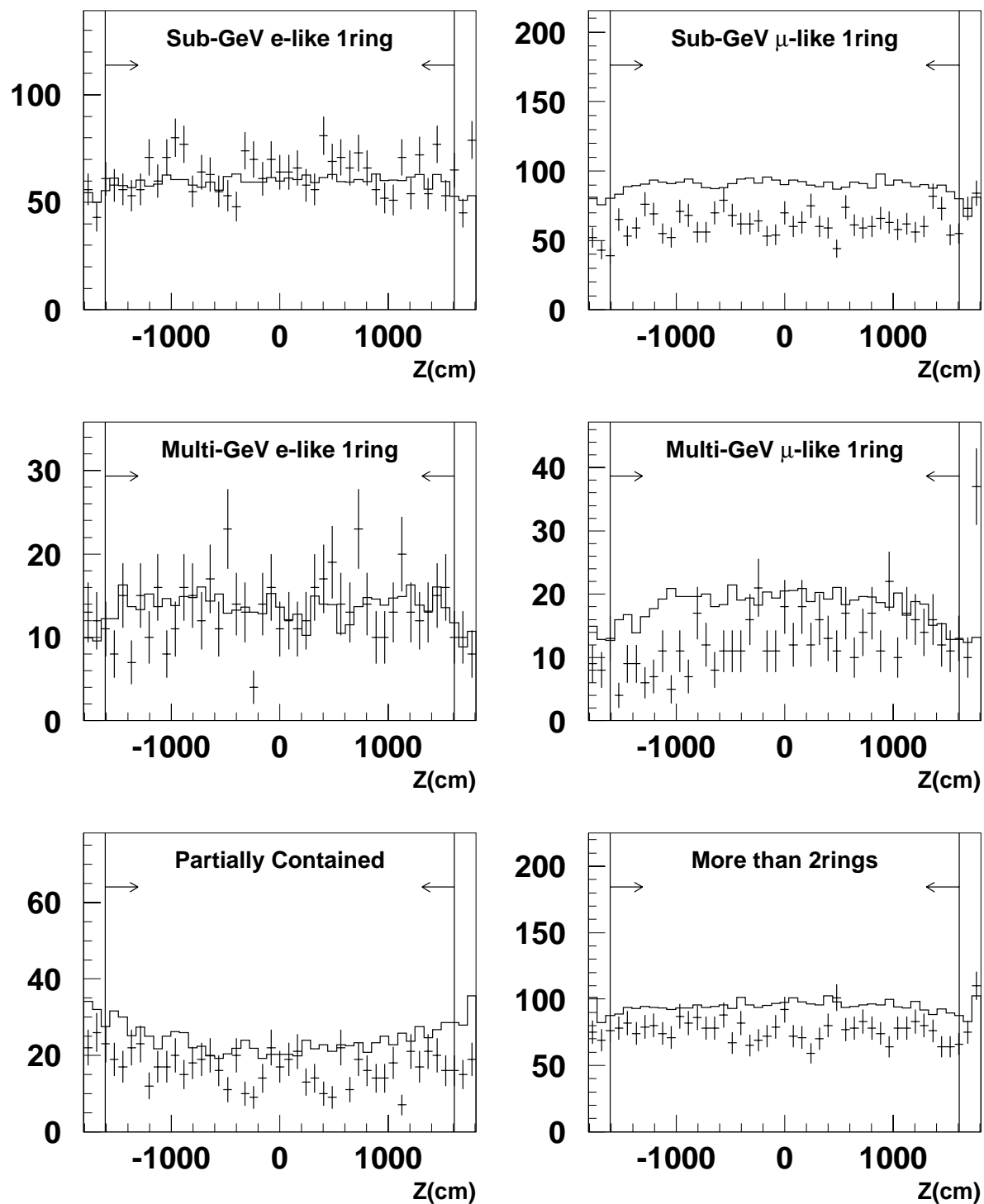


Figure 8.1: Vertex distributions projected to Z axis. Events with  $R < 14.9$  m are plotted. The arrows indicate the fiducial volume.

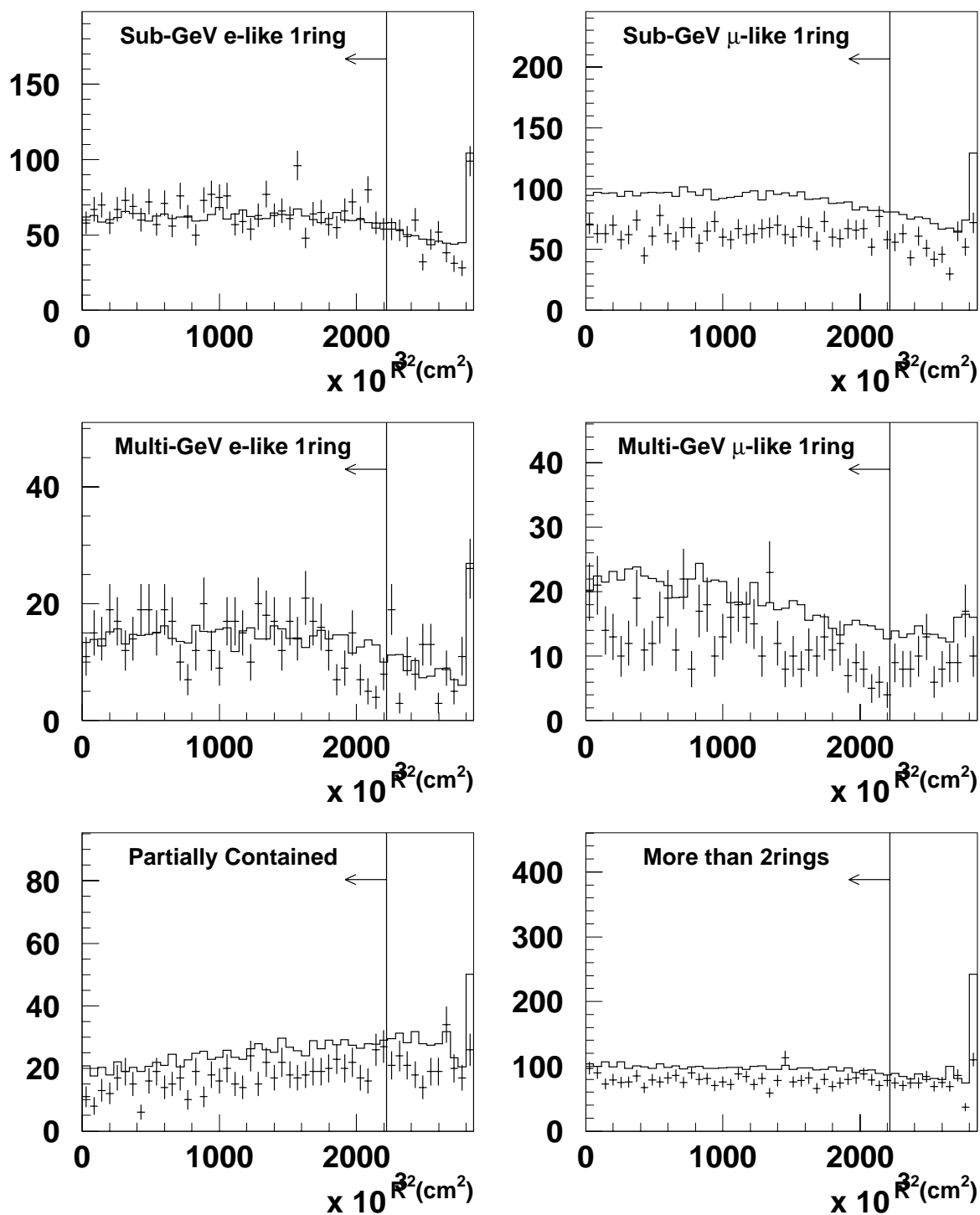
$R^2$  Distribution

Figure 8.2: Vertex distributions projected to the  $R^2$  direction. Events with  $|Z| < 16.1$  m are plotted. The arrows indicate the fiducial volume.

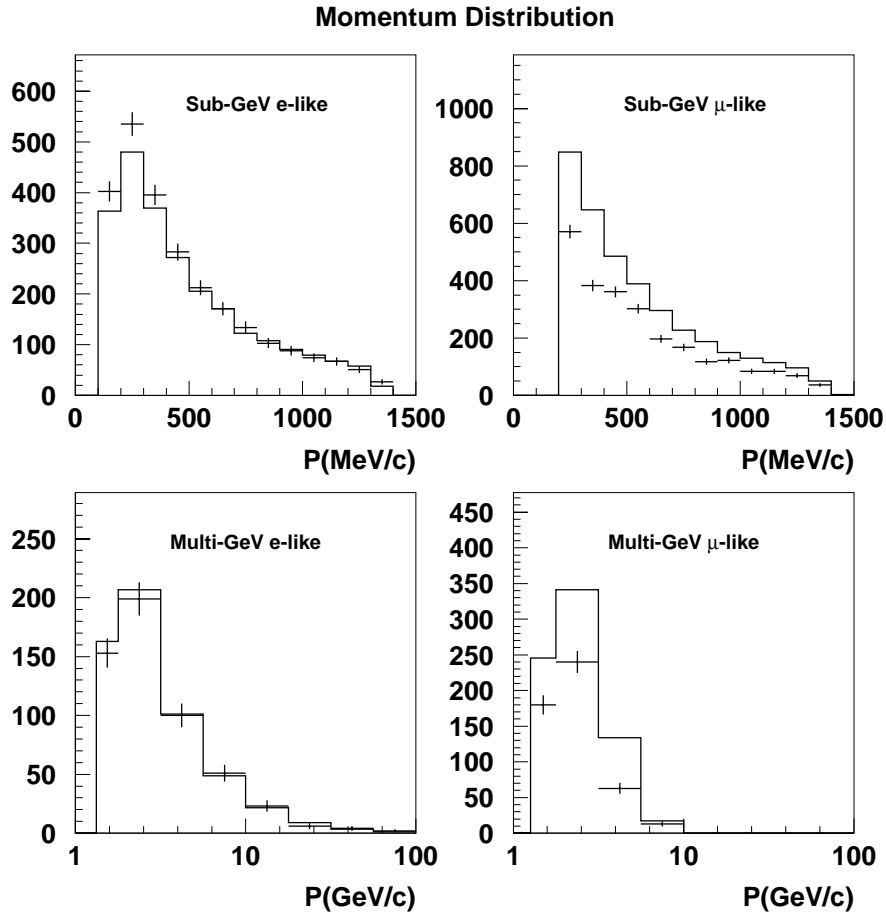


Figure 8.3: Momentum distributions for each sample. Monte Carlo is normalized by the livetime.

### 8.1.2 Momentum Distributions

Reconstructed momentum distributions for FC 1-ring events are shown in Fig. 8.3. The data and MC show a good agreement except for the significantly small numbers of the FC  $\mu$ -like events. Fig. 8.4 shows the  $E_{vis}$  distribution for PC events. The data are lower than the MC prediction, but the shape agrees well.

### 8.1.3 Number of Rings and PID distribution

Fig. 8.5 shows the number of ring distributions for the data and the MC normalized by the livetime. The shape of the distributions for the data agree with the MC predictions, while the absolute number of events is smaller than the MC predictions.

The results of the particle identification is already shown in Fig. 6.10 in Section 6.4. The shape of the distributions are slightly different between the data and MC, but the systematic

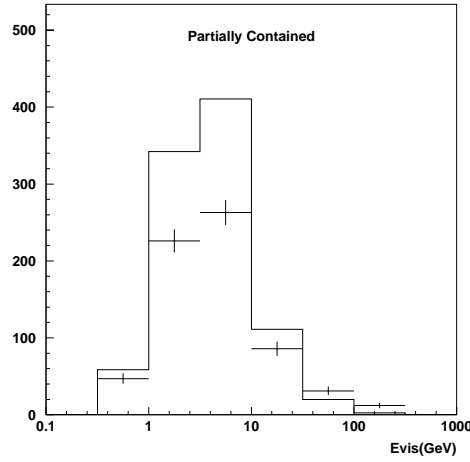


Figure 8.4:  $E_{vis}$  distribution for PC events. MC prediction is normalized by the livetime.

error in the number of  $e$ -like and  $\mu$ -like events is estimated to be small.

#### 8.1.4 Background Estimation

Possible sources of background in Sub-GeV, Multi-GeV and PC samples are as follows:

- Cosmic ray  $\mu$  : for FC  $\mu$ -like and PC events
- Flashing PMT : for FC  $e$ -like events
- Neutron from rock : for FC  $e$ -like events

Background events are effectively rejected by the reduction steps described in Chapter 5 and by the fiducial volume cuts. The contamination of the remaining background for each sample is expected to be small, and the estimated background contaminations are 0.43%, 0.07%, 0.19%, 0.09%, and 0.23% for Sub-GeV  $e$ -like, Sub-GeV  $\mu$ -like, Multi-GeV  $e$ -like, Multi-GeV  $\mu$ -like, and PC events, respectively. The estimated numbers of the background contamination are summarized in Table 8.3.

#### Cosmic Ray Muons

Most of the incoming cosmic ray muons are rejected by using the OD signals, however, some of them pass through the insensitive region of OD and could contaminate to the FC  $\mu$ -like and PC samples.

To estimate the contamination of the cosmic ray muons, we calculate a quantity,  $D_{track}$ , which is defined as the distance of the vertex from the inner detector wall along the particle

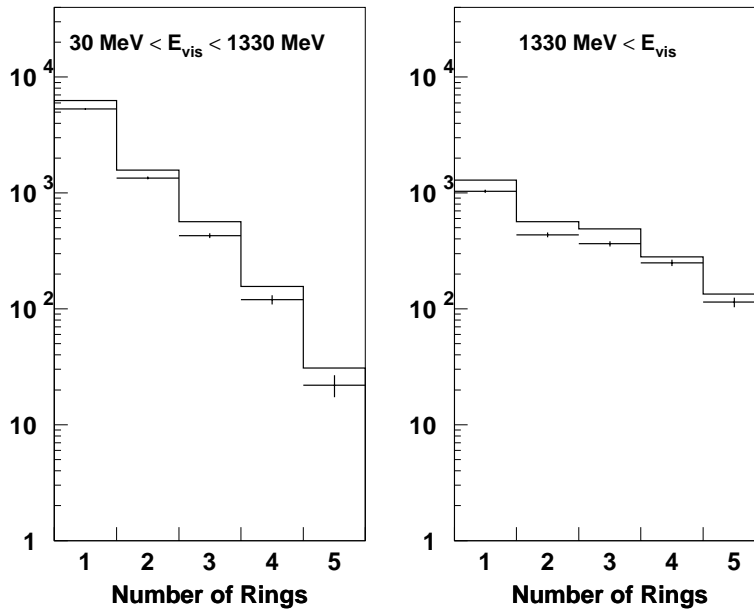
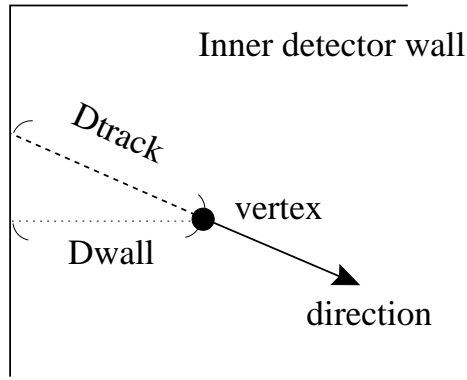


Figure 8.5: The number of ring distributions for Sub-GeV and Multi-GeV energy regions. Points show the data and histograms show the MC predictions which are normalized by the livetime.

	Sub-GeV		Multi-GeV		PC (%)
	<i>e</i> -like(%)	$\mu$ -like(%)	<i>e</i> -like(%)	$\mu$ -like(%)	
Cosmic ray $\mu$	—	0.07	—	0.09	0.23
Flashing PMT	0.42	—	0.16	—	—
Neutron event	0.1	—	0.1	—	—

Table 8.3: Summary of the estimated upper limit of the contamination of the background events for each final samples.

Figure 8.6: Definition of  $D_{wall}$  and  $D_{track}$ .

direction, ( see Fig. 8.6 ). Fig. 8.7 shows the  $D_{track}$  distributions for FC Sub-GeV and Multi-GeV  $\mu$ -like, and PC events before fiducial cuts. Figures in the upper row show the data and the atmospheric neutrino Monte Carlo events. The peak near  $D_{track}=0$  in the data for Multi-GeV  $\mu$ -like is due to the remaining cosmic ray muons. Figures in the middle row show the  $D_{track}$  distributions for cosmic ray muons selected by eye-scannings. They have small  $D_{track}$  values as expected.

We estimated the cosmic ray muon background by comparing the shapes of  $D_{track}$  distributions between the data and atmospheric neutrino MC events plus cosmic ray muons by a  $\chi^2$  test.

Lower figures of Fig. 8.7 show the upper limit of the background events. Shaded histograms are the estimated 90% C.L. upper limit of the cosmic ray muon background. The upper limit of the contamination for each sample before the fiducial volume cut are estimated to be 4.3%, 23.8%, and 3.1% for Sub-GeV  $\mu$ -like, Multi-GeV  $\mu$ -like, and PC events, respectively. After the fiducial volume cuts, contaminations are estimated to be 0.07%, 0.09%, and 0.23% for Sub-GeV  $\mu$ -like, Multi-GeV  $\mu$ -like, and PC events, respectively.

### Flashing PMTs

A flashing PMT makes a diffused pattern of hit PMTs, therefore it can be background for  $e$ -like events.

As described in Chapter 5, a typical flashing PMT makes a broad hit timing distribution, and the goodness of the vertex fitting is worse than that for a Cherenkov ring. And the estimated vertex should be near the PMT wall if the event reconstruction is successful.

To estimate the contamination of the flashing PMTs in  $e$ -like samples, we checked both the goodness of the vertex fitting,  $G_T$  (see Section 6.2), and  $D_{wall}$  distributions.

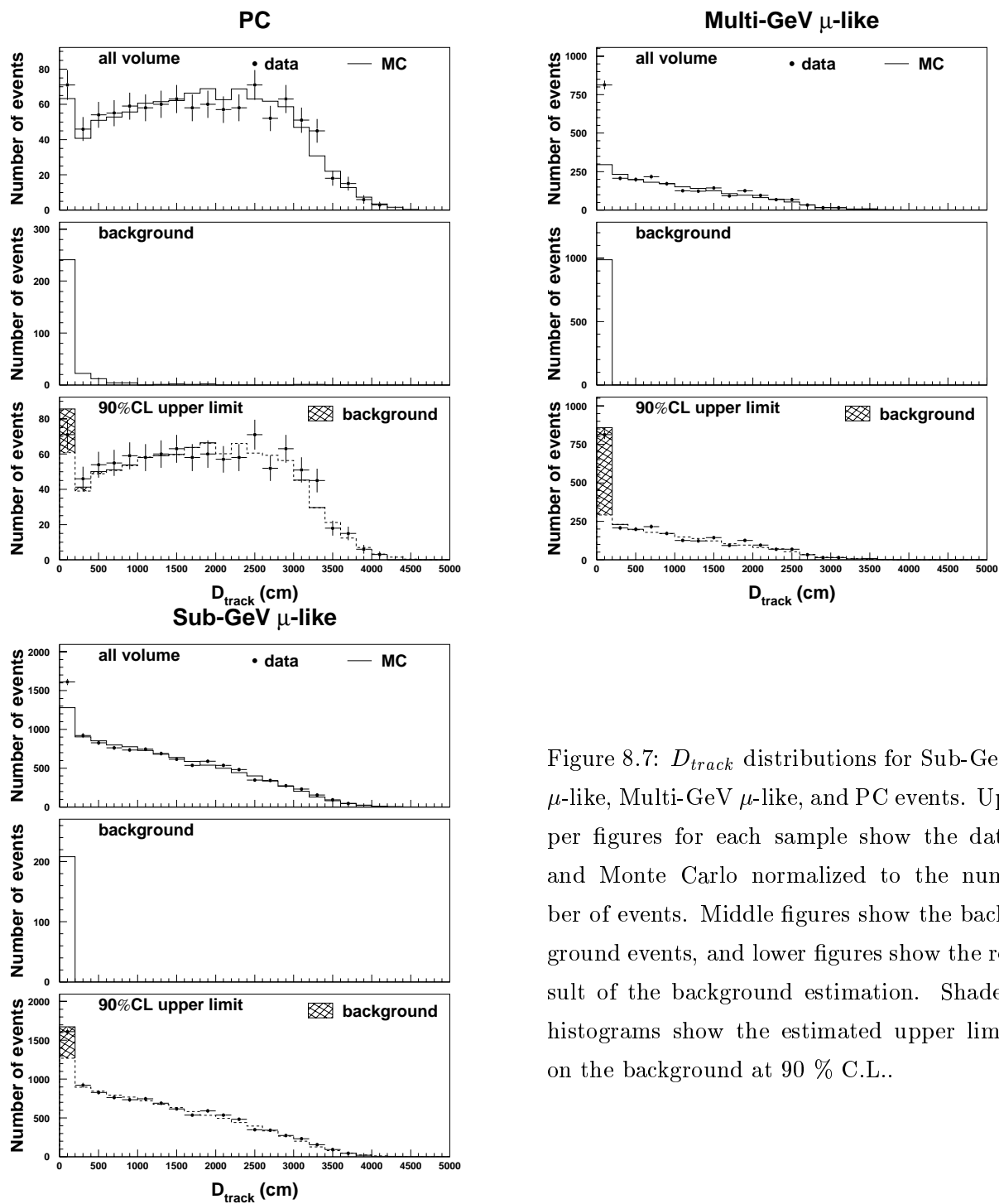


Figure 8.7:  $D_{track}$  distributions for Sub-GeV  $\mu$ -like, Multi-GeV  $\mu$ -like, and PC events. Upper figures for each sample show the data and Monte Carlo normalized to the number of events. Middle figures show the background events, and lower figures show the result of the background estimation. Shaded histograms show the estimated upper limit on the background at 90 % C.L..

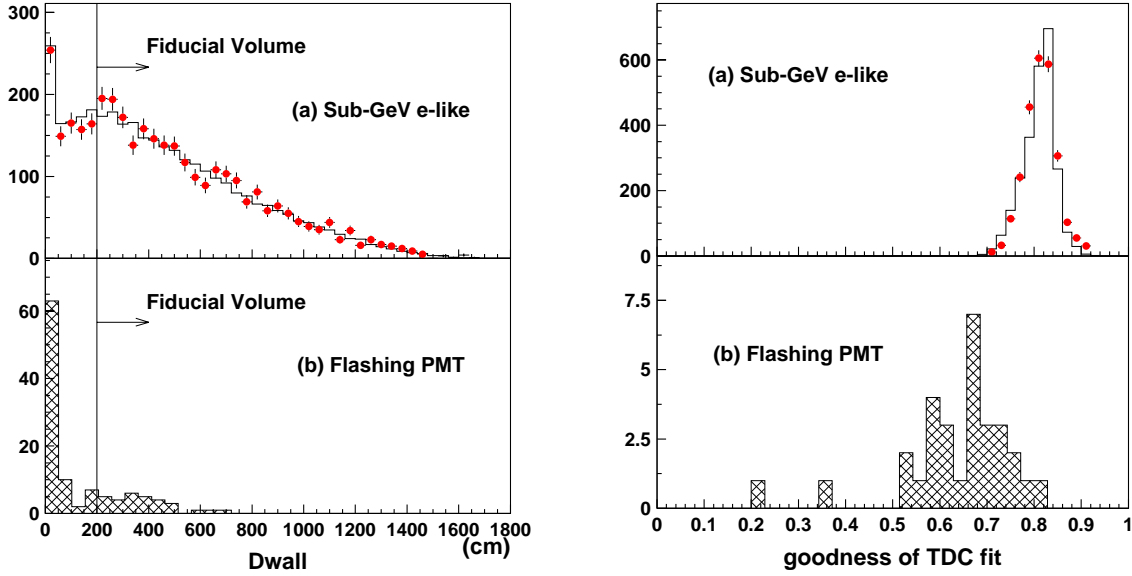


Figure 8.8: The *goodness* of TDC fit and  $D_{wall}$  distributions for Sub-GeV *e*-like sample and flashing PMT events which satisfy the Sub-GeV *e*-like cuts.

Fig. 8.8 shows the  $D_{wall}$  and  $G_T$  distributions for Sub-GeV 1-ring *e*-like events before fiducial volume cut, and those for the flashing PMT events which satisfy the Sub-GeV 1-ring *e*-like cut. The flashing PMT events were selected by eye-scanning after the FC 3rd reduction. The flashing PMTs have smaller  $G_T$  and smaller  $D_{wall}$  values than those for the atmospheric MC events. However, the data and atmospheric neutrino MC events agree well and there is no clear evidence for the flashing PMT contamination.

We looked at the number of events with  $G_T < 0.65$  where 50% of the flasher events exist. No event with *goodness*  $< 0.65$  was found for the Sub-GeV *e*-like final sample, and the upper limit of the flasher event is estimated to be 2.3 event in this region (4.6 event in total events). Then, the contamination in the Sub-GeV *e*-like sample is conservatively estimated to be 0.16%. For Multi-GeV energy range, we found no flashing PMT event by the eye-scanning. We assumed that the *goodness* distribution for flashing PMTs in Multi-GeV energy range is similar as in Sub-GeV energy range, and the upper limit of the contamination for Multi-GeV *e*-like sample is estimated to be 0.42%.

### Neutrons from Rock

If energetic neutrons knocked off by the cosmic ray muons in the surrounding rock enter into the detector, they can make hadrons by the interactions with the detector materials. If a  $\pi^0$  is produced by the neutron, it could be a background for *e*-like events. MC study of neutron events shows that attenuation length of neutrons in water is about 40(64) cm for Sub-GeV(Multi-GeV)

energy region, and the the neutrons should be absorbed by the 2 m thick water in OD. Even if the neutrons survive into the inner detector, neutron-induced events should have their vertex near the wall, and therefore are rejected by the fiducial volume cut.

As shown in Fig. 8.8,  $D_{wall}$  distribution of the data have no clear excess near the wall, then the rate of neutron-induced background event is expected to be small. We estimated the upper limit of the neutron background by comparing the vertex distribution for the FC  $e$ -like data and the combination of the atmospheric neutrino MC events and neutron MC events. Estimated 90% C.L. upper limit on the neutron background is 0.1% for both Sub-GeV and Multi-GeV  $e$ -like samples.

### 8.1.5 $\mu/e$ Double Ratio $R$

As described in Chapter 2, the flavour ratio of the atmospheric neutrino,  $(\nu_\mu + \bar{\nu}_\mu)/(\nu_e + \bar{\nu}_e)$ , is predicted with a 5% accuracy. As shown in Table 8.2, the particle identification for single-ring events gives a good estimation of the flavour of the parent neutrinos, and the ratio of the number of  $e$ -like events and  $\mu$ -like events,  $(N_\mu/N_e)_{\text{Data}}$ , gives a good test for the flavour ratio of the atmospheric neutrinos.

We calculate *Double Ratio*,  $R$ , which is defined as:

$$R \equiv \frac{(N_\mu/N_e)_{\text{Data}}}{(N_\mu/N_e)_{\text{MC}}} \quad (8.1)$$

where  $N_\mu$  ( $N_e$ ) is the number of  $\mu$ -like( $e$ -like) events, and suffix 'Data' and 'MC' indicate the data and the Monte Carlo prediction, respectively. If the data and the prediction agree,  $R$  should be unity.

The results are as follows:

$$\text{Sub-GeV} \quad : \quad R = 0.651_{-0.018}^{+0.019} (\text{stat.}) \pm 0.040_{(\text{sys.})} \quad (8.2)$$

$$\text{Multi-GeV} + \text{PC} \quad : \quad R = 0.711_{-0.036}^{+0.039} (\text{stat.}) \pm 0.085_{(\text{sys.})} \quad (8.3)$$

where suffix 'stat.' means statistical errors and 'sys.' means systematic errors. Because the fraction of CC  $\nu_\mu$  event in PC sample is very high (97%), PC sample was treated as  $\mu$ -like event and was combined to Multi-GeV  $\mu$ -like sample. For both Sub-GeV and Multi-GeV+PC sample,  $R$  is significantly smaller than unity. Deviation from unity is  $5.4\sigma$  for the Sub-GeV sample and  $2.2\sigma$  for the Multi-GeV+PC sample.

Systematic error of the  $R$  includes both theoretical and experimental. Table 8.4 shows the sources of the systematic uncertainties in  $R$ . The estimated systematic errors are 6.2% for Sub-GeV and 12.3% for Multi-GeV + PC sample. The sources of the uncertainty of  $R$  are described below.

	Sub-GeV(%)	Multi-GeV + PC(%)
Prediction of $\nu_e/\nu_\mu$ ratio	5	5
$E_\nu$ spectral index	0.6	1.6
$\nu$ cross section	1.6	9.2
Hadron simulation	0.5	1
Reduction	$\ll 1$	3.0
$\mu/e$ separation	2.2	3.2
Ring finding	1.5	3.4
Fiducial volume determination	0.6	1.4
Energy calibration	0.8	2.0
Non- $\nu$ background	$<0.5$	$<0.3$
MC statistics	0.7	1.4
Total	6.2	12.3

Table 8.4: Sources of the systematic uncertainty in  $R$  for the Sub-GeV and Multi-GeV+PC sample.

### Systematic Uncertainty of the Calculated Atmospheric Neutrino Fluxes

- Flavour Ratio of the Atmospheric Neutrinos

The flavour ratio  $(\nu_\mu + \bar{\nu}_\mu)/(\nu_e + \bar{\nu}_e)$  has about 5% uncertainty below 10 GeV energy region. This uncertainty causes 5% changes in  $R$  for both Sub-GeV and Multi-GeV+PC samples.

- Energy spectrum of the Atmospheric Neutrino Flux

As described in Chapter 2, neutrino flux approximately obeys a single power function  $E_\nu^\gamma$ . The uncertainty in the energy spectrum of the atmospheric neutrinos is estimated to  $E_\nu^{\pm 0.05}$ . This uncertainty causes 0.6%(1.6%) uncertainty in  $R$  for Sub-GeV(Multi-GeV+PC) sample.

### Systematic Uncertainty of Neutrino and Hadron Interactions

- Neutrino Cross Sections

The difference between  $\nu_e$  interaction and  $\nu_\mu$  interaction is only the difference of the mass of the charged leptons, and the ratio,  $N_\mu/N_e$ , cancels the uncertainty from the neutrino cross sections if the charged lepton masses are negligible. But as shown in Table 8.2, the contribution of each interaction mode (Q.E., single  $\pi$  production, etc) is different for  $e$ -like sample and  $\mu$ -like sample, and the uncertainty in the cross section of the neutrino interaction causes the uncertainty in  $(N_\mu/N_e)_{MC}$ .

We conservatively estimated the uncertainty by changing the cross sections of Q.E. scattering by 10% and single-pion production and multi-pion production by 30%, and also about 20% uncertainty of the CC/NC ratio is considered. For PC sample, we varied the cross sections by 10%. The cross sections are incoherently varied for FC and PC samples. In total, the uncertainty is 1.6% for the Sub-GeV sample and 9.2% for the Multi-GeV+PC sample.

- Hadron Simulation in the Detector

The uncertainty of the simulations of the hadron propagation in water is a source of the systematic uncertainty in  $(N_{\mu/N_e})_{MC}$ . We compared the results of the two different simulation programs, CALOR and FLUKA. The difference of  $R$ s is 0.5% for Sub-GeV sample and 1.0% for Multi-GeV+PC sample.

### Systematic Uncertainty Related to Event Reconstruction

If the MC simulation is a complete one, the reconstruction procedures make no systematic uncertainty for the  $(\mu/e)_{data}/(\mu/e)_{MC}$  ratio. The MC simulation was designed to reproduce the real situations, but not completely. The possible systematic errors due to the event reconstruction and their estimated values are described below.

- $\mu/e$  Separation

Probability of particle misidentification is estimated 1.1% and 1.6% for Sub-GeV and Multi-GeV from a MC simulation study. The systematic uncertainty of  $R$  coming from the particle misidentification was estimated to be 2.2%(3.2%) for Sub-GeV(Multi-GeV+PC) by simply doubling the misidentification probability.

- 1-ring/multi-ring Separation

To estimate the effect of the ring counting procedure, we compared  $R$  between different versions of the ring counting procedure. The uncertainty of  $R$  is estimated to be 1.5% for Sub-GeV and 3.4% for Multi-GeV+PC sample, respectively.

- Fiducial Volume Uncertainty

The systematic difference of the vertex reconstruction between the real data and the MC simulated events gives the fiducial volume uncertainty. To estimate the systematic uncertainty, we compared the results from different vertex fitters, TDCfit and MSfit (see Chapter 6). We estimated the systematic error from the uncertainty of the fiducial volume to be 0.6%(1.4%) for Sub-GeV(Multi-GeV+PC) sample.

- Energy Calibration

As described in Chapter 4, the difference of the absolute energy scale is within 2.5% between the data and MC. This uncertainty causes 0.8% uncertainty for the Sub-GeV sample and 2.0%

for the Multi-GeV+PC sample, respectively. These numbers were estimated by changing the reconstructed momentum of the Monte Carlo events by  $\pm 2.5\%$ .

- Reduction

For the FC sample, the uncertainty due to the reduction steps is known as very small by a MC study. For PC events, the uncertainty of the reduction is estimated to be 5%. This uncertainty causes about 3.0% uncertainty in  $R$  for the Multi-GeV+PC sample.

- Non-Neutrino Background

Background estimation is already described in Section 8.1.4. The effects of the backgrounds are less than 0.5% for the Sub-GeV and 0.3% for the Multi-GeV+PC sample.

In addition to the systematic uncertainties described above, statistical error of MC events is included.

### 8.1.6 Zenith Angle Distributions

Fig. 8.9 shows the zenith angle distributions for FC  $e$ -like and  $\mu$ -like events for various energy intervals.  $\cos \Theta = -1$  ( $\cos \Theta = 1$ ) indicates upward-going (downward-going) direction. Sub-GeV events are separated into two part ( $p_l \leq 400$  MeV and  $p_l > 400$  MeV). In the momentum range below 400 MeV/ $c$ , angular correlation between neutrino and outgoing lepton is very poor (see Fig. 2.9), and the shape of the atmospheric neutrino flux is largely washed out and the zenith angle distributions for the charged leptons become flat.

While the data and the MC predictions for  $e$ -like events agree well, the data for the  $\mu$ -like events have clear deficits. In addition, the deficits of  $\mu$ -like events have a zenith angle dependence.

### 8.1.7 $Up/Down$ ratio

To test the zenith angle distribution, we calculate  $Up/Down$  ratio which is defined as the ratio of the number of upward-going events ( $\cos \Theta < -0.2$ ) and downward-going events ( $\cos \Theta > 0.2$ ). Table 8.5 shows the summary of  $Up/Down$  ratio for each sample. FC  $\mu$ -like events with the momentum greater than 400 MeV/ $c$  and PC events show a significantly smaller  $Up/Down$  ratio. The  $Up/Down$  ratio is a very robust quantity, because the systematic uncertainties from several sources such as  $\nu$  cross section, event reconstruction, *etc.*, are largely cancelled. Sources of the systematic uncertainty in the  $Up/Down$  ratio are summarized in Table 8.6.

Fig. 8.11 shows the  $Up/Down$  ratio as a function of reconstructed momentum for FC  $e$ -like and  $\mu$ -like sample.  $Up/Down$  ratio for PC events is also shown. Although the  $e$ -like data show a

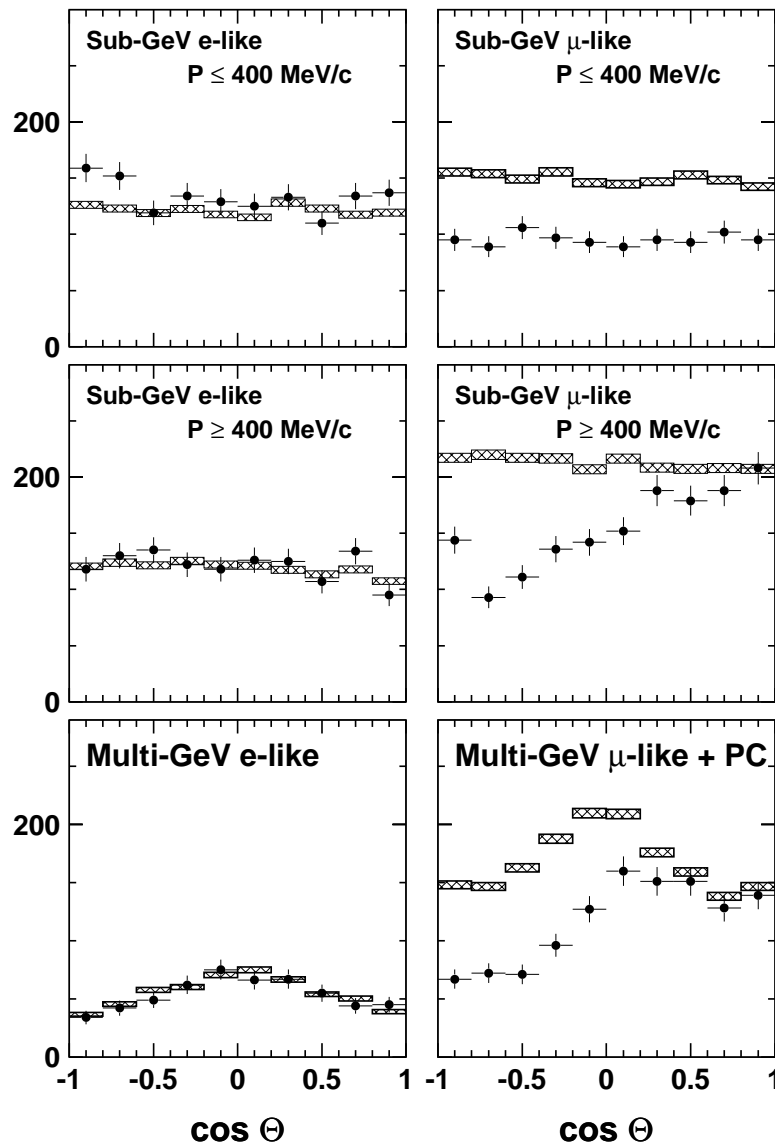


Figure 8.9: Zenith angle distribution for Sub-GeV and Multi-GeV plus PC samples.  $\cos \Theta$  is zenith angle of each events, and  $\cos \Theta = -1$  ( $\cos \Theta = 1$ ) indicate upward-going (downward-going) direction. Points show the data and histograms show MC predictions, and the error boxes of the histograms show the statistical errors of MC simulation. Figures in the upper row show the events with the momentum less than  $400 \text{ MeV}/c$ , and figures in the middle row are for the events with the momentum greater than  $400 \text{ MeV}/c$ . Figures in the lower row are for Multi-GeV plus PC events.

good agreement with MC prediction, FC  $\mu$ -like and PC events show significantly smaller values than the expected in the higher momentum region.

The sources of the systematic uncertainty in the  $Up/Down$  ratio are described below.

- The up-down ratio of the  $\nu$  flux

As described in Chapter 2, in the range of neutrino energy over a few GeV, the neutrino flux is up-down symmetric. In the range lower than a few GeV, the neutrino flux has up-down asymmetry due to the geomagnetic field effects on the primary cosmic rays, but the asymmetry is largely smeared out due to the poor angle correlation between the neutrino and the outgoing lepton. We estimated this uncertainty by comparing the results using independent calculated fluxes (Honda flux [78] and Bartol flux [79]), and the uncertainty is estimated to be about 2.5%, 2.1%, 1.6% and 1.0% for Sub-GeV  $e$ -like(Sub-GeV  $\mu$ -like), Multi-GeV  $e$ -like, and Multi-GeV  $\mu$ -like + PC events, respectively.

- Effect of the mountain above Super-Kamiokande

Honda flux and Bartol flux don't take into account the existence of a 1.0 km thick mountain above the Super-Kamiokande detector. The mountain decreases the flux of downward-going high energy neutrinos, a fraction of the cosmic ray muons before reaching the ground is decreased by that mountain. This effect is estimated by a simple model of the neutrino production height distributions. This effect is important only for Multi-GeV energy range, and the estimated systematic uncertainty is 2.0% for Multi-GeV  $e$ -like and 1.0% for Multi-GeV  $\mu$ -like + PC events.

- The up-down asymmetry of the energy scale

The up-down asymmetry of the energy scale of the Super-Kamiokande detector is estimated using decay electrons from the stopping muons. Fig. 8.10 shows the mean reconstructed energy of the decay electron from stopping muons as a function of zenith angle of the decay electron. The up-down asymmetry of the energy scale is estimated to be within 0.6%, and it causes the up-down uncertainty of 0.1%(0.2%) for Sub-GeV  $e$ -like ( $\mu$ -like) events and 0.9%(0.7%) for Multi-GeV  $e$ -like( $\mu$ -like + PC) events, respectively.

- Non-neutrino Background

The result of the background estimation was described in Section 8.1.4. The up-down asymmetry from the non-neutrino backgrounds is conservatively estimated by assuming that the all non-neutrino backgrounds are in either upward-going or downward-going direction. And also we assumed that the cosmic ray muons contaminate in the downward-going direction events. The systematic uncertainty in the up-down ratio due to the non- $\nu$  background is estimated to be less than 1.1%, 0.15%, 0.5%, and 0.3% for Sub-GeV  $e$ -like, Sub-GeV  $\mu$ -like, Multi-GeV

		Data			Monte Carlo		
		Up	Down	$Up/Down$	Up	Down	$Up/Down$
Sub-GeV ( $p < 400$ MeV/c)	$e$ -like	564	514	$1.10^{+0.07}_{-0.07} \pm 0.012$	491.1	488.2	$1.01 \pm 0.02 \pm 0.03$
	$\mu$ -like	387	385	$1.01^{+0.08}_{-0.07} \pm 0.003$	614.1	590.5	$1.04 \pm 0.02 \pm 0.02$
Sub-GeV ( $p > 400$ MeV/c)	$e$ -like	505	461	$1.10^{+0.07}_{-0.07} \pm 0.012$	491.2	456.0	$1.08 \pm 0.02 \pm 0.03$
	$\mu$ -like	484	763	$0.63^{+0.04}_{-0.04} \pm 0.002$	871.0	831.3	$1.05 \pm 0.01 \pm 0.02$
Multi-GeV + PC	$e$ -like	187	211	$0.89^{+0.094}_{-0.085} \pm 0.09$	200.1	209.8	$0.95 \pm 0.03 \pm 0.02$
	$\mu$ -like+PC	306	569	$0.54^{+0.039}_{-0.037} \pm 0.004$	645.1	619.6	$1.04 \pm 0.02 \pm 0.02$

Table 8.5: Summary of  $Up/Down$  ratio for each sample.  $Up(Down)$  events is defined as the number of events with  $\cos \Theta < -0.2$  ( $\cos \Theta > 0.2$ ).

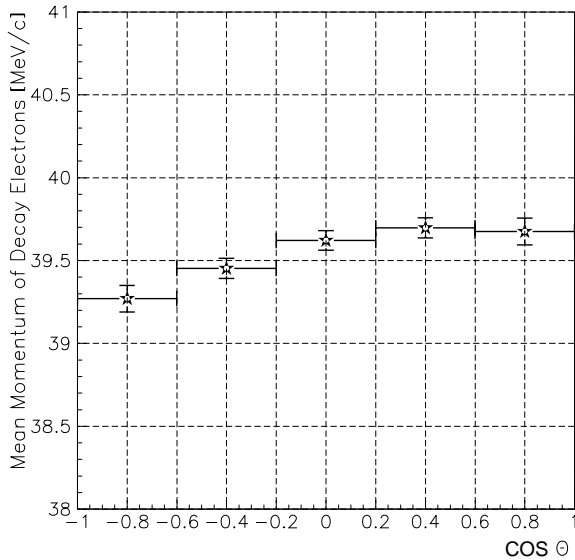


Figure 8.10: The mean reconstructed momentum of the decay electrons of the cosmic ray muons stopping in the detector as a function of the zenith angle. The up-down difference is estimated to be  $\pm 0.6\%$ .

$e$ -like, and Multi-GeV  $\mu$ -like + PC events, respectively.

### 8.1.8 East-West Effect

In this section, we describe the azimuthal angle distributions of the neutrino events. It is well known that the secondary cosmic ray flux have azimuthal anisotropy caused by the geomagnetic field effects on primary protons. This azimuthal anisotropy of cosmic rays, called the 'East-West Effect', was discovered in the 1930's as a deficit of the secondary cosmic ray muons arriving from the easterly direction compared to the westerly direction [158].

Fig. 8.12 shows the contour map of the cutoff rigidity for the neutrino arrival direction at the Kamioka site. At the Kamioka site, the averaged cutoff momentum for primary protons is

	Sub-GeV		Multi-GeV	
	e-like(%)	$\mu$ -like(%)	e-like(%)	$\mu$ -like+PC(%)
Monte Carlo Prediction				
Predicted flux (Honda vs Bartol)	2.5	2.1	1.6	1.0
Mountain over Super-Kamiokande	$\ll 1$	$\ll 1$	2.0	1.5
Total	2.5	2.1	2.6	1.8
Data				
Energy scale $\pm 0.6\%$	0.1	0.2	0.9	0.7
Non- $\nu$ background	1.1	0.15	0.5	0.3
Total	1.1	0.25	1.0	0.8

Table 8.6: Sources of the systematic uncertainty in the  $Up/Down$  ratio for Sub-GeV and Multi-GeV +PC sample. Systematic errors are listed separately for prediction and observation.

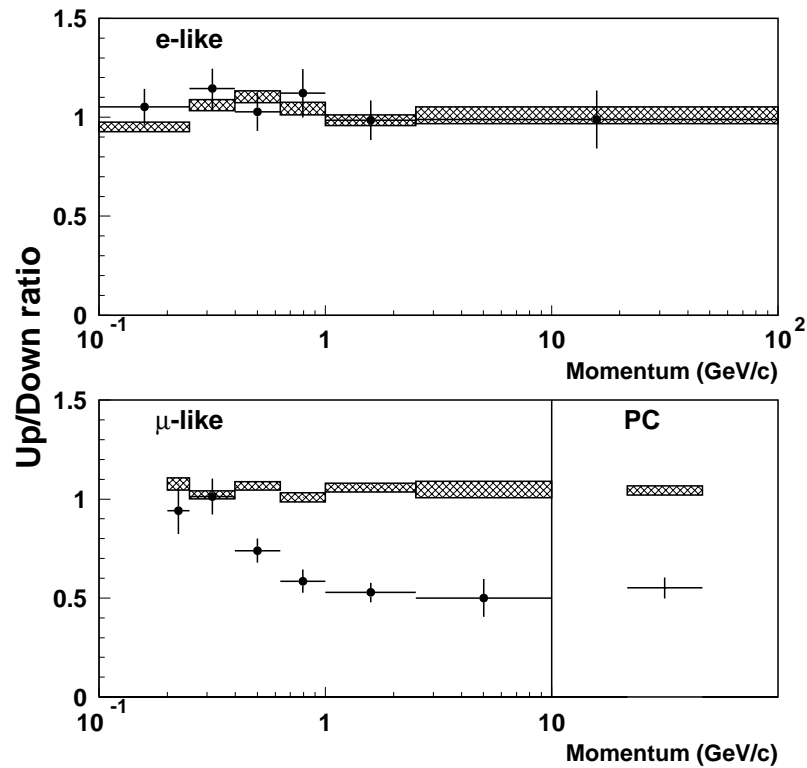


Figure 8.11:  $Up/Down$  ratio as a function of momentum for each sample. Dots show the data and boxes show the Monte Carlo predictions with their statistical errors. Error bars shows statistical only.

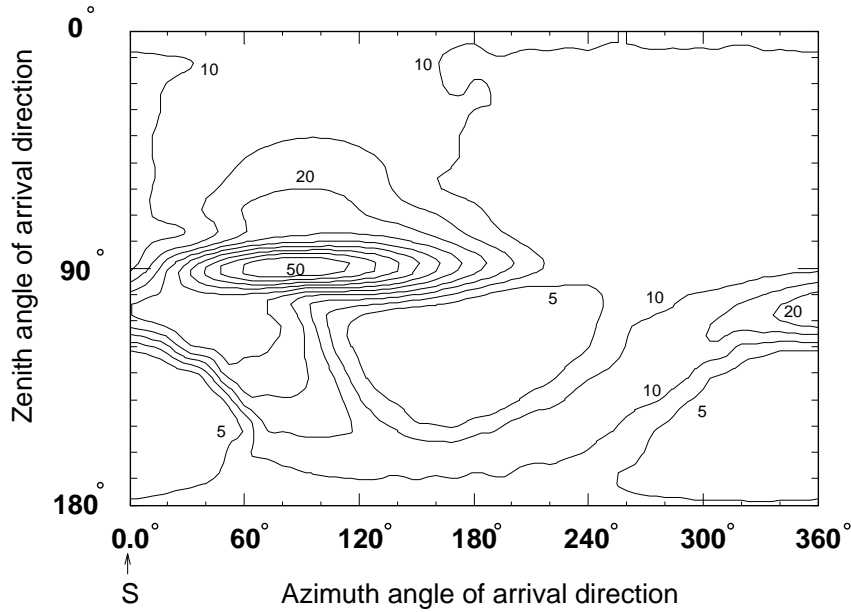


Figure 8.12: The contour map of a calculated cutoff rigidity ( $\text{GeV}/eZ$ ) for the neutrino arrival directions at Kamioka site [78]. Azimuthal angles of  $0^\circ$ ,  $90^\circ$ ,  $180^\circ$ ,  $270^\circ$  show direction to the south, east, north and west of the detector, respectively. Zenith angle  $0^\circ$  shows the direction of overhead.

about  $10 \text{ GeV}/c$ , and the cutoff momentum for horizontally arriving protons from the east is  $\sim 50 \text{ GeV}/c$ , considerably higher than the average. It reduces the flux of the primary protons entering into the Earth, and consequently reduces the neutrino flux from the easterly direction.

To study the azimuthal angle distribution of the neutrino events, we required the following event selection criteria for FC 1-ring  $e$ -like and  $\mu$ -like samples:

- (1)  $-0.5 < \cos \Theta < 0.5$
- (2)  $400 \text{ MeV}/c < p_l < 3000 \text{ MeV}/c$

The momentum cut is set to maximize the significance of the East-West effect. The geomagnetic effect is expected to be larger for lower energy neutrinos, but the angular correlation between neutrino and outgoing lepton becomes poor and vice versa.

Fig. 8.13 shows the azimuthal angle distribution of the neutrino events.  $\phi$  represents the azimuthal direction, where  $\phi=0$ ,  $\pi/2$ ,  $\pi$ , and  $3\pi/2$  show the particles going to the north, west, south, and east direction, respectively. The MC predictions are normalized by the total number of the data for each sample. The result shows that the shape of the MC predictions and the data agree well for both  $e$ -like and  $\mu$ -like events, and the number of neutrino events from the easterly

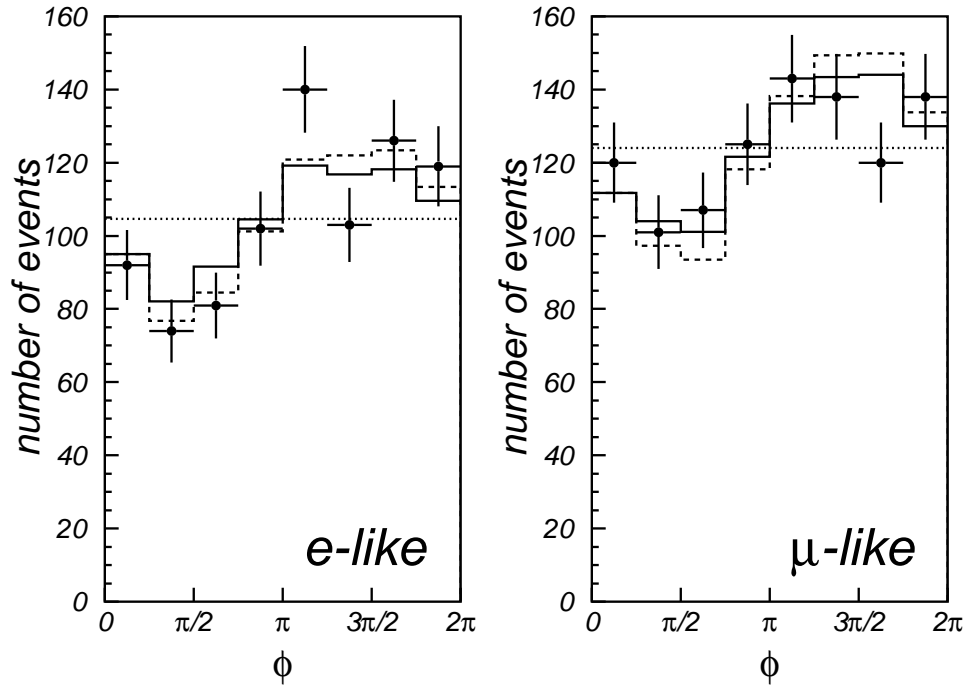


Figure 8.13: Azimuthal angle distributions of the atmospheric neutrino events. Crosses show the data and solid(dashed) histograms show the Monte Carlo predictions based on the flux of [78]([79]).  $\phi$  represents the azimuthal angle.  $\phi = 0, \pi/2, \pi,$  and  $3\pi/2$  represent to northward, westward, southward, and eastward directions, respectively.

direction is fewer as expected. Since the flight length of neutrinos should be independent of the azimuthal direction, this result is independent of neutrino oscillation and neutrino decay.

Fig. 8.14 shows the east-west asymmetry,  $(N_E - N_W)/(N_E + N_W)$ , as a function of the reconstructed momentum.  $N_W(N_E)$  is the number of westward(eastward)-going events defined as the events with  $0 < \cos \phi < \pi$  ( $\pi < \cos \phi < 2\pi$ ). MC predictions and the data agree well for both  $e$ -like and  $\mu$ -like.

These results suggest that the geomagnetic field effect is reasonably taken into account in the calculation of the atmospheric neutrino flux, and our Monte Carlo simulation reasonably reproduces the angular correlation between neutrinos and charged leptons.

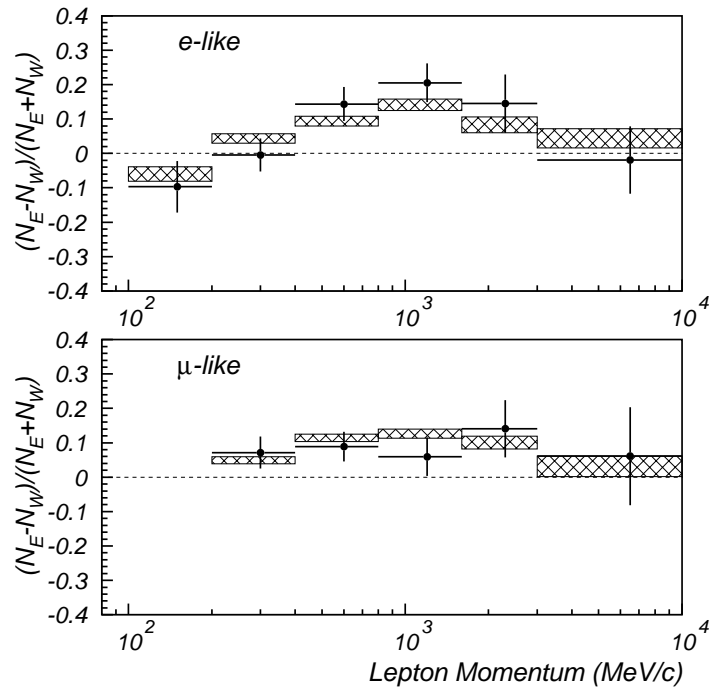


Figure 8.14: The east-west asymmetry  $(N_E - N_W)/(N_E + N_W)$  as a function of reconstructed lepton momentum.

## 8.2 Upward-going Muons

The averaged flux over the zenith angle for the upward through-going and upward stopping muons are as follows:

Upward thr.-going muon flux	$(10^{-13} \text{cm}^2 \text{sec}^{-1} \text{sr}^{-1})$
Observed	: $1.70 \pm 0.05_{(\text{stat.})} \pm 0.02_{(\text{sys.})}$
Expected	: $1.84 \pm 0.41_{(\text{sys.})}$
Upward stopping muon flux	$(10^{-13} \text{cm}^2 \text{sec}^{-1} \text{sr}^{-1})$
Observed	: $0.41 \pm 0.03_{(\text{stat.})} \pm 0.02_{(\text{sys.})}$
Expected	: $0.68 \pm 0.15_{(\text{sys.})}$

The observed flux of the upward through-going muons is consistent with the predicted flux within the estimated error, and the observed flux of the upward stopping muons is smaller than the expected flux by 1.8 standard deviation.

The systematic uncertainties of the observed and predicted fluxes are listed in Table 8.7 and Table 8.8.

The possible sources of the systematic uncertainty in the observed fluxes are track reconstruction, detection efficiency, background contamination, and direction reconstruction. The systematic uncertainty in the reconstructed track length is estimated to be about 5% by comparing the cosmic ray muons and MC simulation, and it causes about 5% uncertainty for the upward stopping muon flux and 0.5% for the upward through-going muon flux. The systematic uncertainty in the detection efficiency was estimated by using the Monte Carlo simulation, and the estimated systematic uncertainties is 1.2% for upward through-going muons and 1.0% for upward stopping muons. The uncertainty in the background subtraction affects only the most horizontal bins, and the uncertainty in the most horizontal bin was estimated to be 0.3% for the upward through-going muons and 8.3% for the upward stopping muons (see Section 5.5). The systematic uncertainty in the direction resolution of the muons is estimated to be  $1.0^\circ$  for both the through-going and stopping muons by comparing the different hand fit results. This systematic uncertainty causes a uncertainty only for the most horizontal bins, and it is estimated to be less than 1% for both through-going and stopping muon fluxes.

The possible sources of the systematic uncertainty in the predicted fluxes are the neutrino flux, neutrino cross section, and the finite angle between neutrino and the observed muons which is not considered in our calculation. The uncertainty of the absolute normalization due to the uncertainty of the absolute neutrino flux is estimated to be 20%. We compared the other calculated upward-going muon flux based on other neutrino cross sections models, and the

Source of Systematic error	Uncertainty	
	Upward thr.-going $\mu$	Upward Stopping $\mu$
Livetime <sup>1</sup>	<1%	<1%
Reconstruction of $\mu$ track length <sup>1</sup>	0.5%	+ 4.9% - 4.1%
Background subtraction <sup>2</sup>	0.3%	8.3%
Reconstruction of direction <sup>2</sup>	< 1%	< 1%
Detection efficiency <sup>1</sup>	1.2%	1.0%

Table 8.7: Systematic uncertainties in the observed fluxes of upward going muons. 1: overall for all bins 2: only most horizontal bins.

Source of Systematic error	Uncertainty	
	Upward thr.-going $\mu$	Upward Stopping $\mu$
$\nu$ flux normalization <sup>1</sup>	20%	20%
Neutrino cross section	10% <sup>1</sup>	10% <sup>1</sup>
	-2% to 1% <sup>3</sup>	-3.7% to 1.6% <sup>3</sup>
$\nu/\bar{\nu}$ ratio <sup>1</sup>	$\pm 0.1\%$	1%
$\theta_{\nu\mu}$ in $\nu$ interaction <sup>2</sup>	1%	4%

Table 8.8: Systematic uncertainty of the calculated fluxes of upward going muons. 1: overall for all bins 2: only most horizontal bins 3: bin-by-bin uncorrelated

systematic uncertainty is estimated to be 10% in the overall flux and  $-2\%$  to  $1\%$  ( $-3.7\%$  to  $1.6\%$ ) the bin-by-bin shape difference in the zenith angle distributions for the upward through-going muons (upward stopping muons).

The multiple scattering of the muons in the rock surrounding Super-Kamiokande and the finite scattering angle between incident neutrino and muon are not considered in the analytical calculations of the expected fluxes of the upward-going muons. The effects of the multiple scatterings and the scattering angle between neutrino and muons are estimated by an phenomenological formula [164] and a MC study. The uncertainty is not negligible only in the most horizontal bins, and is estimated to be 1% for upward through-going muons and 4% for upward-stopping muons.

The ratio of the upward-stopping muon flux,  $\Phi_{stop}$ , to upward through-going muon flux,  $\Phi_{through}$  is more robust than the absolute fluxes. The ratio largely cancels the systematic uncertainties in the neutrino flux normalization and the neutrino interaction cross sections.

Experimental systematic uncertainties	
Source of Systematic error	Uncertainty
$\mu$ track reconstruction	5%
Stop/Thr. misidentification	1%
Reconstruction efficiency	1%
total	5.2%

Theoretical Systematic uncertainties	
Source of Systematic error	Uncertainty
$E_\nu$ spectrum index $\pm 0.05$	13%
Predicted flux (Honda vs Bartol)	1%
Neutrino cross section	2.4%
total	13.3%

Table 8.9: Systematic uncertainties in the flux ratio  $\Phi_{stop}/\Phi_{through}$ .

$\Phi_{stop}/\Phi_{through}$  ratio is obtained as:

$$\begin{aligned} \text{Observed} & : 0.24 \pm 0.02_{(\text{stat.})} \pm 0.01_{(\text{sys.})} \\ \text{Expected} & : 0.37 \pm 0.05_{(\text{sys.})} \end{aligned}$$

The observed ratio is clearly smaller than the expected, and the deviation is about 2.7 standard deviations. Table 8.9 shows the systematic errors of the ratio  $\Phi_{stop}/\Phi_{through}$ . The systematic uncertainty is estimated to be 5.2% for the observation and 13.6% for the prediction.

### 8.2.1 Zenith Angle Distribution for Upward-going Muons

Fig. 8.15 shows the zenith angle distributions for upward through-going and upward stopping muons. Error bars in Fig. 8.15 are statistical only. The shape of the zenith angle distribution for the upward through-going muons is not well reproduced by the prediction. We consider bin-by-bin systematic errors and the statistical errors, and the shape test gives  $\chi^2 = 23.0/9$  d.o.f. after multiplying a factor 0.91 to the prediction.

The observed flux of the upward stopping muons is systematically lower than the expected flux in the all zenith angle bins. The shape test gives  $\chi^2 = 6.8/4$  d.o.f. after multiplying a factor 0.57 to the prediction. The shape of the zenith angle distribution for the upward stopping muons seem to agree with the prediction, but the normalization factor is significantly smaller than 1,

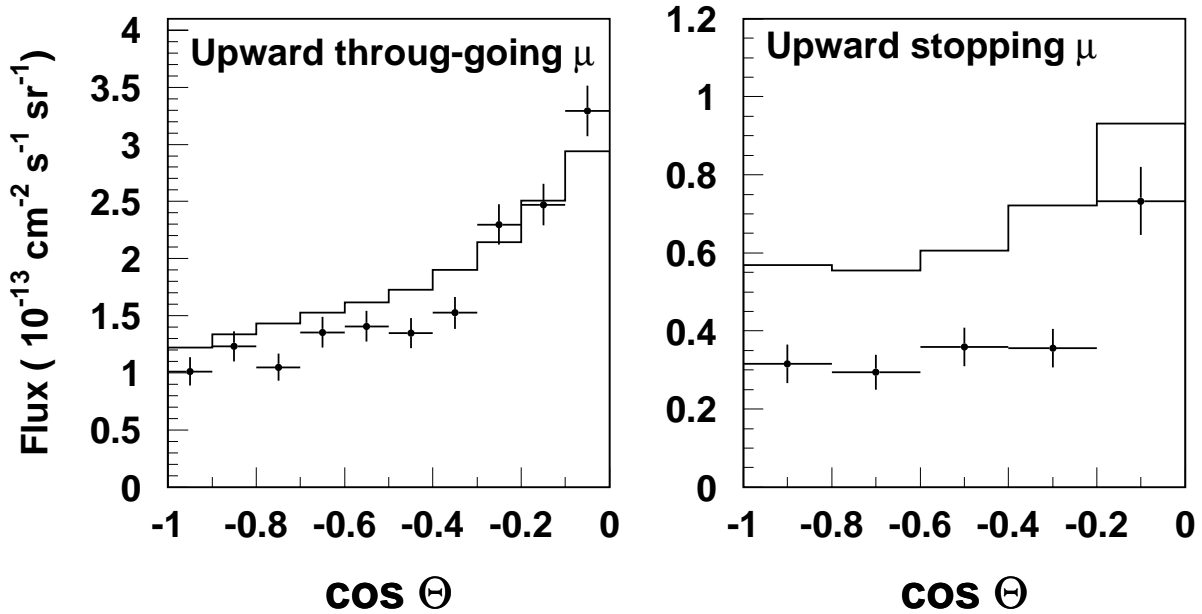


Figure 8.15: Zenith angle distributions for upward through-going muons and upward stopping muons. Crosses show the observed fluxes and histograms show the prediction based on the Honda flux [78]. Error bars show the statistical only.

and also the normalization factors for the upward through-going muons and upward stopping muons are significantly different from each other.

Fig 8.16 shows the flux ratio  $\Phi_{stop}/\Phi_{through}$  as a function of the zenith angle. Error bars are statistical only. As described before, the ratio largely cancels several systematic uncertainties and is more robust than the absolute fluxes. The flux ratio is systematically smaller than the expected values in the all zenith angle bins.

### 8.3 Summary

In this chapter, we summarized the results of our observation of the atmospheric neutrinos. The results show that the number of  $\nu_{\mu} + \bar{\nu}_{\mu}$  events is clearly smaller than expected, while the number of  $\nu_e + \bar{\nu}_e$  events seems to agree with expected. Also, the deficit of the  $\nu_{\mu} + \bar{\nu}_{\mu}$  events has a clear zenith angle and energy dependences. These deficits of the  $\nu_{\mu} + \bar{\nu}_{\mu}$  cannot be explained by any systematic uncertainties in either experimental or theoretical.

One possible way to explain the observed data is the neutrino oscillations. The results of the neutrino oscillation analyses are described in Chapter 9. The other possible mechanism which could explain the atmospheric neutrino anomalies, (violation of the Equivalent principle, FCNC, neutrino decays), are also described in the next chapter.

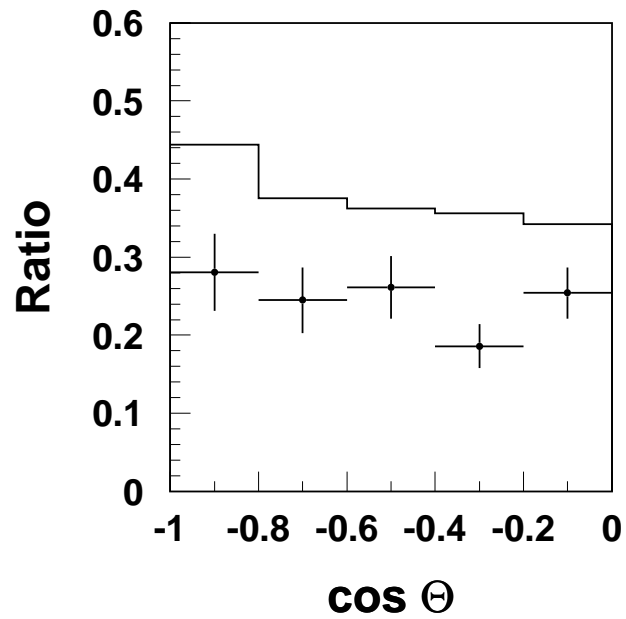


Figure 8.16: The flux ratio  $\Phi_{stop}/\Phi_{through}$  as a function of the zenith angle. Crosses show the observed ratio and histogram shows the prediction. Error bars show the statistical only.



## Chapter 9

# Analysis and Results

In this chapter, we discuss the results of the  $\nu_\mu \leftrightarrow \nu_\tau$  2-flavour neutrino oscillation and neutrino decay analyses. We tested several possible theories of neutrino oscillations and neutrino decay using FC single-ring events, PC events, and upward-going muons. In addition, FC Multi-ring events were used in the neutrino decay analysis described in Section 9.7.1.

A  $\chi^2$  test was used to evaluate the goodness of the fit between the data and the expectation. Systematic uncertainties are considered in the analyses.

### 9.1 Definition of $\chi^2$

The data are binned according to the event category, zenith angle and momentum. Fig. 9.1 shows a schematic view of the binning. FC Sub-GeV  $e$ -like and  $\mu$ -like sample are divided into 5 momentum bins and 10 equal sized zenith angle bins from  $\cos \Theta = -1.0$  to 1.0. In total, there are  $5 \times 10 = 50$  bins. The FC Multi-GeV  $e$ -like sample is divided into  $2 \times 10 = 20$  bins and the FC Multi-GeV  $\mu$ -like sample is divided into  $1 \times 10 = 10$  bins. The PC sample is divided into 10 zenith angle bins. Upward through-going muons are divided into 10 zenith angle bins equally separated in  $\cos \Theta$  from  $-1.0$  to 0.0, and upward-stopping muons are divided into 5 bins.

In general,  $\chi^2$  is defined as:

$$\chi^2 = \Delta^T M^{-1} \Delta \tag{9.1}$$

where  $\Delta$  is the vector of the differences between the theoretical and the experimental values and  $M$  is the error matrix [159]. If we assume that  $M$  is diagonalized for the data residuals,  $\chi^2$  is

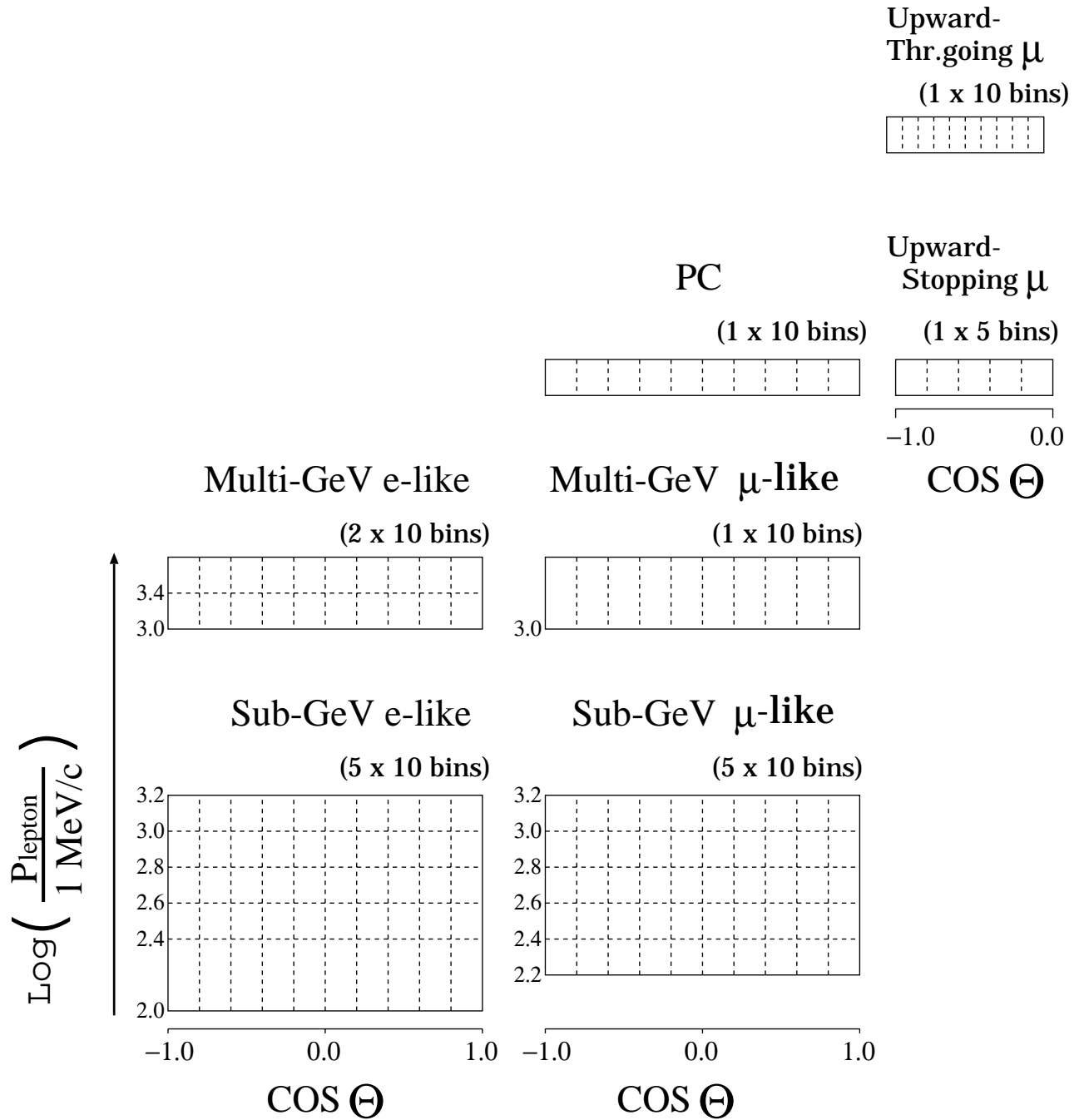


Figure 9.1: Definition of the binning. There are 155 bins in total. Both the Multi-GeV  $\mu$ -like and the highest momentum bin of Multi-GeV e-like samples have no momentum upper limit. The PC and upward-going muons are divided only in zenith angle bins.

expressed as:

$$\chi^2 = \sum_i \frac{(N_{obs}^i - N_{exp}^i(a_1, a_2, \dots, \vec{\varepsilon}))^2}{\sigma_i^2} + \sum_i \frac{\left( \left( \frac{d\Phi}{d\Omega} \right)_{obs}^i - \left( \frac{d\Phi}{d\Omega} \right)_{exp}^i(a_1, a_2, \dots, \vec{\varepsilon}) \right)^2}{\sigma_i^2} + \vec{\varepsilon}^T M_s^{-1} \vec{\varepsilon} \quad (9.2)$$

The first term in Eq.(9.2) is  $\chi^2$  for FC and PC events, the second term is for the upward-going muons, and the third term is for the systematic errors.  $N_{obs}^i$  is the observed number of events for the  $i$ th bin, and  $N_{exp}^i(a_1, a_2, \dots, \vec{\varepsilon})$  is the expected number of events for  $i$ th bin for a set of neutrino oscillation (or decay) parameters  $(a_1, a_2, \dots)$ , with the parameters  $\vec{\varepsilon} \equiv (\varepsilon_1, \varepsilon_1, \dots)$  accounting for the systematic errors. The calculation method of  $N_{exp}^i$  is described in Section 9.2.1. The  $\sigma_i$  in the first term is the statistical errors for both data and Monte Carlo.

$(d\Phi/d\Omega)_{obs}^i$  and  $(d\Phi/d\Omega)_{exp}^i$  are the observed and expected flux of muons, respectively.  $\sigma_i$  is a quadratic sum of the statistical error of the data and the bin-by-bin uncorrelated systematic error for the  $i$ th bin. The bin-by-bin uncorrelated systematic error is described in Section 8.2. The calculation method of  $(d\Phi/d\Omega)_{exp}^i$  is described in Section 9.2.3.  $M_s$  is the error matrix for the systematic errors. If the  $\varepsilon_i$ 's are uncorrelated,  $M_s$  is a diagonal matrix. The systematic errors and their correlations are described in the following sections.

## 9.2 Calculation Methods of Expected Event Rates

### 9.2.1 Expected Event Rate of FC and PC events

The expected number of FC and PC events for neutrino oscillations (or decay) with a given set of neutrino oscillation (or decay) parameters  $(a_1, a_2, \dots)$  is calculated by re-weighting the Monte Carlo events. The expected number of events for the  $i$ th bin,  $N_{MC}^i$ , is calculated as:

$$N_{MC}^i(a_1, a_2, \dots) = \frac{\mathcal{L}_{Data}}{\mathcal{L}_{MC}} \times \sum_{MC \text{ events}} P(a_1, a_2, \dots; E_\nu, \cos \Theta_\nu) \quad (9.3)$$

where  $\mathcal{L}_{Data}$  and  $\mathcal{L}_{MC}$  are the livetime of the data and the Monte Carlo simulation, and  $P(a_1, a_2, \dots; E_\nu, \cos \Theta_\nu)$  is the survival probability of the neutrino with an energy  $E_\nu$  and the zenith angle  $\Theta_\nu$  for a given parameter set  $(a_1, a_2, \dots)$ .

The flight length of the neutrino,  $L_\nu$ , is calculated as:

$$L_\nu = \begin{cases} L_{air} - 2R_\oplus \cos \Theta_\nu & \text{for } \cos \Theta_\nu < 0 \\ L_{air} & \text{for } \cos \Theta_\nu > 0 \end{cases} \quad (9.4)$$

where  $L_{air}$  is the slant height of the neutrino production in the atmosphere, and  $R_\oplus$  is the radius of the Earth. We calculate the production height of neutrinos from Ref. [160]. The systematic

uncertainty of the calculated production height is estimated to be about 10 %. This systematic uncertainty is considered in the neutrino oscillation and decay analyses.

The rate of CC interactions of the  $\nu_\tau$ 's generated by  $\nu_\mu \rightarrow \nu_\tau$  neutrino oscillations is much smaller than the rate of  $\nu_\mu$  and  $\nu_e$  CC interactions because of the high threshold energy ( $E_{th} = 3.5\text{GeV}$ ). The rate is estimated to be about 60~70 events in Super-Kamiokande for 1144 days exposure (70.4 kton·year) assuming  $\sin^2 2\theta=1.0$  and  $\Delta m^2=3.0 \times 10^{-3}\text{eV}^2$ . For FC single-ring events, the rate of the CC  $\nu_\tau$  events is expected to be much smaller, because only the leptonic decays,  $\tau^- \rightarrow e^- \nu_\tau \bar{\nu}_e$  (16% branching ratio) and  $\tau^- \rightarrow \mu^- \nu_\tau \bar{\nu}_\mu$  (17% branching ratio), are likely to produce the single-ring events. The number of FC single-ring events induced by  $\nu_\tau$  CC interaction is simply estimated to be about 20 events for 1144 days exposure. It is much smaller than the FC 1-ring event rate (about 6000 events), and we can safely neglect the  $\nu_\tau$  CC interactions in our analyses.

## 9.2.2 Systematic Uncertainties

We have several systematic uncertainties in the zenith angle and momentum distributions for both observation and prediction. To consider these systematic uncertainties, The expected event rate,  $N_{exp}^i$ , is calculated as:

$$N_{exp}^i = (1 + \alpha) \left( \frac{\overline{E}_\nu^i}{E_0} \right)^\delta (1 + \eta_{s,m} \cos \Theta_i) (1 + \kappa_f (|\cos \Theta_i| - 0.5)) \times W_f \times N_{MC}^i \quad (9.5)$$

$$W_f = \begin{cases} (1 - \beta_s/2) & \text{for Sub-GeV } e\text{-like events} \\ (1 + \beta_s/2) & \text{for Sub-GeV } \mu\text{-like events} \\ (1 - \beta_m/2) & \text{for Multi-GeV } e\text{-like events} \\ (1 + \beta_m/2) & \text{for Multi-GeV } \mu\text{-like events} \\ (1 + \beta_m/2)(1 + \rho) & \text{for PC events} \end{cases} \quad (9.6)$$

where  $\alpha, \beta_{s,m}, \eta_{s,m}, \kappa_f, \delta, \rho$  are the parameters representing the systematic uncertainties. The meanings and their estimated uncertainties of the parameters are described below.

### $\alpha$ : Absolute Normalization

The absolute normalization uncertainty is estimated to be about 25%. It comes from the uncertainty in the absolute flux of neutrino ( $\sim 20\%$ ) and the uncertainty in the total neutrino cross sections (15%). We treated the parameter  $\alpha$  as a free parameter in our analysis because of its large uncertainty.

	$\eta_s$ (%)	$\eta_m$ (%)
Geomagnetic effects (Honda $\leftrightarrow$ Bartol )	$\pm 2.5$	$\pm 1.6$
Mountain over Super-Kamiokande	$\ll 1$	$\pm 2.0$
Asymmetry of the energy scale ( $\pm 0.6\%$ )	$\pm 0.1$	$\pm 0.9$
Non- $\nu$ background	1.1	0.5
Total	2.7	2.8

Table 9.1: Sources of the uncertainties in  $\eta_s$  and  $\eta_m$ .

### $\delta$ : Energy Spectrum of Neutrinos

As described in Section 2.2, the spectrum of the neutrino flux approximately obeys the power function  $E_\nu^{-\gamma}$ , where  $\gamma$  is estimated to be about 3.0 for  $\nu_\mu$  and about 3.5 for  $\nu_e$ . The systematic uncertainty in the index of the neutrino flux  $E_\nu^{\gamma \pm \delta}$  introduces a uncertainty in the momentum distributions. This uncertainty is expressed as:

$$N^{i'} = \left( \frac{\overline{E}_\nu^i}{E_0} \right)^\delta \times N^i \quad (9.7)$$

where  $E_0$  is a reference energy arbitrarily taken to be 2 GeV, and  $\overline{E}_\nu^i$  is the averaged neutrino energy for the  $i$ th bin.  $\sigma_\delta$  is estimated to be 0.05 from the uncertainty of the primary cosmic ray flux spectrum.

### $\eta_{s,m}$ :Up-Down Ratio

The uncertainties in the zenith angle distributions are assumed to be of a linear form in  $\cos \Theta$ :

$$N^{i'} = \left( 1 + \frac{\eta_{s,m}}{2} \cos \Theta_i \right) \times N^i \quad (9.8)$$

where  $\Theta_i$  is the central value of zenith angle for the  $i$ th bin, and  $\eta_s$  and  $\eta_m$  represent the up-down uncertainties for the Sub-GeV and Multi-GeV samples, respectively. We use a common parameter  $\eta$  for both  $e$ -like and  $\mu$ -like. The sources of the uncertainty of  $\eta_s$  and  $\eta_m$  are listed in Table 9.1. The details of the sources are described in Section 8.1.7.  $\sigma_{\eta_s}$  and  $\sigma_{\eta_m}$  are estimated to be 2.7% and 2.8%.

### $\beta_{s,m}$ : $\mu/e$ Ratio

The systematic uncertainty in the  $\mu/e$  ratio is represented by the following multiplicative factor:

$$N^{i'} = \left( 1 \pm \frac{\beta_{s,m}}{2} \right) \times N^i \quad (9.9)$$

	$\beta_s$ (%)	$\beta_m$ (%)
Predicted $\nu_e/\nu_\mu$ ratio	5	5
$\nu$ cross section		
Q.E. ( $\pm 10\%$ )	$\pm 0.5$	$\pm 1.0$
$1-\pi$ /Q.E. ( $\pm 30\%$ )	$\mp 1.0$	$\pm 0.8$
DIS/Q.E. ( $\pm 30\%$ )	$\mp 0.4$	$\mp 3.8$
Hadron simulation(CALOR $\leftrightarrow$ FLUKA)	0.5	1.0
FC Reduction	$\ll 1$	$\ll 1$
$\mu/e$ separation	2.2	3.2
Ring counting	1.5	5.5
Fiducial volume determination	0.6	1.0
Energy calibration ( $\pm 2.5\%$ )	$\pm 0.8$	$\mp 0.6$
Non- $\nu$ background	$<0.5$	$<0.2$
Total	6.0	9.2

Table 9.2: Sources of uncertainty in  $\beta_s$  and  $\beta_m$ .

where  $\beta_s$  is for the FC Sub-GeV sample and  $\beta_m$  is for the FC Multi-GeV sample, and plus is for  $\mu$ -like and minus is for  $e$ -like. The sources of systematic uncertainty in the  $\mu/e$  ratio are listed in Table 9.2. Since the uncertainty in the energy spectrum index ( $\pm 0.05$ ) is taken into account in a separate term, all the sources except for this are included in the uncertainty  $\beta_s$  and  $\beta_m$ .  $\sigma_{\beta_s}$  and  $\sigma_{\beta_m}$  are estimated to be 6.0% and 9.2%, respectively.

### $\kappa_f$ : Horizontal/Vertical Ratio

If the neutrino oscillation length is approximately the same as the flight length of the neutrinos from the horizontal direction, then the estimation of  $\Delta m^2$  can be sensitive to uncertainty in the horizontal/vertical ratio of the neutrino flux. The horizontal/vertical ratio uncertainty is represented by the following factor:

$$N^{i'} = (1 + \kappa_f(|\cos \Theta_i| - 0.5)) N^i \quad (9.10)$$

where  $\Theta_i$  is the central value of the zenith angle for the  $i$ th bin, and  $\kappa_f$  represents the horizontal/vertical ratio uncertainty.

The horizontal/vertical uncertainty for FC events comes mainly from the neutrino flux calculation. The neutrino flux used in our simulation is based on a 1-dimensional approximation, in which the direction of the produced neutrino is assumed to be parallel to the direction of the parent cosmic ray. Recent preliminary results of flux calculations based on a 3-dimensional treatment predict an enhancement of the low energy neutrino flux in the horizontal direction [83] which is not predicted by a 1-dimensional calculation. The difference between the 1-dimensional

approximation and the 3-dimensional treatment becomes smaller as the neutrino energy becomes higher, because the angle between the neutrino direction and the primary cosmic ray direction becomes smaller due to the Lorentz boost.

By comparing the zenith angle distribution of the outgoing leptons based on the Honda flux (1-dimensional) and the preliminary results based on a 3-dimensional treatment,  $\sigma_{\kappa_p}$  is estimated to be 4% for FC events with momentum greater than 400 MeV/ $c$ . For events with momentum less than 400 MeV/ $c$ , the horizontal/vertical uncertainty is assumed to be zero, because the angular correlation between the neutrino and the outgoing leptons is very poor (see Fig. 2.9), and the zenith angle distribution of the neutrinos is largely washed out. For the PC sample, the horizontal/vertical uncertainty is not applied, because the neutrino energy is high enough to neglect the difference between 1-dimensional and 3-dimensional calculations.

### $\rho$ : Relative Normalization between PC and FC Multi-GeV $\mu$ -like

The FC and PC events have different event topologies and different reduction streams. For example, we make use of the number of reconstructed rings for the FC events, but not for the PC events. The typical parent neutrino energy is different between the FC and PC events ( $\langle E_\nu \rangle = 1$  GeV for the FC sample and  $\langle E_\nu \rangle = 15$  GeV for the PC sample). These differences introduce an uncertainty of the relative rate of FC and PC events. The relative normalization uncertainty is expressed as:

$$N_{\text{PC}}^i{}' = (1 + \rho)N_{\text{PC}}^i \quad (9.11)$$

where  $N_{\text{PC}}^i$  is the number of events in the  $i$ th bin of PC event. The sources of this uncertainty are listed in Table 9.3. Since the uncertainty in the absolute neutrino cross section is considered in  $\alpha$ , we estimated the uncertainty due to the neutrino cross sections by changing the fraction of the interaction modes. We changed (1- $\pi$  production)/(Q.E. scattering) cross section ratio and (DIS)/(Q.E.scattering) cross section ratio by 10%. The estimated systematic uncertainty is 10.5%.

### Uncertainty of $L_\nu/E_\nu$

In the calculation of the expected event rate with neutrino oscillation, the systematic uncertainty of  $L_\nu/E_\nu$  is crucial. The uncertainty of  $L/E$  is expressed as:

$$N^{i'}(\sin^2 2\theta, \Delta m^2) = N^i(\sin^2 2\theta, (1 + \lambda)\Delta m^2) \quad (9.12)$$

The main source of the uncertainty in  $L_\nu/E_\nu$  is the uncertainty of the production height of neutrinos (estimated to be 10% for the vertically downward events). The uncertainty of  $E_\nu$  is dominated by the systematic uncertainty of the energy scale ( $\pm 2.5\%$ ). The uncertainty of

	$\rho$ (%)
$\nu$ cross section	
1- $\pi$ / Q.E. ( $\pm 10\%$ )	$\pm 4.0$
DIS / Q.E. ( $\pm 10\%$ )	$\pm 6.3$
Hadron simulation(CALOR $\leftrightarrow$ FLUKA)	1.0
PC Reduction	5.0
Ring-counting	4.0
Fiducial volume determination	1.6
FC/PC separation	0.5
Energy calibration ( $\pm 2.5\%$ )	$\pm 3.0$
Non- $\nu$ background	$< 0.3$
<b>Total</b>	<b>10.5</b>

Table 9.3: Sources of systematic uncertainty in  $\rho$ .

the  $L_\nu/E_\nu$  is conservatively estimated to be 15%. The systematic uncertainty of the production height is negligible for the upward-going events, but, we assume the above systematic uncertainty for all zenith angles.

### 9.2.3 Expected flux of Upward-going muons

The expected flux of the upward-going muons is calculated by an analytical calculation. The method is described in Appendix B.

### 9.2.4 Systematic Uncertainties

Correlated systematic uncertainties are taken into account in a similar fashion as is done for the FC and PC events. The uncertainty in the absolute normalization,  $\alpha$ , and the uncertainty in the energy spectrum index  $\delta$  is the same for both FC, PC, and upward-going muons. The modified flux is written as:

$$\frac{d\Phi}{d\Omega_{exp}} = (1 + \alpha) \left( \frac{\overline{E}_\nu^i}{E_0} \right)^\delta (1 + \rho_s) \times W \times \frac{d\Phi}{d\Omega}, \quad (9.13)$$

$$W = \begin{cases} 1 + \kappa_u & \text{Through-going muons} \\ 1 + \rho_t & \text{Stopping muons} \end{cases} \quad (9.14)$$

#### $\rho_t$ : Stopping-Through Relative Normalization

This systematic uncertainty is expressed by the following factor:

$$\frac{d\Phi^{\text{Stop}'}}{d\Omega} = (1 + \rho_t) \frac{d\Phi^{\text{Stop}}}{d\Omega} \quad (9.15)$$

	$\rho_t$ (%)
$\nu$ cross section	
1- $\pi$ / Q.E.( $\pm 10\%$ )	$\pm 1.2$
DIS / Q.E.( $\pm 10\%$ )	$\mp 2.1$
7 m track cut	5.0
Thr. going /Stopping separation	1.0
<b>Total</b>	<b>5.6</b>

Table 9.4: Sources of systematic uncertainty of relative normalization between upward stopping muons and upward through-going muons.

The sources of the systematic uncertainty of the relative normalization of the two samples are summarized in Table 9.4. Since the uncertainty in the energy spectrum index ( $\pm 0.05$ ) is taken into account in a separate term, all the sources except for this are included in the uncertainty  $\rho_t$ . The main source of the uncertainty  $\rho_t$  is the track reconstruction of muons(5%). The systematic uncertainty of  $\rho_t$  is estimated to be 5.6%.

#### $\rho_s$ : (FC 1-ring)-(Upward-gong Muons) Relative Normalization

The relative normalization between FC 1-ring events and upward-gong muons is represented by:

$$\frac{d\Phi^{\text{Thr.}'}}{d\Omega} = (1 + \rho_s) \frac{d\Phi^{\text{Thr.}}}{d\Omega} \quad \text{and} \quad \frac{d\Phi^{\text{Stop}'}}{d\Omega} = (1 + \rho_s) \frac{d\Phi^{\text{Stop}}}{d\Omega} \quad (9.16)$$

The sources of the uncertainty are listed in Table. 9.5. We estimated the uncertainty due to the neutrino cross sections by changing the fraction of the interaction modes. We changed (1- $\pi$  production)/(Q.E. scattering) cross section ratio and (DIS)/(Q.E.scattering) cross section ratio by 10%. The uncertainty of  $\rho_s$  is estimated to be 9.2% in total.

#### $\kappa_u$ : Horizontal/Vertical Ratio

For the upward-going muons, the neutrino energy is high enough to neglect the systematic uncertainty from the 1-dimensional approximation. The source of the horizontal/vertical uncertainty for upward through-going muons is the uncertainty of the  $K/\pi$  production ratio in the air shower. The uncertainty in the  $K/\pi$  production ratio is estimated to be about 20%, and this uncertainty translates to a 4% vertical/horizontal uncertainty [84]. For the upward-stopping muons, we don't consider the uncertainty because of the same reasons as for the PC samples.

	$\rho_s$ (%)
$\nu$ cross section	
1- $\pi$ / Q.E. ( $\pm 10\%$ )	$\mp 2.6$
DIS / Q.E. ( $\pm 10\%$ )	$\pm 8.6$
7 m track cut	1.4
FC ring-counting	0.3
FC Fid. vol. determination	0.7
Energy calibration ( $\pm 2.5\%$ )	$\pm 0.3$
Up- $\mu$ detection efficiency	1.0
Total	9.2%

Table 9.5: Sources of systematic uncertainty of relative normalization between FC 1-ring and upward-going muons.

### 9.3 Correlations between the Systematic errors

Some of the systematic errors described above come from same sources, and they have correlations. In general,  $\chi^2$  has the form:

$$\chi^2 = \vec{\varepsilon}^T M_s^{-1} \vec{\varepsilon} \quad (9.17)$$

where  $\vec{\varepsilon}$  is the vector of the systematic parameters, and  $M_s$  is the error matrix for the parameters  $\varepsilon$ . The error matrix  $M_s$  is defined as:

$$(M_s)_{ij} = \text{cov}(\varepsilon_i, \varepsilon_j) \quad (9.18)$$

where  $\text{cov}(\varepsilon_i, \varepsilon_j)$  is the covariance of  $\varepsilon_i$  and  $\varepsilon_j$ .

Table. 9.6 shows the estimated correlation coefficients,  $\rho \equiv \text{cov}(x, y) / \sigma_x / \sigma_y$ , between the systematic uncertainties. In this calculation, we assume that the sources of the systematic errors obey to the Gaussian distributions. In principle, the uncertainties in the predicted neutrino flux ( absolute normalization,  $\nu_\mu / \nu_e$  ratio, energy spectrum, geomagnetic effects, neutrino production heights, etc.) may be correlated, but we assume they are independent uncertainties. Therefore, we treat  $\alpha$ ,  $\delta$ ,  $\lambda$ ,  $\kappa_f$ , and  $\kappa_u$  as independent systematic errors.

The correlated parameters are divided into two subgroups: (1)  $\beta_s, \beta_m, \rho, \rho_s, \rho_t$ , (2)  $\eta_s, \eta_m$ . The estimation of the correlations are described in the following subsections.

$x \setminus y$	$\alpha$	$\delta$	$\beta_s$	$\beta_m$	$\rho$	$\rho_s$	$\rho_t$	$\eta_s$	$\eta_m$	$\lambda$	$\kappa_f$	$\kappa_u$
$\alpha$	1	0	0	0	0	0	0	0	0	0	0	0
$\delta$	0	1	0	0	0	0	0	0	0	0	0	0
$\beta_s$	0	0	1	0.31	-0.17	-0.03	0.0	0	0	0	0	0
$\beta_m$	0	0	0.31	1	-0.34	-0.004	0.0	0	0	0	0	0
$\rho$	0	0	-0.17	-0.34	1	0.58	-0.17	0	0	0	0	0
$\rho_s$	0	0	-0.03	-0.004	0.58	1	-0.25	0	0	0	0	0
$\rho_t$	0	0	0.0	0.0	-0.17	-0.25	1	0	0	0	0	0
$\eta_s$	0	0	0	0	0	0	0	1	0.62	0	0	0
$\eta_m$	0	0	0	0	0	0	0	0.62	1	0	0	0
$\lambda$	0	0	0	0	0	0	0	0	0	1	0	0
$\kappa_f$	0	0	0	0	0	0	0	0	0	0	1	0
$\kappa_u$	0	0	0	0	0	0	0	0	0	0	0	1

Table 9.6: Correlation coefficients  $\rho(x, y) \equiv \text{cov}(x, y)/\sigma_x/\sigma_y$ , where  $\text{cov}(x, y)$  is the covariance of  $x$  and  $y$ .

Finally, the  $\chi^2$  for the systematic errors can be written as:

$$\begin{aligned}
\chi^2 &= \vec{\varepsilon}^T M_s^{-1} \vec{\varepsilon} & (9.19) \\
&= \left(\frac{\delta}{\sigma_\delta}\right)^2 + \left(\frac{\lambda}{\sigma_\lambda}\right)^2 + \left(\frac{\kappa_f}{\sigma_{\kappa_f}}\right)^2 + \left(\frac{\kappa_u}{\sigma_{\kappa_u}}\right)^2 \\
&\quad + 1.10 \left(\frac{\beta_s}{\sigma_{\beta_s}}\right)^2 + 1.29 \left(\frac{\beta_m}{\sigma_{\beta_m}}\right)^2 + 1.82 \left(\frac{\rho}{\sigma_\rho}\right)^2 + 1.66 \left(\frac{\rho_s}{\sigma_{\rho_s}}\right)^2 + 1.07 \left(\frac{\rho_t}{\sigma_{\rho_t}}\right)^2 \\
&\quad - 0.60 \left(\frac{\beta_s \beta_m}{\sigma_{\beta_s} \sigma_{\beta_m}}\right) + 0.20 \left(\frac{\beta_s \rho}{\sigma_{\beta_s} \sigma_\rho}\right) - 0.04 \left(\frac{\beta_s \rho_s}{\sigma_{\beta_s} \sigma_{\rho_s}}\right) + 0.02 \left(\frac{\beta_s \rho_t}{\sigma_{\beta_s} \sigma_{\rho_t}}\right) \\
&\quad + 1.17 \left(\frac{\beta_m \rho}{\sigma_{\beta_m} \sigma_\rho}\right) - 0.68 \left(\frac{\beta_m \rho_s}{\sigma_{\beta_m} \sigma_{\rho_s}}\right) + 0.02 \left(\frac{\beta_m \rho_t}{\sigma_{\beta_m} \sigma_{\rho_t}}\right) + 0.50 \left(\frac{\rho_s \rho_t}{\sigma_{\rho_s} \sigma_{\rho_t}}\right) \\
&\quad + 1.6 \left(\frac{\eta_s}{\sigma_{\eta_s}}\right)^2 + 1.6 \left(\frac{\eta_m}{\sigma_{\eta_m}}\right)^2 - 1.98 \left(\frac{\eta_s \eta_m}{\sigma_{\eta_s} \sigma_{\eta_m}}\right) & (9.20)
\end{aligned}$$

where  $\sigma$ 's are the estimated errors due to the systematic uncertainties described in the previous subsections.

### 9.3.1 Correlations between $\beta_m$ , $\beta_s$ , $\rho$ , $\rho_s$ and $\rho_t$

The sources and their uncertainties are listed in Tables 9.2-9.5. The correlations between the sources are estimated as follows.

**$\nu_\mu/\nu_e$  ratio**

Several calculations predict the  $\nu_\mu/\nu_e$  flux ratio within 5% uncertainty. We assume that the uncertainty in the  $\nu_\mu/\nu_e$  flux ratio is 5% and uncorrelated between the Sub-GeV and Multi-GeV energy range.

**Neutrino interactions**

The uncertainty of the neutrino cross sections is estimated to be about 10% for high energy region (over 10 GeV). For low energy regions, the cross sections have other sources of the systematic uncertainties such as the Fermi motion of the target nucleons, threshold effects, nuclear effects, and so on. Therefore, we assume that the cross section uncertainties in FC event energy range (typically  $E_\nu = 1$  GeV) and in PC and upward-going muon event energy range ( $E_\nu > 10$  GeV) are uncorrelated.

**Ring-counting**

We estimate the uncertainties from the ring-counting procedure by comparing two different versions. We assume that the uncertainties in Sub-GeV and Multi-GeV energy range come from same reasons, and we take them as correlated.

 **$\mu/e$  separation**

We estimate the uncertainties from the particle identification procedure simply from the estimated mis-identification probabilities. We assume that the uncertainties in Sub-GeV and Multi-GeV energy range are due to the same reasons, and we take them as correlated.

**Energy calibration ( $\pm 2.5\%$ )**

We estimate the effects due to the energy calibration uncertainty ( $\pm 2.5\%$ ) by changing the reconstructed momentum of the Monte Carlo events.

**Vertex fitter**

The vertex fitters for FC and PC final samples are different (see Chapter 6) and they have different systematic uncertainties. We assume that the uncertainties in FC and PC events are uncorrelated.

**Non-neutrino Background**

We assume that the uncertainty in the backgrounds for each sample are uncorrelated.

### 9.3.2 Correlation between $\eta_s$ and $\eta_m$

#### Geomagnetic effects

We estimate the uncertainties coming from the geomagnetic effects by comparing two independent neutrino flux calculations (Honda and Barol). We assume that the effects are correlated in Sub-GeV and Multi-GeV energy range.

#### Asymmetry of the energy scale ( $\pm 0.6\%$ )

We estimate the effect by changing the reconstructed momentum of the Monte Carlo events. The effects are correlated in  $\eta_s$  and  $\eta_m$ .

#### Non-neutrino background

We assume that the effects of the non-neutrino background in  $\eta_m$  and  $\eta_m$  are correlated.

## 9.4 $\nu_\mu \leftrightarrow \nu_\tau$ Oscillation

We describe the result of a  $\nu_\mu \leftrightarrow \nu_\tau$  2-flavour neutrino oscillation analysis with the 'standard' neutrino oscillation mechanism. The survival probability of  $\nu_\mu \leftrightarrow \nu_\tau$  neutrino oscillation due to nonzero neutrino masses is written as:

$$P(\nu_\mu \rightarrow \nu_\mu) = 1 - \sin^2 2\theta \sin^2 \left( 1.27 \Delta m^2 \frac{L_\nu}{E_\nu} \right) \quad (9.21)$$

where  $\theta$  is the mixing angle and  $\Delta m^2 = m_3^2 - m_2^2$  is the difference of the squared masses of  $\nu_3$  and  $\nu_2$ . We scanned the parameter space  $(\sin^2 2\theta, \Delta m^2)$ , minimizing the  $\chi^2$  at each point by optimizing the systematic error parameters,  $(\alpha, \beta_{s,m}, \delta \dots)$ . The unphysical parameter region ( $\sin^2 2\theta > 1$ ) was also scanned in order to demonstrate the validity of the analysis.

The minimum  $\chi^2$  is 140.0/152 d.o.f. at  $(\sin^2 2\theta, \Delta m^2) = (1.00, 2.8 \times 10^{-3} \text{ eV}^2)$ . Including the unphysical region, the minimum  $\chi^2$  is found at  $(\sin^2 2\theta, \Delta m^2) = (1.01, 2.8 \times 10^{-3} \text{ eV}^2)$ , and is 0.05 lower than the minimum in the physical region. The  $\chi^2$  value without neutrino oscillation is 352.8/154 d.o.f., and therefore the hypothesis of no oscillations is strongly rejected. Table 9.4 shows the summary of the best fit systematic error parameters.

Fig. 9.2 shows the contour plot of the allowed region of the parameters  $(\sin^2 2\theta, \Delta m^2)$ . The contours show the 68, 90, and 99% C.L. allowed regions which are defined to be  $\chi^2 = \chi_{min}^2 + 2.3$ ,  $\chi^2 = \chi_{min}^2 + 4.6$ , and  $\chi^2 = \chi_{min}^2 + 9.2$ , respectively. The 90% allowed parameter region is:

$$1.8 \times 10^{-3} \text{ eV}^2 < \Delta m^2 < 4.5 \times 10^{-3} \text{ eV}^2 \quad (9.22)$$

$$0.89 < \sin^2 2\theta \quad (9.23)$$

$\alpha$	Absolute Normalization	3.1%	(free)
$\beta_s$	Sub-GeV $\mu/e$ Ratio	-1.9%	(6.0%)
$\beta_m$	Multi-GeV $\mu/e$ Ratio	-5.8%	(9.2%)
$\rho$	PC/FC relative normalization	4.5%	(10.5%)
$\eta_s$	Sub-GeV Up/Down ratio	-1.3%	(2.7%)
$\eta_m$	Multi-GeV Up/Down ratio	-0.4%	(2.8%)
$\delta$	$E_\nu$ spectrum	-0.023	(0.05)
$\lambda$	$L/E$ uncertainty	8.5%	(15%)
$\rho_t$	Up-stop $\mu$ /Up-thr $\mu$ relative norm.	-2.1%	(5.6%)
$\rho_s$	FC 1-ring/Up- $\mu$ relative norm.	13.8%	(9.2%)
$\kappa_f$	H/V ratio of FC	-0.3%	(4%)
$\kappa_u$	H/V upward thr. $\mu$	-0.03%	(3%)

Table 9.7: Summary of the best fit systematic uncertainty parameters of the  $\nu_\mu \leftrightarrow \nu_\tau$  oscillation analysis. The best fit parameters are shown in the second column, and the estimated systematic uncertainties are shown in the third column.

Fig. 9.3 shows the  $\chi^2 - \chi_{min}^2$  distribution sliced along  $\sin^2 2\theta = 1.0$  and  $\Delta m^2 = 2.8 \times 10^{-3} \text{ eV}^2$ . The distributions have a good parabola shape.

Figs. 9.4 and 9.5 show the zenith angle distributions for FC, PC, and upward-going muons compared with the best fit results of  $\nu_\mu \leftrightarrow \nu_\tau$  oscillation. The observed zenith angle distributions are well reproduced by the  $\nu_\mu \leftrightarrow \nu_\tau$  oscillation for all energy regions.

Figs. 9.6, 9.7, and 9.8 show  $Up/Down$  ratio, flavour ratio  $R$ , and  $\Phi_{stop}/\Phi_{thr.}$  ratio as a function of  $\Delta m^2$ . The observed values consistently suggest that  $\Delta m^2$  is  $10^{-2} \sim 10^{-3} \text{ eV}^2$ . The  $Up/Down$  ratio and  $R$  are well explained by the  $\nu_\mu \leftrightarrow \nu_\tau$  neutrino oscillation with  $(\sin^2 2\theta, \Delta m^2) = (1.00, 2.8 \times 10^{-3} \text{ eV}^2)$ . The observed  $\Phi_{stop}/\Phi_{thr.}$  ratio is slightly lower than the expected value from the neutrino oscillation, but the deviation is consistent with the systematic uncertainty of the prediction.

## 9.5 Neutrino Oscillations with $L/E^n$ Dependence

As described in Section 1.2, the general form of the survival probability is:

$$P(\nu_\mu \rightarrow \nu_\mu) = 1 - \sin^2 2\theta \sin^2 \left( \beta \frac{L\nu}{E_\nu^n} \right) \quad (9.24)$$

where  $E_\nu$  and  $L_\nu$  are the energy and flight length of a neutrino,  $\theta$  is the mixing angle of neutrinos and  $\beta$  is a parameter which represents the oscillation frequency. The index  $n$  depends

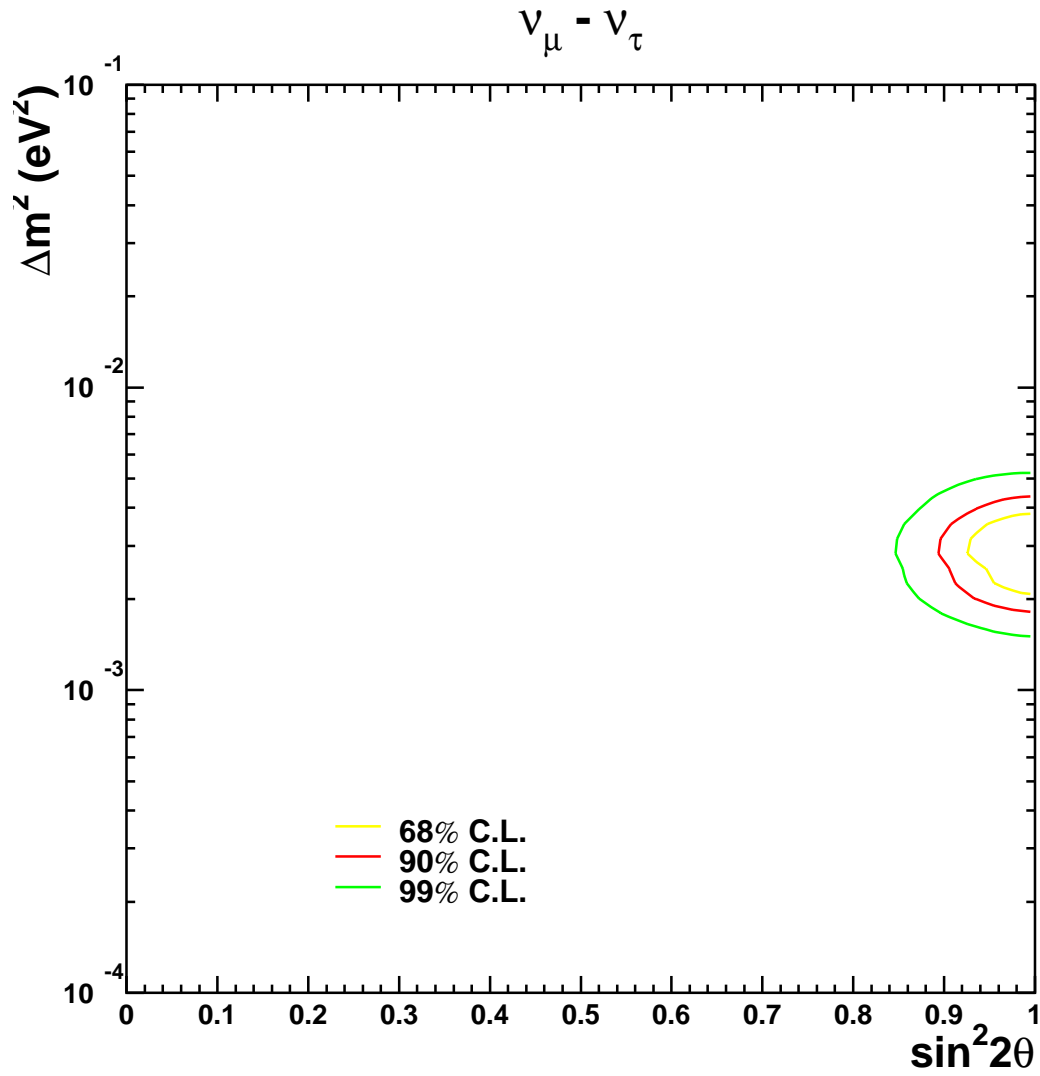


Figure 9.2: Contour plots of allowed regions of the parameters  $(\sin^2 2\theta, \Delta m^2)$ . Light gray, black, and dark gray lines show the 68%, 90%, and 99% C.L. allowed regions, respectively.

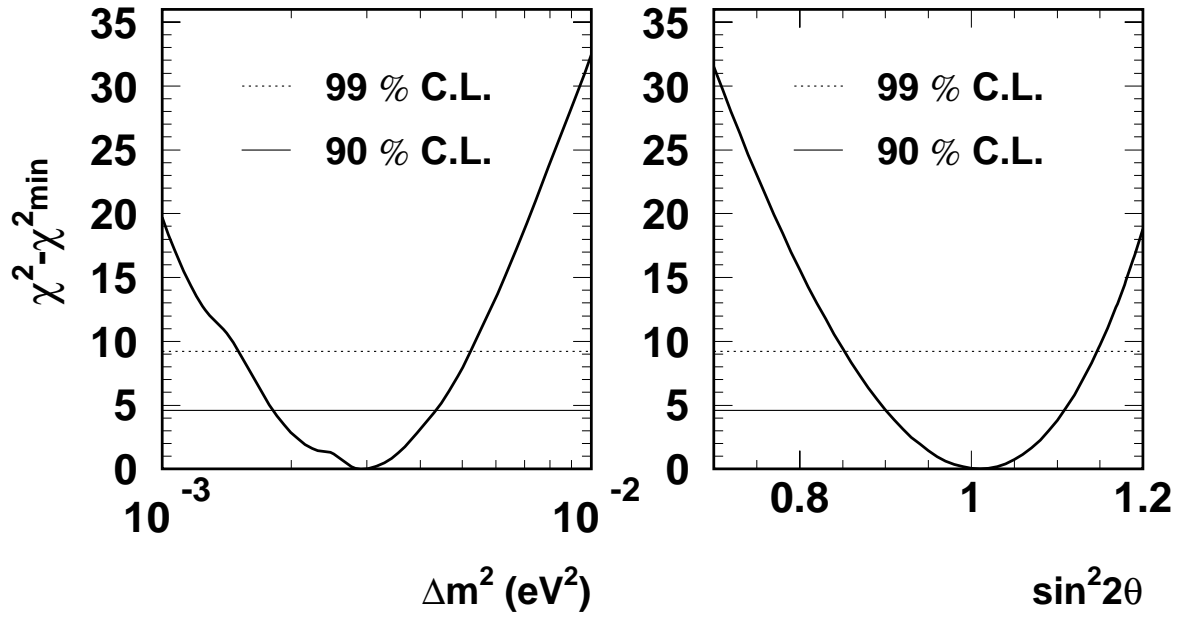


Figure 9.3: The  $\Delta\chi^2 = \chi^2 - \chi^2_{\min}$  distributions as a function of  $\Delta m^2$  (left figure) and  $\sin^2 2\theta$  (right figure).  $\sin^2 2\theta$  is set to 1.0 in the left figure and  $\Delta m^2$  is set to  $2.8 \times 10^3 \text{ eV}^2$  in the right figure. The horizontal solid and dotted lines show the  $\Delta\chi^2$  values for the 90% and 99% C.L. intervals, respectively.

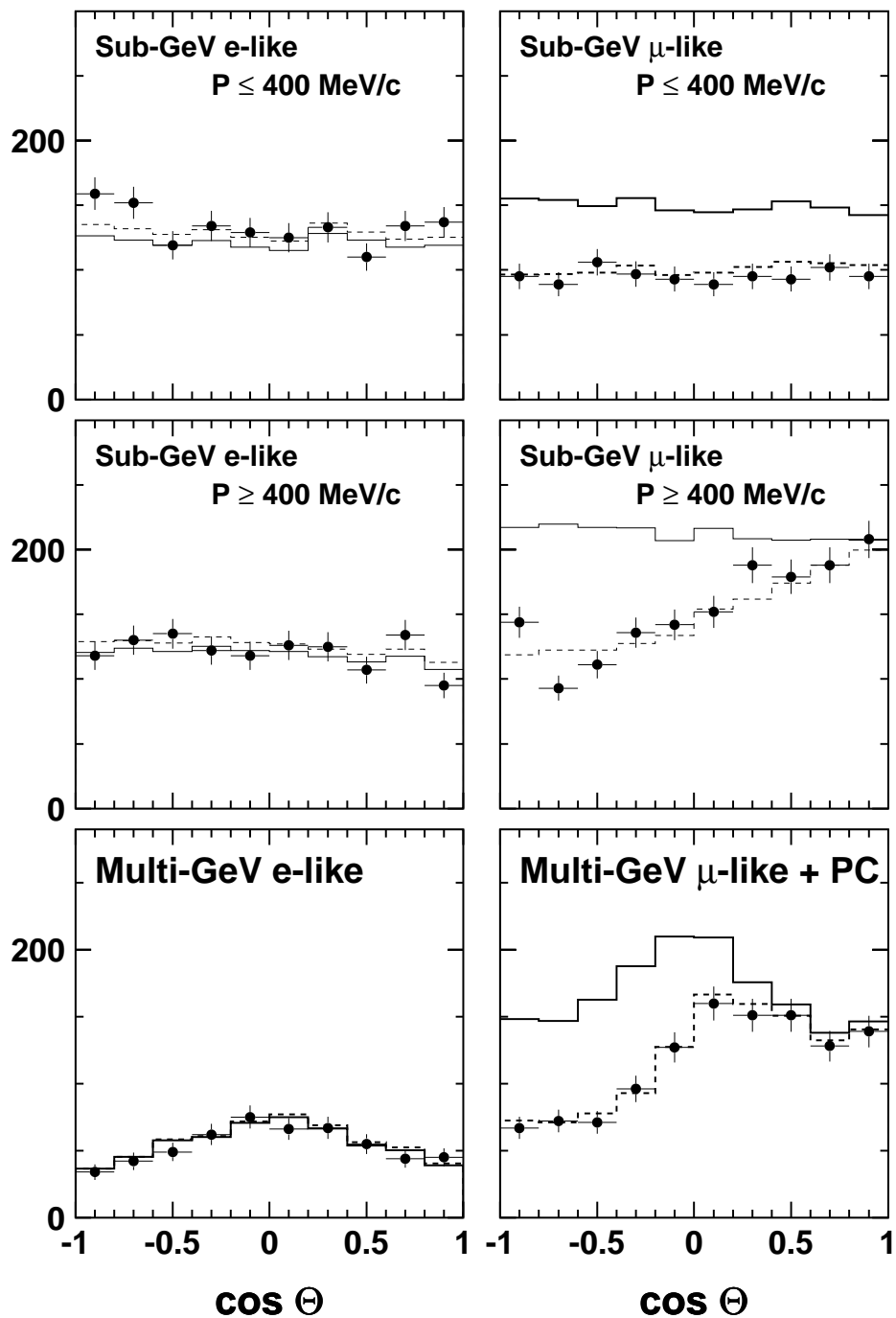


Figure 9.4: The zenith angle distributions for FC and PC events. Dots show the data, the solid line shows the expectation without neutrino oscillation, and the dashed line shows the best fit result from the  $\nu_\mu \leftrightarrow \nu_\tau$  neutrino oscillation analysis.

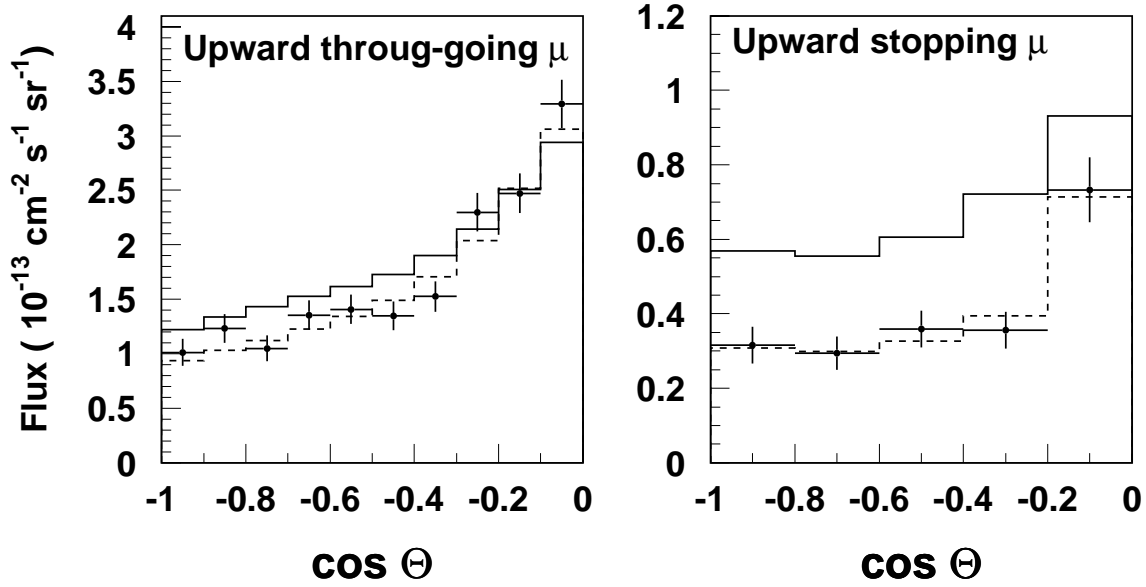


Figure 9.5: The zenith angle distribution for upward-going muons. Dots show the data, the solid line shows the expectation without neutrino oscillation, the dashed line shows the best fit result from the  $\nu_\mu \leftrightarrow \nu_\tau$  neutrino oscillation analysis.

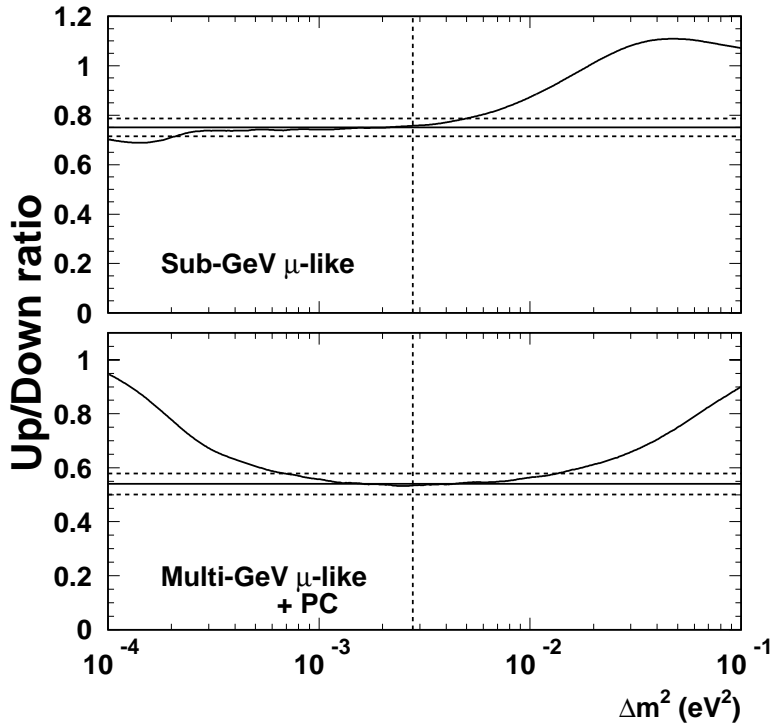


Figure 9.6: The expected  $Up/Down$  ratio as a function of  $\Delta m^2$  for Sub-GeV single-ring  $\mu$ -like (upper figure) and Multi-GeV  $\mu$ -like + PC events (lower figure). The horizontal lines show the observed and one standard deviation values.  $\sin^2 2\theta$  is chosen to be 1.0 in the figures. The vertical dashed line shows  $\Delta m^2 = 2.8 \times 10^{-3} \text{eV}^2$ .

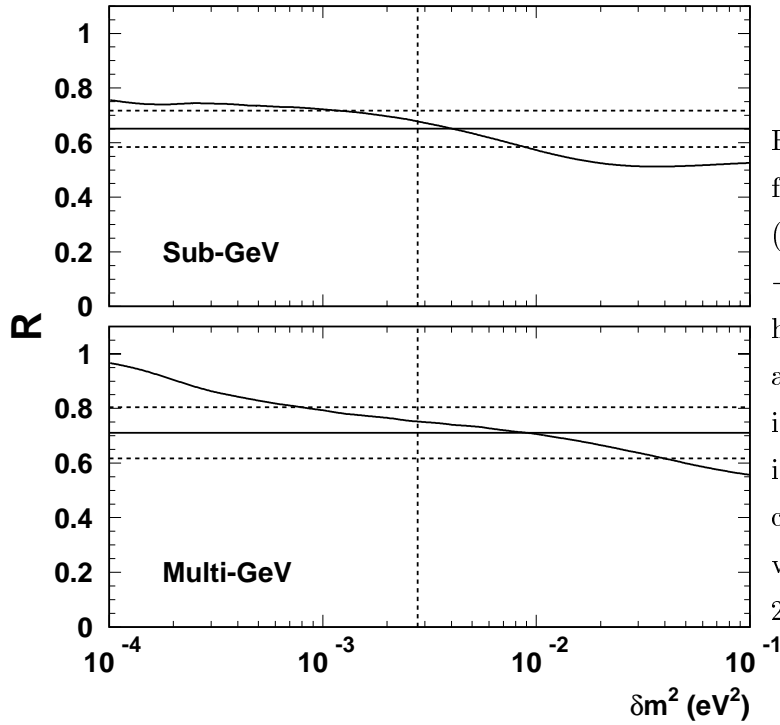


Figure 9.7: The expected  $R$  as a function of  $\Delta m^2$  for Sub-GeV events (upper figure) and Multi-GeV  $\mu$ -like + PC events (lower figure). The horizontal line shows the observed and one standard deviation values including both statistical and experimental systematic errors.  $\sin^2 2\theta$  is chosen to be 1.0 in the figures. The vertical dashed lines show  $\Delta m^2 = 2.8 \times 10^{-3} \text{eV}^2$ .

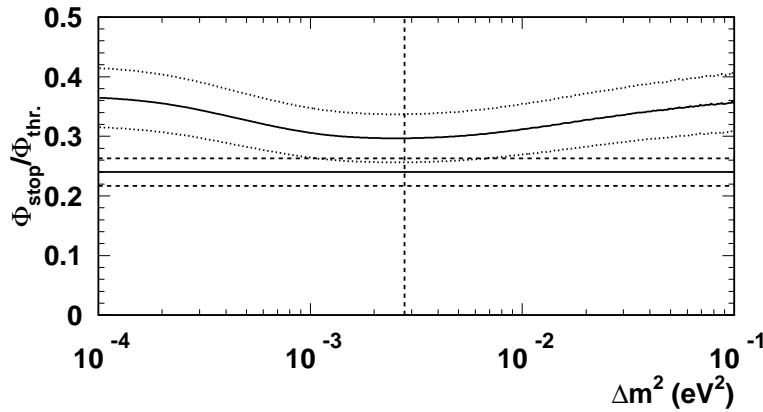


Figure 9.8: The expected  $\Phi_{\text{stop}}/\Phi_{\text{thr}}$  ratio as a function of  $\Delta m^2$  with its systematic uncertainty. The horizontal lines show the observed values and their one standard deviation including both statistical and experimental systematic errors.  $\sin^2 2\theta$  is chosen to be 1.0 in the figure. The vertical dashed line shows  $\Delta m^2 = 2.8 \times 10^{-3} \text{eV}^2$ .

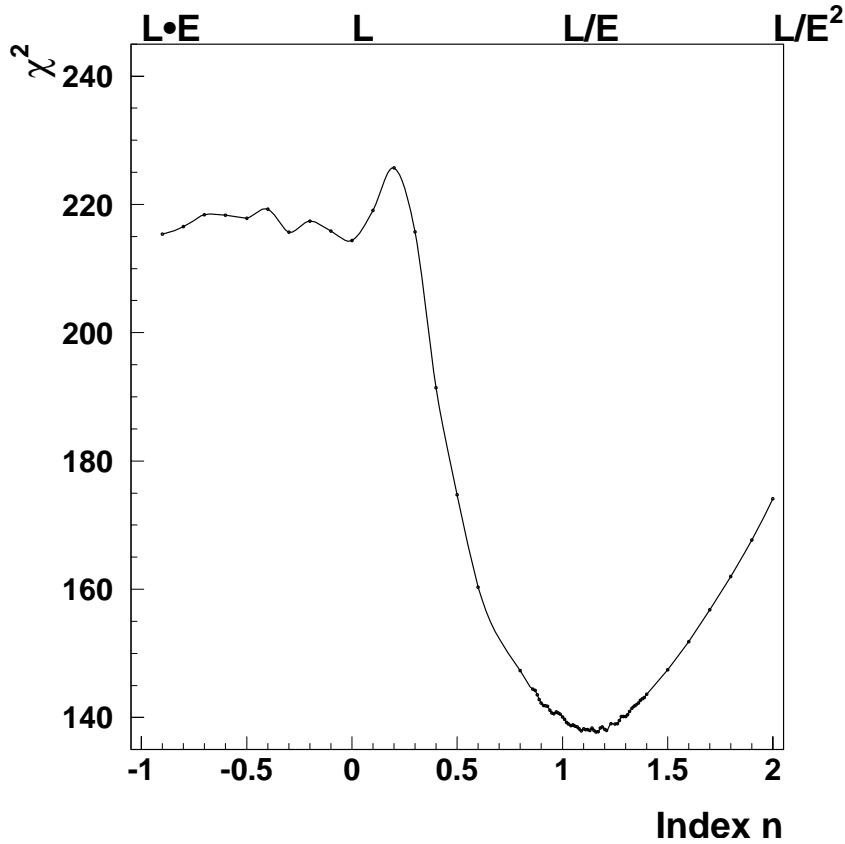


Figure 9.9:  $\chi^2$  distribution as a function of energy index  $n$ . The horizontal axis shows the energy index  $n$  and vertical axis shows  $\chi^2$  of the best fit point for each  $n$ . The minimum  $\chi^2$  was 137.7/152 d.o.f. at  $n = 1.16$ .

on the theory. Neutrino oscillation induced by finite neutrino masses predicts  $n = 1$ . To test the possible theories of neutrino oscillations with different energy indices (violation of Lorentz invariance ( $n = -1$ ), violation of equivalent principle ( $n = -1$ ), CPT violation ( $n = 0$ ), and so on), we scanned the parameter space ( $\sin^2 2\theta, \beta, n$ ). The predicted energy indices  $n$  are all integer numbers, however, the scanning included non-integer  $n$  in this analysis. We scanned from  $-2$  ( $L/E^2$  case) to  $1$  ( $L \cdot E$  case) with a step size of  $0.1$ , and with a smaller step size of  $0.01$  between  $1.4$  and  $0.85$ . The scanned region of  $\beta$  is chosen for each  $n$  so as not to miss the global  $\chi^2$  minimum point. The definition of  $\chi^2$  is described in Section 9.1, but we didn't consider the  $L/E$  systematic uncertainty in this analysis. Figure 9.9 shows the  $\chi^2$  distribution as a function of index  $n$ . The minimum value of the  $\chi^2$  is 137.7/152 d.o.f. at  $n = 1.16$ . We fit a parabola function to the  $\chi^2$  distribution and we estimate  $n$  to be  $1.14 \pm 0.11$ . Fig. 9.10 shows the fit result. From this analysis, non-standard neutrino oscillation hypotheses which predict  $n \neq 1$  are strongly disfavored.

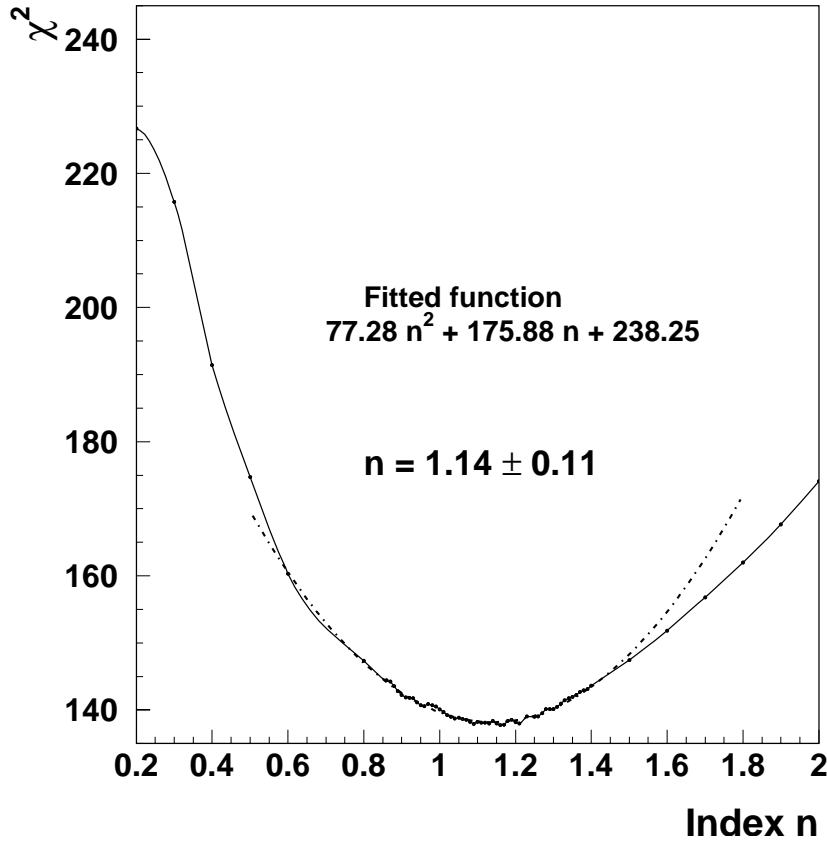


Figure 9.10:  $\chi^2$  distribution as a function of energy index  $n$ . Horizontal axis shows energy index  $n$  and vertical axis shows  $\chi^2$  of the best fit point for each  $n$ . A Parabola function was used to fit the  $\chi^2$  distribution, and  $n$  is estimated to  $1.14 \pm 0.11$ .

## 9.6 Flavour Changing Neutral Current

If a flavour changing neutral current (FCNC) interaction exists, neutrino oscillations occur while passing through matter even if the neutrinos are massless. The general form of the survival probability of the neutrino oscillation due to FCNC interaction is as described in Section 1.2.4:

$$P(\nu_\mu \rightarrow \nu_\mu) = 1 - \frac{\epsilon^2}{\epsilon^2 + (\epsilon'/2)^2} \sin^2 \left( \sqrt{2} G_F X_f \sqrt{\epsilon^2 + (\epsilon'/2)^2} \right) \quad (9.25)$$

Here,  $\epsilon$  is the relative amplitude of the  $\nu_\mu + f \rightarrow \nu_\tau + f$  forward scattering to the non-flavour-changing NC interaction in the Standard Model,  $\epsilon'$  represents the difference of the  $\nu_\mu + f \rightarrow \nu_\mu + f$  and  $\nu_\tau + f \rightarrow \nu_\tau + f$  forward scattering amplitude,  $G_F$  is the Fermi coupling constant, and  $X_f$  is a fermion column density along the neutrino path (number of fermions/cm<sup>2</sup>). In the Standard Model,  $\epsilon = \epsilon' = 0$ . The above survival probability for massless neutrinos has no energy dependence, and it is determined by the column density  $X_f$ .

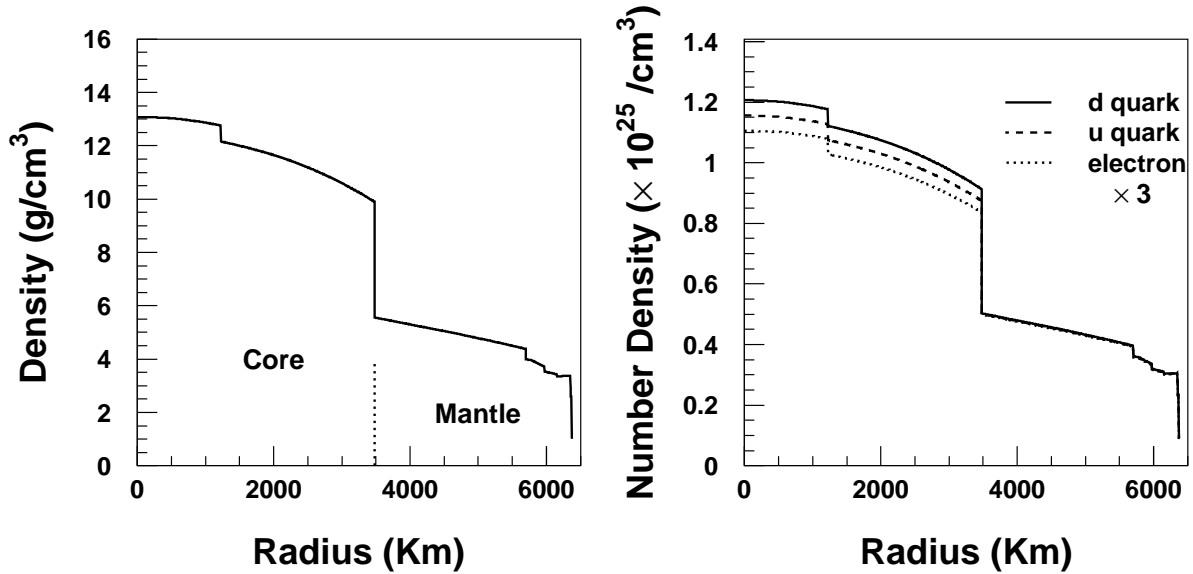


Figure 9.11: (Left figure) Mass density distribution as a function of the radius of the Earth from Ref.[26]. (Right figure) The number density for  $d$ -quark,  $u$ -quark, and electron as a function of the radius of the Earth.

In the analysis, we assume that the FCNC interaction in matter is only with  $d$ -quarks. Any other scenario can be obtained from our results by rescaling, because  $n_d \simeq n_u \simeq 3n_e$  in the Earth, where  $n_d$ ,  $n_u$  and  $n_e$  are the number density for  $d$ -quark,  $u$ -quark, and electron, respectively. Also, we simply assume that  $\epsilon$  and  $\epsilon'$  for anti-neutrinos are the same as those for neutrinos.

The matter density in the Earth is well understood from a large set of seismic measurements. We employed the PREM(Preliminary Reference Earth Model [26]) in our calculation. Fig. 9.11 shows the PREM mass density. The charge to mass ratio ( $Z/A$ ) for the nuclei is estimated to be 0.468 for the core and 0.472 for the mantle [27]. Fig. 9.11 shows the number density for  $d$ -quark,  $u$ -quark, and electrons. The density function shapes are the same to within 5%.

Neutrino oscillations induced by a FCNC interaction for massless neutrinos cause an energy-independent disappearance probability. This fact causes a mismatch between the data and the expectation especially in the  $\Phi_{\text{stop}}/\Phi_{\text{thr}}$  ratio. Fig. 9.12 shows the calculated  $\Phi_{\text{stop}}/\Phi_{\text{thr}}$  ratio as a function of  $\beta \equiv \sqrt{\epsilon^2 + (\epsilon'/2)^2}$ . The  $\Phi_{\text{stop}}/\Phi_{\text{thr}}$  ratio is not affected by the neutrino oscillation by FCNC, therefore the smallness of the observed  $\Phi_{\text{stop}}/\Phi_{\text{thr}}$  ratio can not be explained in this scheme.

The best fit parameter set  $(\epsilon, \epsilon')$  was searched for using the  $\chi^2$  method. The definition of the  $\chi^2$  is the same as Eq. 9.2, but the  $L/E$  uncertainty is not considered because the uncertainty of the flight length of the neutrinos in the atmosphere doesn't affect the survival probability of

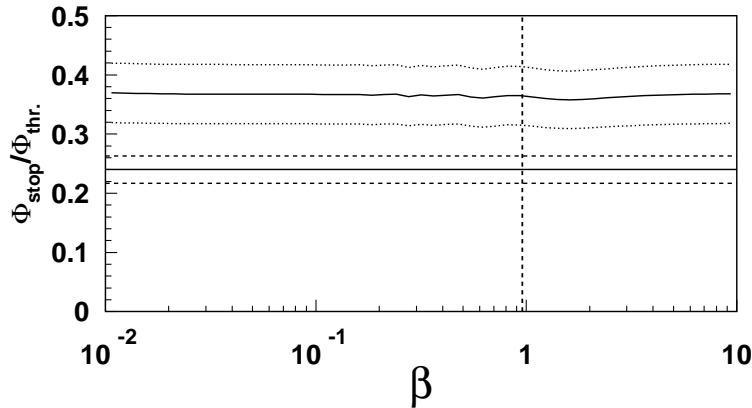


Figure 9.12: The expected  $\Phi_{\text{stop}}/\Phi_{\text{thr.}}$  ratio as a function of  $\beta \equiv \sqrt{\epsilon^2 + (\epsilon'/2)^2}$ . The dashed curves show the systematic uncertainty in the prediction (13.3%). The oscillation amplitude  $\epsilon^2 / (\epsilon^2 + (\epsilon'/2)^2)$  is set to the best fit value (0.89). The horizontal lines show the observed value and one standard deviation including both statistical and experimental systematic errors. The vertical dotted line shows the best fit  $\beta$  (0.95).

the neutrinos. We obtained  $\chi_{\text{min}}^2 = 209.9/152$  d.o.f at  $(\epsilon, \epsilon') = (0.90, 0.63)$ , with a probability of 0.1%. We note that  $\chi_{\text{min}}^2$  for  $\nu_\mu \rightarrow \nu_\tau$  oscillation induced by finite neutrino masses is 140.0/152 d.o.f., and the  $\chi_{\text{min}}^2$  value for FCNC hypothesis is larger than that by 69.9. Therefore, we conclude that the FCNC hypothesis is excluded as the primary source of the observed atmospheric neutrino data. Fig. 9.13 compares the zenith angle distribution for the data and the expectation from FCNC with a best fit parameters. Table 9.8 shows the summary of the fitting parameters from the FCNC analysis.

## 9.7 Neutrino Decay

Neutrino decay to a sterile state may explain the observed deficit of the upward-going  $\nu_\mu$ s. Here, we consider the case where the mass eigenstate  $\nu_3$  has a decay channel to a sterile state:

$$\nu_3 \rightarrow X \quad (9.26)$$

where  $X$  represents inactive particles which do not interact with matter. Several theories provide candidates for  $X$ , e.g., right-handed neutrinos and iso-singlet bosons [38], sterile neutrinos and Majorons [39], and so on. The survival probability can be written by the same formula irrespective of the details of the theories. We don't consider the neutrino decay to an active neutrino here. Neutrino decay to an active neutrino is described later. Here we consider the

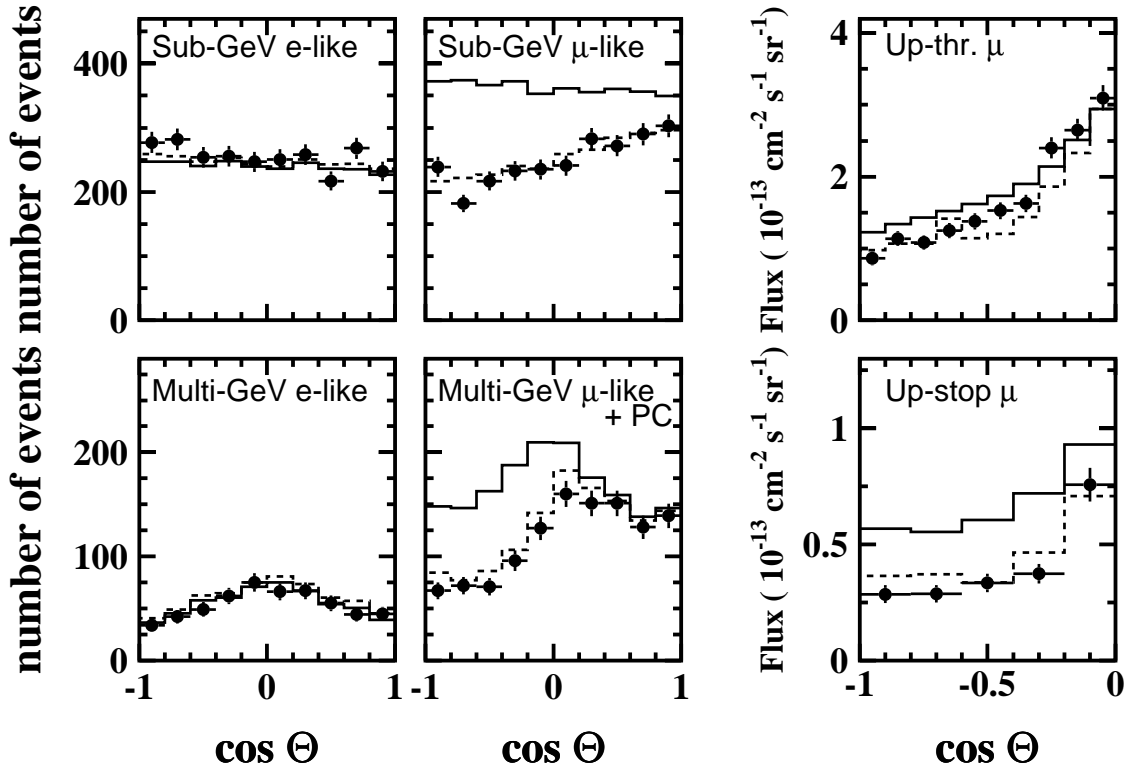


Figure 9.13: Zenith angle distribution for FCNC with the best fit parameters which are summarized in Table 9.8.

$\alpha$	Absolute Normalization	0.0%	(free)
$\beta_s$	Sub-GeV $\mu/e$ Ratio	-15.3%	(6.0%)
$\beta_m$	Multi-GeV $\mu/e$ Ratio	-18.0%	(9.2%)
$\rho$	PC/FC relative normalization	-2.8%	(10.5%)
$\eta_s$	Sub-GeV Up/Down ratio	-0.8%	(2.7%)
$\eta_m$	Multi-GeV Up/Down ratio	0.7%	(2.8%)
$\delta$	$E_\nu$ spectrum	0.034	(0.05)
$\rho_t$	Up-stop $\mu$ /Up-thr $\mu$ relative norm.	-14.2%	(5.6%)
$\rho_s$	FC 1-ring/Up- $\mu$ relative norm.	24.2%	(9.2%)
$\kappa_f$	H/V ratio of FC	-3.4%	(4%)
$\kappa_u$	H/V upward thr. $\mu$	1.7%	(3%)

Table 9.8: Summary of the best fit systematic uncertainty parameters of the FCNC analysis.

case where  $\nu_\mu$  and  $\nu_\tau$  are superpositions of  $\nu_2$  and  $\nu_3$ :

$$\begin{pmatrix} |\nu_\mu\rangle \\ |\nu_\tau\rangle \end{pmatrix} = \begin{pmatrix} \cos\theta & \sin\theta \\ -\sin\theta & \cos\theta \end{pmatrix} \begin{pmatrix} |\nu_2\rangle \\ |\nu_3\rangle \end{pmatrix} \quad (9.27)$$

We assume  $m_3 > m_2 > 0$ . In general, neutrino decay co-exists with neutrino oscillation due to finite neutrino masses. The survival probability for neutrino decay to a sterile state co-existing with neutrino oscillation is written as:

$$\begin{aligned} P(\nu_\mu \rightarrow \nu_\mu) = & \cos^4\theta + \sin^4\theta \exp\left(-\frac{m_3 L_\nu}{\tau_3 E_\nu}\right) \\ & + \frac{1}{2} \sin^2 2\theta \exp\left(-\frac{m_3 L_\nu}{2\tau_3 E_\nu}\right) \cos\left[\frac{\Delta m^2}{2E_\nu} L_\nu\right] \end{aligned} \quad (9.28)$$

where  $E_\nu$  is the neutrino energy,  $L_\nu$  is the flight length of neutrino,  $\theta$  is the mixing angle of neutrinos,  $\Delta m^2$  is the difference of the mass squared of the two mass eigenstates  $\nu_2$  and  $\nu_3$ ,  $\tau_3$  and  $m_3$  are the lifetime and the mass of  $\nu_3$ , respectively. In general, the survival probability is parameterized by  $(\sin^2\theta, \tau_3/m_3, \Delta m^2)$ . However, we considered the following two special cases:

- Neutrino decay dominant case ( $\Delta m^2 \rightarrow 0$ ):

$$\begin{aligned} P(\nu_\mu \rightarrow \nu_\mu) &= \cos^4\theta + \sin^4\theta \exp\left(-\frac{m_3 L_\nu}{\tau_3 E_\nu}\right) + \frac{1}{2} \sin^2 2\theta \exp\left(-\frac{m_3 L_\nu}{2\tau_3 E_\nu}\right) \\ &= \left(\cos^2\theta + \sin^2\theta \exp\left(-\frac{m_3 L_\nu}{2\tau_3 E_\nu}\right)\right)^2 \end{aligned} \quad (9.29)$$

- Neutrino oscillation dominant case ( $\Delta m^2 \rightarrow \infty$ ):

$$P(\nu_\mu \rightarrow \nu_\mu) = \cos^4\theta + \sin^4\theta \exp\left(-\frac{m_3 L_\nu}{\tau_3 E_\nu}\right) \quad (9.30)$$

The first case is that where there is no neutrino oscillation, or the neutrino oscillation length  $\lambda_{\text{osc}}$  is much longer than the neutrino decay length  $\lambda_{\text{decay}}$ , and the effect of the oscillation is negligibly small. This case is mathematically expressed by the limit  $\Delta m^2 \rightarrow 0$ . The second case is that where  $\lambda_{\text{osc}}$  is much shorter than  $\lambda_{\text{decay}}$ , and the effect of neutrino oscillation is averaged. This case is mathematically expressed by the limit  $\Delta m^2 \rightarrow \infty$ . In both cases, the survival probability is parameterized by two parameters,  $(\sin^2\theta, m_3/\tau_3)$ .

We carried out the  $\chi^2$  test for the two cases. The definition of  $\chi^2$  is same as for  $\nu_\mu \leftrightarrow \nu_\tau$  2-flavour neutrino oscillation analyses, but the  $L/E$  systematic uncertainty is not considered. We scanned  $(\sin^2\theta, m_3/\tau_3)$  space.

For  $\Delta m^2 \rightarrow \infty$ , we obtained  $\chi_{\text{min}}^2 = 260.6/152$  d.o.f. at  $(\sin^2\theta, m_3/\tau_3) = (0.48, 3.2 \times 10^{-3} \text{GeV/km})$ . This scheme predicts not only the deficit of upward-going  $\nu_\mu$ 's, but also the

deficit of the downward-going  $\nu_\mu$ 's due to neutrino oscillation. The probability for this scheme is less than  $10^{-5}\%$ . We therefore conclude that the hypothesis is excluded as a primary source of the observed muon neutrino deficit.

For  $\Delta m^2 \rightarrow 0$  case, we obtained  $\chi_{min}^2 = 148.2/152$  d.o.f. at  $(\sin^2 \theta, m_3/\tau_3) = (0.33, 1.26 \times 10^{-2} \text{ GeV/km})$ . The  $\chi_{min}^2$  is larger by 8.2 than that for  $\nu_\mu \leftrightarrow \nu_\tau$  oscillation induced by finite neutrino masses. Therefore we can not distinguish these two hypotheses from the study of FC 1-ring + PC + upward-going muons at a high confidence level. Fig. 9.14 shows the zenith angle distributions for FC, PC, and upward-going muons for the  $\Delta m^2 \rightarrow 0$  limit. Table 9.9 shows the best fit systematic error parameters.

In the case where a neutrino decays to an active neutrino  $\nu_2$ , for example,  $\nu_3 \rightarrow \bar{\nu}_2 + J$  where  $J$  is a Majoron, the effective interaction is written as:

$$\mathcal{L} = g_{23} \overline{\nu_{2L}^c} \nu_{3L} J + \text{h.c.}, \quad (9.31)$$

where  $g_{23}$  is a coupling constant [161].

The lifetime of  $\nu_3$  in the  $\nu_3$  rest frame is given by:

$$\tau_3 = \frac{16\pi}{g_{23}^2} \frac{m_3^3}{\Delta m^2 (m_2 + m_3)^2}, \quad (9.32)$$

where  $m_i$  is the mass of  $\nu_i$ , and  $\Delta m^2 = m_3^2 - m_2^2$ . From the experimental limits from searches for  $K \rightarrow \mu + \text{neutrals}$ , a bound on  $g_{23}$  is derived as  $g_{23}^2 < 2.4 \times 10^{-4}$  [162]. In order to explain the deficits of the upward-going muon neutrinos by neutrino decay, especially FC events ( $L/E \sim 10000 \text{ km/GeV}$ ),  $\tau_3/m_3$  should be less than  $10^4 \text{ (km/GeV)}$ . From these conditions, a bound on  $\Delta m^2$  is estimated as:

$$\Delta m^2 = \frac{16\pi}{g_{23}^2} \frac{1}{\left(\frac{m_2}{m_3} + 1\right)^2} \cdot \frac{m_3}{\tau_3} \gtrsim 1 \text{ eV}^2 \quad (9.33)$$

This condition corresponds to the  $\Delta m^2 \rightarrow \infty$  case described above. In addition, the produced  $\bar{\nu}_2$ 's increase the upward-going  $\nu_\mu$  event rate, and the fit to the data is expected to be poorer than in the case where neutrinos decay to a sterile state.

### 9.7.1 Neutrino Decay Analysis using Neutral Current Events

One feature of the neutrino decay to a sterile state,  $\nu_3 \rightarrow X$ , is that the number of NC interactions is decreased by the same amount as the CC interactions. On the other hand,  $\nu_\mu \leftrightarrow \nu_\tau$  flavour oscillation doesn't decrease the number of NC interactions. Therefore, we can distinguish  $\nu_\mu \leftrightarrow \nu_\tau$  oscillation and neutrino decay to a sterile state by studying NC events.

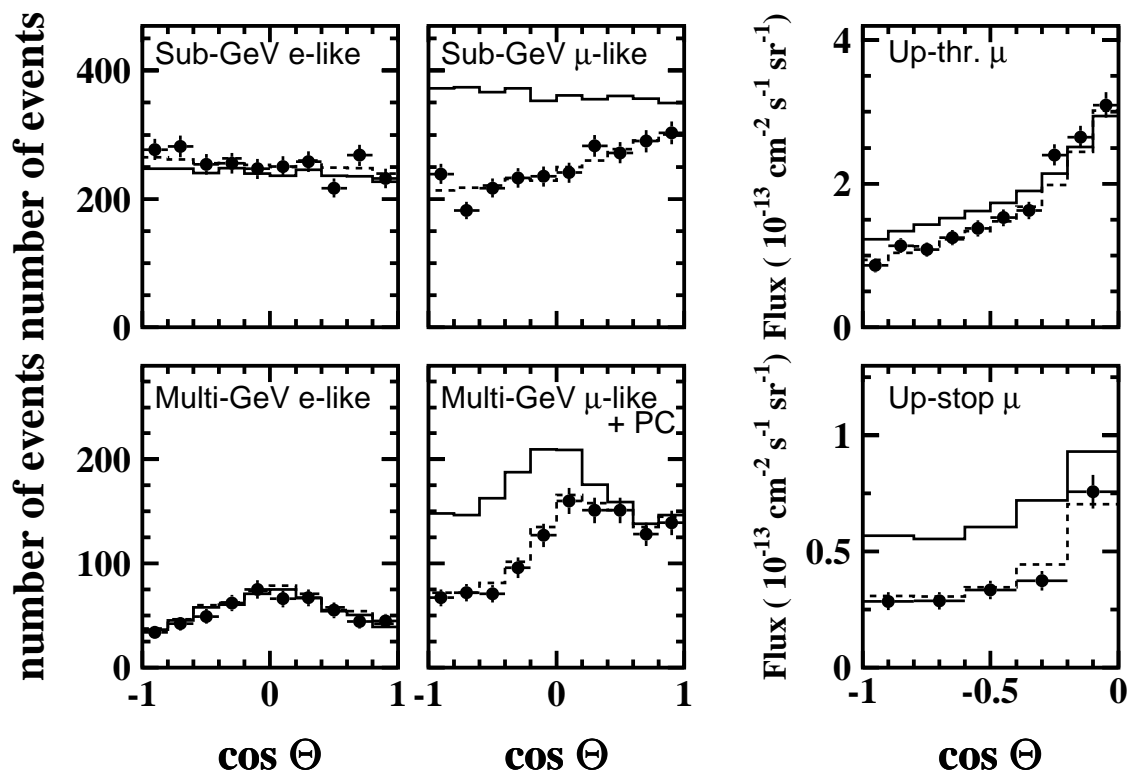


Figure 9.14: Zenith angle distribution of FC, PC, and upward-going muons with the best fit result from neutrino decay ( $\Delta m^2 \rightarrow 0$ ). Solid lines show the zenith angle distribution without neutrino decay, dashed lines show the best fit expectation from neutrino decay analysis.

		$\Delta m^2 \rightarrow 0$	$\Delta m^2 \rightarrow \infty$	
$\alpha$	Absolute Normalization	6.2%	36.9%	(free)
$\beta_s$	Sub-GeV $\mu/e$ Ratio	2.7%	30.8%	(6.0%)
$\beta_m$	Multi-GeV $\mu/e$ Ratio	-5.1%	24.9%	(9.2%)
$\rho$	PC/FC relative normalization	-0.7%	-4.6%	(10.5%)
$\eta_s$	Sub-GeV Up/Down ratio	-1.1%	-1.5%	(2.7%)
$\eta_m$	Multi-GeV Up/Down ratio	-0.03%	3.5%	(2.8%)
$\delta$	$E_\nu$ spectrum	-0.020	0.031	(0.05)
$\rho_t$	Up-stop $\mu$ /Up-thr $\mu$ relative norm.	-4.2%	-7.2%	(5.6%)
$\rho_s$	FC 1-ring/Up $\mu$ relative norm.	12.7%	15.3%	(9.2%)
$\kappa_f$	H/V ratio of FC	-0.9%	-3.0%	(4%)
$\kappa_u$	H/V ratio of upward thr. $\mu$	0.4%	2.0%	(3%)

Table 9.9: Summary of the best fit systematic uncertainty parameters of the neutrino decay analysis for  $\Delta m^2 \rightarrow 0$  and  $\Delta m^2 \rightarrow \infty$  cases.

We carried out a further test of the neutrino decay hypothesis using the *Up/Down* ratio of a NC enriched event sample. If the neutrino decay to a sterile state is the solution of the deficit of the upward-going  $\nu_\mu$ s, we should also see the deficit in the upward-going NC samples, and therefore a small *Up/Down* ratio.

The selection criteria of the NC enriched sample are as follows:

- (1) FC sample, number of rings  $> 1$
- (2) PID for the brightest ring is *e*-like
- (3)  $E_{vis} > 400$  MeV

The purpose of the first and second criteria are to enrich the NC events. The NC interactions are detected by Cherenkov photons from multiple hadrons (mostly pions). Because of this, NC interactions are likely to be detected as multi-ring events. The brightest rings of multi-hadron production events are likely to be identified as *e*-like, because they are mainly made by electromagnetic showers from  $\pi^0$ s or hadronic showers which create smeared Cherenkov rings images. The third criterion is used to obtain a good angular correlation between the incident neutrino and the reconstructed direction. The direction of the NC enriched sample,  $\vec{d}_m$ , is defined as:

$$\vec{d}_m = \frac{\sum_i \vec{p}_i}{|\sum_i p_i|} \quad (9.34)$$

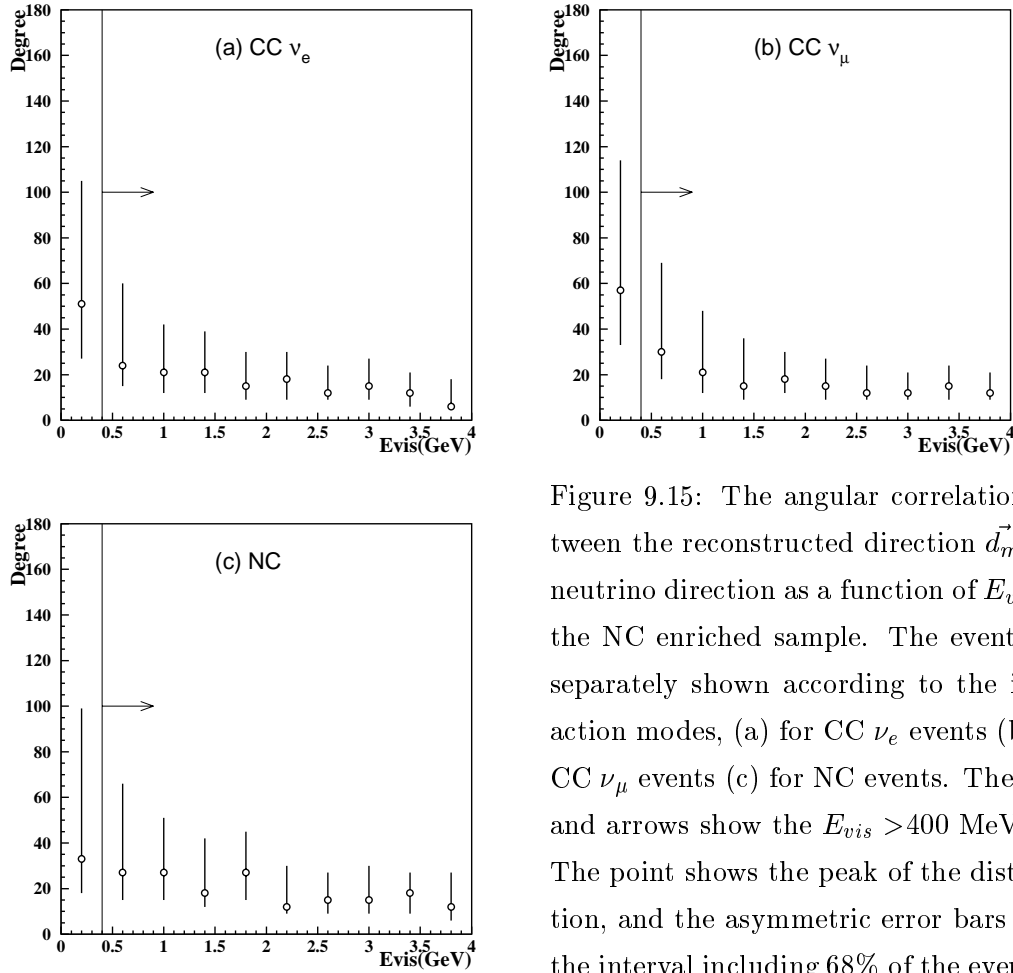


Figure 9.15: The angular correlation between the reconstructed direction  $\vec{d}_m$  and neutrino direction as a function of  $E_{vis}$  for the NC enriched sample. The events are separately shown according to the interaction modes, (a) for CC  $\nu_e$  events (b) for CC  $\nu_\mu$  events (c) for NC events. The lines and arrows show the  $E_{vis} > 400$  MeV cut. The point shows the peak of the distribution, and the asymmetric error bars show the interval including 68% of the events of each side of the peak.

where  $\vec{p}_i$  is the 3-momentum of the  $i$ th ring calculated by assuming the ring was produced by an electron. Fig. 9.15 shows the angular correlation between the neutrino direction and reconstructed direction  $\vec{d}_m$  as a function of  $E_{vis}$ . The angular correlation is about  $30^\circ$  at  $E_{vis} \sim 1$  GeV. Table 9.10 shows the fraction of event types. The fraction of  $\nu_\mu$  NC events in this sample is estimated to be about 22%.

Fig. 9.16 shows the expected  $Up/Down$  ratio for neutrino decay and  $\nu_\mu \rightarrow \nu_\tau$  neutrino oscillation as a function of  $m_3/\tau_3$  and  $\Delta m^2$ . The  $Up$  events are defined as the events with  $\cos \Theta < -0.2$ , and the  $Down$  events are defined as the events with  $\cos \Theta > 0.2$ . In the figures,  $\sin^2 \theta$  is set to the best fit values from the FC 1-ring + PC + upward-going muons analyses ( $\sin^2 \theta = 0.33$  for neutrino decay and  $\sin^2 2\theta = 1.00$  for  $\nu_\mu \leftrightarrow \nu_\tau$  oscillation). Vertical lines show the best fit parameters,  $m_3/\tau_3 = 1.26 \times 10^{-2}$  (GeV/km) and  $\Delta m^2 = 2.8 \times 10^{-3}$  eV<sup>2</sup>. The horizontal solid lines show the observed  $Up/Down$  ratio and the dashed lines indicate one

CC $\nu_e + \bar{\nu}_e$	46.0%
CC $\nu_\mu + \bar{\nu}_\mu$	24.9%
NC $\nu_e + \bar{\nu}_e$	7.5%
NC $\nu_\mu + \bar{\nu}_\mu$	21.6%

Table 9.10: Estimated fraction of the interaction modes in NC enriched sample.

standard deviation including both statistical and systematic errors. Solid curves and dotted curves show the predicted  $Up/Down$  ratio and their  $\pm 1\sigma$  systematic uncertainty. These figures show that the  $Up/Down$  ratio of NC enriched sample can be used to distinguish between neutrino decay to a sterile state and  $\nu_\mu \leftrightarrow \nu_\tau$  neutrino oscillation.

Fig. 9.17 shows the zenith angle distribution of the NC enriched sample. The solid line shows the expectation for  $\nu_\mu \rightarrow \nu_\tau$  neutrino oscillation, and dashed line shows the expectation for neutrino decay ( $\Delta m^2 \rightarrow 0$  limit). The expected distributions are made with the best fit parameters from the FC 1-ring + PC + upward-going muons analyses, and are normalized by the number of the downward-going events. Neutrino decay predicts a clear deficit of upward-going NC events.

The observed  $Up/Down$  ratio and the expected value for  $\nu_\mu \leftrightarrow \nu_\tau$  oscillation and neutrino decay with  $\Delta m^2 \rightarrow 0$  limit are:

$$\text{Observed} \quad : \quad Up/Down = 0.96 \pm 0.072_{(\text{stat.})} \pm 0.005_{(\text{sys.})} \quad (9.35)$$

$$\text{Null oscillation} \quad : \quad Up/Down = 0.99 \pm 0.03_{(\text{sys.})} \quad (9.36)$$

$$\nu_\mu \leftrightarrow \nu_\tau \text{ oscillation} \quad : \quad Up/Down = 0.97 \pm 0.03_{(\text{sys.})} \quad (9.37)$$

$$\text{Neutrino decay } (\Delta m^2 \rightarrow 0) \quad : \quad Up/Down = 0.86 \pm 0.02_{(\text{sys.})} \quad (9.38)$$

The observed  $Up/Down$  ratio is consistent with unity, and consistent with  $\nu_\mu \rightarrow \nu_\tau$  neutrino oscillation with best fit parameters from FC 1-ring + PC + upward-going muons analysis, and also consistent with null oscillation. However, neutrino decay ( $\Delta m^2 \rightarrow 0$ ) predicts a smaller  $Up/Down$  ratio than is observed in data.

### 9.7.2 Systematic Uncertainty in the $Up/Down$ Ratio of the NC Sample

The  $Up/Down$  ratio largely cancels out systematic uncertainties, such as the  $\nu$  cross section, absolute flux, event reconstruction, and so on. The  $Up/Down$  ratio has a total systematic

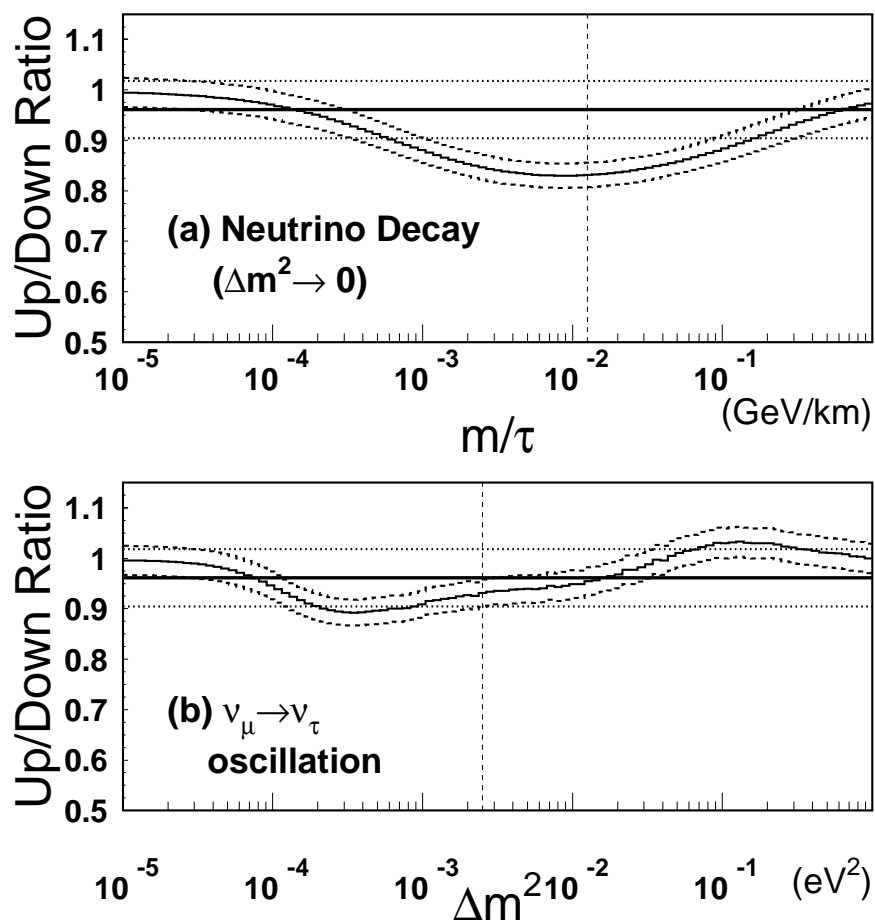


Figure 9.16: The expected  $Up/Down$  ratio for (a) neutrino decay (b)  $\nu_\mu \rightarrow \nu_\tau$  neutrino oscillation as a function of the neutrino decay width and  $\Delta m^2$ . The mixing angle is chosen to be the best fit value from the FC 1-ring + PC + upward-going muons analysis in each case. The horizontal solid straight lines show the observed  $Up/Down$  ratio =  $568/591 = 0.96$  and the dashed lines show  $\pm 1\sigma$  including both statistical and systematic uncertainty. The solid and dotted curves show the expected  $Up/Down$  ratio and  $\pm 1\sigma$  systematic uncertainty, respectively. The Vertical dotted line shows (a)  $m_\nu/\tau_\nu = 1.26 \times 10^{-2}$  km/GeV and (b)  $\Delta m^2 = 2.8 \times 10^{-3}$   $\text{eV}^2$ .

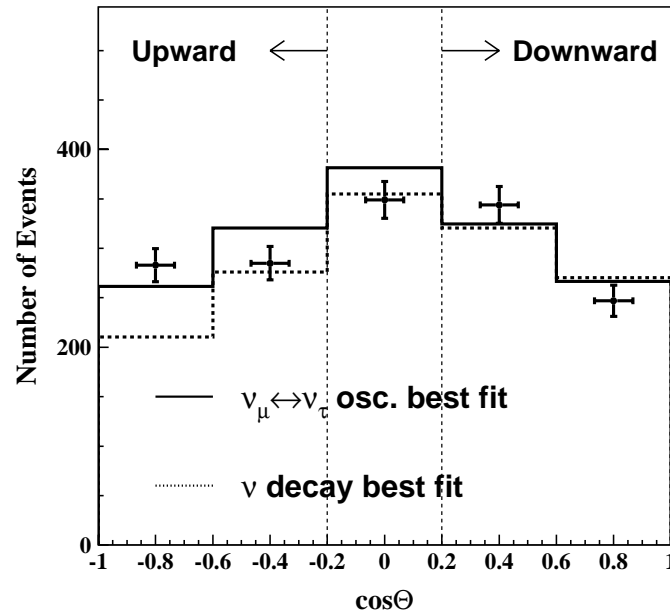


Figure 9.17: The zenith angle distribution for NC enriched event sample. The markers show the data with their statistical errors. The solid line shows the expectation for  $\nu_\mu \rightarrow \nu_\tau$  neutrino oscillation with  $(\sin^2 2\theta, \Delta m^2) = (1.0, 2.8 \times 10^{-3} \text{eV}^2)$ , and the dashed line shows the expectation for neutrino decay with  $\Delta m^2 \rightarrow 0$  and  $(\sin^2 \theta, m_3/\tau_3) = (0.33, 1.26 \times 10^{-2} \text{GeV/km})$ . The normalization is independently made to the number of the downward-going events.

	Source	Systematic uncertainty(%)
Data	B.G. contamination	0.3
	Energy scale ( $\pm 0.6\%$ )	0.4
Total		0.5
MC	Predicted flux(Honda vs Bartol)	0.8
	Mountain over Super-K	2.6
	$E_\nu$ spectral index	0.1
	Neutrino interaction	0.9
Total		2.9

Table 9.11: Summary of the systematic uncertainty of the  $Up/Down$  ratio of NC enriched sample.

uncertainty of 0.5% in the data and 2.9% in the prediction. The systematic uncertainties in the  $Up/Down$  ratio for the NC enriched sample are summarized in Table 9.11.

The remaining systematic uncertainties in the data come from the up-down asymmetry of the energy scale and non-neutrino backgrounds. The asymmetry of the energy scale is estimated to be about  $\pm 0.6\%$ , and it causes a  $\pm 0.4\%$  uncertainty in the ratio. The non-neutrino backgrounds in the NC enriched sample are assumed to be flashing PMTs, and their effect is estimated to be 0.3%.

The uncertainty in the prediction comes mainly from the uncertainty in the up-down ratio of the calculated neutrino flux. To estimate this uncertainty, we compared results from two independent calculated neutrino fluxes [78, 79]. The effect of this uncertainty on the  $Up/Down$  ratio is estimated to be 0.8%. The effect of the mountain above Super-Kamiokande is also a source of the systematic uncertainty. The mountain above Super-Kamiokande is not taken into account in the calculated fluxes, and we estimate 2.6% uncertainty from this effect. The uncertainty of the energy index of the neutrino flux causes less than 0.1% systematic uncertainty. We estimate the effect of the uncertainty due to the ratio of NC/CC interaction cross sections to be 0.9%.

### 9.7.3 Definition of $\chi^2$ and Results

We carried out a  $\chi^2$  hypothesis test using the NC enriched sample. The definition of the  $\chi^2$  is:

$$\chi_{\text{NC}}^2 = \frac{(N_{\text{obs}}^U - (1 + \alpha)(1 - \epsilon/2)N_{\text{exp}}^U)^2}{\sigma_{U,\text{stat}}^2} + \frac{(N_{\text{obs}}^D - (1 + \alpha)(1 + \epsilon/2)N_{\text{exp}}^D)^2}{\sigma_{D,\text{stat}}^2} + \left(\frac{\epsilon}{\sigma_{\text{sys}}}\right)^2 \quad (9.39)$$

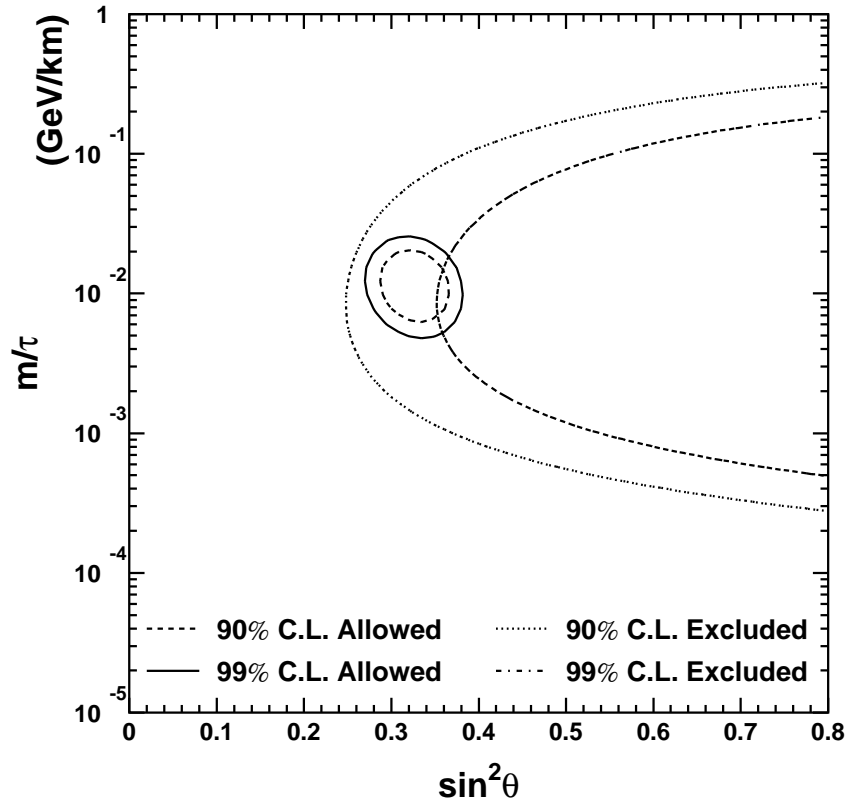


Figure 9.18: Contour plots of the allowed region ( $\sin^2 \theta, \tau_\nu/m_\nu$ ) for  $\Delta m^2 \rightarrow 0$  case. The dashed and solid circles show the 90% and 99% allowed region from the FC 1-ring + PC + upward-going muons analysis, respectively. The dashed and dotted curves show 90% and 99% C.L. excluded region from the NC enriched event sample analysis. The allowed region from FC 1-ring + PC + upward-gong muons analysis is excluded by the NC enriched sample analysis at 90% C.L.

where  $N^U(N^D)$  represents the number of upward(downward) going events,  $\sigma_{U,stat}^2(\sigma_{D,stat}^2)$  represents the statistical errors of upward(downward) events, and  $\epsilon$  represents the systematic uncertainty of the  $Up/Down$  ratio.  $\alpha$  represents the uncertainty of the absolute normalization, and is treated as a free parameter in this analysis. The degree of freedom of the  $\chi^2$  is  $2 - 1 = 1$ .

Fig 9.18 shows a contour plots of the allowed regions from the FC 1-ring + PC + upward-gong muons analysis and the excluded region from the NC enriched sample analysis. The excluded regions at 90% and 99% C.L. are set to be the contour of  $\chi^2 = 2.71$  and 6.63. The result from the NC enriched sample analysis and from the FC 1-ring + PC + upward-going muons analysis are in conflict with each other. The allowed region from the FC 1-ring + PC + upward-going muons analysis is disfavored by the NC enriched sample analysis at the 90% C.L. . Therefore, we conclude that neutrino decay to a sterile state ( $\Delta m^2 \rightarrow 0$ ) is disfavored at the 90% C.L.

# Chapter 10

## Conclusions

We have measured atmospheric neutrinos in Super-Kamiokande. We accumulated 1144.4 days FC and PC events, 1138 days upward through-going muons, and 1117 days upward stopping muons. We measured the flavour ratio  $R \equiv (N_\mu/N_e)_{\text{Data}} / (N_\mu/N_e)_{\text{MC}}$  and *Up/Down* ratio for FC 1-ring + PC events:

$$R = \begin{cases} 0.651_{-0.018}^{+0.019} (\text{stat.}) \pm 0.040 (\text{sys.}) & \text{Sub-GeV} \\ 0.711_{-0.036}^{+0.039} (\text{stat.}) \pm 0.087 (\text{sys.}) & \text{Multi-GeV + PC} \end{cases} \quad (10.1)$$

$$Up/Down = \begin{cases} 0.76 \pm 0.03 (\text{stat.}) \pm 0.002 (\text{sys.}) & \text{Sub-GeV } \mu\text{-like} \\ 0.54_{-0.037}^{+0.039} (\text{stat.}) \pm 0.004 (\text{sys.}) & \text{Multi-GeV + PC} \end{cases} \quad (10.2)$$

These numbers imply that the number of upward-going  $\nu_\mu$ 's are decreased. We tested several possible hypotheses against the data.

- We tested  $\nu_\mu \leftrightarrow \nu_\tau$  2-flavour neutrino oscillations due to several mechanisms. For example, finite masses of neutrinos, violation of the equivalence principle, and violation of the Lorentz invariance. These models predict a  $L/E^n$  ( $n = -1, 0, 1$ ) type energy dependence of the survival probability. We scanned the energy index  $n$ , and the result is  $n = 1.14 \pm 0.11$ . Neutrino oscillation due to massive neutrinos is the most favored mechanism.
- We tested neutrino oscillation induced by Flavour Changing Neutral Current (FCNC). FCNC interaction predicts a energy-independent neutrino survival probability. This causes a mismatch between the prediction and the data, especially in the upward-stopping muon/upward through-going muon ratio. We found that the fit of the prediction for the data is much poorer than the neutrino oscillation induced by finite neutrino masses ( $\chi_{min}^2 = 209.9/152$  d.o.f.,  $P = 0.1\%$ ) The  $\chi_{min}^2$  larger by 69.9 than that for the neutrino oscillation induced

by finite neutrino masses. Therefore, we concluded that the neutrino oscillation induced by FCNC was excluded as a primary source of the observed atmospheric neutrino data.

- Finally, we tested neutrino decay to a sterile state. We studied two special cases: (1) Neutrino oscillation co-exists with the neutrino decay, but the oscillation length is much shorter than the neutrino decay length and the effect of the neutrino oscillation is averaged. (mathematically expressed by the limit  $\Delta m^2 \rightarrow \infty$ ). (2) There is no neutrino oscillation, or the neutrino oscillation length is much longer than the neutrino decay length and the effect of the oscillation is negligibly small. (mathematically expressed by the limit  $\Delta m^2 \rightarrow 0$ ).

The first scheme is quickly excluded by the analysis using FC 1-ring + PC + upward-going muons ( $\chi_{min}^2 = 260.6$ ,  $P < 10^{-5}\%$ ). The second scheme agrees well with FC 1-ring + PC + upward-going muon data, but 99% C.L. allowed parameter region from FC 1-ring + PC + upward-going muons analysis is excluded at 90% C.L. by the analysis using *Up/Down* ratio of the NC enriched Multi-ring sample. Thus, we concluded that neutrino decay to a sterile state is disfavored at 90% C.L..

The most favored mechanism is  $\nu_\mu \leftrightarrow \nu_\tau$  2-flavour neutrino oscillation due to finite masses of the neutrinos. It consistently explains the observed data. We can conclude that our observation of atmospheric neutrinos are strong evidence for the finite mass of the neutrino.

The best fit parameter for  $\nu_\mu \rightarrow \nu_\tau$  2-flavour neutrino oscillation is  $(\sin^2 2\theta, \Delta m^2) = (1.00, 2.8 \times 10^{-3} \text{eV}^2)$ , and the allowed parameter region at 90% C.L. is:

$$1.8 \times 10^{-3} \text{eV}^2 < \Delta m^2 < 4.5 \times 10^{-3} \text{eV}^2 \quad (10.3)$$

$$0.89 < \sin^2 2\theta \quad (10.4)$$

# Appendix A

## THRMU-fit

THRMUfit finds the entrance point and the direction of the muons using ID PMTs. First, the THRMU-fit selects the PMTs with larger photoelectron than the threshold (optimized to 1.94 p.e.) to eliminate the dark hit PMTs. The first guess of the entrance point of the muon is at the position of inner PMT which have the largest number of p.e.s within 5 nsec from the earliest PMT which accompanied with more than 2 neighbouring hit PMTs. The direction of the muons is determined to the line connecting the entrance point and the center of the p.e.s in the ID. The evaluation function of the goodness of the fitting,  $G$ , is defined as:

$$G = \frac{1}{\sum \sigma_j^2} \sum_{i=1}^N \left( \frac{t_i - T_i}{\sigma_i} \right)^2 \quad (\text{A.1})$$

where  $N$  is the number of the picked-up PMTs,  $t_i$  is the hit timing of  $i$ th PMT, and  $\sigma_i$  represents the timing resolution of  $i$ th PMT which is set to 3 nsec.  $T_i$  is the expected hit timing of the  $i$ th PMT:

$$T_i = T^0 + \frac{l_\mu}{v_\mu} + \frac{l_{ph}}{c/n} \quad (\text{A.2})$$

where  $T^0$  is the timing of muon entering in the detector,  $v_\mu$  is the muon velocity (set to be  $c$ ),  $c/n$  is the light velocity in the water,  $l_\mu$  and  $l_{ph}$  is the travel length of muon and Cherenkov photon, respectively. Emission angle of the Cherenkov light is assumed to be  $42^\circ$ . Fig. A.1 shows the definition of these variables.  $G$  is maximized by scanning the direction around the initial values. If the final  $G$  is larger than the threshold value (optimized to 0.75), the fitter decide that the event is a muon event.

The performance of THRMU-fit was checked by using the downward cosmic ray muons, and the 99.5% of the downward-going cosmic ray muons are reconstructed as a downward-going muons.

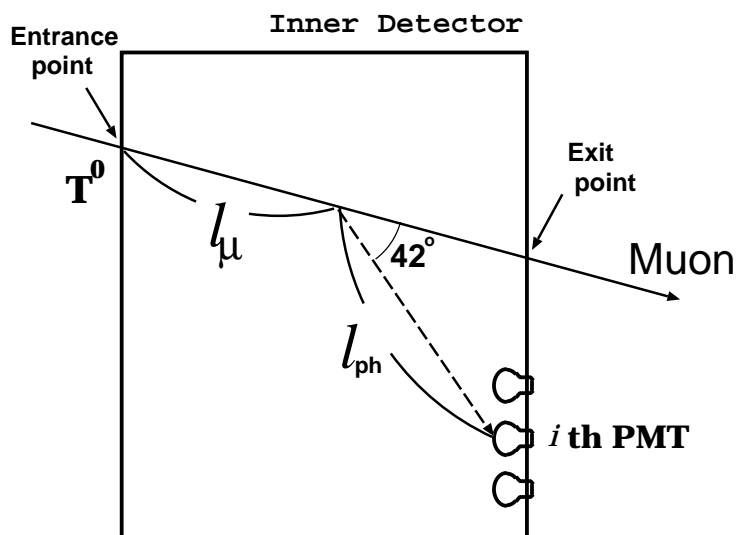


Figure A.1: The definition of the variables used in THRMU-fit.

## Appendix B

# Calculation of Expected Flux of Upward-going Muons

We describe the calculation methods of expected flux of upward-going muons. We employed an analytical method for the expected flux calculation. The reasons are: (1) Full Monte Carlo simulation including muon propagation in the rock needs a huge amount of computer time, (2) we only observe single muon and we don't need detailed simulations such as hadron production or propagations of multi particle in the detector. (3) event reconstruction is easy because of the simpleness of the event pattern, and the effect of the resolution of the event reconstruction is negligibly small for neutrino analysis.

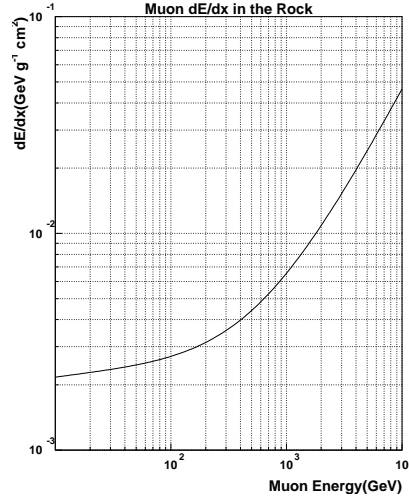
We also carried out Monte Carlo simulations in order to check the reasonableness of the analytical calculation. The results are consistent with each other.

### B.1 Calculation of Upward Going Muon Flux

Neutrino cross sections and the atmospheric neutrino flux are the same ones as used in FC and PC Monte Carlo simulations, but we consider only CC interactions. We adopt a energy loss function of muons in the rock from Lohman *et al.* [163]. The calculation includes the effects of all major process of energy loss: ionization, bremsstrahlung, direct pair production, and photo-nuclear interactions. Fig. B.1 shows the calculated  $dE/dx$  as a function of muon energy.

In the following calculation, we approximate muon zenith angle  $\cos \Theta_\mu \simeq \cos \Theta_\nu$  and simply describe  $\cos \Theta$ . The differential flux of muons induced by atmospheric muon neutrinos is given by:

$$\frac{d^2 \phi_\mu(E_\mu, \cos \Theta)}{dE_\mu d\Omega} = \int_{E_\mu}^{\infty} dE_\nu \int_0^1 dx \int_0^1 dy \delta(E_\mu - (1-y)E_\nu) \frac{d^2 \sigma_\nu}{dx dy} \cdot \frac{d^2 \phi_\nu(E_\nu, \cos \Theta)}{dE_\nu d\Omega} \quad (\text{B.1})$$

Figure B.1: Calculated muon  $dE/dx$  in the standard rock [163].

where  $E_\mu$  and  $E_\nu$  are the muon and neutrino energies,  $\cos \Theta$  is zenith angle of muons and neutrinos,  $d^2\phi_\mu/dE_\mu/d\Omega$  and  $d^2\phi_\nu/dE_\nu/d\Omega$  are differential fluxes of the muons and the neutrinos, and  $d^2\sigma_\nu/dx/dy$  is the differential neutrino cross section of CC interactions described in Chapter 7, respectively.  $\delta(x)$  is the delta function defined as:

$$\int dx f(x) \cdot \delta(x - x_0) = f(x_0) \quad (\text{B.2})$$

for any given function  $f(x)$ . Integration is over the Bjorken parameter  $x$  and  $y$  in a kinematically allowed region.

The muon flux with a energy greater than a given threshold energy,  $E_{th}$ , after traveling a distance  $X$  is given by

$$\frac{d^2\phi_\mu(E_\mu \geq E_{th}, \cos \Theta)}{d\Omega} = \int_0^\infty dX \int_{E_{th}}^\infty dE_\mu \frac{d^2\phi_\mu(E_\mu, \cos \Theta)}{dE_\mu d\Omega} \cdot g(X, E_\mu, E_{th}) \quad (\text{B.3})$$

where  $g(X, E_\mu, E_{th})$  is the probability that a muon generated with a energy of  $E_\mu$  survives with a energy greater than  $E_{th}$  after traveling a distance  $X$ . The function  $g(X, E_\mu, E_{th})$  can be written as:

$$g(X, E_\mu, E_{th}) = \Theta(R(E_\mu, E_{th}) - X) \quad (\text{B.4})$$

where  $R(E_\mu, E_{th})$  is the range of the muon whose energy decreases from  $E_\mu$  to  $E_{th}$ , and  $\Theta$  is the step function:

$$\Theta(x) = \begin{cases} 1 & \text{for } x \geq 0 \\ 0 & \text{for } x < 0 \end{cases} \quad (\text{B.5})$$

The integral over  $X$  is simply replaced by  $R(E_\mu, E_{th})$ :

$$\frac{d\phi_\mu(E_\mu \geq E_{th}, \cos \Theta)}{d\Omega} = \int_{E_{th}}^{\infty} dE_\mu \frac{d^2\phi_\mu(E_\mu, \cos \Theta)}{dE_\mu d\Omega} \cdot R(E_\mu, E_{th}) \quad (\text{B.6})$$

Inserting Eq.(B.1) into Eq.(B.6) and integrate over  $E_\mu$ , Eq.(B.6) is rewritten as:

$$\begin{aligned} & \frac{d\phi_\mu(E_\mu \geq E_{th}, \cos \Theta)}{d\Omega} \\ &= \int_{E_{th}}^{\infty} dE_\mu \left[ \int_{E_{th}}^{\infty} dE_\nu \int_0^1 dx \int_0^1 dy \delta(E_\mu - (1-y)E_\nu) \frac{d^2\sigma_\nu}{dx dy} \cdot \frac{d^2\phi_\nu(E_\nu, \cos \Theta)}{dE_\nu d\Omega} \right] \cdot R(E_\mu, E_{th}) \\ &= \int_{E_{th}}^{\infty} dE_\nu \int_0^1 dx \int_0^{y_{th}} dy \frac{d^2\sigma_\nu}{dx dy} \cdot \frac{d^2\phi_\nu(E_\nu, \cos \Theta)}{dE_\nu d\Omega} \cdot R((1-y)E_\nu, E_{th}) \\ &= \int_{E_{th}}^{\infty} dE_\nu \left[ \int_0^1 dx \int_0^{y_{th}} dy \frac{d^2\sigma_\nu}{dx dy} \cdot R((1-y)E_\nu, E_{th}) \right] \frac{d^2\phi_\nu(E_\nu, \cos \Theta)}{dE_\nu d\Omega} \\ &= \int_{E_{th}}^{\infty} dE_\nu P(E_\nu, E_{th}) \cdot \frac{d^2\phi_\nu(E_\nu, \cos \Theta)}{dE_\nu d\Omega} \end{aligned} \quad (\text{B.7})$$

where  $y_{th} = (E_\nu - E_{th})/E_\nu$  and

$$P(E_\nu, E_{th}) \equiv \int_0^1 dx \int_0^{y_{th}} dy \frac{d^2\sigma_\nu}{dx dy} \cdot R((1-y)E_\nu, E_{th}) \quad (\text{B.8})$$

The function  $P(E_\nu, E_{th})$  is interpreted as the probability that a neutrino of energy  $E_\nu$  is observed at the detector with a muon energy larger than  $E_{th}$ .

Combining the  $\nu_\mu$  and  $\bar{\nu}_\mu$  fluxes, Eq.(B.7) is replaced by:

$$\begin{aligned} & \frac{d\phi_\mu(E_\mu \geq E_{th}, \cos \Theta)}{d\Omega} \\ &= \int_{E_{th}}^{\infty} dE_\nu \left[ P_{\nu_\mu}(E_\nu, E_{th}) \cdot \frac{d^2\phi_{\nu_\mu}(E_\nu, \cos \Theta)}{dE_\nu d\Omega} + P_{\bar{\nu}_\mu}(E_\nu, E_{th}) \cdot \frac{d^2\phi_{\bar{\nu}_\mu}(E_\nu, \cos \Theta)}{dE_\nu d\Omega} \right] \end{aligned} \quad (\text{B.9})$$

The through-going muons flux is calculated by integrating the muon flux in Eq.(B.9) multiplied by the effective area of the detector:

$$\frac{d\phi^{\text{thr.}}(\cos \Theta)}{d\Omega} = \frac{1}{S(\cos \Theta, 7m)} \int_{7m}^{l_{\text{max}}} dl \frac{dS(\cos \Theta, l)}{dl} \cdot \frac{d^2\phi_\mu(E_\mu \geq E_{th}(l), \cos \Theta)}{d\Omega} \quad (\text{B.10})$$

where  $S(\cos \Theta, l)$  is the effective area of the detector for the through-going muons whose track length in ID is greater than  $l_{th}$  (see Fig B.2),  $l_{\text{max}}$  is the maximum thickness of the ID, and  $E_{th}(l)$  is the minimum energy to pass through a distance  $l$  in water. The minimum track length of the upward-going muons is set to be 7 m.

Flux of stopping muons are calculated by subtracting  $d\phi^{\text{thr.}}/d\Omega$  from  $d\phi^{7m}/d\Omega$  which is the flux of muons with the track length longer than 7m.

$$\frac{d\phi^{\text{stop}}(\cos \Theta)}{d\Omega} = \frac{d\phi^{7m}(\cos \Theta)}{d\Omega} - \frac{d\phi^{\text{thr.}}(\cos \Theta)}{d\Omega} \quad (\text{B.11})$$

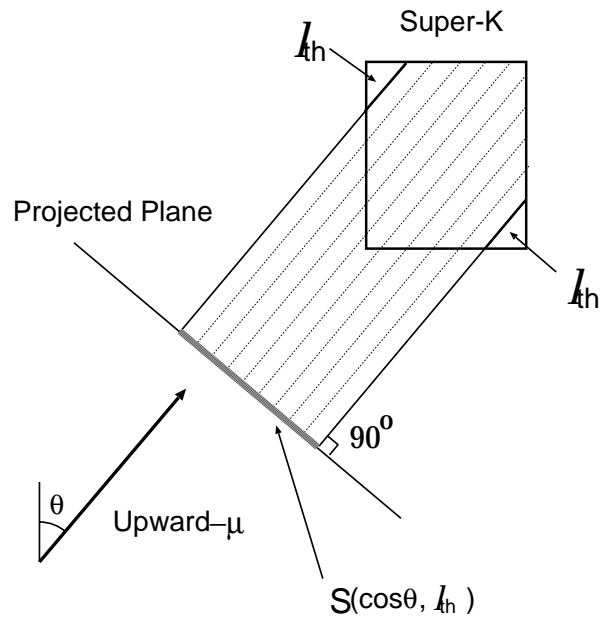


Figure B.2: The definition of the effective area  $S(\cos\theta, l_{th})$  in which the track length of the through-going muons is longer than  $l_{th}$ .

# Bibliography

- [1] W.Pauli, in *Letter open to the participants of the conference in Tübingen, 1930*
- [2] F.Reines and C.L.Cowan, *Nature* 178 (1956) 446
- [3] G.Danby et al., *Phys. Rev. Lett.* 9 (1962) 36
- [4] M.Goldhaber et al., *Phys. Rev.* 109 (1958) 1015
- [5] T.D.Lee and C.N.Yang, *Phys. Rev.* 104 (1956) 254
- [6] C.S.Wu et al., *Phys. Rev.* 105 (1957) 1413
- [7] S.L.Glashow, *Nucl. Phys.* 22 (1961) 579
- [8] S.Weinberg, *Phys. Rev. Lett.* 19 (1967) 1264
- [9] A.Salam, in *Elementary particle Theory, Proc. of the 8th Nobel Symposium, Aspenasgarden, 1968*, ed. by N.Svartholm (Almqvist and Wiksell, Stockholm, 1968) 367
- [10] F.Hasert et al., *Phys. Lett.* B46 (1973) 121
- [11] G.Arnison et al., *Phys. Lett.* B122 (1983) 103 ; *Phys. Lett.* B126 (1983) 398
- [12] M.Banner et al., *Phys. Lett.* B122 (1983) 476 ; *Phys. Lett.* B129 (1983) 130
- [13] G.S.Abrams et al., *Phys. Rev. Lett.* 63 (1989) 2173
- [14] B.Adeva et al., *Z. Phys.* C51 (1991) 179
- [15] G.Alexander et al., *Z. Phys.* C42 (1991) 175
- [16] P.Abren et al., *Nucl. Phys.* B367 (1991) 511
- [17] D.Decamp et al., *Z. Phys.* C53 (1992) 1
- [18] D.Decamo et al., *Phys. Lett.* B276 (1991) 247

- [19] Particle Data Group, *Review of Particle Physics* Euro. Phys. Journal C15 (2000)
- [20] K.A.Assamagan et al., Phys. Lett. B335 (1994) 231
- [21] R.Barate et al., Euro. Phys. Journal C2 (1998) 395
- [22] T.Yanagida, *Proceedings of the Workshop on the Unified Theory and Baryon Number in the Universe*, edited by O.Sawada and A.Sugamoto (KEK report 79-18,1979) 95
- [23] M.Gell-Mann et al., *Supergravity*, (North Holland, Amsterdam,1979)
- [24] L.Wolfenstein, Phys. Rev. D17 (1978)2369; Phys. Rev. D20 (1979) 2636
- [25] V.N.Zharkov, *Interior Structure of the Earth and Planets*, Harwood Academic Publisher, N.Y., 1986
- [26] A.M.Dziewonski and D.L.Anderson, Phys. Earth Planet. Interior 25 (1981)207
- [27] J.Bahcall and P.Krastev, Phys. Rev. 56 (1997) 2839
- [28] Z.Maki, M.Nakagawa, and S.Sakata, Prog. Theo. Phys. 28 (1962) 870
- [29] S.Coleman and S.L.Glashow, Phys. Lett. B405 (1997) 249
- [30] M.Gasperini, Phys. Rev. D38 (1988)2635 ; Phys. Rev. D39 (1989) 3606
- [31] S.Coleman and S.L.Glashow, Phys. Rev. D59 (1999) 116008
- [32] V.DeSabbata and M.Gasperini, Nuovo Cimento A65 (1981) 479
- [33] J.Schecheter and J.W.F.Valle, Phys. Rev.D22 (1980) 2227
- [34] A.Zee, Phys. Lett. B93 (1980) 389
- [35] L.Hall and M.Suzuki, Nucl. Phys. B231 (1984) 419
- [36] G.G.Ross and J.W.F.Valle, Phys. Lett. B151 (1985) 375
- [37] V.Barger et al., Phys. Rev. Lett. 82 (1999) 2640
- [38] A.Ackner, et al., Phys. Rev. D45 (1992) 907
- [39] G.Gelmini et al., Phys. Lett. B99 (1981) 411
- [40] D.A.krakauer et al., Phys. Rev. D44 (1991)R6
- [41] M.Aglietta et al., Euro. Phys. Lett. 8 (1989) 611

- [42] K.Daum et al., Z. Phys. C66 (1995) 417 ; C.Berger et al., Phys. Lett. B245 (1990) 489 ;  
C.Berger et al., Phys. Lett. B227 (1989) 489
- [43] K.S.Hirata et al., Phys. Lett. B205 (1988) 416
- [44] R.Becker-Szendy et al., Phys. Rev. D46 (1992) 3720; D.Casper et al., Phys. Rev. Lett. 66  
(1991) 2561
- [45] R. Clark et al., Phys. Rev. Lett. 79 (1997) 491
- [46] W.W.M.Allison et al., Phys. Lett. B449 (1999)137
- [47] Y.Fukuda et al., Phys. Lett. B335 (1994) 237
- [48] M.Ambrosio et al., Phys. Lett. B434 (1998) 451
- [49] Y.Fukuda et al., Phys. Lett. B433 (1998) 9
- [50] Y.Fukuda et al., Phys. Lett. B436 (1998) 33
- [51] Y.Fukuda et al., Phys. Rev. Lett. 81 (1998) 1562
- [52] Y.Futagami et al., Phys. Rev. Lett. 82 (1999) 1810
- [53] R.Becker-Szendy et al., Phys. Rev. Lett.69 (1992) 1010
- [54] S. Hatakeyama et al., Phys. Rev. Lett. 81 (1998) 2016
- [55] S.Mikheyev et al., in *Proceedings of TAUP'97*, Nucl. Phys. B70 (1999) 371
- [56] Y.Fukuda et al., Phys. Rev. Lett. 82 (1999) 2644; Y.Fukuda et al., Phys. Lett. B467 (1999)  
185
- [57] J.L.Vuilleumier et al., Phys. Lett. B144 (1982) 298
- [58] B.Achkar et al., Nucl. Phys. B434 (1995) 503
- [59] M.Apollonio et al., Phys. Lett. B466 (1999) 415
- [60] F.Boehm et al., hep-ex/0107009
- [61] R.Davis, Harmer and K.C.Hoffman, Phys. Rev. Lett. 21 (1968) 1205
- [62] K.S.Hirata et al., Phys. Rev. Lett. 65 (1990) 1297; Phys. Rev. D44 (1991) 2441, D45 (1992)  
2170E

- [63] SAGE collaboration, Phys. Rev. Lett. 83 (1999) 4686
- [64] W.Hampel et al., Phys. Lett. B388 (1996) 384
- [65] Y.Fukuda et al., Phys. Rev. Lett. 86 (2001) 5651 ; Y.Fukuda et al., Phys. Rev. Lett. 86 (2001) 5656; Y.Fukuda et al., Phys. Rev. Lett. 82 (1999) 2430
- [66] Q.R.Ahmad et al., Phys. Rev. Lett. 87 (2001)071301
- [67] E.Eskut et al., Phys. Lett. B497 (2001) 8
- [68] P.Astier et al., Nucl. Phys. B611 (2001) 3
- [69] This number is taken from <http://neutrino.kek.jp/news/2001.07.10.News/index-e.html>
- [70] N.Ushida et al., Phys. Rev. Lett. 23 (1986) 2897
- [71] F.Dydak et al., Phys. Lett. B134 (1984) 281
- [72] W.A.Mann, et al., hep-ex/0007031
- [73] M.Spurio et al., hep-ex/0101019
- [74] C.Athanassopoulos et al., Phys. Rev. C54 (1996) 2685; Phys. Rev. Lett. 77 (1996) 3082; Phys. Rev. Lett. 81 (1998) 1774
- [75] A.Aguilar et al., hep-ex/0104049
- [76] Klaus Eitel et al., *Proceeding of the 9th International Workshop on Neutrino Telescopes*, to be published.
- [77] Y.Fukuda et al., Phys. Lett. B335 (1994) 237
- [78] M.Honda et al., Phys. Rev. D52 (1995) 4985
- [79] V.Agrawal et al., Phys. Rev. D53 (1996) 1314
- [80] M.C.Gonzalez-Garcia, et al., Phys. Rev. D55 (1997) 1297
- [81] L.Pasquali et al., Phys. Rev. D59 (1999) 093003
- [82] M.Cercella et al., in *Proceedings of the 17th International Cosmic Ray Conference*, Calgary, Canada, 1993, edited by D.A.Leahy, R.B.Hickjs, and D.Venkatesan, Vol.4, p.503
- [83] G.Battistoni et al., hep-ph/9907408 ;Astropart. Phys. 12 (2000) 315-333

- [84] M.Honda, Private communications
- [85] I.Frank and I.Tamm, C.R.Acad.Sci. USSR 14,109 (193)
- [86] H.Kume et al., Nucl. Inst. and Meth.,205 (1983) 443
- [87] A.Suzuki et al., Nucl. Inst. and Meth.,A329 (1993) 299
- [88] T.Yamaguchi, Master Thesis, Osaka Univ., Mar. 1995
- [89] R.Beckerzندی et al., Nucl. Inst. and Meth, A234 (1993)363
- [90] R.Claus et al., Nucl. Inst. and Meth., A261 (1987)540
- [91] KEK Online Data Acquisition Development Group, KEK Report 85-10 (1985)
- [92] H.Ikeda et al., Nucl. Inst. and Meth.,A320 (1992)310
- [93] The ZEBRA System, CERN Program Library Long Writeups Q100/Q101
- [94] Y.Kitaguchi,*Attenuation Length Measurement in Super-Kamiokande, Master Thesis, Niigata Univ., Mar. 1996*
- [95] S.Inaba,*Scatter Light Measurement in Super-Kamiokande, Master Thesis, Niigata Univ., Mar. 1996*
- [96] P.Hanggi et al., Phys. Lett.B51 (1974)119
- [97] M.Yamada et al., Phys. Rev. D44 (1991) 617
- [98] M.Nakahata et al., Nucl. Instr. Meth. A421 (1999) 113
- [99] C.H.Llewellyn Smith, Phys. Rep. 3, 261 (1972)
- [100] R.P.Feynman, M.Gell-Mann, Phys. Rev. 109 (1958) 193
- [101] Particle data group, Rev. Mod. Phys. 52 (1980) S1
- [102] A.S.Vovenko et al., Yad. Fiz. 30 (1979) 1014
- [103] S.Barish et al., Phys. Rev. D16 (1977) 3103
- [104] S.Bonetti et al., Nuovo Cimento 38 (1977) 260
- [105] M.Pohl et al., Nuovo Cimento 26 (1979) 332, N.Arimenise et al., Nucl. Phys. B152 (1979) 365

- [106] A.S.Vovenko et al., *Yad. Fiz.* 30 (1979) 1014
- [107] S.Belikov et al., *Z. Phys.* 320 (1985) 625
- [108] C.H.Albright et al., *Phys. Rev. D* 14 (1976) 1780
- [109] K.Abe et al., *Phys. Rev. Lett.* 56 (1986) 1107
- [110] D.Rein and L.M.Sehgal, *Ann. of Phys.* 133 (1981) 1780
- [111] R.Feynman et al., *Phys. Rev. D* 3 (1971) 2706
- [112] M.Hirata et al., *Ann. Phys. (N.Y.)* 108 (1977) 116
- [113] G.Radecky et al., *Phys. Rev. D* 25 (1982) 116
- [114] T.Kitagaki et al., *Phys. Rev. D* 34 (1986) 2554
- [115] P.Allen et al., *Nucl. Phys. B* 264 (1986) 221
- [116] P.Allen et al., *Nucl. Phys. B* 176 (1980) 269
- [117] W.Lerche et al., *Phys. Lett.* 4 (1978) 510
- [118] J.Bell et al., *Phys. Rev. Lett.* 15 (1978) 1008
- [119] D.Allisia et al., *Ann. Phys.* 1983
- [120] S.J.Barish et al., *Phys. Lett. B* 91 (1980) 161
- [121] M.Derrick et al., *Phys. Rev. D* 23 (1981) 569
- [122] H.Grabosch et al., *Z. Phys. C* 41 (1989) 527
- [123] D.Rein and L.M.Sehgal, *Nucl. Phys B* 233 (1983) 29
- [124] C.H.Albright, C.Jarlskog, *Nucl Phys. B* 84 (1975) 467
- [125] M.Glück, E.Reya, and A. Vogt, *Z. Phys. D* 57 (1995) 433
- [126] H.Plochow-Besch CERN Program Library W5051 (1995)
- [127] S.Barlag et al., *Z.Phys. C* 11 (1982) 283
- [128] Paul Musset and Jean-Pierre Vialle, *Phys. Rep. C* 39 (1978) 1
- [129] J.E.Kim et al., *Rev. Mod. Phys.* 53 (1981) 211

- [130] T.Sjöstrand et al., CERN-TH-7112-93 (1994)
- [131] S.J.Barish et al., Phys. Rev. D17 (1978) 1
- [132] P.S.Auchincloss et al., Z. Phys. C48 (1990) 411
- [133] P.Berger et al., Z. Phys. C35 (1987) 443
- [134] S.Campolillo et al., Phys. Lett. 84B (1979) 281
- [135] O.Erriquez et al., Phys. Lett. 89B (1979) 309
- [136] J.V. Allaby et al., Z. Phys. C38 (1988) 403
- [137] N.J.Baker et al., Phys. Rev. D25 (1982) 617
- [138] C. Baltay et al., Phys. Rev. Lett. 44 (1980) 916
- [139] D.C.Colley et al., Z. Phys. C2 (1979) 187
- [140] V.B. Anikeev et al., Z. Phys. C70 (1996) 39
- [141] A.S.Vovenko et al., Yad. Fiz. 30 (1979) 187
- [142] D.B.MacFarlane et al., Z. Phys. C26(1984) 1
- [143] D.S.Baranov et al., Phys. Lett. 81B (1979) 255
- [144] K.Nakamura, et al., Nucl. Phys. A268 (1976) 381
- [145] L.Salcedo et al., Nucl. Phys. A484 (1998) 79
- [146] G.Rowe et al., Phys. Rev. C18 (1978) 584
- [147] E.Bracci et al., CERN/HERA 72-1, (1972)
- [148] A.S.Carrol et al., Phys. Rev. C14 (1976) 635
- [149] C.Ingram et al., Phys. Rev. C27 (1983) 1578
- [150] T.Fujii et al., Nucl. Phys. B120 (1977) 395
- [151] K.Baba et al., Nucl. Phys. A306 (1978) 292
- [152] J.Arends et al., Nucl. Phys. A526 (1991) 479
- [153] J.Hyslop et al., Phys. Rev. D46 (1992) 961

- [154] CERN Program Library W5013 (1994)
- [155] T.A.Gabriel et al., IEEE Trans. Nucl. Sci. 36 (1989) 14
- [156] M.Nakahata et al., J.Phys. Soc. Jpn. 55 (1986) 3786
- [157] O.G. Ryazhskaya, JETP Lett. 60 (1994) 617
- [158] T.H.Johnson, Phys. Rev. 43 (1933) 307; Phys. Rev. 43 (1933) 381 ; Phys. Rev. 48 (1935) 287
- [159] G.D'Agostini, Nucl. Instr. Meth. A346 (1994) 306
- [160] T.K.Gaisser et al., Phys. Rev. D57 (1998) 1977
- [161] V.Barger et al., Phys. Rev. Lett. 82 (1999) 2640
- [162] V.Barger et al., Phys. Rev. D25 (1982) 907
- [163] W.Lohmann, R.Kopp and R.Voss, 'Energy loss of Muons in the Energy Range 1-10000 GeV', CERN 85-03 (1985)
- [164] V.S.Berezenskii,C.Castagnoli and P.Geleotti, Nuovo Cimento C 8,185 (1985)